KINETO-DYNAMIC ANALYSES OF VEHICLE SUSPENSION FOR OPTIMAL SYNTHESIS

Krishna Prasad Balike

A thesis
In the Department of
Mechanical and Industrial Engineering

Presented in Partial Fulfillment of the Requirements
for the Degree of Doctor of Philosophy at
Concordia University
Montreal, Quebec, Canada

September 2010

CONCORDIA UNIVERSITY

SCHOOL OF GRADUATE STUDIES

This is to certify that the thesis prepared

By: **Krishna Prasad Balike**

Entitled: **Kineto-Dynamic Analyses of Vehicle Suspension for Optimal Synthesis**

and submitted in partial fulfillment of the requirements for the degree of

DOCTOR OF PHILOSOPHY (Mechanical Engineering)

complies with the regulations of the University and meets the accepted standards with respect to originality and quality.

Signed by the final examining committee:

_____ Chair
Dr. V. Chvatal

_____ External Examiner
Dr. J. McPhee

_____ External to Program
Dr. R. Zmeureanu

_____ Examiner
Dr. R. Sedaghati

_____ Examiner
Dr. H. Hong

_____ Thesis Co-Supervisor
Dr. S. Rakheja

_____ Thesis Co-Supervisor
Dr. I. Stiharu

Approved by

Dr. W-F. Xie, Graduate Program Director

September 29, 2010

_____
Dr. Robin A.L. Drew, Dean
Faculty of Engineering & Computer Science

ABSTRACT

Kineto-dynamic Analyses of Vehicle Suspension for Optimal Synthesis

Krishna Prasad Balike, Ph. D.
Concordia University, 2010.

Design and synthesis of a vehicle suspension is a complex task due to constraints imposed by multiple widely conflicting kinematic and dynamic performance measures, which are further influenced by the suspension damper nonlinearity. In addition, synthesis of suspension for hybrid vehicles may involve additional design compromises among different measures in view of the limited lateral packaging space due to larger sub-frame requirements for placing the batteries. In this dissertation research, a coupled kineto-dynamic analysis method is proposed for synthesis of vehicle suspension system, including its geometry and joint coordinates, and asymmetric damping properties. Quarter-car and two-dimensional roll plane kineto-dynamic models of linkage suspensions are proposed for coupled kinematic and dynamic analyses, and optimal suspension geometry and damper syntheses.

The kinematic responses of quadra-link and double wishbone types of suspensions are evaluated using the single-wheel kinematic models. Laboratory measurements were performed and the data were applied to demonstrate validity of the 3- dimensional kinematic model. A sensitivity analysis method is proposed to study influences of various joint coordinates on kinematic responses and to identify a desirable synthesis. A kineto-dynamic quarter car model comprising linkage kinematics of a double wishbone type of suspension together with a linear, and single- and two-stage asymmetric damper is subsequently proposed for coupled kinematic and dynamic analyses. The coupling between the various kinematic and dynamic responses, and their significance are

discussed for suspension synthesis. The effects of damping asymmetry on coupled responses are thoroughly evaluated under idealized bump/pothole and random road excitations, which revealed conflicting design requirements under different excitations. A constrained optimization problem is formulated and solved to seek design guidance for synthesis of a two-stage asymmetric damper that would yield an acceptable compromise among the kinematic and dynamic performance measures under selected excitations and range of forward speeds.

The coupled kinematic and dynamic responses in the roll plane are further analyzed through development and analysis of a kineto-dynamic roll-plane vehicle model comprising double wishbone type of suspensions, asymmetric damping and an antiroll bar. The results are discussed to illustrate conflicting kinematic responses such as bump/roll camber and wheel track variations, and an optimal geometry synthesis is derived considering the conflicting kinematic measures together with the lateral space constraint. A full-vehicle model comprising double wishbone type of suspensions is also developed in the ADAMS/car platform to study influences of faults in suspension bushings and linkages on the dynamic responses. The results of the study suggest that an optimal vehicle suspension synthesis necessitates considerations of the coupled kinematic and dynamic response analyses.

AKNOWLEDGEMENTS

The author is sincerely grateful to his supervisors, Dr. S. Rakheja and Dr. I. Stiharu, for their guidance, encouragement and financial support during this research dissertation. The author is also thankful to Dr. R. B. Bhat for his moral support and for being a source of inspiration throughout this study.

The author wishes to thank Mr. Bon Harold for his help in experimental setup and experimentation. The author further wishes to acknowledge his friends, colleagues, faculty and staff at the Mechanical Engineering Department and CONCAVE center, who have contributed to this work either directly or indirectly.

The author also thanks his brothers Mahesh and Ravi for both moral and financial support during the PhD program. The author is indebted to his parents and in-laws for their encouragements.

Finally, the author would like to make a special mention of his wife and daughter at this place for their full-fledged support and compromises throughout this work. The author dedicates this thesis to his wife, Asha and daughter, Ananya.

TABLE OF CONTENTS

LIST OF FIGURES

LIST OF TABLES

NOMENCLATURE

a, b, c, d, e, f, g, h	Relative joint coordinates in the kinematic equations
$a_{11}, a_{12}, a_{13}, a_{21}, a_{22}, a_{23}, a_{31}, a_{32}, a_{33}$	Elements of displacement matrix
$a_k, b_k, c_k, d_k, e_k, f_k, g_k, h_k, x_{1k}, x_{2k}$	Relative joint coordinates in the kinematic equations of roll plane model with k= R, L denoting right and left suspensions
cg	Center of gravity
f_{dis}	Discontinuous force component of an asymmetric damper
$f_{dj\text{-}c}$	Compression mode damping force on sprung and unsprung mass (j=s, u where s=sprung mass and u=unsprung mass)
$f_{djk\text{-}c}, f_{djk\text{-}r}$	Damping forces of the two-stage asymmetric dampers in compression and rebound on sprung and unsprung mass (j= s, u and k = R, L)
$f_{dj\text{-}r}$	Rebound mode damping force on sprung and unsprung mass
f_{ds}, f_{du}	Suspension damping force on sprung and unsprung mass
f_{dsk}, f_{duk}	left- and right-suspension damping forces acting on sprung and unsprung masses
f_{sL}, f_{sR}	Left and right suspension forces
f_{ss}, f_{su}	Suspension spring force on sprung and unsprung mass
f_{ssk}, f_{suk}	left- and right-suspension spring forces acting on the sprung and unsprung masses
f_{tbs}, f_{tbuk}	Forces transmitted to the sprung and unsprung masses due to the torsion bar
f_{tk}	Left and right tire forces (k=L, R)
f_{tls}, f_{tlu}	Wheel forces on sprung and unsprung masses due to tire lateral compliance

f_{tlsk}, f_{tluk}	Vertical tire forces acting on the sprung and unsprung masses due to the right and left tire lateral compliance
f_{tsu}, f_{tdu}	Wheel forces due to vertical stiffness and damping properties of the tire
h_{cg}	Center of gravity height
h_{rc}	Roll center height
l_{MN}, l_{OP}	Upper and lower control arms lengths of double wishbone suspension
l_{OA}	Distance of strut mount location A with respect to chassis joint O
$l_{P'P}$, $l_{P'C}$	Distances of points P and C from the instantaneous center
l_{s0}	Strut initial length
m_s, m_u	Sprung and unsprung mass
m_{uR}, m_{uL}	Right and left unsprung mass
q	Vector of unknown joint velocities
rms	Root mean square
s	Parameter vector
t	Time
$\bar{u}$	Unit vector
$\bar{u}_0$	Unit vector along quadra-link suspension upper control arm revolute axis
u_x, u_y, u_z	x- y- and z- components of a unit vector u
v	Design vector
w, w_1, w_2, w_3	Weighting factors
y_u	Wheel center lateral displacement

z_0	Vertical road input
z_{0max}	Maximum input displacement amplitude
z_{0R}, z_{0L}	Right and left road inputs
z_s	Sprung mass vertical displacement
z_u	Unsprung mass vertical displacement
z_{uL}, z_{uR}	Left and right unsprung mass vertical displacement
z_{umax}, z_{umin}	Upper and lower limits of wheel displacement inputs
z'_s, y'_s	Roll plane model sprung mass vertical displacement at center of gravity
$(\ddot{z}_s)_{p\text{-}1}$	First peak acceleration of sprung mass
$(\ddot{z}_s)_{p\text{-}2}$	Second peak acceleration of sprung mass
$\ddot{z}_{sRMS}$	RMS acceleration of sprung mass
A, B	Lower and upper strut mounts of double wishbone suspension
C	Wheel center
C_c	Compression damping coefficient
C_{crit}	Critical damping ratio
CDR	Camber displacement ratio
C_{eqv}	Linear equivalent damping coefficient
CIR	Camber increment ratio
C_r	Rebound damping coefficient
C_s, C_t	Suspension and tire damping coefficients
D	Dissipative energy
$D_{chassis}$	Chassis displacement matrix
Den	Denominator of linearized kinematic expressions

DLC	Dynamic load coefficient
$D_{spindlek}$	Left and right wheel spindle displacement matrix (k=L, R)
$D_{wheelspindle}$	Displacement matrix for wheel spindle
$F(v)$	Objective function
$F_1(v)$, $F_2(v)$	Components of objective function corresponding to ride quality and road holding measures
$F_{1\text{-}nom}$, $F_{1\text{-}nom}$	Magnitudes of F_1 and F_2 evaluated with nominal damper parameters
$F_{t\text{-}s}$, $F_{t\text{-}d}$	Static and dynamic tire forces
F_s	Spring axial force
F_w, F_{Wd}	Equivalent spring and damping vertical force at the wheel center double wishbone suspension
F_{WN}, F_{PN}	Equivalent spring force at the wheel center of double wishbone suspension acting normal to a line joining the instantaneous center with the wheel center.
G	Roll plane model sprung mass center
I_M	Input vector (wheel vertical velocity)
I_{ux}	Mass moment of inertia of the wheel about x- axis
I_{uxR}, I_{uxL}	Right and left unsprung mass moment of inertia about roll axis
I_x	Mass moment of inertia of sprung mass about the roll axis
J, K	Joint centers of S-S, R-S or R-R type of links
J_M	A matrix composed of joint coordinates
J_x, J_y, J_z and K_x, K_y, K_z	Instantaneous coordinates of J and K
J_{x0}, J_{y0}, J_{z0} and K_{x0}, K_{y0}, K_{z0}	Initial coordinates of J and K
K_{eq}, C_{eq}	Equivalent suspension and damper rate
K_M, K_O	Torsional stiffness of the bushings at joints M and O

K_s, K_t, K_{tl}	Suspension spring, tire vertical and lateral stiffness coefficients
K_{tb}	Antiroll bar stiffness
LCA	Lower control arm
M, *N*, *O*, *P*	Upper and lower control arms joints with chassis and knuckle of double wishbone suspension
M′, *N′*, *O′*, *P′*	Optimal double wishbone suspension joints centers
M1, M2, N1	Quadra-link suspension upper control arm joints with chassis and knuckle
M_R, O_R, M_L, O_L	Left and right chassis-suspension joint centers
N_m	Number of links in a mechanism
NWL	Normalized wheel lift-off
O1, P1	Front lower link joints with chassis and knuckle of quadra-link suspension
O2, P2	Rear lower link joints with chassis and knuckle of quadra-link suspension
O3, P3	Trailing link joints of quadra-link suspension
Opt-1$_b$, *Opt-2*$_b$,	Optimal solutions corresponding to compression mode damping ratio 0.1 and 0.2 obtained under bump input
Opt-1$_{bp}$, *Opt-2*$_{bp}$,	Optimal solutions corresponding to compression mode damping ratio 0.1 and 0.2 obtained under both bump and pothole inputs
Opt-1$_p$, *Opt-2*$_p$	Optimal solutions corresponding to compression mode damping ratio 0.1 and 0.2 obtained under pothole input
P′	Instantaneous center of rotation of double wishbone suspension
PSD	Power spectral density
R	Effective tire radius

Rc	Roll center
RDR_{max}	Maximum allowable rattle space ratio
RD_{RMS}	RMS of suspension deflection
RDR_p	Peak relative displacement ratio
RDR_{pp}	Peak to peak relative displacement ratio
R_m	Number of revolute joints in a mechanism
R-R	Revolute-revolute link
R-S	Revolute-spherical link
S_m	Number of spherical joints in a mechanism
SQP	Sequential quadratic programming
SRDR	Sprung mass relative displacement ratio
S-S	Spherical-spherical link
SSAR	Sprung mass shock acceleration ratio
T	Kinetic energy of the model
T_{cL}, T_{cR}	Antiroll bar attachment points at left and right side of the chassis
TDFR	Tire dynamic force ratio
$T_{dsk\text{-}c}$, $T_{dsk\text{-}r}$	Moments of damping forces developed in compression and rebound imposed on the forces on the sprung mass
TFR	Tire force ratio
T_L, T_R	Left and right wheel-ground contact points
T_{sL}, T_{sR}	Antiroll bar attachment points at left and right suspensions
T_{ssk}, T_{dsk}	Moments due to right- and left- suspension spring and damping forces
T_{tbs}	Torque transmitted to the sprung mass due to the torsion bar

T_{tlsk}	Moments of the forces imposed on the sprung mass due to the right- and left- tire lateral compliances
UCA	Upper control arm
U	Potential energy of the model
V	Vehicle forward velocity
V_1, V_2	Vehicle forward velocity range limits
WLDR	Wheel center lateral displacement ratio
WLO	Wheel lift off
α_r, α_c	Velocity of transition from low- to high-speed damping in rebound and compression
β	Maximum allowable absolute camber angle corresponding to cumulative probability of 0.95
β_l, β_u	Lower and upper limit constraints for roll center height variation
γ	Pulse severity parameter of a rounded pulse displacement input
$\Delta(\phi_R)_{\text{jou}}$, $\Delta(\phi_R)_{\text{reb}}$	Peak bump camber angles of right wheel under jounce and rebound
$\Delta\phi_R$	Camber variation of right wheel
Δ(RCH)	Variation in the roll center height with respect that of the nominal suspension geometry
$\Delta(\text{TW})_{\text{jou}}$, $\Delta(\text{TW})_{\text{reb}}$	Peak variations in wheel track width under 100 mm of wheel jounce and rebound
ΔTW	Change in track width
Δl, Δz_t	Strut and tire deflections
δ_{mean}	Mean shift in sprung mass position from the equilibrium
δ_{st}	Static deflection
ζ_c	Compression mode damping ratio

θ	Wheel spindle rotation about *y*- axis (caster angle)
$\theta_M,\ \theta_O$	Upper and lower control arm rotation angles
θ_s	Spring inclination angle
θ_T	Angular deformation of the antiroll bar
θ_w	Angle made by the effective force normal to a line from the instantaneous point to the wheel center, with the vertical axis
λ_r, λ_c	Rebound and compression mode damping reduction factors
ρ	Damper asymmetry ratio
σ_1, σ_2	Limit constraints on the lateral packaging space
ψ	Wheel spindle rotation about *z*- axis (toe angle)
$\Psi,\ \Psi_d$	Geometry factors those relate the equivalent spring and damping rates to the suspension rates.
ω_0	Rounded pulse rising frequency
ϕ	Wheel spindle rotation about *x*- axis (Camber angle)
φ	Rotation of wheel spindle about the screw axis
$\phi_L,\ \phi_R$	Left and right wheel camber angles
ϕ_{RMS}	Root mean square of camber angle variation
ϕ_s	Chassis roll angle
ϕ_{smin}, ϕ_{smax}	Upper and lower limits of chassis roll inputs

CHAPTER 1

INTRODUCTION AND LITERATURE REVIEW

1.1 Introduction

The design and synthesis of a vehicle suspension is known to be a highly complex task due to widely conflicting design constraints imposed by the various performance measures, namely the ride, handling and directional control. The design compromises between the ride comfort, road holding and the working space have been widely studied considering the dynamic responses of the vehicle models. Syntheses of suspension systems considering various vehicle performance measures have been extensively reported in the literature. These studies could be grouped in two different categories on the basis of the performance measures, (i) synthesis of suspension geometry focusing on selected kinematic performance criteria; and (ii) synthesis of forcing elements such as springs, dampers, and the antiroll bar (passive, semi-active or active), which consider various dynamic performance measures. These studies have considered suspension and vehicle models of varying complexities, although linear or nonlinear quarter-car models have been most widely used to evaluate the ride, rattle space and the dynamic tire force responses of suspension design concepts, and synthesis of semi-active and active suspension control strategies. The dynamic performance measures are also strongly coupled with the kinematic response measures, while such coupling effects are rarely considered in vast majority of the reported vehicle models with the exception of comprehensive models formulated in multibody dynamics simulation softwares. For instance, the road holding and handling dynamic performance of vehicles are strongly related to wheel orientation which is a complex function of various kinematic measures

such as wheel camber, toe and caster angles. It has been suggested that minimizing the variation in these angles through consideration of coupled effects could help achieve improved road holding performance [1, 2].

Dynamic analyses of one-, two-, and three- dimensional models have substantially contributed to suspension design for enhancement of ride, pitch, lateral and roll dynamic performances of the vehicles. The contributions due to non-linear kinematic motions of the linkages and bushings, however, could not be identified. Furthermore, conventional dynamic vehicle models assume constrained motions of the unsprung masses along the vertical direction. In an independent suspension system, the wheel carrier or the spindle is generally connected to the chassis through the suspension linkages, which induce rotational motion of the wheel about the vehicle longitudinal axis apart from the vertical motion. Suspension kinematics thus contributes considerably to the vertical and roll dynamic responses. Furthermore, both the dynamic and kinematic responses of a road vehicle are strongly dependent upon the suspension damper properties in a highly complex manner.

Automotive suspension dampers invariably exhibit asymmetric damping characteristics in compression and rebound, with considerably greater damping during rebound than in compression, while the contributions due to damping asymmetry have not been adequately addressed in the reported studies. The damping asymmetry coupled with the nonlinear kinematic responses of the suspension could significantly alter the dynamic responses, particularly the drift in the vehicle equilibrium position. Although the asymmetric suspension damping is widely implemented and is highly desirable in view of the road holding performance, the reasons for such asymmetry have not been explicitly

defined, which in-part can be attributed to limited understanding of influences of damper asymmetry on the kinematic and dynamic responses of the vehicle. The design guidance for such asymmetry have been limited to a general rule of thumb suggesting that a rebound to compression damping ratio in the order of 2 or 3 would reduce the force transmitted to the sprung mass while negotiating a bump [1, 2].

Systematic study of asymmetric damping together with coupled kinematic and dynamic effects would thus be desirable to establish design guidelines. Such a study would also be beneficial in realizing suspension synthesis for emerging hybrid vehicles that impose greater challenges related to sprung mass and sub-frame space requirements, and thus the chassis design [3]. The larger space requirements of the hybrid vehicles also necessitate considerations of the suspension synthesis with limited lateral space, which would most likely involve complex compromises among the different performance measures. Furthermore, such a study would enable the considerations of flexibility due to joint bushings, which influence the dynamic responses of the vehicle considerably. Inclusion of the bushing properties in the vehicle dynamic model, however is challenging due to highly nonlinear properties of the flexible bushings. Moreover, the bushing wear and joint clearances can affect not only the dynamics of the vehicle, but also the operational safety. A timely detection of the bushing clearance or the onset of probable failure would thus help prevent potential vehicle break down. Apart from the suspension kinematics and joints flexibility, the tire lateral compliance can also influence the dynamic responses of the vehicle. The synthesis of automotive suspension thus necessitates a thorough understanding and considerations of the couplings between the

suspension linkage kinematics with the dynamic responses of the vehicle, together with the tire and joint compliances, and the asymmetric damping.

The primary objective of this dissertation research is thus formulated towards synthesis of a vehicle suspension system including its geometry and joint coordinates, and asymmetric damping properties through coupled kinematic and dynamic analysis. This dissertation research involves developments in kinematic, and one- and two-dimensional kineto-dynamic models of the vehicle suspension system incorporating the coupled kinematic and dynamic responses and the lateral tire compliance. The influences of joint coordinates on the kinematic and dynamic response characteristics are investigated and discussed in view of the track variation and lateral space requirements in hybrid vehicles. The study is further concerned with the selection of optimal joint coordinates and asymmetric parameters of a two-stage damper considering the design conflicts among the different kinematic and dynamic responses. Influences of suspension faults including those in joint bushings, damper and linkages on the dynamic responses of the suspension are also presented.

1.2 Literature Review

The suspension synthesis process involves considerations of influences of suspension components on the various dynamic responses of the vehicle including ride, roll, handling dynamics and directional stability. The analyses and syntheses of independent suspension systems thus require an essential fundamental knowledge of the component properties, the ride and handling dynamics of the vehicle, suspension kinematics, tire-road interactions, modeling methods, characterization of joint bushings, and more. The reported relevant studies are thus thoroughly reviewed and briefly discussed in the

following sections to gain fundamental knowledge and to formulate the scope of the dissertation research.

1.2.1 Synthesis of Independent Suspensions for Road Vehicles

The independent suspension designs offer considerable advantages over the dependent type of suspension such as smaller space requirement, easier steerability, lower weight and absence of mutual wheel influence. It has been identified that the absence of mutual wheel influence is beneficial in good road holding, particularly during cornering on a bumpy road surface [4]. MacPherson strut and double wishbone type of suspension constitute the majority of the independent suspensions in the road vehicles [1, 2], while multi-link suspensions, including the quadra-link and five-link types, are increasingly being employed in the passenger cars [5, 6]. The study of suspension kinematics or suspension geometry involves the analyses of coupling between the unsprung mass and the sprung mass [1]. The kinematic design of an independent suspension is considered to be a complex task due to couplings between various kinematic responses of the suspension including the wheel center trajectories in the pitch and roll planes, and variations in camber, toe and caster angles. These kinematic properties of the suspension are strongly coupled with the vertical and roll motions of the vehicle. For instance, a suspension designed for minimal camber variation during wheel vertical travel yields a large camber variation during vehicle roll [4, 7-9].

Earlier stages of the conventional suspension design process involve kinematic analysis of the suspension mechanisms, particularly, the wheel centre trajectory and changes in the wheel aligning parameters with the wheel vertical travel [4,10]. The changes in the track width, roll centre height and motion ratios are other parameters of

interest in the kinematic analysis [10]. In such analyses, the chassis, suspension links and the wheel-tire assembly are generally assumed as rigid bodies, while the contributions due to joints flexibility are considered negligible [5, 6, 10-12].

The suspension kinematic responses have been studied using graphical, analytical or experimental means. Graphical methods were widely used in the earlier studies to estimate the suspension kinematic parameter changes, before the wide spread use of computers [4, 13]. The graphical method poses considerable complexities for predicting the trajectories of spatial suspension mechanisms and may yield considerable errors. Numerous analytical models of varying complexities have been developed to study the kinematic responses of various types of commonly used suspensions including the MacPherson strut, double wishbone and multilink suspensions [6, 11, 12, 14-17]. The planar kinematic properties of a suspension can be effectively analyzed considering the suspension system as a planar mechanism. The position analyses of planar mechanism can generally be carried out by solving the mechanism loop closure equations [11, 18] or by displacement matrix methods [19, 20]. While the planar representation of the suspension makes it possible to analyze some of the kinematic properties, such as camber variation with roll or bump in the roll-plane, such models ignore the existence of steering mechanisms and kinematic effects of steer or caster angles. It would be possible to represent the mechanism in the pitch or yaw-plane to estimate such kinematics effects.

Three-dimensional or spatial kinematic analyses are considered instrumental for determination of variations in the steer, camber or caster angles simultaneously, taking into account the coupled kinematic effects of suspension linkages. The reported spatial kinematic models use loop closure equations, displacement and transformation matrices

for the displacement analysis, while the orientations of the wheel are derived from the geometrical relations [6, 11, 12, 14, 16, 17, 21]. Cronin [11] proposed a kinematic model of a MacPherson suspension based upon vector algebra. The mechanism was assumed to have two- degrees of freedom (DOF) including the jounce motion of the wheel carrier and rotation of the knuckle about the strut axis to represent the steering motion. Position loop equations were written for displacement of each of the two mechanism loops (chassis-wheel knuckle-strut-chassis and chassis-knuckle-tie rod-rack-chassis). Further, nonlinear scalar expressions in terms of the suspension geometry were obtained for the displacement of each link. A similar kinematic models of the MacPherson suspension have also been proposed by Suh [14] employing the displacement matrix method, and using Euler transformation [21].

Suh [14, 19, 20] proposed the use of displacement matrices for analysis and synthesis of the spatial suspension mechanisms, defined by multi loop spatial guidance mechanisms with single-DOF assigned to each loop. The motions of the mechanisms were described by using displacement, velocity and acceleration matrices together with the constraint equations for each of the suspension link. The application of displacement matrix method was demonstrated for a double wishbone suspension. Rae *et al*. [15] demonstrated that Euler angles and Euler parameters can be effectively used to describe the motion of the wheel carrier of the double A-arm suspension.

A vast number of studies have also reported spatial kinematic analysis of complex five-link rear suspension mechanisms [5, 6, 12, 17, 22, 23]. The five-link rear suspension is considered as the basic multi-link suspension configuration with five distinct links connecting the wheel carrier to the chassis. Unlike the MacPherson or double wishbone

suspensions the kingpin axis is not clearly defined in the multi-link suspension, which makes the kinematic modeling a challenging task [6, 12]. Lee *et al*. [6] proposed a method to estimate the wheel centre and linkage joint trajectories as a function of wheel vertical movement using rigid body velocity vector relations. The instantaneous velocities of different joint centers in the wheel carrier were expressed by vector sum of wheel center velocity and cross product of angular velocity and position vector from wheel center to the joints. Another set of equation was obtained from the condition that the dot product of velocity of each joint at wheel carrier and their position vectors from the chassis would be zero. These equations could be solved to yield velocities of each joint for a given wheel vertical velocity. The study concluded that the solutions of the equations were sensitive to the wheel vertical velocity.

Knapczyk *et al*. [12, 26] performed kinematic analysis of a five-link suspension considering a transformed mechanism with upper two links removed. The joint positions of the transformed mechanism were described by the spring length and two orientation angles formed by the control arms. An optimization problem was formulated describing the condition that the distances between the coupling joints remain equal to the lengths of the disconnected members. The optimal solutions for the joint positions were applied to determine the camber and toe angles, and coordinates of the wheel-road contact point through the vector relations. Simionescu [5] formed a motion generation synthesis problem for the synthesis and later for the kinematic analysis of a five-link suspension. The study formulated an optimization problem that allowed the wheel carrier, released from its joints, to move in successive positions along an ideal trajectory (vertically upwards in the case of suspension), while the distance between the joints of individual

links vary as little as possible. The solution of the minimization problem resulted in wheel carrier displacement and orientation. All of the reported analyses of five-link suspension have shown similar kinematic responses.

The kinematic analyses of suspension mechanisms have employed various multi-body dynamic tools, such as ADAMS [10, 27, 28]. The ADAMS/car and ADAMS/chassis modules provide platforms to build suspension models and permit the kinematic analysis with or without considering the joints compliance [27, 28]. The parallel wheel analyses of suspensions in ADAMS/car module provide various kinematic responses, including variations in the camber, caster and toe angles, and roll center height as a function of wheel vertical motion. Shim *et al*. [27] developed front MacPherson and rear multilink suspension mechanisms models in ADAMS/car platform to perform the parallel wheel analyses, which were subsequently integrated to the full vehicle model. The validity of the MacPherson and rear multilink suspension models was demonstrated using the measured kinematic properties.

Although, the kinematic analyses of different suspension mechanism have been widely reported, only a few studies have investigated the suspension linkage kinematics through laboratory experiments [21, 26, 27, 29]. The measured data reported in these studies have been widely used for model verifications. The reported studies have shown reasonably good agreements between the model responses and the measured data in terms of camber change and contact-point trajectory, while considerable differences in the toe angle response were observed. Mantaras [21] demonstrated the validity of the MacPherson suspension mechanism model by using the measured kinematic responses. Ozdalyan *et al*. [29] in a similar manner used measured data acquired from a McPherson front

suspension set-up to validate the model developed in the ADAMS platform. Knapczyk *et al*. [26] used a half-car five-link suspension set-up to experimentally investigate the kinematics and elasto-kinematics of the suspension with the goal of evaluating the influence of deflections of the elastic bushings on spatial displacements of the wheels. The model validity was demonstrated using the measured camber, toe and steer angles. It was shown that the wheel contact-point and the wheel center trajectory, and camber and caster angles, predicted by the model were reasonably close to the measured data with peak difference being below 10%, while the toe angle response showed larger deviation.

The reported studies have suggested that kinematic responses of an independent suspension are highly influenced by the joint coordinates and linkage lengths in a complex manner, while identification of most influential joint coordinates continues to be one of the most challenging tasks in the synthesis process [30]. Raghavan [7, 13] specified the requirements of the suspension mechanisms for limiting the wheel motion in the vertical plane, irrespective of the vehicle attitude. The wheel motion, however, was strongly coupled with vertical and roll motion of the vehicles. A suspension designed for minimal camber variation during wheel vertical travel would thus yield a large camber variation during vehicle roll [4, 7-9]. It has thus been recognized that changes in the camber angle and the wheel track cannot be avoided under roll motions and that compromises in various performance measures are inevitable with the existing suspension configurations.

A number of studies have attempted to synthesize optimal suspension geometry that could achieve better compromise between the conflicting kinematic response characteristics of various suspension mechanisms, including the MacPherson's, double

wishbone and multilink types of suspensions [5, 24, 30-34]. Majority of these studies have employed, predefined kinematic target measures, in the form of desired wheel path, and variations in camber and toe angles with the wheel vertical travel considering only a single suspension [5, 30, 31]. Li *et al*. [34] considered minimal track-width, camber and toe angles variations with the wheel vertical travel, as the objective functions for optimizing the geometry of a multilink suspension developed in the ADAMS/car platform. While the model assumed fixed chassis, the optimal suspension geometry showed reduced camber angle and track width variations, with increased variations in the toe angle when compared to the responses of the original suspension.

Relatively fewer studies have considered the suspension systems on both sides of axle to incorporate the contributions of the chassis roll. Habibi [24] employed genetic algorithm to identify optimal joint coordinates of a MacPherson's suspension mechanism in order to yield design compromise among the roll steer and bump steer responses. Fijita *et al*. [32] proposed an optimization methodology for the synthesis of front and rear wheels multilink suspensions by minimizing an objective function comprising the deviations from the desired toe and camber angle variations, roll centre height, and sprung mass responses e.g. roll angle, lateral acceleration and vertical vibration amplitude. The methodology involved identification of 92 design parameters that included the coordinates of the suspension joints and suspension rates. Significant improvements in the vehicle ride and handling dynamic responses were claimed to be achieved by the study, although related results were not presented by the study.

Numerous studies have proposed alternate suspension configurations, or modification to the existing kinematic designs in order to reduce the couplings effects [7, 9, 35, 36].

Raghavan [7] proposed addition of an intermediate linkage between the independent suspension and the sprung mass to achieve zero camber angles during vehicle roll. The additional linkage with revolute joint was expected to provide an additional DOF to the system. The physical implementation of the concept, however, was considered to be complex due to additional link. Deo *et al*. [35] proposed a novel six bar suspension mechanism to reduce couplings between the different kinematic parameters. The axiomatic design method, employed in the study, identified that the wheel aligning parameters and the suspension vertical travel are coupled in the existing four-bar type of suspension mechanisms. The study suggested that the identified couplings can be decoupled by increasing the number of links in the mechanism. However, the camber angle variations due to sprung mass roll could not be incorporated into the design problem. Furthermore, the proposed mechanism had limitations due to the increased number of links and joints and associated higher cost and unsprung weight [35].

Heuze *et al*. [9] proposed an optimal contact patch (OCP) suspension mechanism to prevent the wheel camber during vehicle roll by providing an additional degree of mobility to the mechanism. The aim of the proposed mechanism was to obtain a negative camber while cornering, only by the application of the ground lateral loads. The study was limited to the roll-plane of the vehicle, which did not thus permit the analyses of the influences of the new configuration on other kinematic parameters. Sharp *et al*. [36] presented a kinematic cross-linked suspension system with two diagonal interconnections between two independent suspensions of an axle. The cross linked suspension allowed the camber angle of right hand side wheel to be influenced by the left wheel bounce. The study showed that such cross-linking reduced the sprung mass roll motion considerably,

and yielded minimal camber variations during wheel bounce and sprung mass roll. However, the suspension design was relatively more sensitive to geometric changes.

Apart from the above mentioned conflicting kinematic measures; namely, bump/roll camber, bump/roll steer (toe angle), caster angle and wheel track variations, the packaging space limitations pose additional challenges during design of the suspension geometry. Raghavan [13] proposed synthesis of a planar suspension configuration considering the lateral packaging space and wheel camber variations as the performance measures. Lateral packaging space limitation becomes a predominant design constraint in the design of suspension systems for hybrid vehicles, which require a large subframe or chassis space for placing the batteries or fuel cells [3, 37].

1.2.2 Suspension Joint Bushings

The vehicle suspension joints bushings are typically composed of a hollow elastomer cylinder contained between inner and outer steel sleeves. The flexible bushings help isolate road induced vibration, reduce noise transmission, accommodate oscillatory motions and accept misalignments of axes. The flexibility of the joint bushings of suspension mechanisms contributes to wheel compliance particularly in the lateral direction, which influences the handling dynamics of the vehicle in a significant manner [4, 38, 39]. The bushing design requirements are thus conflicting in that the vehicle handling performance requires stiff bushings, while the ride comfort demands highly compliant joint bushings [40]. Furthermore, the bushing properties are highly nonlinear in translational and rotational directions due to the nature of the elastomeric material [38, 41-43].

Various studies have reported compliance properties of suspension joint bushings in terms of linear or nonlinear force-displacement or force-velocity relations [22, 26, 38, 43-45]. These have generally suggested two different approaches to obtain force-displacement relations for the elastomeric bushings: (i) through solutions of the analytical boundary value problem of classical mechanics; and (ii) through experiments on sample specimens [38]. Within the classical mechanics approach, a three-dimensional equation relating the stresses and strains under a range of deformation and time conditions were formulated. The approach, however, was considered highly cumbersome [38, 41]. Consequently the experimental approach of determining the force-displacement properties has been widely used. This approach, however, does not permit identification of a general relationship and requires repeated measurements for bushings at different stages of wear and for new bushing designs [38, 43]. Further, the response of the flexible material at local levels cannot be determined.

Experiments conducted on the joint bushings materials have shown that the displacement reaches within 2% of the fully relaxed value 20 seconds after the application of the force, which is attributable to the visco-elastic properties of the bushings [41, 43]. Further studies have shown that the force-displacement or moment-rotation relations of bushing materials are influenced by the type of loading. For instance, under coupled mode (radial and torsional) of deformation, the radial force decreases with an increase in the torsion to reach a minimum value, while a further increase in torsion causes increase in the radial force [41]. The dynamic characteristics of the bushings have been captured through identifications of the model components properties, which may include a simple spring or a spring with a viscous damping element with or without

consideration of the friction damping [44, 45, 46]. Dzierzek [46] proposed a bushing model comprising springs, viscous and friction damping in conjunction with two sets of in-series springs and viscous damping elements, all assumed to be in parallel. Pu *et al*. [44, 45] considered nonlinear bushing model to include in-parallel spring and damper that are connected in series to another spring element. The parameters were identified by comparing the frequency responses of the proposed model with the experimental data. The proposed model with the identified parameters was shown to yield comparable force force-displacement and force-velocity characteristics to those of the measured data.

The compliance in the suspension joint bushings can shift the joint centers when the mechanism is assembled, which can thus alter the kinematic and dynamic responses [47, 48]. Messonnier *et al*. [47] proposed an identification method for the bushing model to study the influences of geometric shifts in the bushing centers. The proposed model comprised springs in three orthogonal directions, and the identification procedure involved measurements of the suspension geometry and use of a multiplication algorithm in conjunction with the force-deflection relations. The force-deflection relations were obtained by simulating the suspension model developed in a multibody dynamic platform. Such identification process, however, required precise measurements of the reference coordinates on the suspension assembly in addition to the multibody dynamic simulation tool for estimating the bushing forces [48].

Suspension joint bushing properties in static or quasi-static conditions have been analyzed by a few studies employing either analytical models [22, 26, 49], or multi-body dynamic tools [42]. Such analysis, also known as *elasto-kinematic analysis*, provides useful information on the influences of bushing compliance on variations in the kinematic

responses such as wheel camber, caster and toe angles during the wheel relative motion with respect to the sprung mass. Knapczyk *et al*. [26, 49] investigated the influences of five-link suspension joints and subframe bushings properties on the wheel compliance by comparing the suspension kinematic responses under three conditions, namely: (i) non-compliant joints; (ii) bushing compliance represented by radial spring alone; and (iii) bushing compliance represented by three linear orthogonal springs. The wheel center displacement, and toe and camber angle responses were evaluated as a function of the wheel vertical travel and compared with the experimental data. The responses of the model with bushings characterized by three orthogonal springs showed a closer resemblance to the experimental data. It was shown that the suspension subframe bushings compliance influence the toe angle and wheel longitudinal displacement, while a negligible influence were observed on the toe angle under a braking force input.

Blundell [42] investigated the influences of joint bushings on the suspension kinematic responses including variations in camber, caster and steer angles, wheel track and roll centre height using a trailing arm rear suspension model in the ADAMS platform. The study compared the responses of the model with non-flexible joints, bushing joints with linear stiffness and bushing joints with nonlinear stiffness. It was revealed that the variations in the camber and caster angles and wheel track increase marginally by including the bushings in the analysis, while the toe angle variation reduced considerably. The suspension with nonlinear bushing model showed comparable responses to those of the model with linear bushing model. Caputo *et al*. [50] performed similar analyses for a five-link suspension and concluded that the bushings of the camber link influence the camber angle and track properties.

Flexible bushings invariably used in suspension joints have also been modeled by translational and rotational springs along three axes, particularly in the model analyzed using multibody dynamic formulations [51] or available software tools [42, 52] for the dynamic analyses. For example, ADAMS software permits bushings models with three translational and three rotational spring and damping elements [28, 42]. Yang *et al*. [52] conducted a sensitivity analysis in order to study the influences of the front suspension bushing rates on the vehicle impact harshness under bump excitation using a full-vehicle model with linear translational bushing compliance developed in ADAMS/car. The study showed that the impact harshness performance was dominantly affected by the fore-aft bushing stiffness of the lower control arm and vertical stiffness of the upper shock mount. It was further shown that the impact response was significantly affected by the vehicle forward velocity significantly. The joint bushing flexibility can also influence the fatigue life of the suspension arm apart from the ride and handling dynamics of the vehicle [53]. The effect on the fatigue life was illustrated through the stress analysis of the MacPherson suspension control arm, and it was shown that the life cycle (S/N ratio) of the suspension components can be increased significantly through careful synthesis of the bushing properties.

1.2.3 Joint Clearances and Fault Diagnostics

Majority of the studies related to the kinematic and dynamic responses of the vehicle suspension have assumed idealized suspension joints with negligible clearances [5, 6, 17]. Although a few studies have shown considerable influences of suspension joints bushing on the dynamic responses, even fewer studies have been reported on the effects of suspension bushing clearances [54, 55]. The effects of bushing clearances on the

kinematic and dynamic responses of various mechanisms, however, have been extensively reported [56-60]. These studies have invariably shown that the clearances in the joints of any mechanism yield most significant repeated impacts between the mating members, apart from the undesirable kinematic responses.

The forces in the clearance joints are generally estimated either by continuous contact models, where the forces arising from the collisions are assumed as continuous function of deformation or by discontinuous contact models that assume instantaneous impacts. Flores *et al*. [56, 57, 60] studied the clearances in revolute joints of a four bar mechanism using continuous contact model with radial spring elements. The study showed abrupt variations in the responses of a rigid four bar mechanism, while the responses were evaluated in terms of velocity and acceleration of the slider, the moment acting on the crank, and the relative motion between the journal and the bearings. Further, a small change in the magnitude of the clearance, in the order of 10 μm showed considerable variation in the responses. The consideration of link elasticity in the model, however, can reduce the peak contact force [58]. The models proposed in the analyses of general mechanisms could be effectively applied to study the effects of bushing clearance on the kinematic and dynamic responses of various suspension mechanisms.

The influence of faulty damper and upper strut bushings on the dynamic responses has been studied by Azadi *et al*. [54, 55]. The study employed a full vehicle model with front- and rear- rigid type of suspension, developed in the ADAMS/car platform. Faulty damper in the study, was modeled by reduced damping coefficient, while the faulty bushing at the upper strut mount was modeled by a discontinuity in the force-displacement characteristic of the bushing. The study showed higher wavelet signal

energy of the sprung mass pitch acceleration of the model with faulty bushings than that with the nominal bushing and the vertical acceleration response of the wheel connected with the faulty damper and bushings was higher than those of other wheels. The observed response trends could be applied for developing a bushing fault detection algorithm, although the study was limited to the clearance in the upper strut bushing only. Suspension fault detection has been attempted in only a few other studies employing simple lumped-parameter vehicle models [61] or finite element full vehicle models [62]. These studies, however, were concerned with the fault detection in the suspension spring or damper, while an optimal number of sensors and their locations were also discussed. The detection of faults in the joint bushings due to clearances, however, was not considered in these studies.

1.2.4 Handling Dynamics of Road Vehicles

The handling dynamic analyses of road vehicles consider forces and moments caused during directional maneuvers. The vehicle ride and handling dynamics in practical vehicle designs have been thoroughly discussed by Crolla [63], while the handling dynamics of vehicles are generally studied under transient and steady-state maneuvers [64, 65]. The transient handling dynamics relates to time-varying directional responses to a given maneuver, which are generally evaluated in terms of lateral acceleration, yaw rate, roll angle, roll rate, understeer coefficient, etc. Such responses have been evaluated under different maneuvers, such as steady state cornering, cornering with braking, straight line braking and path change type of maneuvers [65]. Steady-state handling performance, on the other hand, is concerned with the directional behavior during a steady turn under non-time varying conditions [65, 66].

An understeer vehicle is known to be unconditionally directionally stable, while an oversteer vehicle could lead to directional instability at speeds near or above the critical speed [1, 65, 66]. Some studies have also suggested that the understeer coefficient of a vehicle should be maintained relatively constant during both the linear and nonlinear slip angle ranges in order to retain consistent drivers' control [67, 68]. Other studies have proposed contradictory handling requirements suggesting that a higher understeer coefficient with increasing lateral acceleration would be desirable, so as to improve vehicle yaw or directional stability [64, 66]. Vehicles tend to understeer while accelerating during cornering, but could lead to oversteering tendency during braking-in-cornering maneuver [69]. The suspension damping together with the kinematic response of the suspension can influence the understeer coefficient of the vehicle in a considerable manner. For example, a higher front suspension damping coupled with a lower rear suspension damping can result in greater understeering tendency [68, 69].

The steering and braking maneuvers cause lateral and longitudinal load transfers, which may result in significant changes in the handling and stability limits of the vehicle [1, 67]. It is well known that the lateral forces and moments developed at the tires strongly determine the lateral or handling dynamics of the vehicle, and the cornering forces are strong nonlinear function of the coefficient of adhesion, normal load, slip angle and the slip ratio [67, 68, 70]. A large number of studies on handling dynamics have employed simple vehicle models with linear or non-linear tire models [71-73], while the contributions due to suspension kinematics and asymmetric damping were ignored in these studies.

The handling dynamics of road vehicles have been extensively studied through linear and nonlinear analytical models of varying DOF. The linear 2- DOF bicycle model that considers vehicle lateral velocity and yaw rate as the degrees-of-freedom had been used in earlier studies on steady-state and transient handling analyses [65, 66, 68, 74, 75]. In the linear bicycle model, the effects of suspension kinematics, vehicle roll and lateral load transfer are ignored and constant forward speed with linear tire characteristics is assumed. Such assumptions would be reasonably valid at lateral accelerations below 0.3 or 0.4g [74, 75, 76]. Although the lateral and longitudinal load transfers have been incorporated in the simple models through suspension roll rates or with an additional roll DOF, the effects of suspension kinematics were still ignored in such models [65, 74]. Further studies have shown that a yaw-plane model with reduced roll DOF could yield considerable deviations from the measured data by as much as 15% at lateral accelerations exceeding 6 m/s^2.

The suspension kinematics can significantly alter the wheel camber, caster and toe, and the roll center heights, and thereby handling properties of vehicles. Numerous have investigated the handling dynamics of vehicles using models comprising the suspension kinematics. The majority of these employed multi-body dynamic models to study the handling responses of vehicles to steering and braking inputs [74, 76-81]. Janson and Oosten [74] employed a 36- DOF multibody dynamic model that included suspension kinematics and joint compliance, which revealed deviations from the measured data in the order of 5%. The reported three- DOF yaw-plane models with reduced roll-DOF and elaborate multibody models had incorporated Magic Formula tire models for calculating

the tire forces, while the yaw-plane models ignored the suspension kinematics and considered a stationary roll axis passing through the suspension roll centers.

Hegazy *et al*. [76] proposed a 34 mass, 94- DOF vehicle model including the suspension nonlinearities for transient handling dynamics analysis under a double lane change type of maneuver at a constant forward speed of 90 km/h, as described in the international standard, ISO-3888 [82]. The model included suspension kinematics and joint compliances, while the tire forces were estimated using the Magic Formula. The study concluded that the model can be effectively used for handling dynamic analysis even though the model validation was not discussed. Further studies by the same authors have shown that the multibody dynamic vehicle model, developed in ADAMS platform, is useful in correlating various forces developed at the tire road interface, such as high magnitude abrupt peaks in the vertical tire forces may be related to suspension bump stop forces in the opposite direction [81]. A simplified 18- DOF multibody dynamic vehicle model was proposed by Sayers *et al*. [80] to study the handling and braking response of a road vehicle. The model considered 6- DOF for the sprung mass and a vertical DOF for each of the four unsprung masses, while auxiliary DOF were considered for the spin rate and tangent of delayed lateral slip angle contributing to the relaxation length of the tires.

Multibody dynamic analysis tools, such as ADAMS, could provide considerable flexibility in modeling the dynamic vehicle system, although very little interpretations could be made from the equations generated within the software [77-79]. Furthermore, such models require considerable data which suggests that the complexity of computer-based modeling is dependent upon the particular application and the objective. For instance, inclusion of bushings while modeling a double wishbone suspension is

considered to have only a minimal influence on the camber change during wheel vertical travel [77]. The transient response analyses under a double lane change maneuver at a speed of 100 km/h could thus be performed using a simple yaw-plane vehicle model with equivalent roll stiffness as opposed to the full suspension linkage model [76, 79, 81]. It was further shown that such a vehicle model would overestimate the lateral acceleration and roll angle responses in the absence of camber effects, while similar yaw rate responses could be obtained without consideration of the camber [79].

The levels of required modeling complexity have long been debated in developing vehicle models for dynamic analyses [83]. The engineers and analysts in the industry often generate quite complex models to achieve greater accuracy. The academic researchers, however, have put forward the view that typical industry-used vehicle models are too complex and inefficient as design tools [10, 70, 84]. Sharp [84] suggested that an ideal model should possess minimum complexity and be capable of solving the concerned problems with an acceptable accuracy.

1.2.5 Ride Dynamics of Vehicles

Ride comfort performance of a passenger vehicle has been the key design goal during the synthesis of the automotive suspension system. The ride performance of road vehicles is generally assessed in terms of two measures: (i) objective vibration performance of the vehicle expressed by the acceleration responses of the chassis evaluated either from field measurements or through simulation; and (ii) subjective evaluations of occupant comfort [1, 66, 85]. The objective evaluations of occupant comfort performance have also been reported on the basis of frequency-weighted acceleration as defined in ISO 2631 [86]. Considering that the road induced vibration is directly associated with the occupant

comfort, extensive efforts have been made to realize suspension designs for attenuating the road induced vibration. These studies generally employed acceleration responses of the sprung mass as measure of the ride quality.

Interactions of the tires with the road roughness serve as the primary excitations when evaluating the ride performance of the suspension, although the rattle space requirement and road holding properties are also incorporated in the analyses [66, 87]. The ride properties of vehicles have been evaluated under varying excitations at the tire-road interface, including harmonic [1, 66, 88, 89], idealized bump and pothole inputs [90, 91] and randomly distributed road roughness inputs. The assessments of the vehicle responses under road roughness excitation, however, are considered vital for suspension designs and evaluations [92, 93, 94]. While time histories of road profiles are generally used as the inputs to the nonlinear analytical vehicle models, the road roughness is generally characterized by its power spectral density (PSD) [93, 95].

The dynamic properties of the tire, road profile and their interactions are critical for suspension development. The most widely used and simplest model of tires representing their fundamental mode of vibration is the linear point-contact spring in parallel with a viscous damping element [2, 66, 87, 96]. Captain *et al*. [96] proposed and compared the responses of four different tire models in a single DOF vertical dynamic model of the vehicles, namely: (i) a point contact tire model; (ii) a rigid tread band tire model, which is the modified form of the point contact tire model with a roller type contact between the tire and the road; (iii) a fixed foot print tire model, which interacts with the ground through a foot print of constant size independent of the tire deflection; and (iv) an adaptive foot print model which consists of flexible tread band inflated by internal

pressure, linked to the wheel center by radially distributed stiffness and damping elements. The study concluded that all the four models yield comparable results under low frequency excitation, while the point contact model can overestimate the transmitted tire force significantly at higher frequencies. An adaptive foot print tire model was shown to yield good results over a wide range of frequencies, while it involves demanding parameter identification and computations.

The analytical studies on ride dynamics involve modeling of essential suspension components with varying degrees of complexities. The reported ride dynamic models include one, two or three dimensional models with varying DOF. One dimensional single- or two- DOF quarter-car models have been widely used to study different concepts in suspension and the vertical dynamics of the vehicles. These models include either linear or nonlinear spring or dampers [2, 66, 97], and tire vertical properties [92, 98]. Two-dimensional half-car, 2- to 4- DOF models with linear or nonlinear suspension and tire models have been used to study the pitch and roll ride response coupled with the vertical dynamics [2, 66, 99, 100]. The vertical ride, roll and pitch dynamic responses of vehicles have been investigated more comprehensively using the three-dimensional full-car models [101, 102]. These include 7-DOF full-car models comprising heave, roll and pitch motions of the sprung mass, and the vertical motions of the independent unsprung masses. Influence of suspension properties including those of the spring rate, damping (passive, semi-active or active), and antiroll bars on vertical, roll and pitch responses have been widely explored by such ride models [101, 102]. Such models, however, ignore longitudinal, lateral and yaw motions of the vehicle, and cannot be employed to analyze handling and directional dynamic responses of the vehicle. A few studies have

employed three-dimensional full car models to study the ride and handling properties of vehicles and role of suspension design [103-105]. These models consider the yaw and lateral motions of the sprung mass in addition to the heave, pitch and roll motions. Such models were proved to be instrumental in studying the influences of road induced vibrations on the handling dynamics of the vehicles.

The ride performances of road vehicles strongly depend on the suspension properties, namely the stiffness and damping parameters. A damper in an automotive suspension system plays a vital role in the ride and handling dynamics of a vehicle, while modeling of damper properties is considered as a challenging task due to its highly nonlinear behavior. The nonlinearity in the damper is attributed to its dependency on the damping valves, gas spring, end bushings, temperature sensitivity and the hysteresis. The damper characteristics are typically represented by force-velocity curves. The suspension damping properties and their effects on various vehicle performance measures have been extensively investigated under different inputs, including the contributions due to gas spring, bushings compliance, and temperature and hysteresis effects [89, 106-111].

Hardware-in-the-loop (HiL) test and analysis techniques have been developed in a few studies to investigate the contributions due to suspension damping. These studies, in general, integrate the measured damping force of the damper hardware in response to suspension deflections that is derived from a quarter-vehicle simulation models [112-114]. The HiL method thus permits consideration of contributions due to nonlinearities effects that are difficult to model, such as the effects of bushings, temperature variations and damping valves. Misselhorn *et al*. [112] investigated the suitability of HiL method of analysis for suspension development using a quarter-car model of a vehicle. It was shown

that the displacement response predicted by the quarter-vehicle model simulation was lower than that derived from the HiL simulation under a step input, while it was higher for a bump input. A delay between the two responses was also observed, which was attributed to the phase lag of the servo-hydraulic actuation system. The study further compared the results attained from HiL simulation with those measured from a quarter-car experimental setup. The study observed the phenomenon of stick-slip within the quarter-car setup, which was in-part attributed to the bushing properties causing large resistive force at low speeds and small resistive force at high speeds. The HiL simulation techniques have also been applied for synthesis of controllers for various semi-active and magneto-rheological fluid dampers [114-116]. Although a HiL technique can provide efficient simulations of suspension nonlinearities, the contributions due to suspension kinematics, particularly the rotation of the damper strut, are entirely ignored.

Automotive suspensions invariably employ asymmetric dampers, which exhibit higher damping coefficient in rebound than in compression. The precise reasons for such asymmetry, however, have not been explicitly quantified [117], which is most likely attributed to highly complex dependence of different performance measures on the damping asymmetry. Furthermore, the effects of damping asymmetry greatly depend upon the nature of excitation and suspension responses. The reported results thus do not permit the design guidance for damping asymmetry, which has been limited to a general rule of thumb suggesting that a rebound to compression damping ratio in the order of 2 or 3 would reduce the magnitude of the force transmitted to the sprung mass, while negotiating a bump [1,2]. Only a few studies, however, have attempted to quantify the

effects of asymmetric damping on the vehicle responses to transient excitations idealizing bumps or potholes [94, 117, 118].

Fukushima *et al*. [119] investigated the influence of asymmetric damping on ride comfort and concluded that a lower damping in compression than in rebound would yield significant reduction in the initial sprung mass acceleration peak response to a bump excitation. The study, however, did not present the effect of damping asymmetry on the subsequent response peaks or the responses to a pothole type of excitation. Verros *et al*. [91] investigated the transient response of a single-degree-of-freedom (DOF) quarter-car model with single stage asymmetric dampers with rebound to compression damping ratios of 3 and 1/3 under pothole excitations. The study showed considerable influences of the damping asymmetry on the sprung mass acceleration and rattle space responses.

A few studies have also suggested that damping asymmetry causes suspension 'packing' or 'jacking down' [88, 89], while no efforts have been made to quantify such phenomenon in relation to the suspension kinematics. Using a quarter-car model employing a nonlinear damper model with asymmetric damping rates, Warner *et al*. [88] showed that the damper asymmetry causes change in the ride height or 'dynamic drift', which is dependent upon the low-speed compression and rebound damping coefficients. Rajalingham and Rakheja [89] presented variations in the vehicle ride height in terms of alternating and mean components of the suspension deflection, where the mean component represented the magnitude of packing down of the asymmetric suspension. In a similar manner, Eslaminasab [120] decomposed the damping force due to a single stage asymmetric damper under harmonic excitations into a symmetric component and a discontinuous component attributed to the damping asymmetry. Simms *et al*. [118] also

showed the presence of drift under random road excitations using a quarter-car model incorporating hysteresis model of a damper. The simulation results obtained with an asymmetric damper with relatively higher rebound damping revealed offset in the suspension rattle space response, which was not evident with the linear damping.

The reported studies generally describe nonlinear asymmetric damping by piecewise linear functions in compression and rebound considering either single-stage or two-stage (low- and high-speed) damping coefficients. Ahmed *et al*. [121] described the nonlinear asymmetric damping by an array of locally linear damping constants using the principle of energy similarity to study the frequency response of a quarter-car model employing a two-stage asymmetric damper. Calvo *et al*. [122] showed that a piecewise linear damper model, which takes into account the differences between the compression and rebound behaviors, and incorporates the low- and high-speed damping, can yield acceptable results in all the driving maneuvers.

Synthesis of optimal damper characteristics in compression and rebound has been a challenging task, which is mostly attributed to couplings among the different performance measures together with complex dependence on various parameters of an asymmetric multi-stage damper. A number of studies have attempted to identify optimal suspension parameters including dampers with linear or piecewise linear force-velocity characteristics in order to achieve better compromises among the ride, suspension deflection and road holding measures. He and McPhee [123] critically reviewed reported automated design synthesis approaches for ground vehicle suspension developments.

Dahlberg [94] optimized the natural frequency of the sprung mass and the damping ratio considering a linear suspension damper to achieve an improved compromise

between the ride comfort and road holding measures under random road excitations. A few other studies [124, 125] suggested the use of genetic algorithm (GA) based multi-objective programming technique for attaining optimal values of linear stiffness and damping coefficients using either simple quarter-car or full-vehicle models.

A few studies have also attempted to identify optimal asymmetric damping using different vehicle models and excitations. Verros *et al*. [92] derived optimal values of the asymmetry ratio using a 2-DOF quarter-car model under random road excitations, and concluded that the optimum values are dependent upon a number of operating factors such as the forward speed, the road roughness and the target performance measure. Georgiou *et al*. [126, 127] employed multi-objective evolutionary methods to derive optimal damping coefficients for the single- and two-stage aymmetric dampers using a conventional quarter-car and a multibody dynamic full vehicle models. These studies considered the deterministic pothole type or random road excitations, and concluded that the optimal damping coefficients depend upon the forward speed of the vehicle and design criteria selected, as suggeted in [92]. Optimal damping characteristics suggested by these studies were thus a complex function of the forward velocity of the vehicle with significant differences in the identified optimal damping coefficients corresponding to lower and higher vehicle velocities. This in-part could be attributed to limited understanding of influences of damper asymmetric properties in relation to the vehicle forward velocities, particulalry under random road excitations.

1.2.6 Influences of Suspension Kinematics on Dynamics of the Vehicle

Influences of suspension kinematics on the handling dynamics have been reported in many studies. These generally suggested that the suspension kinematics strongly

influence the lateral load transfer, wheel camber and toe angles and thereby significantly alters the forces developed at the tire-road interface [4, 5, 18, 75, 76, 79]. The chassis roll is also known to cause changes in the camber and steer angles and thus the handling performance. The roll camber influences both transient and steady handling responses, while the roll steer does not have significant influence on the transient response of the vehicle since it increases gradually with the chassis roll [5, 18, 81]. It is, however, suggested that inclusion of roll steer in the handling analysis is crucial owing to its considerable influence on the steady state responses [67]. The changes in the camber and toe angles during a wheel bump also causes lateral forces to develop at the tires. These forces influence the sensation of poor handling and require additional efforts from the driver in terms of corrective steering to overcome the change in direction due to tire slip angles [7]. The suspension kinematics in many of these studies is characterized by equivalent roll stiffness.

Nalecz *et al*. [18, 67] proposed a three-mass (sprung, front and rear unsprung masses) 3- DOF nonlinear model to study the influence of suspension linkage kinematics on vehicle stability. The model considered lateral, yaw and roll motions with vehicle roll motion about the roll axis, while the cornering stiffness was determined as a nonlinear function of instantaneous normal load, comprising the static as well as the dynamic lateral weight transfer. The tire forces were determined using 'friction ellipse concept', with lateral forces as nonlinear function of normal load, slip angle and tire skid number. The stability analysis was based upon lateral acceleration, yaw rate and roll angle responses to various handling maneuvers, including combined braking and steering. The study concluded that representation of roll stiffness in lieu of suspension kinematics is

not adequate since 20-70% of the total lateral load transfer can be attributed to the body roll and the roll center movement. Furthermore, 6-8% of the total lateral load transfer can be due to the unsprung masses depending upon the type of suspension used. Further studies by the same authors considered the tire forces due to wheel camber and toe obtained through spatial kinematic analysis [18]. The handling responses to ramp-steer input showed that the lateral forces developed at the tires due to camber and steer angles can have negative influence on the stability of the vehicle. Minimal variations in these angles were thus considered as desirable. The findings, however, were based on responses to ramp steer inputs alone, while the variations in the effective spring rate due to suspension kinematics were ignored.

A simplified 18- DOF multibody dynamic vehicle model was proposed by Sayers *et al*. [80] to study the handling and braking response of a road vehicle. The model considered 6- DOF for the sprung mass and vertical DOF for each of the four unsprung masses, while auxiliary DOF were considered for the spin rate and tangent of delayed lateral slip angle contributing to the relaxation length of tires. Furthermore, the model incorporated suspension kinematic effects of toe-change and camber change via look-up tables. Lateral acceleration and yaw rate responses to a step-steer input showed similar trends as those of the detailed (suspension kinematics) model while the simple model underestimated the roll angle response at speeds greater than 20 m/s. Further studies on the multibody dynamic full vehicle model with suspension linkages have shown that such a vehicle model overestimates the lateral acceleration and roll angle responses in the absence of camber effects, while similar yaw rate responses could be obtained without consideration of the camber [79].

Influence of suspension kinematic properties on vehicle roll response was studied by Shim *et al*. [8]. The roll angle response of the vehicle model with front MacPherson and rear multi-link suspension, developed in ADAMS/car, was investigated under a fishhook maneuver. The study showed that an increase in toe-in reduces the sprung mass roll angle with an increase in the understeer gradient. A decrease in the camber-change reduces the sprung mass roll angle response, while the understeer gradient increases. The study further showed that increases in the roll-center height and caster angle cause the roll response to decrease.

Although influences of suspension kinematics on handling and roll dynamic responses under steering input have been reported in many studies, the vast majority of the vertical ride dynamic models ignore the contributions of suspension kinematics. Conventional ride models serve as effective tools for assessing different concepts in suspension components, the complex contributions due to linkages and bushing properties cannot be evaluated [63, 87]. In an independent suspension system, the wheel carrier or the spindle is generally connected to the chassis through the suspension linkages, which induce rotational motion of the wheel apart from the vertical motion. The center of rotation of the wheel greatly relies on the suspension geometry and tends to influence the dynamic responses of the vehicle. Furthermore, the suspension strut is generally mounted away from the unsprung mass center (cg) and thus the point of application of spring and damping forces and the unsprung mass are not colinear. Furthermore, the vast majority of the suspension yield asymmetric kinematic responses during bump and rebound, which would add to the asymmetry in the dynamic responses attributed to asymmetric damping properties.

Only a few studies have attempted to incorporate the suspension kinematic nonlinearities into the vertical dynamic model [90, 128-133], using different approaches, particularly for the quarter-car models. Kim *et al*. [90] identified equivalent suspension parameters namely, the sprung and unsprung masses, suspension spring rate, and damping rates in compression and rebound, of a simple quarter car model using the responses of a 3-D model developed in ADAMS software. The study showed that the identified parameters of a double wishbone suspension vary considerably with changes in the control arms lengths or the strut inclination angle. The parameters of a MacPherson suspension, however, were less sensitive to geometric variations. Similarly, the responses of a nonlinar multibody dynamic MacPherson suspension model were obsereved to be comparable to those of a linear quarter-car model with identified parameters [129]. The identification of equivalent parameters of a linkage suspension may require measurements of repsonses of the physical suspension system which would be cumbersome. Considering the strong effects of variations in the suspension geometry and joint coordinates, such variations in a physical suspension, however, would be extremely demanding.

Other studies have proposed models of the linkage suspensions, although the vast majority have focussed on the MacPherson suspension. Stenson *et al*. [131] proposed a planar non-linear dynamic model of a MacPherson suspension using the kinematic relations derived from the suspension geometry. The dynamic analyses were conducted asuming the chassis as fixed, while the tire dynamics was neglected. Hong *et al*. [128] developed a two-DOF quarter-car model, as illustrated in Fig. 1.1 (a), considering sprung mass vertical displacement and the control arm rotation as the generalized coordinates.

The model included the kinematics of the control arm and the strut, while the strut was assumed to be mounted on the control arm. Fallah *et al*. [132] extended the MacPherson suspension model, proposed in [128], by locating the strut on the wheel spindle, as shown in Fig. 1.1 (b). The dynamics of the system were derived considering the camber rotation and lateral displacement of the wheel. The study also investigated the variations in the wheel track, and camber, caster and kingpin angles during dynamic events. The above-cited studies on MacPherson suspension quarter-car models [128, 132] considered the tire as a vertical spring, while the contribution due to its lateral compliance was ignored. Moreover, these studies compared the responses of the kineto-dynamic models with those of a conventional quarter-car model assuming that the strut positioned on the wheel center provides equivalency between the two models, therby ignoring the kinematics of the strut.

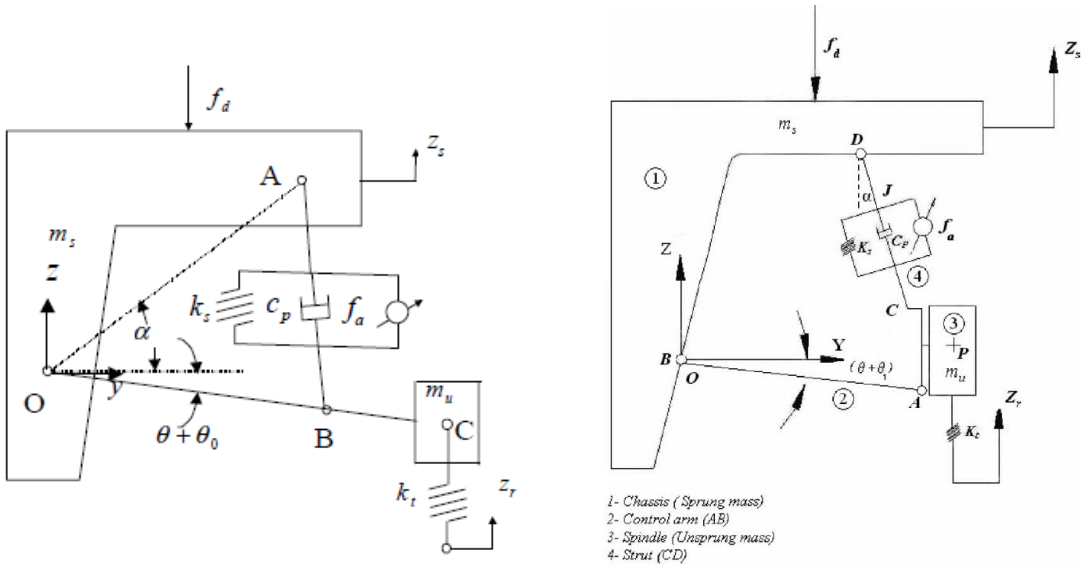

(a) (b)

Figure 1.1: Schematics of the quarter-car model comprising linkage kinematics of the MacPherson suspension configuration: (a) strut on the control arm [128]; and (b) strut on the wheel knuckle [132].

Kim *et al*. [90] concluded that the contribution of the MacPherson suspension kinematics on the equivalent parameters and the dynamic responses are considerably small. The strut location away from the wheel center, however, yields some effects of the kinematics. The kinematics of a double wishbone suspension may yield considerably stronger effects on the dynamic responses compared to the MacPherson suspension. This is attributable to kinematics associated with the additional control arm, strut location on the lower control arm and additional kinematic constraints. The identification of coupling between the linkage kinematics of a double wishbone suspension and the dynamics has been attempted in a single study, although such a suspension has been most widely used. Joo [133] proposed a kineto-dynamic quarter-car model of a double wishbone suspension considering the control arm lengths and angles as the geometric parameters for developing an active control strategy, while, the tire lateral compliance was ignored. Furthermore, vertical spring and damping elements were considered, and thus the effects of strut inclinations were ignored, as shown in Fig. 1.2. The study had concluded that the model responses were sensitive to the joint coordinate variations, while a synthesis of the suspension geometry considering such influences was not considered in the study.

The conventional roll-plane vehicle ride models with vertical- and roll- DOF of the sprung mass have generally ignored the contributions due to suspension kinematics and considered the vehicle roll axis passing through the sprung mass center or sprung mass roll motion about a roll center [83, 134-136]. A few studies have used extended models with incorporating the lateral degree-of-freedom of the sprung mass [83, 134]. Majority of these studies, however, consider a dependent type of suspension, used in heavy vehicles, where suspension kinematics would be of negligible importance.

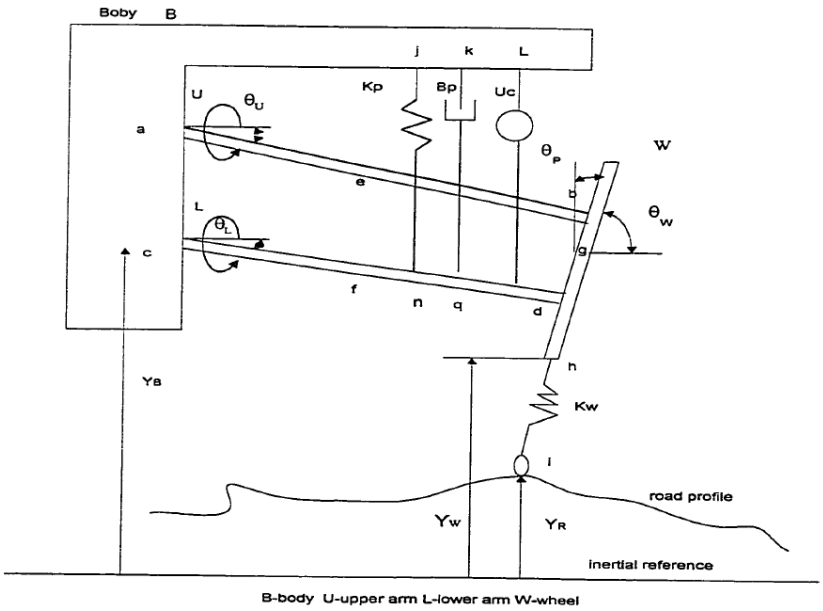

Figure 1.2: Quarter-car model comprising linkage kinematics of double wishbone type of suspension configuration [133]

Stone and Cebon [135] considered five- DOF roll-plane model of a vehicle with independent type trailing arm suspension. The influence of linkage kinematics of independent type of suspensions has been reported in another study on the synthesis of an active suspension for minimizing the body roll [136]. The study considered a simple suspension model comprising a single suspension arm between the chassis and the wheel assembly. The unsprung mass in both the models, however, was permitted only a vertical DOF with no consideration of its rotation about the vehicle longitudinal axis.

Consideration of joint bushing properties in the dynamic analyses requires a more comprehensive vehicle model with suspension linkages and the types of joints and their coordinates. Multibody dynamic tool, ADAMS/car, was used by Azadi *et al*. [56] in order to study the influences of faulty damper and upper damper bushings on the dynamic responses of the vehicle. The full vehicle model in this study comprised of rigid type

suspension (both front and rear) with A-arms connecting the chassis and the axle with joints bushings.

1.3 Scope of the Proposed Dissertation Research

From the review of literature it is evident that vehicle suspension design involves considerable challenges in order to realize acceptable compromises in ride, handling, directional control and road holding performances with reasonable durability. It involves a thorough analysis of the suspension kinematics, and its contributions to the dynamic responses of the vehicle, such as the ride, handling and directional control performances. Moreover, the dynamic responses are highly influenced by the vertical and lateral properties of the tire. Conventional studies on the suspension synthesis and related concepts consider kinematics of the suspension in the initial stages of suspension design, which are generally performed to achieve a compromise among variations in roll and bump camber, toe angles, and wheel track and wheelbase. These kinematic measures are mostly selected considering the handling dynamics and the road holding performances only, while the influences of these responses on the vertical dynamics of the vehicle are completely ignored. On the other hand, the conventional suspension synthesis process also involves design of suspension components including spring, damper or anti-roll bars considering the dynamic responses only, and ignoring the influences of these elements properties on the kinematic responses, which would further influence the dynamic responses. Furthermore, possible influences of tire lateral compliance properties on the vertical dynamics is ignored in the conventional suspension design studies. Suspension synthesis involving the couplings between the suspension linkage kinematics and tire

lateral compliances with the vertical dynamics responses would thus be highly desirable, while the majority of the existing vehicle models do not permit such coupled analyses.

The literature further reveals that the suspension kinematic and dynamic responses are strongly affected by the joint coordinates in a complex manner. The current trends in hybrid vehicles developments impose considerable challenges related to the sprung mass and the sub-frame space requirements and thus the chassis design. The larger space requirements of the hybrid vehicles also necessitate considerations of the suspension synthesis with limited lateral space, which would most likely involve complex compromises among performance measures related to vehicle ride and handling. The synthesis of a suspension with constrained lateral space thus necessitates investigations of the influences of joint coordinates on the kinematic and dynamic responses, and the related measures including the variations in the wheel load.

The kinematic and dynamic responses are further influenced by the asymmetric force-velocity properties of the dampers in compression and rebound. The design guidelines for such asymmetry has thus far been limited to a general rule of thumb suggesting that a rebound to compression damping ratio in the order of 2 or 3 would reduce the magnitude of the force transmitted to the sprung mass. Further, the asymmetry in the dampers causes mean shift in the sprung mass position relative to that of the unsprung mass, which is also known as ‘damper jacking’. The influence of the damper jacking on the suspension kinematic responses, particularly variations in the camber angle, which are directly related to the suspension deflection, are generally ignored while synthesizing a suspension damper. An optimal synthesis of suspension damper would thus involve consideration of the kinematic measures (camber change etc.) apart from the widely

known complexities involving design compromises to satisfy the conflicting ride comfort, rattle space and road-holding measures. Furthermore, the synthesis of suspension damper with asymmetric properties in rebound and compression necessiates study of influences of the damper asymmetry on the dynamic and kinematic responses as a function of the vehicle forward speed under various inputs including bump, pothole and random road excitations. A systematic kineto-dynamic analysis of the suspension with asymmetric damper could thus yield design guidance for the damping asymmetry.

The majority of the studies on suspension kinematics have assumed idealized mechanisms and joints, neglecting the contributions due to joints clearances, attributed to joint bushing aging and wear. Clearances in different joints may cause deteriorated kinematic and dynamic performances of the mechanism; the effects, however, have been investigated in a very few studies using particular suspensions syntheses. The influences of magnitudes of joint clearances on the kinematic and dynamic performance characteristics of general mechanisms, however, have shown increased joint reaction forces due to clearances. These methodologies can be applied for systematic studies on qualitative and quantitative effects of nonlinearities due to joint clearances in the suspension mechanisms, which are highly desirable for developing a suspension fault diagnostic system.

1.4 Objectives of the Dissertation Research

The proposed dissertation research is formulated with an overall objective of synthesis of an optimal independent suspension system comprising asymmetric damper, linkage kinematics, tire lateral compliances, and joints clearances in order to enhance the

dynamic performance of the suspension. The specific objectives of the proposed dissertation research are summarized as follows:

a. Develop a kinematic model of a candidate suspension mechanism, and investigate the influences of joint coordinates on the kinematic performance measures through sensitivity analyses;
b. Develop laboratory experimental setup comprising essential suspension links and measure kinematic response parameters, and examine the validity of the kinematic modeling methodology;
c. Develop a kineto-dynamic quarter-car model of a road vehicle incorporating the suspension linkage kinematic effects and tire lateral compliances, and investigate the coupling between the suspension kinematics, tire lateral compliance and torsional compliance of joint bushings with the vertical dynamic performance measures;
d. Investigate the influences of damping asymmetry on the coupled dynamic and kinematic responses of the suspension under different road excitations over a wide range of vehicle speeds;
e. Synthesize an optimal two-stage asymmetric damper so as to yield compromise among the kinematic and dynamic performance measures;
f. Develop a kineto-dynamic half-car roll-plane model of the road vehicle incorporating the suspension linkage kinematic effects and tire lateral compliances, and investigate the coupling between the suspension kinematics, tire lateral compliance and the vertical and roll dynamic performance measures;

g. Select optimal joint coordinates considering the kinematic performance measures, and investigate the effects of the change in coordinates on the dynamic and kinematic performance measures;

h. Investigate the influences of damping asymmetry on the coupled dynamic and kinematic responses of the roll-plane half-car model under different road and lateral excitations;

i. Extend the kineto-dynamic model to incorporate suspension faults including joint clearances, linkage deformation and leaked damper, and investigate the effects on the dynamic performance measures of the suspension systems

1.5 Organization of the Dissertation

This dissertation is organized into seven chapters with the first chapter focusing on the review of relevant literature and the scope and objectives of the dissertation research.

Chapter 2 presents the study of influences of suspension joints coordinates on the kinematic responses of the suspension, and synthesis of suspension geometry considering the kinematic performances of the suspension. Kinematic models and their analytical formulations of quadra-link and double wishbone type of suspensions are presented together with the design of experiment and validations of the proposed analytical models. The influences of the joint coordinates on the suspension kinematic responses under wheel vertical displacement excitations are further investigated through sensitivity analyses. The kinematic model of the double wishbone suspension is formulated in such a manner that the linkage kinematics can be easily integrated into the dynamic model.

Chapter 3 of this dissertation is concerned with the kineto-dynamic analyses of a quarter-vehicle model comprising double wishbone supension. A quarter-car model is

formulated integrating the kinematic relations of the suspension linkages described in Chapter 2 using the Lagrange's energy method. Transient dynamic responses of the model are analyzed under different road excitations, and simulation results are presented so as to illustrate the contributions of suspension kinematics on the dynamic responses. Synthesis of suspension linkage joints coordinates considering the lateral space constraints, with an application to the hybrid vehicles is discussed in the chapter. This chapter further presents the kineto-dynamic analyses of model with flexible joint bushings. The influences of suspension joints flexibility on the kinematic and dynamic responses are investigated, and influences of the variations in the flexibility are also presented so as to yield design guidelines for the synthesis of joint bushings.

In Chapter 4, an optimal synthesis of two-stage asymmetric damper is presented giving due considerations to the different conflicting demands related to the kinematic and dynamic performance measures. Initially, influences of damper asymmetry is analyzed on the kinematic and dynamic performance measures under harmonic, bump and pothole excitations. An optimal synthesis of two-stage asymmetric damper is presented considering design conflicts under bump and pothole type of excitations. The influences of the damping asymmetry on the kinematic and dynamic performance measures under random rough road excitations are further analyzed to indentfy the conflicting requirements on the damper synthesis. Finally, this chapter presents the optimal synthesis of two-stage asymmetric damper parameters considering the design compromises related to kinematic and dynamic performance measures corresponding to ride, rattle space, roadholding and camber angle variations.

Roll-plane kineto-dynamic analyses of the vehicle are presented in Chapter 5. A kinematic roll-plane vehicle model comprising double wishbone suspension is deveoped, and the formulations of kinematic responses such as bump camber, roll camber and wheel track variation are derived. The responses are analyzed under wheel vertical motions, chassis roll motions and simultaneous motions of wheel and the chassis. Influences of the joints coordinates on the kinematic performance measures under these excitations are discussed and conflicting design criteria are identified. Selection of optimal joint coordinates considering only the kinematic performance measures is presented. This chapter further presents development of kineto-dynamic roll-plane vehicle model including double wishbone suspension linkages kinematics. The roll and vertical dynamic responses of the model under vertical and lateral centrifugal force excitations are analyzed. A methodology of suspension geometry synthesis considering both kinematic and dynamic response characteristics of the model is further presented in this chapter.

Chapter 6 presents the study of influences of suspension faults on the dynamic performance of the vehicle. Modeling of bushing clearances in ADAMS platform is discussed in this chapter. A preliminary study on the fault diagnostic system has also been presented briefly in this chapter. In Chapter 7, the major conclusions drawn from the dissertation research are described followed by the potential future studies in this field.

CHAPTER 2

KINEMATIC ANALYSIS AND SYNTHESIS OF SUSPENSION GEOMETRY USING A QUARTER CAR MODEL

2.1 Introduction

Synthesis of suspension is a complex task due to many conflicting kinematic and dynamic performance measures. Various studies have suggested that kinematic responses of independent suspension systems such as variations in camber, caster and toe angles, and wheel track and base could significantly influence the handling dynamics of the vehicle and the tire wear characteristics [2, 4, 7, 137]. It has been further suggested that the kinematic responses are highly influenced by the joint coordinates and the lengths of suspension linkages in a complex manner. Synthesis of a suspension geometry (locations of joint coordinates and lengths of linkages) thus poses considerable challenges as evident from the large number of reported studies [5, 7, 8, 14, 13], although the vast majority focus on achieving minimal kinematic response variations under suspension vertical travel. Current trends in hybrid vehicles developments impose additional design challenges related to the sub-frame space requirements and thus the chassis design [3], which necessitate considerations of the suspension synthesis with limited lateral space. Synthesis of suspension geometry with constrained lateral space has been addressed only in a few studies [13, 31, 32], which would most likely involve additional design compromises among performance measures related to the kinematic as well as dynamic responses.

Synthesis of suspension geometry involves the study of kinematic responses of the suspension under wheel and chassis excitations, and influences of joint coordinates on the

kinematic responses. Identification of most influential joint coordinates has been considered as an essential and most challenging process during suspension geometry synthesis [30]. In this chapter, a kinematic model of a suspension mechanism is formulated together with the essential excitations and the performance measures. The influences of the joint coordinates on the suspension kinematic responses are systematically evaluated under wheel vertical displacement excitations, for two different widely used suspension mechanisms: a quadra-link and a double wishbone type of suspension. The validity of the proposed kinematic model of the quadra-link suspension is examined by comparing the responses of the model with those attained from the laboratory measurement.

2.2 Features of Kinematic Analysis

Early stages of the suspension synthesis process involve kinematic analysis of the suspension mechanisms, particularly, the variations in the camber, toe and caster angles and the wheel track under wheel vertical travel. It has been suggested that a kinematic model of a single wheel station comprising the suspension linkages, chassis and the wheel spindle can be conveniently used to study the essential kinematic responses of a suspension [10]. Such simplified models could also incorporate contributions due to the roll motion of the chassis through analysis of the roll center. Numerous analytical models of varying complexities have been developed to study the kinematic responses of various types of commonly used suspension configurations such as MacPherson strut [11, 20, 21], double wishbone [14, 15] and multi-link (five-link) [5, 6, 14, 17]. The kinematic responses are analyzed considering the suspension system either as planar or spatial mechanisms. Planar analyses permit analyses of a few of the kinematic responses in a

highly efficient manner, such as variation in camber angle and half wheel track during wheel jounce and rebound motions, although the contributions due to steering mechanism and kinematic effects of steer and caster angles are ignored. Kinematic analysis of three-dimensional suspension mechanism is thus essential for determination of variations in the steer, camber or caster angles simultaneously, while taking into account the coupled kinematic effects of suspension linkages.

The kinematic analysis of a mechanism, in general, involves determination of position, velocity and acceleration of a body relative to another body without considering the force that causes the motions. The relative position, velocity and acceleration responses are dependent upon the geometry of the mechanism, type of links, and the associated mobility and the constraints. Development of a kinematic model of an automotive suspension thus necessitates knowledge of various kinematic constraints and corresponding equations. Various kinematic joint constraints and types of links employed in vehicle suspension mechanisms are briefly reviewed and discussed in the following section.

2.2.1 Kinematic Constraints in a Suspension Mechanism

The motions of a mechanism are strongly dependent upon the kinematic constraints that describe the joints in a multi-body system, types of links and joints. The types of links employed in a suspension mechanism are often classified on the basis of the type of joints supporting a link such as spherical-spherical, revolute-revolute and revolute-spherical. A brief description of these types of links and the respective constraint equations are given below.

A *Spherical-Spherical* (*S-S*) link comprises spherical joints at each ends [138]. These types of links are generally found in multi-link type of suspensions with one of the spherical joints located at the chassis and the other at the wheel spindle. The constraint equation of a *Spherical-Spherical* link can be derived from the constant length between the two spherical joints before and after a displacement. Considering two points *J* and *K* as the centers of the spherical joints at two ends of a *S-S* link with (J_{x0}, J_{y0}, J_{z0}) and (K_{x0}, K_{y0}, K_{z0}) as the initial *x-* *y-* and *z-* coordinates, the constraint equations for the *S-S* link *JK* can be related to the coordinates of the joint centers (J_x, J_y, J_z) and (K_x, K_y, K_z) following a finite displacement, as illustrated in Fig. 2.1 (a), such that:

$$(J_x-K_x)^2+(J_y-K_y)^2+(J_z-K_z)^2=(J_{x0}-K_{x0})^2+(J_{y0}-K_{y0})^2+(J_{z0}-K_{z0})^2 \quad (2.1)$$

A *Revolute-Spherical* (*R-S*) link, as the name suggests, consists of a revolute joint at one end and a spherical joint at the other end. The control arms of MacPherson strut, double wishbone and quadra-link suspension configurations are generally *R-S* type. The control arms in such suspensions forms a revolute joint with the chassis and a spherical joint with the wheel spindle. The motions of these links are governed by the condition that the link must rotate about a revolute axis at the revolute joint. Two specific conditions define the motion of *R-S* types of link, namely: (i) the distance between the revolute axis and the spherical joint remains constant during any motion; and (ii) the vector from the revolute axis to the spherical joint is normal to the revolute axis during the motion. Mathematically, the dot product of the unit vector representing the revolute axis and the vector from the revolute axis to spherical joint is zero.

Considering the point J as the intersection of a unit along the revolute axis and a normal vector from the spherical joint K to the revolute axis (Fig. 2.1 (b)), the constraint equations for a *R-S* type of link can be written as:

(2.2)

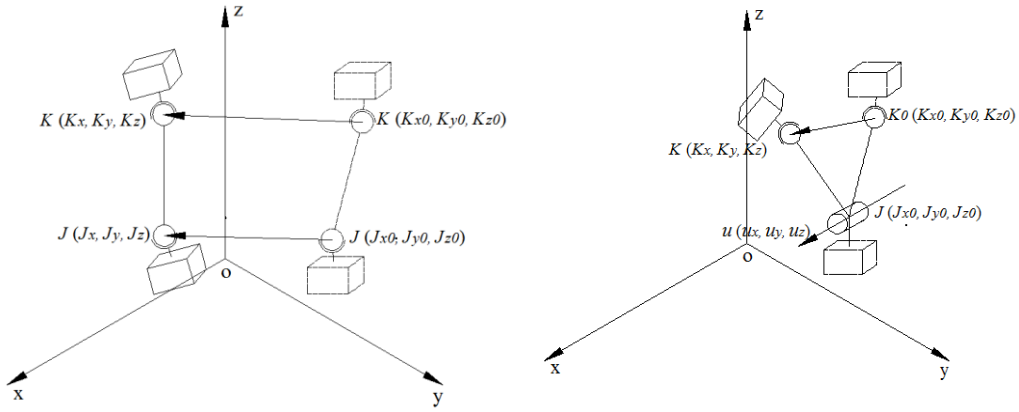

(a) (b)

Figure 2.1: Schematics of: (a) spherical-spherical link; and (b) revolute and spherical link [138]

Revolute-Revolute (*R-R*) type of link with revolute joints each at both the ends is seldom found in vehicle suspension mechanisms since such a link permits rotational motion about the two parallel revolute axes only. In planar suspension models, both the *S-S* and *R-S* types of links act as *R-R* type of link due to the possible rotational motion of the rigid bodies about axes normal to the plane. The constraint equation of a *R-R* type of link can be derived from the constant length between the two revolute joints before and after a displacement. Considering two points J and K as the centers of the revolute joints at the two ends of a *R-R* link in the *y-z* plane with (J_{y0}, J_{z0}) and (K_{y0}, K_{z0}) as the initial coordinates, the constraint equations are to be obtained by relating to the coordinates of the joint centers (J_y, J_z) and (K_y, K_z) following a finite displacement of the link, such that:

$$(J_y-K_y)^2+(J_z-K_z)^2=(J_{y0}-K_{y0})^2+(J_{z0}-K_{z0})^2 \quad (2.3)$$

2.2.2 Kinematic Responses of Automotive Suspensions

The suspension kinematics are widely known to influence handling dynamics of a vehicle under lateral excitations arising from a steering input or wind gusts [1, 4, 7]. The kinematic responses, particularly, the variations in the wheel orientation angles (camber, toe and caster angles), the wheel-track and wheel-base during suspension travel may yield additional undesirable lateral forces at the tires. Furthermore, the variations in the wheel orientation angles, and the lateral and longitudinal motions of the spindle could yield accelerated tire wear. Various studies have suggested that minimal variations in these responses during wheel vertical motion are desirable for good handling performance of a vehicle [4, 5, 137]. Kinematic responses of a suspension mechanism are thus evaluated in terms of variations in the wheel track and wheel base, and the camber, caster and toe angles during the wheel vertical travel with respect to those corresponding to static conditions. The kinematic performance measures of a suspension system are thus often defined in terms of variations in these responses under a given suspension travel.

2.3 Kinematic Analysis of a Quadra-link Suspension

A quadra-link suspension configuration, as the name suggests, comprises four links connecting the chassis and the wheel spindle. The structure of a quadra-link suspension lies in between those of double wishbone and a five-link type of suspensions [1, 2, 5]. While a double wishbone suspension comprises two control arms only, the five-link suspension consists of five distinct links connecting the wheel spindle with the chassis. The quadra-link type of suspension considered in this study, comprises an upper control

arm, two lower links and a trailing arm, as illustrated in Fig. 2.2. This suspension configuration is widely used in rear suspensions of passenger cars including the Chrysler-Breeze and Sebring [139]. The strut in quadra-link type of suspension is located on the wheel spindle. The spatial stucture of the quadra-link suspension, as seen in the figure, suggests that the kinematic response analyses and subsequent synthesis of the suspension necessitate a three-dimensional analysis.

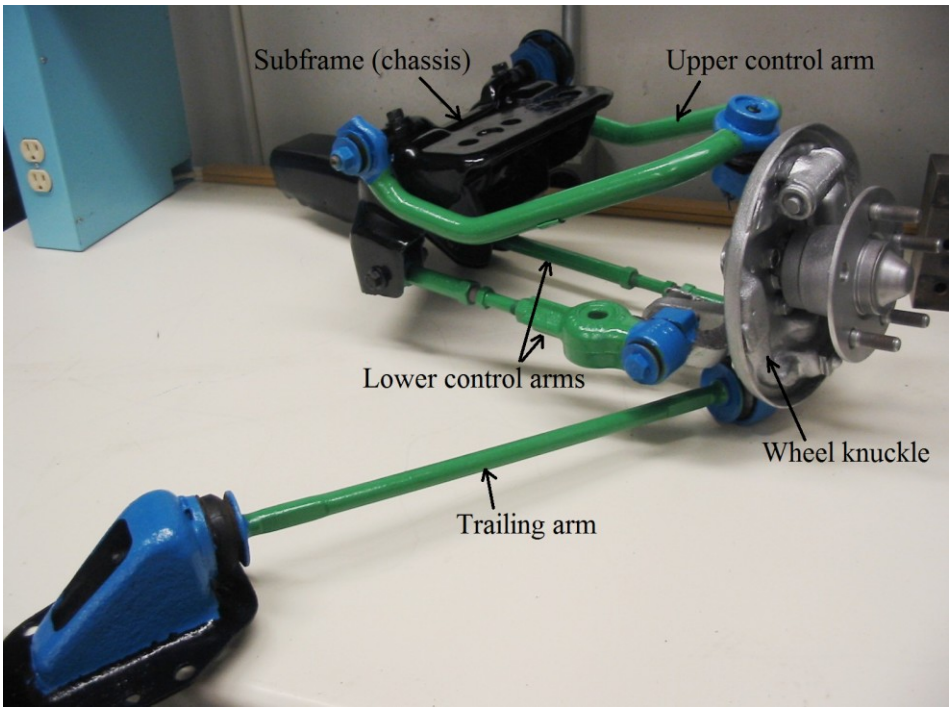

Figure 2.2: Schematic image of a quadra-link suspension

Although a number of spatial kinematic models of different suspension mechanisms have been suggested for kinematic analysis and subsequent synthesis such as MacPherson, double wishbone and five-link suspension mechanisms, such analyses of a quadra-link type of suspension could be found in a single study only [140]. The reported study on the quadra-link suspension was conducted using the multi-body dynamic tool, ADAMS/chassis, with an objective to yield optimal joint bushing stiffness. The study of

the kinematic responses such as variations in the camber and toe angle, and wheel track and base, and the influences of the joint coordinates on the kinematic responses however were not considered. In this study, an analytical model of the quadra-link suspension is formulated for the kinematic analysis and synthesis in order to evaluate variations in the orientations of the wheel at different positions of the wheel center with respect to the chassis.

2.3.1 Kinematic Model of the Quadra-link Suspension

A spatial model of the quadra-link suspension incorporating all the linkages, subframe (chassis) and the wheel spindle is formulated as illustrated in Fig. 2.3. The upper control arm (*M1-N1-M2*) of the quadra-link suspension forms a revolute joint with the chassis, and permits rotational motion of the control arm about the revolute axis *M1-M2*. The upper control arm is connected to the wheel spindle through a spherical joint, thereby forming a *R-S* link . The lower links *O1-P1* and *O2-P2*, and the trailing link *O3-P3* form spherical joints with both the chassis and the wheel spindle, which can be identified as *S-S* type of links. The point *C* in the Fig. 2.3 (b) represents the wheel center. The chassis, the control arms and links, and the wheel spindle are assumed to be rigid bodies, while the tire is assumed to be integral part of the wheel spindle. The suspension kinematic relations are derived with an assumption that all the joints are frictionless.

2.3.2 Mobility Analysis

In a quadra-link suspension mechansim, the chassis, the upper control arm, the lower links, the trailing arm and the wheel spindle are components of the closed kinematic chain, while coupling with the fixed chassis forms the mechanism. The mobility of the

quadra-link suspension mechansim, as shown in the Fig. 2.3 (b), can be estimated from Grubler's criteria for mobility of spatial mechanisms [19], such that:

$$DOF=6(N_m-1)-5R_m-3S_m \tag{2.4}$$

where N_m is the the number of links, and R_m and S_m are the number of revolute and spherical joints, respectively.

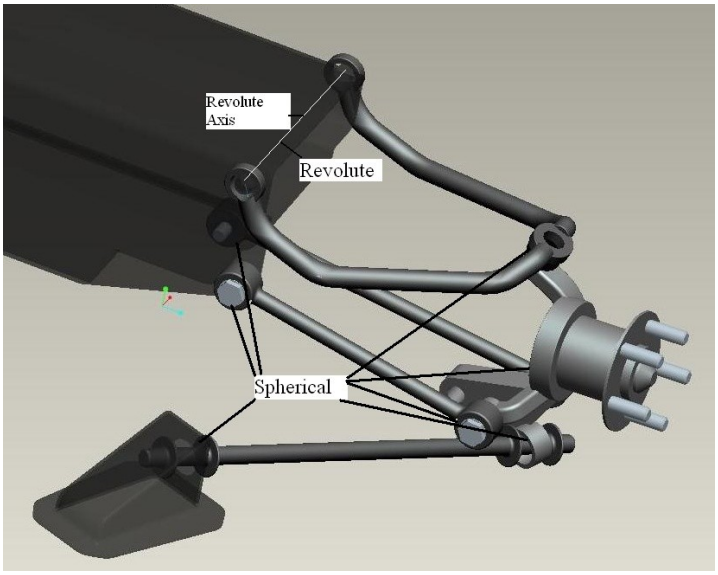

(a)

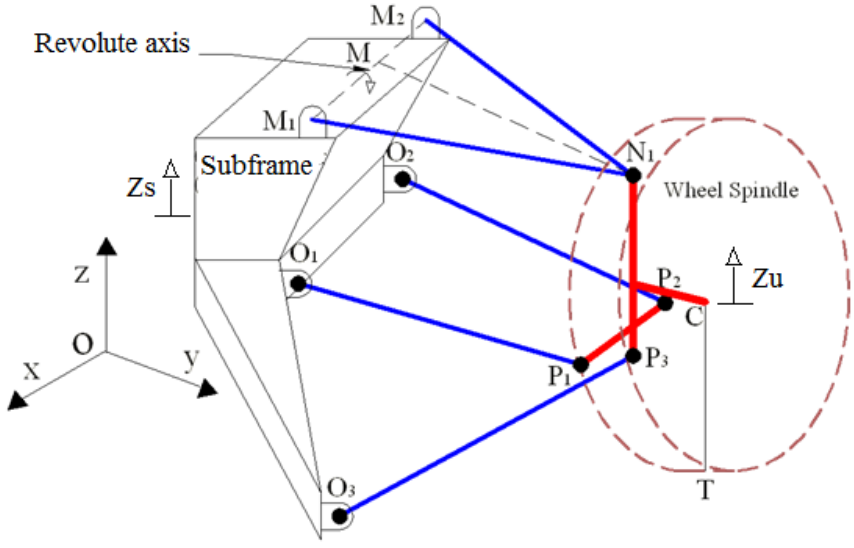

(b)

Figure 2.3: (a) Schematic illustration; and (b) kinematic model of a quadra-link suspension

The mechanism comprises 6 rigid bodies (chassis, wheel spindle and four rigid links connecting the chassis and the wheel spindle), one revolute joint (between upper control arm and the chassis) and 7 spherical joints (3 between the chassis and the lower and trailing links, 3 between wheel spindle and the lower and trailing links, and one between the upper control arm and the wheel spindle). The quadra link suspension mechanism coupled with a fixed chassis thus possess four degrees-of-freedom (DOF). An examination of the mechanism, however, suggests that three of the DOF are associated with the rotations of the trailing arm and the lower links about their respective longitudinal axes. Such rotational motions, however, do not influence articulation of the suspension, and are generally referred to as idle DOF [12]. The active degree of freedom of the mechanism is thus estimated as one, which is the vertical motion of the wheel spindle with respect to the chassis. The motion of the chassis with respect to the ground coordinate system can facilitate kinematic analysis of the suspension with simultaneous motions of the chassis and the wheel spindle. The generalized coordinates of the kinematic quadra-link suspension model are thus chosen as the vertical displacements of the sprung mass and the wheel spindle.

2.3.3 Kinematic Formulations

For the wheel spindle of the quadra-link suspension, the positions of joint centers, *N1*, *P1*, *P2* and *P3,* and the wheel center *C* are identified as the parameters of particular interest, where ($N1_{x0}$, $N1_{y0}$, $N1_{z0}$), ($P1_{x0}$, $P1_{y0}$, $P1_{z0}$), ($P2_{x0}$, $P2_{y0}$, $P2_{z0}$), ($P3_{x0}$, $P3_{y0}$, $P3_{z0}$), and (C_{x0}, C_{y0}, C_{z0}) define the initial coordinates of *N1*, *P1*, *P2*, *P3* and *C*, respectively. The first subscript of the variable represents the coordinate (*x*, *y* or *z*), while the second subscript (‘*0*’) designates the initial position. For a finite displacement of the wheel

spindle in the given coordinate frame, the displacement matrix can be formulated as [19, 132]:

$$[D]_{wheel\,\text{spindle}} = \begin{bmatrix} a_{11} & a_{12} & a_{13} & C_x - (a_{11}C_{x0} + a_{12}C_{y0} + a_{13}C_{z0}) \\ a_{21} & a_{22} & a_{23} & C_y - (a_{21}C_{x0} + a_{22}C_{y0} + a_{23}C_{z0}) \\ a_{31} & a_{32} & a_{33} & C_z - (a_{31}C_{x0} + a_{32}C_{y0} + a_{33}C_{z0}) \\ 0 & 0 & 0 & 1 \end{bmatrix} \tag{2.5}$$

where

a_{11}=cosψ cosθ ; a_{12}= -sinψ cosϕ+cosψ sinθ sinϕ; a_{13}= sinψ sinϕ+cosψ sinθ cosϕ;

a_{21}=sinψ cosθ; a_{22}= cosψ cosϕ+sinψ sinθ sinϕ; a_{23}= -cosψ sinϕ+ sinψ sinθ cosϕ;

a_{31}= -sinθ ; a_{32}= cosθ sinϕ; and a_{33}=cos θ cos ϕ

Also, ϕ, θ, and ψ are the roll (about x- axis), pitch (about y- axis) and yaw (about z- axis) rotations, respectively, and C_x, C_y and C_z are the instantaneous coordinates of the wheel center C.

The instantaneous coordinates of ($N1_x$, $N1_y$, $N1_z$), ($P1_x$, $P1_y$, $P1_z$), ($P2_x$, $P2_y$, $P2_z$), ($P3_x$, $P3_y$, $P3_z$) of joint centers $N1$, $P1$, $P2$, $P3$ and the wheel center C under a given wheel spindle vertical displacement z_u are derived from the displacement matrix as:

$$\begin{bmatrix} N1_x & P1_x & P2_x & P3_x \\ N1_y & P1_y & P2_y & P3_y \\ N1_z & P1_z & P2_z & P3_z \\ 1 & 1 & 1 & 1 \end{bmatrix} = [D]_{wheel\,\text{spindle}} \begin{bmatrix} N1_{x0} & P1_{x0} & P2_{x0} & P3_{x0} \\ N1_{y0} & P1_{y0} & P2_{y0} & P3_{y0} \\ N1_{z0} & P1_{z0} & P2_{z0} & P3_{z0} \\ 1 & 1 & 1 & 1 \end{bmatrix} \tag{2. 6}$$

The above formulation exhibits 17 unknown parameters corresponding to a given wheel center vertical displacement (z_u), namely, the x, y and z coordinates of $N1$, $P1$, $P2$ and $P3$, the x- and y- coordinates of C and the wheel rotation angles ϕ, θ, and ψ. Equation (2.6) is solved in conjunction with the constraint conditions imposed by the suspension mechanism to obtain kinematic responses. For the quadra-link suspension, the constraint

equations may be formulated considering the *R*-*S* (upper control arm *M1*-*N1*-*M2*) and *S*-*S* links (lower links *O1*-*P1*, *O2*-*P2*, and trailing link *O3*-*P3*), such that:

$$
\begin{aligned}
&(N1_x - M_x)^2 + (N1_y - M_y)^2 + (N1_z - M_z)^2 = (N1_{x0} - M_{x0})^2 + (N1_{y0} - M_{y0})^2 + (N1_{z0} - M_{z0})^2 \\
&(P1_x - O1_x)^2 + (P1_y - O1_y)^2 + (P1_z - O1_z)^2 = (P1_{x0} - O1_{x0})^2 + (P1_{y0} - O1_{y0})^2 + (P1_{z0} - O1_{z0})^2 \\
&(P2_x - O2_x)^2 + (P2_y - O2_y)^2 + (P2_z - O2_z)^2 = (P2_{x0} - O2_{x0})^2 + (P2_{y0} - O2_{y0})^2 + (P2_{z0} - O2_{z0})^2 \\
&(P3_x - O3_x)^2 + (P3_y - O3_y)^2 + (P3_z - O3_z)^2 = (P3_{x0} - O3_{x0})^2 + (P3_{y0} - O3_{y0})^2 + (P3_{z0} - O3_{z0})^2 \\
&u_{0x}(N1_x - M_x) + u_{0y}(N1_y - M_y) + u_{0z}(N1_z - M_z) = 0
\end{aligned}
\tag{2.7}
$$

In the above, (M_x, M_y, M_z) and (M_{x0}, M_{y0}, M_{z0}) refer to the coordinates of *M*, the point of intersection of a unit vector along the revolute axis (u_0) and a normal vector from the point *N1*. Moreover, $M_x=M_{x0}$, $O1_x=O1_{x0}$, $O2_x=O2_{x0}$, $O3_x=O3_{x0}$, $M_y=M_{y0}$, $O1_y=O1_{y0}$, $O2_y=O2_{y0}$, $O3_y=O3_{y0}$, $M_z=M_{z0}+z_s$, $O1_z=O1_{z0}+z_s$, $O2_z=O2_{z0}+z_s$, $O3_z=O3_{z0}+z_s$ and $C_z=C_{z0}+z_u$, while z_s is vertical displacement of the sprung mass from its static equilibrium position.

The unit vector $\overline{u}_0$ along the revolute axis is obtained as:

$$
\overline{u}_0 = \frac{(M1_{x0} - M2_{x0})x + (M1_{y0} - M2_{y0})y + (M1_{z0} - M2_{z0})z}{\sqrt{(M1_{x0} - M2_{x0})^2 + (M1_{y0} - M2_{y0})^2 + (M1_{z0} - M2_{z0})^2}} \tag{2.8}
$$

The coordinates of *M* can be obtained from equation of the position vector $\overline{M}$, written as:

$$
\overline{M} = \overline{M2} + \overline{u}_0.(\overline{N1} - \overline{M2}).\overline{u}_0 \tag{2.9}
$$

The solution of Eq. (2.6) yields a system of nonlinear equations, as:

$$
\begin{aligned}
N1_x &= a_{11}(N1_{x0} - C_{x0}) + a_{12}(N1_{y0} - C_{y0}) + a_{13}(N1_{z0} - C_{z0}) + C_x \\
N1_y &= a_{21}(N1_{x0} - C_{x0}) + a_{22}(N1_{y0} - C_{y0}) + a_{23}(N1_{z0} - C_{z0}) + C_y \\
N1_z &= a_{31}(N1_{x0} - C_{x0}) + a_{32}(N1_{y0} - C_{y0}) + a_{33}(N1_{z0} - C_{z0}) + C_z \\
P1_x &= a_{11}(P1_{x0} - C_{x0}) + a_{12}(P1_{y0} - C_{y0}) + a_{13}(P1_{z0} - C_{z0}) + C_x \\
P1_y &= a_{21}(P1_{x0} - C_{x0}) + a_{22}(P1_{y0} - C_{y0}) + a_{23}(P1_{z0} - C_{z0}) + C_y \\
P1_z &= a_{31}(P1_{x0} - C_{x0}) + a_{32}(P1_{y0} - C_{y0}) + a_{33}(P1_{z0} - C_{z0}) + C_z
\end{aligned}
$$

$$
\begin{aligned}
P2_x &= a_{11}(P1_{x0} - C_{x0}) + a_{12}(P2_{y0} - C_{y0}) + a_{13}(P2_{z0} - C_{z0}) + C_x \\
P2_y &= a_{21}(P1_{x0} - C_{x0}) + a_{22}(P2_{y0} - C_{y0}) + a_{23}(P2_{z0} - C_{z0}) + C_y \\
P2_z &= a_{31}(P1_{x0} - C_{x0}) + a_{32}(P2_{y0} - C_{y0}) + a_{33}(P2_{z0} - C_{z0}) + C_z \\
P3_x &= a_{11}(P3_{x0} - C_{x0}) + a_{12}(P3_{y0} - C_{y0}) + a_{13}(P3_{z0} - C_{z0}) + C_x \\
P3_y &= a_{21}(P3_{x0} - C_{x0}) + a_{22}(P3_{y0} - C_{y0}) + a_{23}(P3_{z0} - C_{z0}) + C_y \\
P3_z &= a_{31}(P3_{x0} - C_{x0}) + a_{32}(P3_{y0} - C_{y0}) + a_{33}(P3_{z0} - C_{z0}) + C_z
\end{aligned} \tag{2.10}
$$

The nonlinear equations can be numerically solved to obtain unknown parameters under given vertical displacements of the chassis and/or the wheel center. The rotational motions of the wheel about *x*- and *z*- axes, ϕ and ψ, yield the wheel camber and toe angle response of the suspension, respectively. The wheel center lateral displacement y_u can be further obtained as $y_u=C_y-C_{y0}$. The lateral displacement of the wheel-ground contact point *T*, with respect to the static position is considered as the variation in the wheel track, which has been directly related to the tire wear characteristics [4]. With the rigid body assumption of the wheel assembly, the lateral motion of the wheel-ground contact point T_y, is obtained as:

$$
T_y = a_{21}(T_{x0} - C_{x0}) + a_{22}(T_{y0} - C_{y0}) + a_{23}(T_{z0} - C_{z0}) + C_y \tag{2.11}
$$

where ($T_{x0,}$ T_{y0}, T_{z0}) are the initial coordinates of the contact point *T*. In a similar manner, the wheel base variation response of the suspension, which is directly related to the displacement of the contact point along *x*- axis during the wheel vertical travel T_x, can be obtained as:

$$
T_x = a_{11}(T_{x0} - C_{x0}) + a_{12}(T_{y0} - C_{y0}) + a_{13}(T_{z0} - C_{z0}) + C_x \tag{2.12}
$$

The velocities of various points in the wheel spindle are obtained by differentiating the expressions for the displacements. Alternately, velocity matrix written in terms of rotation of the wheel spindle about its instantaneous screw axis can be employed to yield

the velocity responses of the wheel spindle [19]. For a finite displacement of the wheel spindle in the given coordinate frame, the general velocity matrix, $\left[\dot{D}\right]_{wheel\text{spindle}}$ is formulated as:

$$\left[\dot{D}\right]_{wheel\text{spindle}} = \begin{bmatrix} 0 & -\dot{\varphi}_z & \dot{\varphi}_y & \dot{C}_x - (-\dot{\varphi}_z C_{y0} + \dot{\varphi}_y C_{z0}) \\ \dot{\varphi}_z & 0 & -\dot{\varphi}_x & \dot{C}_y - (\dot{\varphi}_z C_{x0} - \dot{\varphi}_x C_{z0}) \\ -\dot{\varphi}_y & \dot{\varphi}_x & 0 & \dot{C}_z - (-\dot{\varphi}_y C_{x0} + \dot{\varphi}_x C_{y0}) \\ 0 & 0 & 0 & 0 \end{bmatrix} \tag{2.13}$$

where φ represents the rotation of the wheel spindle about the screw axis, and the dot over the variable denotes the time derivative. The screw axis can be obtained from the joint coordinates, as explained in [19]. The method, however, is not presented since it is not necessary for obtaining considered kinematic responses. The velocity matrix in Eq (2.13) can be employed to compute velocities of joints *N1*, *P1*, *P2*, and *P3*, as:

$$\begin{bmatrix} \dot{N}1_x & \dot{P}1_x & \dot{P}2_x & \dot{P}3_x \\ \dot{N}1_y & \dot{P}1_y & \dot{P}2_y & \dot{P}3_y \\ \dot{N}1_z & \dot{P}1_z & \dot{P}2_z & \dot{P}3_z \\ 1 & 1 & 1 & 1 \end{bmatrix} = \left[\dot{D}\right]_{wheel\text{spindle}} \begin{bmatrix} N1_x & P1_x & P2_x & P3_x \\ N1_y & P1_y & P2_y & P3_y \\ N1_z & P1_z & P2_z & P3_z \\ 1 & 1 & 1 & 1 \end{bmatrix} \tag{2.14}$$

The solutions of the Eq (2.14) together with the time derivatives of the constraint equations in Eq (2.7) yield a system of equation in velocities of the suspension joints and the wheel center, such that:

$$\begin{aligned}
&(N1_x - M_{x0})\dot{N}1_x + (N1_y - M_{y0})\dot{N}1_y + (N1_z - M_{z0})\dot{N}1_z = 0 \\
&u_{0x}\dot{N}1_x + u_{0y}\dot{N}1_y + u_{0z}\dot{N}1_z = 0 \\
&(P1_x - O1_{x0})\dot{P}1_x + (P1_y - O1_{y0})\dot{P}1_y + (P1_z - O1_{z0})\dot{P}1_z = 0 \\
&(P2_x - O2_{x0})\dot{P}2_x + (P2_y - O2_{y0})\dot{P}2_y + (P2_z - O2_{z0})\dot{P}2_z = 0 \\
&(P3_x - O3_{x0})\dot{P}3_x + (P3_y - O3_{y0})\dot{P}3_y + (P3_z - O3_{z0})\dot{P}3_z = 0 \\
&\dot{N}1_x + \dot{\varphi}_z(N1_y - C_{y0}) - \dot{\varphi}_y(N1_z - C_{z0}) - \dot{C}_x = 0 \\
&\dot{N}1_y - \dot{\varphi}_z(N1_x - C_{x0}) + \dot{\varphi}_x(N1_z - C_{z0}) - \dot{C}_y = 0
\end{aligned}$$

$$
\begin{aligned}
&\dot{N}1_z + \dot{\varphi}_y(N1_x - C_{x0}) - \dot{\varphi}_x(N1_y - C_{y0}) = \dot{C}_z \\
&\dot{P}1_x + \dot{\varphi}_z(P1_y - C_{y0}) - \dot{\varphi}_y(P1_z - C_{z0}) - \dot{C}_x = 0 \\
&\dot{P}1_y - \dot{\varphi}_z(P1_x - C_{x0}) + \dot{\varphi}_x(P1_z - C_{z0}) - \dot{C}_y = 0 \\
&\dot{P}1_z + \dot{\varphi}_y(P1_x - C_{x0}) - \dot{\varphi}_x(P1_y - C_{y0}) = \dot{C}_z \\
&\dot{P}2_x + \dot{\varphi}_z(P2_y - C_{y0}) - \dot{\varphi}_y(P2_z - C_{z0}) - \dot{C}_x = 0 \\
&\dot{P}2_y - \dot{\varphi}_z(P2_x - C_{x0}) + \dot{\varphi}_x(P2_z - C_{z0}) - \dot{C}_y = 0 \\
&\dot{P}2_z + \dot{\varphi}_y(P2_x - C_{x0}) - \dot{\varphi}_x(P2_y - C_{y0}) = \dot{C}_z \\
&\dot{P}3_x + \dot{\varphi}_z(P3_y - C_{y0}) - \dot{\varphi}_y(P3_z - C_{z0}) - \dot{C}_x = 0 \\
&\dot{P}3_y - \dot{\varphi}_z(P3_x - C_{x0}) + \dot{\varphi}_x(P3_z - C_{z0}) - \dot{C}_y = 0 \\
&\dot{P}3_z + \dot{\varphi}_y(P3_x - C_{x0}) - \dot{\varphi}_x(P3_y - C_{y0}) = \dot{C}_z
\end{aligned}
\tag{2.15}
$$

where $\dot{C}_z = \dot{z}_u$. The above equations are obtained with an assumption that the chassis is fixed (z_s=0). The velocities along *x*-, *y*- and *z*- axes of joints *N1*, *P1*, *P2* and *P3* together with the velocity of wheel center *C* along *x*- and *y*- axes, and the wheel rotation velocities for known values of wheel spindle vertical velocities can be obtained though solution of Eq (2.15). It can be observed that unlike the displacement equations given in Eqs (2.7) and (2.10), the velocity equations are linear.

2.4 Measurements of Kinematic Responses

Laboratory experiments were performed to measure the kinematic responses of a quadra-link suspension. For this purpose, designs of test apparatus described in the reported studies were reviewed in terms of their complexities and limitations. Kinematic and Compliance (K&C) test rigs have been widely used in the industry for measuring kinematic responses of vehicle suspensions, including camber, caster and toe angle variations, and variations in wheel track and base during wheel vertical travel [141-143]. The K&C test rig supports the vehicle on its four posts, which can be actuated independently, while the responses are attained through 6-DOF sensors mounted on each

wheel. Although such test rigs are considered to yield measurements with high accuracy, the test rigs are quite complex and very expensive. Alternately, single wheel experimental setups have been used in a few studies for measuring the kinematic responses of prototype suspensions which could provide reasonably accurate kinematic responses [29]. In this study, an experimental set-up of single wheel station prototype quadra-link suspension was realized in the laboratory in order to measure the wheel spindle rotational motions during its vertical travel.

Figure 2.4 illustrates the experimental set-up employed for measuring the kinematic responses, which comprises: a hydraulic actuator to generate the desired excitation; servo controller to operate the actuator in displacement feedback control; a feedback displacement sensor (LVDT); an inertia frame representing the fixed chassis; and a two-axis inclinometer to measure the camber (rotation about *x*- axis) and caster (rotation about *y*- axis) angles of the wheel. The suspension components included in the experiment set-up are: the cross-member, the strut, the upper control arm, the lower and trailing links, and the wheel spindle. The upper control arm and lower links are connected to the cross-member, while the cross-member is fixed to the frame through a custom made fixture, as seen the figure. The trailing link is attached to the frame through another fixture. In order to realize the actuator motion at the wheel center, as in the case of kinematic model, a rigid link comprising spherical joints at each ends was introduced between the wheel spindle and the actuator. The two- axes digital inclinometer was installed on a plate fixed to wheel spindle, as shown in the figure.

2.4.1 Measurements and Data Analysis

The wheel displacement was progressively varied in the upward and downward directions, and the resulting rotational motions of the wheel spindle about *x*- and *y*- axes (camber and caster angles) were measured using the LVDT and the inclinometers, respectively. The wheel spindle was displaced vertically through the link connected to the servo-hydraulic actuator. The wheel displacement and the camber and caster angles were measured at each interval of 5 mm change in the wheel spindle vertical travel. The inclinometer signals were recorded only when the actuator approached its steady position in order to minimize the contribution due to inertia effect. The suspension strut was also removed from the setup in order to eliminate possible influences of the strut on the wheel spindle kinematics. The measurements were performed over a ±50 mm wheel travel.

Figure 2.4: Laboratory setup for measurements of kinematic properties of a quadra-link suspension

The measured variations in the camber and caster angles of the wheel spindle are illustrated in Fig. 2.5 over the ±50 mm spindle travel. The results suggest that the quadra-link suspension considered in this study exhibits asymmetric variations in wheel camber and caster during jounce and rebound motions of the wheel. The suspension exhibits

greater camber variation during jounce than in rebound, while an opposite trend is observed in the caster angle response exhibited by the suspension.

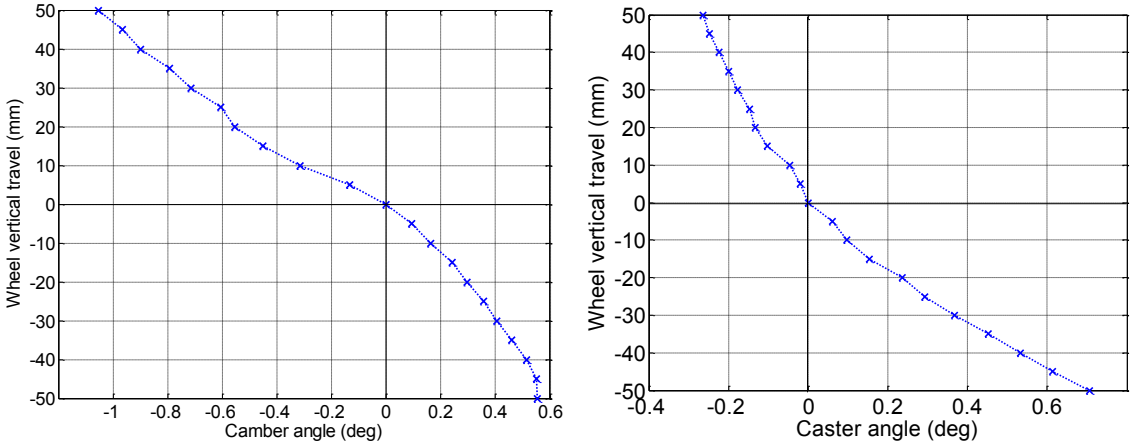

(a) (b)

Figure 2.5: Variations in camber and caster angle responses of the quadra-link suspension under 50 mm jounce and rebound motion of wheel spindle: (a) Camber; and (b) Caster.

2.5 Kinematic Model Validation

The laboratory measured data are used to examine the validity of the kinematic model formulations presented in Eqs (2.4) and (2.6). For this purpose, coordinates of the joints, *M1*, *O1*, *O2*, *O3*, *N1*, *P1*, *P*2 and *P3*, and the wheel center *C* of the candidate suspension were measured with respect to the fixed frame using a vernier scale. The measured coordinates of the linkage joints were subsequently transformed to a coordinate system fixed in the chassis. Table 2.1 summarizes the coordinates of the joints in the fixed chassis coordinates system.

The kinematic responses of quadra-link suspension model, particularly, the rotation of the wheel spindle about *x*- and *y*- axes were evaluated under a harmonic excitation at the wheel center, $z_u(t)=50\sin(0.2\pi t)$ mm. The model responses are compared with the measured data in Figs. 2.6 (a) and (b) to examine the validity of the kinematic model. The

Table 2. 1: Coordinates of various suspension link joints in the fixed chassis coordinates system.

Joint	Coordinates (x, y, z) in mm	Joint	Coordinates (x, y, z) in mm
M1	(120, 243, 443)	*C*	(0, 630, 313)
M2	(-154, 229, 446)	*N1*	(-40, 530, 390)
O1	(-105, 143, 268)	*P1*	(-132, 516, 193)
O2	(99, 229, 332)	*P2*	(106, 493, 239)
O3	(446, 380, 243)	*P3*	(9, 541, 178)

comparisons suggest considerable differences between the model and measured responses near extremities of the wheel travel. The model response exhibits relatively smaller asymmetry in the camber angle but greater asymmetry in the caster during jounce and rebound travel of the wheel, compared to those observed from the experimental data. The model responses suggest that a 50 mm wheel jounce yields camber variation of -1.25º, while a 50 mm rebound causes camber variation of nearly 1º. The measured data on the other hand, exhibits camber variations of 1.05º and -0.57º in jounce and rebound, respectively. The model responses, however, are quite comparable with the measured data in the 40 mm to -20 mm wheel travel range.

The caster angle response of the model exhibits greater asymmetry compared to the measured data. The peak caster variations of the model approach 0.08º at 50 mm jounce and 0.8º at 50 mm rebound, while the measured data revealed approximately 0.28º and 0.72º peak caster in jounce and rebound, respectively. The caster responses of the model are quite comparable with the measured data under wheel rebound motion. The model response, however, shows larger deviation from the measured data during upward motion of the wheel. It is thus observed from the figures that the model responses in camber angle during jounce and in caster angle during rebound motion of the wheel deviate considerably from the experimental data. Such deviations are most likely caused by

errors in the coordinates of various joints that were measured using a simple vernier scale.

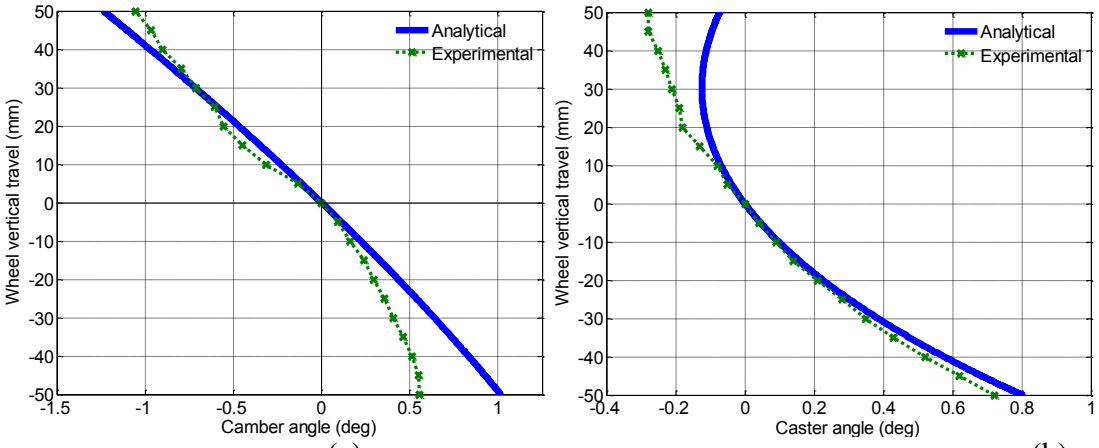

Figure 2.6: Comparisons of the camber and caster angle responses of the quadra-link suspension kinematic model under wheel center vertical excitation, $z_u(t)=50\sin(0.2\pi t)$ mm with the measured data: (a) camber; and (b) caster.

The influence of possible inaccuracy in measurement of coordinates of the joints was investigated through simulations of the model responses under slight variations in the coordinates. The results revealed that only slight variations in the coordinates could alter the camber and caster responses substantially. A tuning of the coordinates was thus performed to achieve model response close to the measured data. Table 2.2 illustrates the tuned coordinates of the linkage joints attained after a few iterations, while the numbers in bold face denote the changed coordinates. The table also illustrates the variations in the coordinates with respect to the measured coordinates. It can be seen that variations in the range of 1 to 5 mm only were needed to achieve responses closer to the measured data. Figure 2.7 shows comparisons of the camber and caster angle responses of the kinematic model with tuned joint coordinates with the measured data. The kinematic model with the modified coordinates exhibits comparable camber angle response until 40 mm of rebound

travel, while it also exhibits comparable caster angle response from 30 mm jounce to 25 mm rebound motion of the wheel spindle.

Table 2.2: Coordinates of the links joints of the quadra-link suspension attained after tuning and their deviations from the measured coordinates.

Joint	Coordinates (x, y, z) in mm	Deviations (x, y, z) in mm	Joint	Coordinates (x, y, z) in mm	Deviations (x, y, z) in mm
M1	(120, 243, **446**)	(0,0,3)	*C*	(0, 630, 313)	(0,0,0)
M2	(-154, 229, **447**)	(0,0,1)	*N1*	(-40, 530, **388**)	(0,0,2)
O1	(-105, **145**, **264**)	(0,2,4)	*P1*	(-132, **521**, **191**)	(0,5,2)
O2	(99, 229, 332)	(0,0,0)	*P2*	(106, 493, **242**)	(0,0,3)
O3	(446, 380, **239**)	(0,0,4)	*P3*	(9, 541, **173**)	(0,0,5)

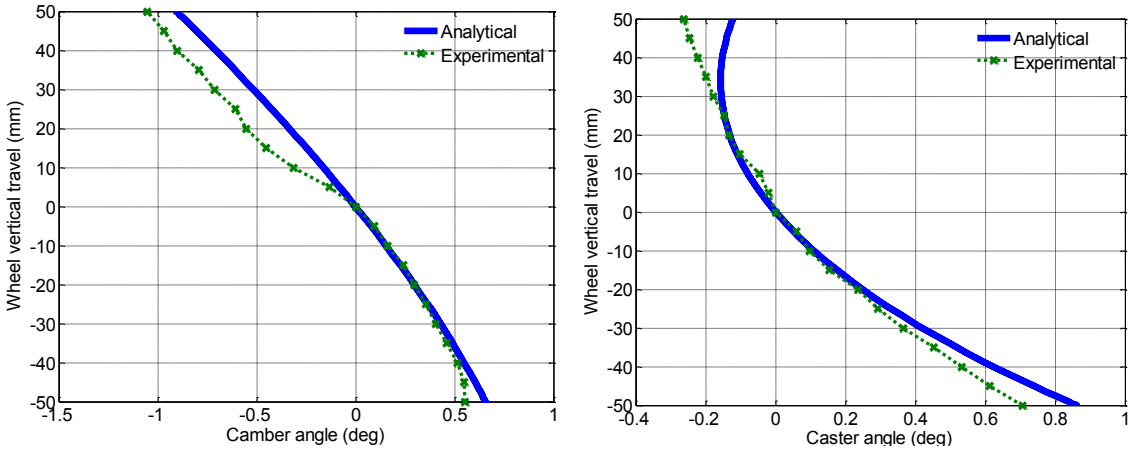

Figure 2.7: Comparisons of the camber and caster angle responses of the quadra-link suspension tuned model under wheel center vertical excitation, $z_u(t)$=50sin(0.2πt) mm with the measured data: (a) camber; and (b) caster.

An accurate measurement of the coordinates using a coordinate mapping system or parameter identification though minimizing an error function could yield more precise joint coordinates and thus comparable responses with the experimental values. However, the deviations between the kinematic model response and the measured angles cannot be entirely eliminated, partly due to lack of consideration of contributions due to compliance of joints/bushings. Furthermore, the actuator motion applied to the wheel center through the rigid link tends to impose a horizontal force on the wheel center. The magnitude of

the horizontal force would increase the vertical displacement. The responses of the proposed kinematic model with the refined coordinates, however, are considered adequate for study of various design factors affecting the suspension kinematic responses.

2.6 Kinematic Response Analysis of the Quadra-Link Suspension

The kinematic responses of the candidate quadra-link suspension are evaluated in terms of variations in the camber and toe angles, and wheel center and tire-ground contact point longitudinal and lateral displacements under wheel jounce and rebound motions. The wheel vertical motion is synthesized by a very low frequency harmonic displacement, $z_u(t)=100\sin(0.2\pi t)$ mm. The kinematic responses of the tuned quadra-link suspension model, evaluated under ±100 mm wheel travel, are presented in Figs. 2.8 (a) to (e) as a function of wheel vertical travel. The camber angle variation response exhibits similar degree of asymmetry with wheel jounce and rebound as observed in Fig. 2.6(a). The suspension under consideration, exhibits a large toe angle variation with peak magnitude of -2.4º at 100mm wheel upward motion and 4.5º at 100mm rebound motion, as also seen in Fig. 2.8 (b). The wheel center longitudinal and lateral displacement responses with wheel vertical travel are also highly asymmetric about the static position, with very larger displacements in rebound than those in jounce travel, as seen in Figs. 2.8 (c) and 2.5 (d), respectively. The peak longitudinal and lateral displacements in rebound and jounce are nearby 12 and -44 mm, and -3.5 and 9 mm, respectively. The variations in the longitudinal and lateral displacement responses of the tire ground contact point (wheel base and track variation) also follow similar trend to those in the wheel center displacements. These results suggest that the wheel track and wheel base vary considerably and asymmetrically under wheel vertical motions.

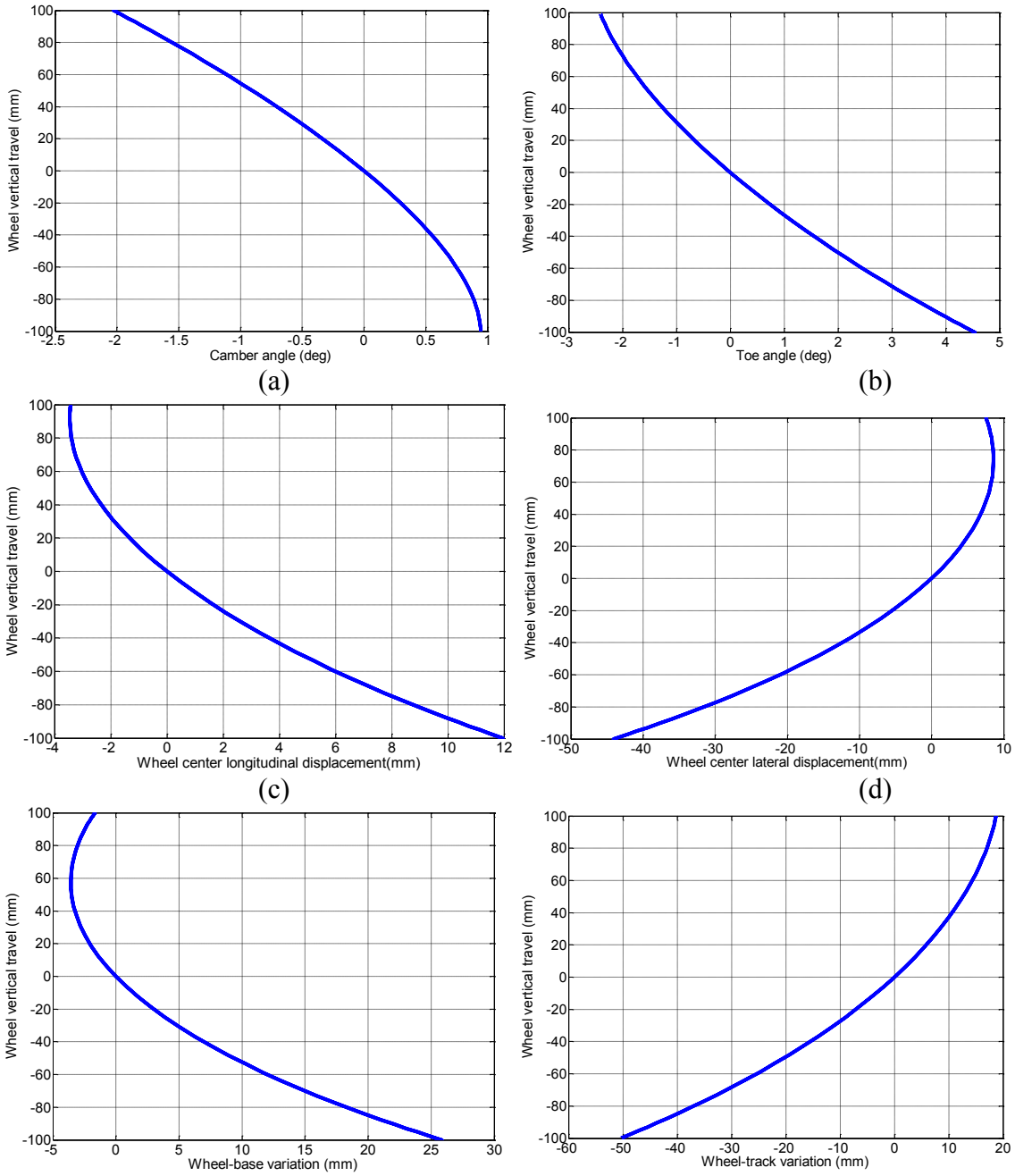

Figure 2.8: Variations in the kinematic responses of the tuned quadra-link suspension model under wheel center vertical excitation, $z_u(t)=100\sin(0.2\pi t)$ mm: (a) camber angle; (b) caster angle; (c) wheel center longitudinal displacement; (d) wheel center lateral displacement; (e) wheel base; and (f) wheel track.

The wheel track variation, which is the net result of camber and wheel center lateral displacement, exhibits a peak magnitude of -50 mm at 100 mm rebound position of the

wheel. The results thus suggest that the positive camber together with the negative wheel center displacement cause large wheel track variations.

2.6.1 Sensitivity of Kinematic Responses to Variations in the Joint Coordinates

The kinematic responses illustrated in Fig. 2.8 exhibit asymmetric and considerably large variations in the camber and toe angles, wheel base and track responses under wheel vertical motions. The degree of asymmetry in the responses would be strongly dependent on the suspension geometry and joint coordinates. With an increasing demand for larger subframe space, particularly for hybrid vehicles for placing the batteries [3], a suspension synthesis that can provide greater lateral subframe space without compromising the kinematic performances would be desirable, although it may involve difficult design compromises. The suspension lateral space availability is directly related to the links geometry, which may be characterized by the coordinates of joints *M1, M2, O1, O2, O3, N1, P1, P2* and *P3*. A sensitivity analysis is thus performed to idenfy the most important joint coordinates that affect the kinematic responses of the suspension in a significant manner.

Conventional sensitivity analyses methods generally involve a trend anlyses in selected responses under systematic variations in each coordinate. Considering that a quadra-link suspension comprises a total of 27 coordinates corresponding to 9 joints, the conventional method of sensitivity analysis would be highly cumbersome. Moreover, identification of relative degree of influences of a coordinate variation on the kinematic responses would be quite complex. Nalecz [144] suggested a matrix method of sensitivity analysis for evaluating the sensitivity of dynamic responses of linear systems to the parameter variations. The matrix method, however, can not be applied to nonlinear

systems, as in the case of displacement responses of the quadra-link suspension model. This approach could be applied to linear system of equations describing the velocities of the joint coordinates given in Eq (2.12). The displacement responses could subsequently be estimated from the velocity responses. Lee *et al*. [6] showed that the wheel spindle velocity equations of a five-link suspension mechanism could yield approximate displacement responses of the suspension by defining unity velocity excitations at the wheel center. In this section, the velocity equations, derived in Eq (2.12) are used to formulate the displacement and wheel rotation analyses. The linear equations are subsequently used to identify sensitivity of kinematic responses to variations in the joint coordinates. The linear system of equations in velocity responses, presented in Eq (2.15), can be expressed in the matrix form, as:

$$[J_M]\{q\} = \{I_M\} \tag{2.16}$$

where $[J_M]$ is a matrix with elements composed of nominal joint coordinates, and $\{q\}$ and $\{I_M\}$ are the joints velocity vector and input vectors, respectively, given by:

$$\{q\} = \left\{\dot{N}1_x \ \dot{N}1_y \ \dot{N}1_z \ \dot{P}1_x \ \dot{P}1_y \ \dot{P}1_z \ \dot{P}2_x \ \dot{P}2_y \ \dot{P}2_z \ \dot{P}3_x \ \dot{P}3_y \ \dot{P}3_z \ \dot{C}_x \ \dot{C}_y \ \dot{\varphi}_x \ \dot{\varphi}_y \ \dot{\varphi}_y\right\}^T$$
$$\{I_M\} = \left\{0 \quad 0 \quad 0 \quad 0 \quad 0 \quad 0 \quad 0 \quad \dot{z}_u \quad 0 \quad 0 \quad \dot{z}_u \quad 0 \quad 0 \quad \dot{z}_u \quad 0 \quad 0 \quad \dot{z}_u\right\}^T$$

Equation (2.16) is solved to determine various joint velocities for known initial joint coordinates and matrix, $[J_M]$, and wheel vertical velocity $\{I_M\}$. The displacement responses at a point in the wheel knuckle within a finite time are estimated from the velocity. The solutions can be conveniently used to study the sensitivity of kinematic responses to variations in the joint coordinates. The parameter sensitivity index is defined as the change in the response with change in a parameter value [143]. Assuming $[J_M]$ being continuous, the parameter vector $\{s\}$ is defined considering the initial coordinates

of the suspension joints as the variables. The sensitivity index of the kinematic responses $\{q\}$ to a change in any element s_i of the parameter vector $\{s\}$ is expressed as:

$$\frac{\partial q}{\partial s_i} = \frac{\partial \left[J_M\right]^{-1}}{\partial s_i}\{I_M\} = -\left[J_M\right]^{-1}\frac{\partial \left[J_M\right]}{\partial s_i}\left[J_M\right]^{-1}\{I_M\}; \quad i = 1\ldots n \tag{2.17}$$

where n is the number of parameters considered.

The sensitivity of the kinematic responses to different parameters is obtained for a finite vertical displacement at the wheel center. Table 2.3 illustrates the sensitivity indices of the wheel center longitudinal (C_x) and lateral (C_y) displacements, and camber, caster and toe angles, respectively, to variations in the coordinates of different joints. The positive numbers indicate an increase in the response caused by a positive change in the coordinate, while the negative numbers indicate decrease in the responses. Furthermore, the sensitivity values presented in the table have been multiplied by 10^6. For instance, a positive change in the *z*- coordinate of joint *M1* would yield a negative change in the wheel center lateral displacement, camber and caster angle responses, and positive change in the wheel center longitudinal displacement and toe angle responses. The results in Table 2.3 suggest that the kinematic responses are complex functions of variations in the joint coordinates. The table shows that the *x*- coordinates of the joints located at the chassis (*M1*, *M2*, *O1*, *O2* and *O3*) do not influence any of the kinematic responses, considered in the analyses, while the *x*- coordinates of the joints located at the wheel spindle (*N1*, *P1*, *P2* and *P3*) cause only small variations in the kinematic responses. The variations in the *y*- and *z*- coordinates of the upper control arm joints (*M1*, *M2* and *N1*) show significant influences on each of the kinematic responses, although the majority of these influences are conflicting. For instance, a positive change in z- coordinate of joint *M2* yields a negative change in camber and toe angle, and C_x and C_y, but positive change

in the caster angle response. Positive changes in the z- coordinates of both the *M1* and *M2* joints cause decrease in C_y, but in opposing influences on C_x. The results of the sensitivity analysis further suggest that the coordinates of upper control arm joints plays most significant role in articulation of the suspension.

Table 2.3: Sensitivity of kinematic responses of quadra-link suspension to variations in the linkage joint coordinates (sensitivity values x 10^6)

Joint	Co-ordinate	Wheel center displacement		Wheel angle		
		Longitudinal	Lateral	Camber	Caster	Toe
M1	*x*	0	0	0	0	0
	y	5	-2	-1	-2	0
	z	28	-10	-4	-9	2
M2	*x*	0	0	0	0	0
	y	-5	-2	-1	2	-1
	z	-27	-12	-6	10	-3
O1	*x*	0	0	0	0	0
	y	4	-4	1	-1	3
	z	12	-11	4	-2	9
O2	*x*	0	0	0	0	0
	y	-2	0	1	0	-1
	z	-11	-1	5	-2	-6
O3	*x*	0	0	0	0	0
	y	2	0	0	2	0
	z	6	0	0	6	-1
N1	*x*	0	4	2	0	0
	y	-5	4	2	2	0
	z	1	20	9	-1	1
P1	*x*	-2	2	-1	0	-2
	y	-4	3	-1	1	-3
	z	-11	10	-4	2	-9
P2	*x*	2	0	-1	0	1
	y	2	0	-1	0	1
	z	10	1	-4	1	5
P3	*x*	1	0	0	1	0
	y	-3	0	0	-3	1
	z	-5	0	0	-5	1

The results further show that variations in *z*- coordinates of joints *O1* and *P1* yield greatest influence on the toe angle response, although in the opposing direction. The joints of the lower link (*O1-P1*) could thus be tuned to yield lower toe angle response. It is interesting to note that the link *O1-P1* is also known as toe control link [145], which is used for setting the static toe angle of the wheel. The table further shows that the lower link also influences other kinematic responses considerably, including the wheel track and base, and camber angle variations. The results thus suggest that toe angle setting using the link *O1-P1* would also yield variations in other kinematic responses during the wheel travel. Apart from the joints of the lower control arm, the coordinates of joints *O2* and *P2* (particularly *z*- coordinates) influence the camber angle variations considerably. The link *O2-P2* also known as the camber control link [145] could also influence toe angle response of the suspension.

The variations in coordinates of joints *O3* and *P3* yield notable influences on the wheel center longitudinal displacement and the caster angle responses, with only slight changes in the toe angle response. The results thus suggest that the trailing link joints can be tuned to yield improved wheel base and caster angle responses. The validity of the proposed sensitivity analysis method is examined by evaluating the responses of the kinematic model of the quadra-link suspension by changing the z- coordinates of joints *M1*, *M2* and *O3* in the positive direction by 10 mm. Variations in the wheel center longitudinal displacement, and caster, camber and toe angle responses are evaluated under wheel center displacement of 100 mm peak jounce and rebound, and compared with those of the model with nominal coordinates, and the comparisons are illustrated in Fig. 2.9. The sensitivity indices of *M1*, *M2* and *O3* corresponding to wheel center

longitudinal displacement are 28, -27 and -6 (Table 2.3), respectively. Figure 2.9 (a) shows that the wheel center longitudinal displacement response decreases considerably when *z*-coordinate of *M2* is increased, while an opposing trend is observed with change in the *z*-coordinate of *M1*. The change in *z*-coordinate of *O3* also results in increase in C_x, while the change is relatively lower than that observed with the change in *z*-coordinate of *M1*.

The sensitivity index values of *M1*, *M2* and *O3* corresponding to camber, caster and toe angle response were obtained as: -4, -6, 0; -9, 10, 6; and 2, 3, -1, respectively (Table 2.3). Figures 2.9 (b) to (d) show variations in camber, caster and toe angle responses of the kinematic response characteristics of the quadra-link suspension model with changes in *z*- coordinates of these joints. Variations in *z*-coordinates of *M1* and *M2*, with relatively larger sensitivity index values, show significant changes in the camber, caster and toe angle responses. Variations in *z*-coordinate of *O3*, with sensitivity index values 6 and -1 for the caster and toe angle responses, yield notable change in the caster and toe angles, while the effect on camber angle is negligible, particularly during the jounce motion. This confirms with the results summarized in Table 2.3, which show a sensitivity index of 0 corresponding to the camber angle, although a slight decrease in camber angle is observed during rebound motion of the wheel. This was attributed to rounding-off of the magnitudes of the sensitivity indices.

The results in Table 2.3 suggest that the kinematic responses are highly influenced by the joint coordinates of the quadra-link suspension. The proposed sensitivity analysis method could thus help identify relative influences of various joint coordinates on the suspension responses, and thereby facilitate an optimal suspension geometry synthesis.

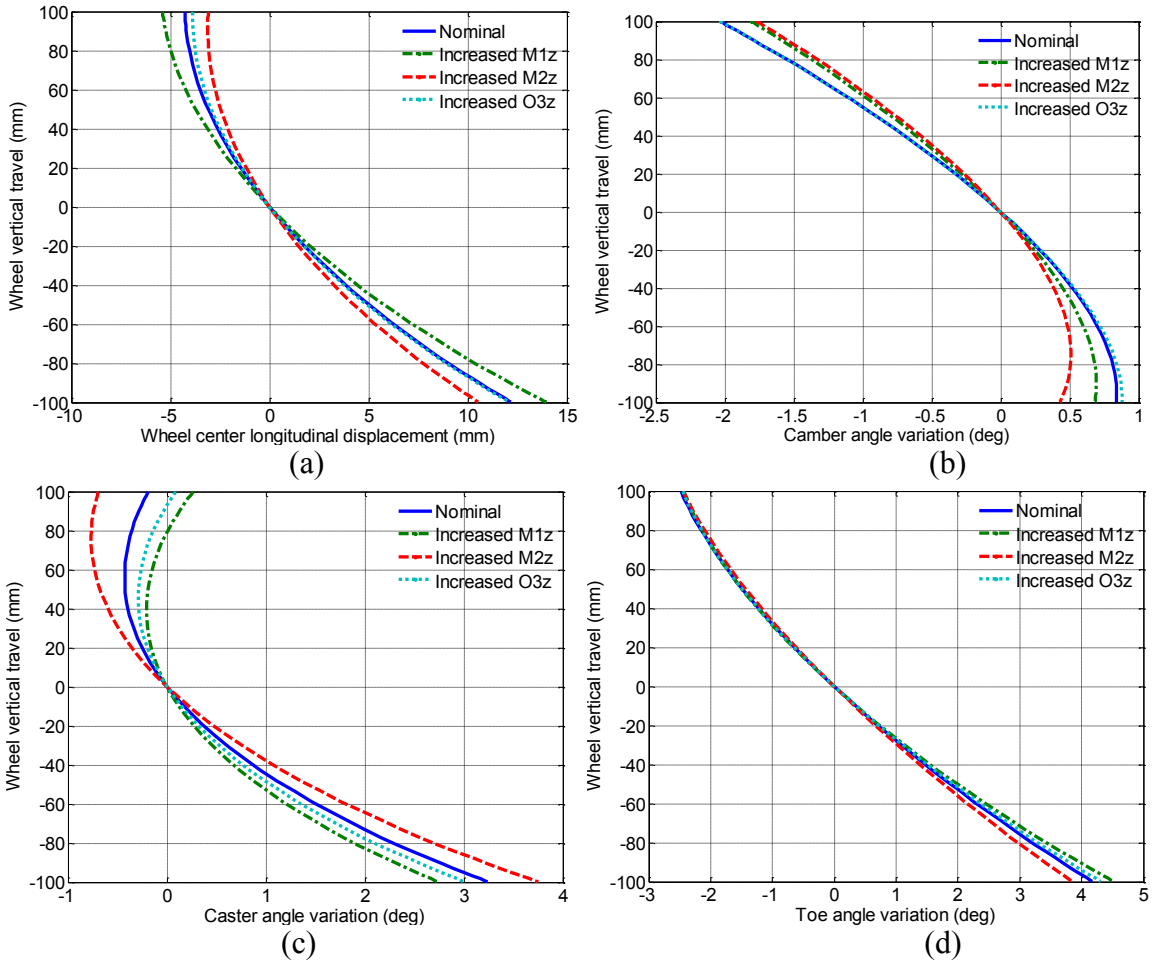

Figure 2.9: Comparisons of kinematic responses of the suspension with +10 mm change in the *z*- coordinate of *M1*, *M2* and *O3* joints with those of the model with nominal coordinates: (a) wheel center longitudinal displacement; (b) camber and (c) caster and (d) toe angle.

2.7 Kinematic Analysis of a Double Wishbone Suspension

A double wishbone suspension, illustrated in Fig. 2.10, is one of the most widely used independent suspension in passenger and racing cars. In its basic form, it consists of two control arms connecting the chassis with the wheel spindle, which also determine the mechanism articulation [2, 137]. The double wishbone suspension is considered to offer specific advantages over other types of suspension owing to its simplicity and minimal toe angle variations during wheel vertical motions [1, 4]. The strut in a double wishbone

suspension is located on either the upper or the lower control arm, while it exhibits minimal influence on the articulation of the suspension mechanism.

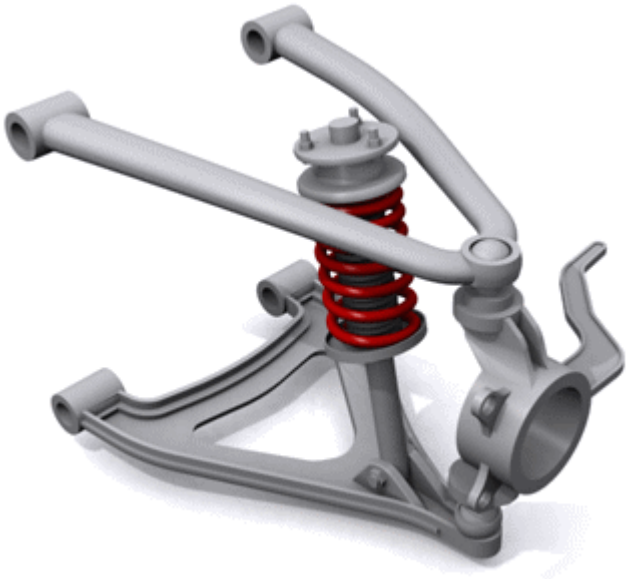

Figure 2.10: A schematic image of double wishbone suspension

2.7.1 Kinematic Model of the Double Wishbone Suspension

The roll-plane kinematic properties of a double wishbone suspension can be effectively evaluated using a planar model [1, 4]. Consequently, a planar model of the suspension is formulated, as shown in the Fig. 2.11, which comprises of upper (*MN*) and lower (*OP*) control arms, and the strut (*AB*) including spring and damper mounted on the lower control arm. The points *M* and *O* represent the revolute joints of the upper and lower control arms with the chassis, while points *N* and *P* represent the upper and lower ball joints (between wheel spindle, and upper and lower control arms), respectively. The upper and lower control arms connecting the chassis with the wheel spindle form *R*-*R* links considering that the ball joints in a plane are similar to the revolute joints. The point *C* in Fig. 2.11 represents the wheel center. The chassis, control arms and the wheel spindle are assumed to be rigid bodies, while the tire is assumed to be integral part of the

wheel spindle. The suspension kinematic relations are derived with an assumption that the revolute joints between the chassis and control arms and between the control arms and wheel spindle are frictionless.

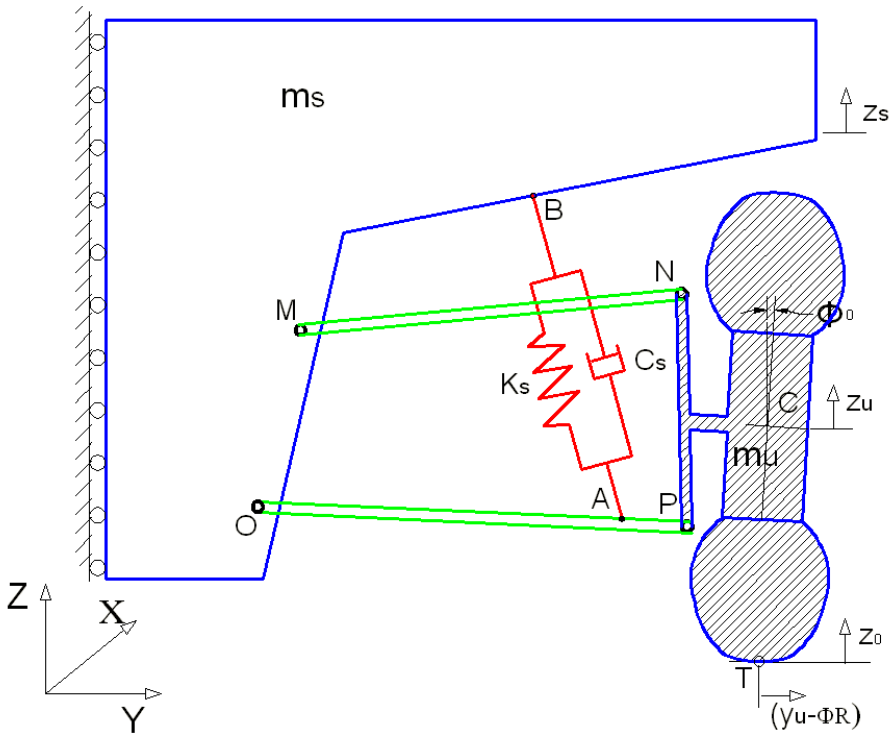

Figure 2.11: Planar kinematic model of a double wishbone suspension

In the planar suspension mechansim, the chassis, control arms and the wheel spindle form the components of the kinematic chain, while consideration of the fixed chassis forms the mechanism. The double wishbone suspension with the chassis, two control arms and the wheel spindle thus forms a four bar mechanism. The mobility of the four bar planar suspension system can be estimated from the Grubler's criteria for mobility [19], such that:

$$DOF=3(N_m-1)-2R_m \tag{2.18}$$

where N_m and R_m denote the number of links and revolute joints, respectively. Considering each of the four links and the revolute joints, a double wishbone suspension

with the fixed chassis has only one degree of freedom. This DOF of the mechanism is the vertical motion of the wheel assembly with respect to the fixed chassis. The translational and rotational motions of the wheel spindle are dependent on its vertical motion.

The kinematic analysis of a suspension is generally performed under prescribed wheel vertical displacement considering fixed chassis. This approach, however, does not permit analysis of wheel motions with a simultaneous chassis movement. In this study, a vertical degree of freedom of the chassis is introduced in addition to that of the wheel spindle in order to study the kinematic responses under vertical motions of both the chassis and the wheel spindle. The generalised coordinates are thus chosen as the vertical displacements of the chassis (z_s) and wheel spindle (z_u). A coordinate system fixed at the ground is assumed, while motion of the chassis is also considered to occur with respect to a ground coordinate system. Initially, the origins of both the coordinates are assumed to coincide.

The orientation of a planar rigid body, in general, can be determined by the positions of any three points in the plane. For the wheel spindle, the two joint centers *N* and *P,* and the wheel center *C* are conveniently chosen, where (N_{y0}, N_{z0}), (P_{y0}, P_{z0}) and (C_{y0}, C_{z0}) define the initial coordinates of *N*, *P* and *C*, respectively. The first subscript of the variable represents the coordinate (*y* or *z*), while the second subscript (*'0'*) designates the initial position, when present. For a finite displacement of the wheel spindle in the given plane, a general displacement matrix can be formulated as [19, 132]:

$$[D]_{wheelspindle} = \begin{bmatrix} a_{22} & a_{23} & C_y - (a_{22}C_{y0} + a_{23}C_{z0}) \\ a_{32} & a_{33} & C_z - (a_{32}C_{y0} + a_{33}C_{z0}) \\ 0 & 0 & 1 \end{bmatrix} \tag{2.18}$$

where $a_{22}=a_{33}=\cos\phi$, $-a_{23}=a_{32}=\sin\phi$, and ϕ is the wheel spindle rotation about x-axis. In the above expression, C_y and C_z are the instantaneous coordinates of the wheel center C. The instantaneous coordinates (N_y, N_z) and (P_y, P_z) of N and P, respectively, following application of a wheel spindle vertical displacement z_u, are derived from the displacement matrix, as:

$$\begin{bmatrix} N_y & P_y \\ N_z & P_z \\ 1 & 1 \end{bmatrix} = [D]_{wheelspindle} \begin{bmatrix} N_{y0} & P_{y0} \\ N_{z0} & P_{z0} \\ 1 & 1 \end{bmatrix} \tag{2.19}$$

The above formulation exhibits 6 unknown parameters corresponding to a given z_u, namely, the y and z coordinates of N and P, the y- coordinate of C and the wheel rotation, ϕ. Equation (2.19) is solved in conjunction with two constraint conditions imposed by the suspension mechanism, which are formulated considering constant lengths of the upper (l_{MN}) and lower (l_{OP}) control arms, such that:

$$(N_y - M_y)^2 + (N_z - M_z)^2 = l_{MN}^2; \text{ and } (P_y - O_y)^2 + (P_z - O_z)^2 = l_{OP}^2 \tag{2.20}$$

The solutions of Eq. (2.19) yield following nonlinear system of equation in displacements of the joints:

$$\begin{aligned} &N_y = a_{22}(N_{y0} - C_{y0}) + a_{23}(N_{z0} - C_{z0}) + C_y;\ N_z = a_{32}(N_{y0} - C_{y0}) + a_{33}(N_{z0} - C_{z0}) + C_z \\ &P_y = a_{22}(P_{y0} - C_{y0}) + a_{23}(P_{z0} - C_{z0}) + C_y; \text{ and } P_z = a_{32}(P_{y0} - C_{y0}) + a_{33}(P_{z0} - C_{z0}) + C_z \end{aligned} \tag{2.21}$$

where $M_y=M_{y0}$, $O_y=O_{y0}$, $M_z=M_{z0}+z_s$, $O_z=O_{z0}+z_s$ and $C_z=C_{z0}+z_u$.

The nonlinear system of equations can be numerically solved to obtain the instantaneous coordinates of the joints and the wheel center following vertical displacements of the chassis and the wheel center. The rotational motion of the wheel, ϕ, directly yields the wheel camber angle response, while the wheel center lateral

displacement y_u can be derived from y_u=C_y-C_{y0}. The lateral displacement T_y of the wheel-ground contact point T with respect to the static position is considered as the variation in the wheel track, which can be directly related to the tire wear characteristics. With the rigid body assumption of the wheel assembly, the lateral motion of the wheel-ground contact point is obtained as:

$$T_y = a_{22}(T_{y0} - C_{y0}) + a_{23}(T_{z0} - C_{z0}) + C_y \tag{2.22}$$

where (T_{y0}, T_{z0}) define the initial coordinates of the contact point T. Alternatively, the lateral displacement of the contact point can also be obtained from the wheel camber and wheel center lateral displacement, such that:

$$T_y = y_u - \phi\,(C_{z0} - T_{z0}) \tag{2.23}$$

The above formulation in T_y assumes small rotation of the wheel, such that (a_{22} =1; a_{23} =ϕ).

The translational velocities of points M, N and C, and the angular velocity of the wheel spindle about the x- axis can be further obtained from time derivatives of the Eqs (2.20) and (2.21), as:

$$\begin{aligned}
&\dot{N}_y = \dot{a}_{22}(N_{y0} - C_{y0}) + \dot{a}_{23}(N_{z0} - C_{z0}) + \dot{C}_y;\ \dot{N}_z = \dot{a}_{32}(N_{y0} - C_{y0}) + \dot{a}_{33}(N_{z0} - C_{z0}) + \dot{z}_u \\
&\dot{P}_y = \dot{a}_{22}(P_{y0} - C_{y0}) + \dot{a}_{23}(P_{z0} - C_{z0}) + \dot{C}_y;\ \dot{P}_z = \dot{a}_{32}(P_{y0} - C_{y0}) + \dot{a}_{33}(P_{z0} - C_{z0}) + \dot{z}_u \\
&(N_y - M_{y0})\dot{N}_y + (N_z - M_{z0} - z_s)(\dot{N}_z - \dot{z}_s) = 0;\ \text{and}\ (P_y - O_{y0})\dot{P}_y + (P_z - O_{z0} - z_s)(\dot{P}_z - \dot{z}_s) = 0
\end{aligned} \tag{2.24}$$

where $\dot{a}_{22} = -\dot{\phi}\sin\phi$, $\dot{a}_{23} = -\dot{\phi}\cos\phi$, $\dot{a}_{32} = \dot{\phi}\cos\phi$ and $\dot{a}_{33} = -\dot{\phi}\sin\phi$. In the above system of equations, a dot over a coordinate or variable denotes the time derivative. Unlike displacement expressions in Eqs (2.20) and (2.21), the velocity expressions are linear (for known chassis and wheel spindle vertical velocities, joint coordinate displacements and wheel rotation).

2.7.2 Kinematic Response Analysis of a Double Wishbone Suspension

The kinematic responses, particularly, the variations in the camber angle (ϕ), wheel center lateral displacement (C_y) and half wheel-track (T_y) are evaluated by considering fixed chassis ($z_s = 0$), while the wheel center is subjected to a very low frequency (0.1Hz) harmonic displacement of 100 mm amplitude, such that $z_u(t)=100\sin(0.2\pi t)$. The y- and z-coordinates of various joints were selected on the basis of a three-dimensional SLA (Short Long Arm) suspension configuration reported in [146], such that: M = (0.430, 0.818); N = (0.644, 0.852); O = (0.365, 0.360); P = (0.743, 0.347); C = (0.787, 0.452); A = (0.660, 0.350) and B = (0.615, 0.920).

The validity of the model and the solution method was examined by comparing the kinematic responses of the kineto-dynamic model with those derived from a 2-dimensional multi-body kinematic model of the same suspension developed in ADAMS/view and illustrated in Fig. 2.12. The upper and lower control arms of the planar multi-body (ADAMS/view) kinematic model are connected to the chassis and the wheel spindle through revolute joints. The chassis was constrained to travel in vertical direction only by defining a translational joint in the vertical direction. A harmonic chassis motion is considered along the vertical direction. Furthermore, a general point motion was defined at the wheel center in vertical direction, which permits the wheel spindle to have translation motion in lateral and vertical directions apart from the rotational (camber) motion. The comparisons of the kinematic responses revealed excellent agreements between the responses of both the models.

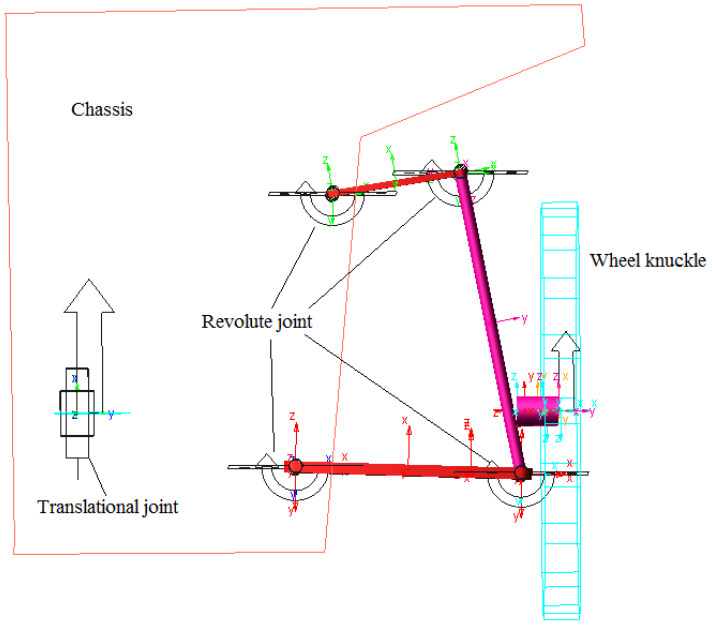

Figure 2.12: Planar multi-body kinematic model of the suspension developed in ADAMS/view

Figure 2.13 illustrates variations in the camber angle, wheel center lateral displacement and half wheel-track variation with the wheel vertical travel. The results show highly asymmetric camber angle variations during compression and rebound, which ranges from -3.18º at 100 mm jounce position vs. 1.14º at 100 mm rebound position of the wheel. The lateral displacement of the wheel center, however, is only slightly asymmetric about the corresponding static equilibrium position. Moreover, the wheel center moves laterally closer to the chassis during both jounce and rebound motion of the suspension. The half wheel track variation which is the combined result of the camber rotation and the wheel center lateral motion, as evident in Eq (2.23), exhibit considerably large asymmetry in the response during compression and rebound. The 100 mm jounce and rebound motions cause peak variations in the half wheel track of 6 mm and -22 mm, respectively. Variations in the camber angle are either positive or negative depending on the jounce or rebound position of the suspension. The results suggest that both the

camber angle and wheel center lateral motion add up to increase the lateral displacement of the tire-ground contact point during the rebound motion.

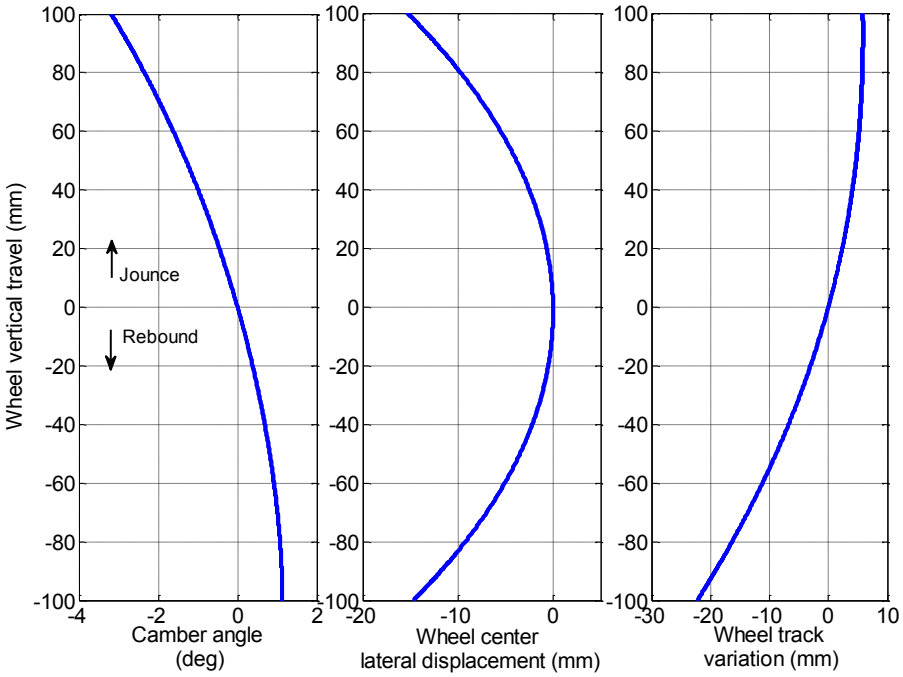

Figure 2.13: Variations in Camber angle, wheel center lateral displacement and half wheel track responses under wheel vertical displacement, z_u= 100 sin (0.2πt) mm

The kinematic responses of the suspension model with differential motion across the suspension is further evaluated by subjecting the model to vertical motions of the chassis and the wheel center such that z_s = 100 $sin(2\pi t)$ mm and z_u = 50 $sin(2\pi t)$ mm. The responses of the proposed model were observed to be identical to those of the ADAMS models. Figure 2.14 illustrates variation in camber angle ϕ, wheel center lateral displacement C_y and half wheel-track T_y of the double wishbone suspension model. The results suggest that the variations in C_y occur at twice the excitation frequency of 1Hz. The results also show asymmetric variations in each of the responses during jounce and rebound, as observed in Fig. 2.13. It can also be seen that the suspension configuration

considered in the study would yield lower effective wheel track under wheel rebound motions, and a higher effective wheel track under the wheel jounce motions.

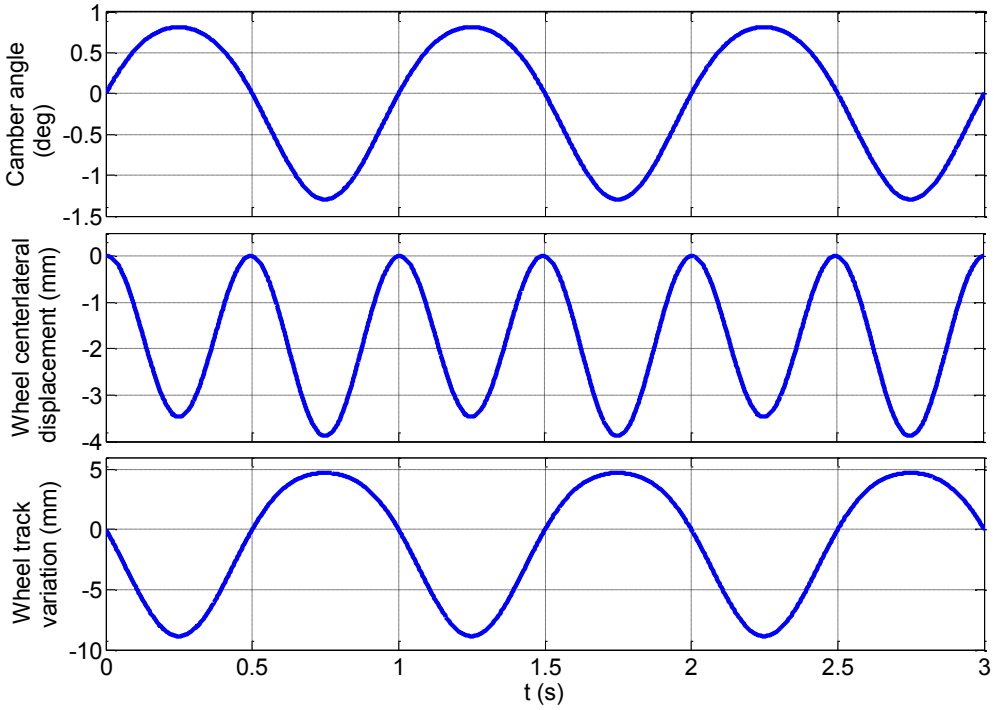

Figure 2.14: Variations in camber angle, wheel center lateral displacement and half wheel-track responses of the suspension under differential excitation, $z_s = 100sin\ (2\pi t)$ mm and $z_u = 50sin\ (2\pi t)$ mm.

2.7.3 Sensitivity of Kinematic Responses to Joint Coordinates

Results in Figs. 2.13 and 2.14 show asymmetric and considerably large variations in the camber angle and wheel track responses under wheel vertical motions. The degree of asymmetry in the responses is expected to strongly depend on the suspension geometry and joint coordinates. With an increasing demand for larger subframe space, particularly for hybrid vehicles for placing the batteries [3], a suspension synthesis that can provide greater lateral subframe space without compromising the kinematic performances would be desirable. The suspension lateral space availability is directly related to the links geometry, which may be characterized by the coordinates of joints *M, N, O* and *P*. A

sensitivity analysis is thus performed to identify the influences of joint coordinates on the kinematic responses of the suspension.

The *y*- and *z*- coordinates of each joint is varied by ±50 mm about the nominal values, while the variation in the *y*- coordinates of *P* is limited only to -50 mm due to limited clearance between the wheel and joint *P*. The effects of variations in the joint coordinates are evaluated under 100 mm positive and negative wheel vertical motion, in terms of peak variations in camber angle and the wheel track during jounce and rebound motion of the wheel, denoted as peak-jounce camber, peak-rebound camber, peak-jounce track and peak-rebound track, respectively. It needs to be emphasized that the responses are evaluated with change in one coordinate and maintaining other coordinates at their respective nominal values. The sensitivity of the kinematic responses to changes in the joint coordinates are presented in Table 2.4, while the table also presents these responses of the suspension with nominal coordiantes. Moreover, the table illustrates (within the parenthesis) percentage change in the responses with respect to those of the nominal suspension geometry per millimeter (mm) change in the joint coordinates. For example, a +50 mm change in the *y*- coordinate of joint *M*, increases the peak jounce camber to -4.52º as compared to -3.19º of peak camber variation with the nominal suspension. A 50 mm positive change in the *y*- coordinate of joint *M* thus results in 42% increment in the peak jounce camber angle. With an assumption that this increment is linear with change in the joint coordinate, a 1 mm positive change in the *y*- coordinate of joint *M* would increase the peak jounce camber by 0.84%, as illustrated in Table 2.4.

The results suggest that the camber angle and wheel track variation responses of the suspension are a complex function of the joint coordinates. Positve changes in *z*-

coordinates of joints *M* and *P*, and negative changes in *z*- coordinates of joints *N* and *O* help reduce the peak changes in the camber cangle and the wheel track during both jounce and rebound travel of the wheel. It is also evident from the table that opposite changes in these coordinates cause opposite effects. The results suggest that the changes in the *z*- coordinates show significantly large influences on the kinematic responses considered in this study. The changes in the *z*- coordinates of the joints *M* and *P* in positive sense, and of the joints *N* and *O* in a negative sense either increase the distance between the upper and lower control arm joint with the chassis or decrease the distance between the upper and lower ball joints. A double wishbone suspension with closer upper and lower ball joints may thus yield lower variations in the camber angle and wheel track responses of the suspension under the wheel jounce and rebound motions.

The results in Table 2.4 further suggest that changes in the *y*- coordinate of any joint yield conflicting influences on the peak jounce and rebound camber angle and the wheel track responses of the model. For instance, a positive change in *y*- coordinate of the joint *M* yields higher peak jounce camber angle (-4.52º) and peak jounce track variation (12.4 mm) but lower peak rebound camber angle (1.02º) and peak rebound track (-21.0 mm) responses. It is further seen that negative changes in *y*- coordinates of joints *M* and *O* or a positve change in *y*- coordinate of the joint *N* yield lower jounce camber angle and wheel track responses, while the opposite changes in the coordinates yield opposite effects. These suggest that increase in the control arms lengths would decrease variations in the camber angle and wheel track responses during wheel jounce motions, while reducing the control arms lengths would yield lower peak variations in camber angle and wheel track during rebound motion of the wheel.

Table 2.4: Sensitivity of peak variations in camber angle and wheel track responses under 100 mm jounce and rebound motion of the wheel to changes in the joint coordinates

Coordinate variation	Peak-jounce camber –deg (% variation/mm change)	Peak-rebound camber-deg (% variation/mm change)	Peak-jounce track-mm (% variation/mm change)	Peak-rebound track-mm (% variation/mm change)
Nominal	**-3.19 (0)**	**1.14 (0)**	**5.9 (0)**	**-22.2 (0)**
M_y +	-4.52 (0.84)	1.02 (-0.21)	12.4 (2.21)	-21.0 (-0.11)
M_y -	-2.39 (-0.50)	1.29 (0.27)	3.5 (-0.81)	-22.9 (0.06)
M_z +	-2.26 (-0.58)	0.05 (-1.92)	0.0 (-1.98)	-6.8 (-1.39)
M_z -	-5.55 (1.48)	3.60 (4.34)	17.3 (3.91)	-33.5 (1.01)
N_y +	-2.50 (-0.43)	1.26 (0.22)	3.7 (-0.74)	-22.8 (0.05)
N_y -	-4.21 (0.64)	1.04 (-0.17)	10.8 (1.69)	-21.2 (-0.09)
N_z +	-5.15 (1.23)	3.28 (3.79)	15.4 (3.25)	-32.0 (0.88)
N_z -	-2.58 (-0.38)	0.05 (-1.91)	0.0 (-1.99)	-6.2 (-1.44)
O_y +	-3.05 (-0.09)	1.46 (0.57)	4.7 -0.41)	-26.4 (0.37)
O_y -	-3.29 (0.07)	0.92 (-0.38)	7.5 (0.55)	-19.1 (-0.28)
O_z +	-4.41 (0.77)	2.76 (2.87)	24.7 (6.43)	-43.4 (1.91)
O_z -	-1.90 (-0.81)	0.10 (-1.82)	1.4 (-1.54)	-14.1 (-0.73)
P_y -	-3.11 (-0.05)	1.41 (0.48)	5.1 (-0.27)	-25.7 (0.32)
P_z +	-2.07 (-0.70)	0.11 (-1.80)	1.2 (-1.58)	-11.4 (-0.97)
P_z -	-4.07 (0.56)	2.51 (2.42)	19.5 (4.67)	-40.1 (1.61)

The results in Table 2.4 suggest that the kinematic responses of a double wishbone suspension including the variations in the camber angle and wheel track are strongly influenced by the joint coordinates. The synthesis of the suspension geometry is thus a complex task particularly with additional constraint on the lateral space. Suspension lateral space is directly related to the *y*- coordinates of the joints, and an additional subframe space requirement would necessiate consideration of positive changes in the *y*-coordinates of joints *M* and *O* (chassis-control arm joints). Such variation in the joint

coordinates would also influence the roll camber response of the suspension, which necessitates consideration of an extended half-car model in the roll-plane of the vehicle.

2.8 Summary

Single-wheel station kinematic models of two types of suspension are formulated to study the kinematic responses of the suspension, which could also be employed for synthesis of suspension geometry. The validity of the three-dimensional kinematic model of a quadra-link suspension is demonstrated by comparing the camber and caster angle variations of the model with the laboratory-measured data. The kinematic responses of the quadra-link suspension including wheel center displacements, variations in the wheel base and track, and camber, caster and toe angles as a function of wheel vertical travel are analyzed. Based on the matrix equations, a sensitivity analysis method is proposed to investigate the influences of variation in the suspension joint coordinates on the kinematic responses. Planar model of a double wishbone suspension is also proposed for anaysis of roll-plane kinematic responses, such as variations in the camber angle, wheel track and wheel center lateral displacement. Validity of the proposed model was examined by comparing the kinematic responses with those of a planar model developed in ADAMS/view platform. The kinematic responses of the double wishbone suspension are studied under wheel vertical motions, and simultaneous vertical motions of the wheel and the chassis. The influences of the joint coordinates on the kinematic responses are investigated through a sensitivity analysis. The results of the sensitivity analyses of both the suspensions are interpreted so as to attain design guidelines for suspension geometry synthesis. The proposed models are further enhanced in the subsequent chapters to investigate kineto-dynamic response characteristics of the suspension system.

CHAPTER 3

KINETO-DYNAMIC ANALYSIS OF A DOUBLE WISHBONE SUSPENSION

3.1 Introduction

Dynamic performances of a vehicle are strongly influenced by its suspension design in a highly complex manner. The synthesis of a vehicle suspension thus involves complex compromises among the various conflicting performance measures through judicious selection of the suspension elements. Linear or nonlinear quarter-car models have been widely used to evaluate the ride, rattle space and the dynamic tire force responses of suspension design concepts, and synthesis of semi-active and active suspension control strategies, assuming negligible contributions due to suspension kinematics [63, 85, 90, 97, 121]. The conventional quarter-car model as illustrated in Fig. 3.1 employs equivalent stiffness and damping properties of the suspension coupling the chassis and the wheel masses, while the suspension is permitted to undergo pure vertical deflections. In an independent suspension system, the wheel carrier or the spindle is generally connected to the chassis through the suspension linkages, which induce rotational motion of the wheel apart from the vertical motion. The center of rotational motion of the wheel relies on the suspension geometry and tends to influence the dynamic responses of the vehicle. Furthermore, the suspension strut is generally mounted away from the unsprung mass center (cg) and thus the point of application of spring and damping forces and the unsprung mass are not colinear. It has been suggested that the suspension kinematics can lead to nonlinear responses and significantly affect the vertical dynamics [90,128].

The identification of a vehicle model that incorporates the contributions due to linkage kinematics, and flexible bushing in the joints may thus be desirable for dynamic analyses of alternate concepts in an effective manner, and could serve as an effective tool to study the influences of the linkage geometry and joint flexibilty on the dynamic responses. Such a model is identified as '*kineto-dynamic'* model, and could also be used for the synthesis of the suspension of a ground vehicle. A kineto-dynamic model would represent physical suspension mechanism by including the suspension kinematics, and can be employed to synthesize a vehicle supension considering both kinematic and dynamic responses.

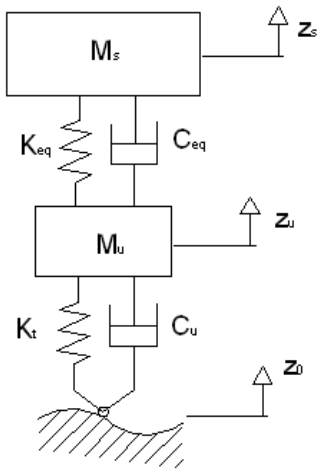

Figure 3.1: Conventional quarter car model

A few studies have been reported with inclusion of the suspension linkage kinematics either by parameter identification of the simple quarter car model [90] or by employing kineto-dynamic models [128-133]. The majority of these reported studies on the influences of suspension linkages on the dynamic responses of the vehicle considered MacPherson type of suspension [128,131, 132], while kineto-dynamic model of a double wishbone suspension has been attempted in a single study [133], although such a suspension has been widely used. Kim *et al*. [90] concluded that the contribution of the

MacPherson suspension kinematics on the equivalent parameter and the dynamic responses are considerably small. The strut location away from the wheel center, however, yields some effects of the kinematics. The kinematics of a double wishbone suspension may yield considerably stronger effects on the dynamic responses compared to the MacPherson suspension. This is attributable to kinematics associated with the additional control arm, strut location on the lower control arm, and additional kinematic constraints.

This chapter presents the study of influences of the linkage kinematics, tire lateral compliance and the flexible joint bushings on the dynamic and kinematic responses of a vehicle comprising a double wishbone type of suspension. The study involves developing a quarter-car kineto-dynamic model incorporating double wishbone linkage kinematics and tire lateral compliance, and identification of equivalent spring and damping rates to be employed in a conventional quarter car model. The responses of the kineto-dynamic model are compared with those of a conventional quarter-car model employing equivalent suspension and damping rates corresponding to static equilibrium under harmonic and idealized bump inputs. It needs to be emphasized here that only the dynamic responses of the proposed model can be compared with the conventional model, while the proposed model can be effectively used to generate responses that cannot be obtained from the conventional model. Suspension joints bushing compliance is further included in the kineto-dynamic model to investigate the influences of flexible bushings on the kinematic and dynamic responses of the model. The proposed kineto-dynamic model is employed to realize synthesis of suspension linkage joint coordinates considering lateral space limitations.

3.2 Model Development

Figure 3.2 illustrates the proposed kineto-dynamic quarter-car model comprising a double wishbone type of suspension system. The proposed planar model includes upper (*MN*) and lower (*OP*) control arms, and a strut (*AB*) mounted on the lower control arm. The strut is modeled assuming linear stiffness and damping properties. The control arms are connected to the chassis and the wheel spindle through revolute joints. The control arms are considered to be massless and the total unsprung mass is assumed to be lumped at the center of gravity (cg) of the wheel assembly. The tire is modeled as a combination of a vertical spring and a damper, while the lateral compliance is represented by lateral linear stiffness. The model is formulated considering vertical displacements of the sprung mass and the wheel as the degrees-of-freedom (DOF) as in the case of a conventional quarter-car model, shown in Fig. 3.2. A coordinate system with its origin fixed at the chassis corresponding to its static equilibrium position is considered.

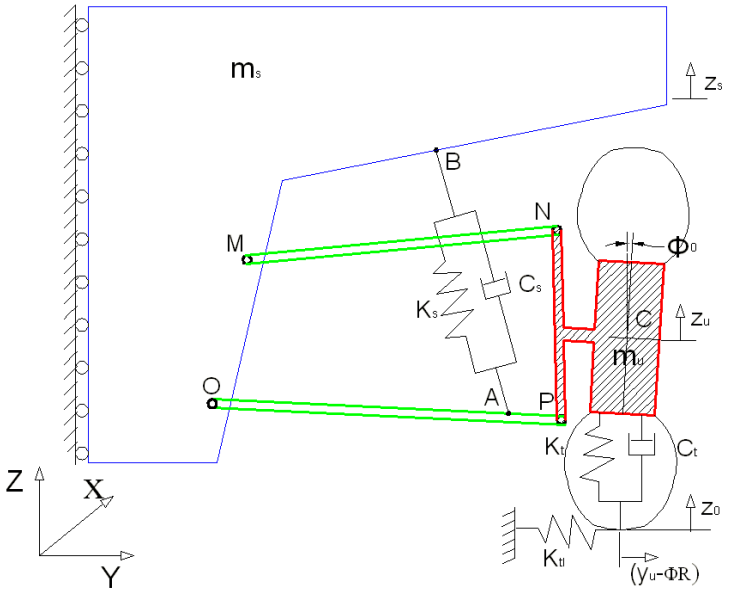

Figure 3.2: Proposed kineto-dynamic quarter car model of a vehicle with double wishbone suspension

3.2.1 Kinematic Analysis

The kinematic relations describing the motions of the wheel knuckle can be produced using displacement matrix and the constraint equations corresponding to the control arm joints as discussed in Section 2.7.1. The nonlinear kinematic relations as obtained in Eqs (2.20) and (2.21) can be written as:

$$
\begin{aligned}
&N_y = a_{22}(N_{y0} - C_{y0}) + a_{23}(N_{z0} - C_{z0}) + C_y \\
&N_z = a_{32}(N_{y0} - C_{y0}) + a_{33}(N_{z0} - C_{z0}) + C_z \\
&P_y = a_{22}(P_{y0} - C_{y0}) + a_{23}(P_{z0} - C_{z0}) + C_y \\
&P_z = a_{32}(P_{y0} - C_{y0}) + a_{33}(P_{z0} - C_{z0}) + C_z \\
&(N_y - M_y)^2 + (N_z - M_z)^2 = l_{MN}^2 \\
&(P_y - O_y)^2 + (P_z - O_z)^2 = l_{OP}^2
\end{aligned}
\tag{3.1}
$$

where $M_y=M_{y0}$, $O_y=O_{y0}$, $M_z=M_{z0}+z_s$, $O_z=O_{z0}+z_s$ and $C_z=C_{z0}+z_u$, while z_s is the vertical displacements of the sprung mass from the static equilibrium position. In Eq (3.1), l_{MN} and l_{OP} are the lengths of upper and lower control arms, respectively. Moreover, $a_{22}=a_{33}=\cos\phi$ and $-a_{23}=a_{32}=\sin\phi$. In order to correlate the kinematic relations to the dynamic responses, closed form solutions of the unknowns in terms of generalized coordinates are desirable, which may be quite complex. A linear system of kinematic relations, however, could be achieved using small angle assumptions, such that $a_{22}=a_{33}=1$ and $-a_{23}=a_{32}=\phi$, and first-order Taylor series approximation of the constraint equations, which yield:

$$
\begin{aligned}
&N_y - \phi(N_{z0} - C_{z0}) - C_y = (N_{y0} - C_{y0}) \\
&N_z + \phi(N_{y0} - C_{y0}) = N_{z0} + z_u \\
&P_y - \phi(P_{z0} - C_{z0}) - C_y = (P_{y0} - C_{y0}) \\
&P_z + \phi(P_{y0} - C_{y0}) = P_{z0} + z_u \\
&(N_{y0} - M_{y0})(N_y - N_{y0}) + (N_{z0} - (M_{z0} + z_s))(N_z - N_{z0}) - (N_z - M_{z0})z_s = 0 \\
&(P_{y0} - O_{y0})(P_y - P_{y0}) + (P_{z0} - (O_{z0} + z_s))(P_z - P_{z0}) - (P_z - O_{z0})z_s = 0
\end{aligned}
\tag{3.2}
$$

Solutions of the above linear system of equations yield following expressions in the generalized coordinates z_s and z_u, as;

$$
\begin{aligned}
\phi &= \frac{1}{Den}\left[\left[e(h-2z_s)-g(f-2z_s)\right]z_u-(eh-gf)z_s\right] \\
C_y &= \frac{1}{Den}\begin{bmatrix}(eb-a(f-2z_s))(hz_s-(h-2z_s)z_u)+(c(h-2z_s)-gd)(fz_s-(f-2z_s)z_u) \\ +C_{y0}(ce(h-2z_s)-ag(f-2z_s))+C_{y0}ge(b-d)\end{bmatrix} \\
N_y &= \frac{1}{Den}\begin{bmatrix}(c(h-2z_s)-g(d-b))(fz_s+eN_{y0}-(f-2z_s)z_u) \\ -a(f-2z_s)(hz_s+gN_{y0}-(h-2z_s)z_u)\end{bmatrix} \\
N_z &= \frac{1}{Den}\begin{bmatrix}\left[ec(h-2z_s)+eg(b-d)\right](N_{z0}+z_u)-ea(h-2z_s)z_u \\ -agfN_{z0}+\left[ag(N_{z0}+M_{z0})+eah\right]z_s\end{bmatrix} \\
P_y &= \frac{1}{Den}\begin{bmatrix}c(h-2z_s)(fz_s+eP_{y0}-(f-2z_s)z_u) \\ -(a(f-2z_s)-e(b-d))(hz_s+gP_{y0}-(h-2z_s)z_u)\end{bmatrix} \\
P_z &= \frac{1}{Den}\begin{bmatrix}\left[eg(b-d)-ga(f-2z_s)\right](P_{z0}+z_u)-cg(f-2z_s)z_u \\ +echP_{z0}-\left[ec(P_{z0}+O_{z0})+gcf\right]z_s\end{bmatrix}
\end{aligned}
\tag{3.3}
$$

where $Den=ge(b-d)+ec(h-2z_s)+ga(f-2z_s)$; $a=N_{y0}-C_{y0}$, $b=N_{z0}-C_{z0}$, $c=P_{y0}-C_{y0}$, $d=P_{z0}-C_{z0}$, $e=N_{y0}-M_{y0}$, $f=N_{z0}-M_{z0}$, $g=P_{y0}-O_{y0}$ and $h=P_{z0}-O_{z0}$. Furthermore, the lateral displacement of the wheel center y_u can be expressed as, $y_u=C_y-C_{y0}$. The coordinates of the lower strut mount A can be obtained from the kinematics of link OP, such that:

$$
A_y=\left(1-\frac{l_{OA}}{l_{OP}}\right)O_{y0}+\frac{l_{OA}}{l_{OP}}P_y \text{; and } A_z=\left(1-\frac{l_{OA}}{l_{OP}}\right)(O_{z0}+z_s)+\frac{l_{OA}}{l_{OP}}P_z \tag{3.4}
$$

where l_{OA} is the distance of strut mount location A with respect to joint O.

The velocities of different joints are derived through time derivatives of linear system of equations in Eq (2.21), such that:

$$
\begin{aligned}
&\dot{N}_y-\dot{\phi}(N_{z0}-C_{z0})-\dot{C}_y=0;\ \ \dot{N}_z+\dot{\phi}(N_{y0}-C_{y0})=\dot{z}_u \\
&\dot{P}_y-\dot{\phi}(P_{z0}-C_{z0})-\dot{C}_y=0;\qquad \dot{P}_z+\dot{\phi}(P_{y0}-C_{y0})=\dot{z}_u \\
&(N_{y0}-M_{y0})\dot{N}_y+(N_{z0}-M_{z0}-2z_s)\dot{N}_z+(M_{z0}+N_{z0}-2N_z)\dot{z}_s=0 \\
&(P_{y0}-O_{y0})\dot{P}_y+(P_{z0}-O_{z0}-2z_s)\dot{P}_z+(P_{z0}+O_{z0}-2P_z)\dot{z}_s=0
\end{aligned}
\tag{3.5}
$$

Alternatively, the velocity responses can also be obtained through time derivative of the displacement expressions in Eq (3.2). The wheel angular velocity and lateral velocity of the wheel center are derived in a similar manner, as:

$$\dot{\phi} = \frac{1}{Den^2}\begin{bmatrix} Den\left[\left[e(h-2z_s)-g(f-2z_s)\right]\dot{z}_u + 2(g-e)z_u\dot{z}_s - (eh-gf)\dot{z}_s\right] \\ +2(ec-ga)\left[\left[e(h-2z_s)-g(f-2z_s)\right]z_u - (eh-gf)z_s\right]\dot{z}_s \end{bmatrix}$$

$$\dot{y}_u = \frac{1}{Den^2}\begin{bmatrix} Den\begin{bmatrix} 2a\dot{z}_s\left(hz_s-(h-2z_s)z_u\right) - 2c\dot{z}_s\left(fz_s-(f-2z_s)z_u\right) \\ +\left(eb-a(f-2z_s)\right)\left(h\dot{z}_s-(h-2z_s)\dot{z}_u+2\dot{z}_s z_u\right) \\ +\left(c(h-2z_s)-gd\right)\left(f\dot{z}_s-(f-2z_s)\dot{z}_u+2\dot{z}_s z_u\right) - 2C_{y0}(ce-ag)\dot{z}_s \end{bmatrix} \\ +2(ec-ga)\begin{bmatrix} \left(eb-a(f-2z_s)\right)\left(hz_s-(h-2z_s)z_u\right) \\ +\left(c(h-2z_s)-gd\right)\left(fz_s-(f-2z_s)z_u\right) \\ +C_{y0}\left(ce(h-2z_s)-ag(f-2z_s)\right)+C_{y0}ge(b-d) \end{bmatrix}\dot{z}_s \end{bmatrix} \tag{3.6}$$

The wheel spindle angular and lateral acceleration can be obtained from the time derivative of Eq (3.6) as:

$$\ddot{\phi} = \frac{1}{Den^2}\begin{bmatrix} Den\left[e(h-2z_s)-g(f-2z_s)\right]\ddot{z}_u + Den\left[2(g-e)z_u-(eh-gf)\right]\ddot{z}_s \\ +2\left[\left(e(h-2z_s)-g(f-2z_s)\right)z_u-(eh-gf)z_s\right](ec-ga)\ddot{z}_s \end{bmatrix}$$

$$\ddot{y}_u = \frac{1}{Den^2}\begin{bmatrix} Den\left[-\left(eb-a(f-2z_s)\right)(h-2z_s)-\left(c(h-2z_s)-gd\right)(h-2z_s)\right]\ddot{z}_u \\ +Den\begin{bmatrix} 2a\left(hz_s-(h-2z_s)z_u\right)+\left(eb-a(f-2z_s)\right)(h+2z_u) \\ -2c\left(fz_s-(f-2z_s)z_u\right)+\left(c(h-2z_s)-gd\right)(f+2z_u)-2C_{y0}(ce-ag) \end{bmatrix}\ddot{z}_s \\ +2(ec-ga)\begin{bmatrix} \left(eb-a(f-2z_s)\right)\left(hz_s-(h-2z_s)z_u\right)+C_{y0}ge(b-d) \\ +C_{y0}\left(ce(h-2z_s)-ag(f-2z_s)\right)+\left(c(h-2z_s)-gd\right)\left(fz_s-(f-2z_s)z_u\right) \end{bmatrix}\ddot{z}_s \end{bmatrix} \tag{3.7}$$

3.2.2 Kineto-dynamic Analysis

The equations of dynamic motion of the kineto-dynamic quarter-vehicle system are derived using Lagrange's method. The kinetic (T) and potential (U) energies of the system are formulated as:

$$T = \frac{1}{2}m_s\dot{z}_s^2 + \frac{1}{2}m_u\left(\dot{y}_u^2+\dot{z}_u^2\right)+\frac{1}{2}I_{ux}\dot{\phi}^2 \text{ and}$$

$$U = \frac{1}{2}K_s(\Delta l)^2 + \frac{1}{2}K_t(\Delta z_t)^2 + \frac{1}{2}K_{tl}(y_u-\phi R)^2 \tag{3.8}$$

where m_s and m_u are the masses of the vehicle body and the wheel, respectively, I_{ux} is the mass moment of inertia of the wheel about x- axis, K_s is the suspension spring rate, R is the effective wheel radius, and K_t and K_{tl} are the tire vertical and lateral spring rates, respectively. In the above expression, Δl and Δz_t are the strut and tire deflections, given by:

$$\Delta l = l_{s0} - \left[(A_y - B_{y0})^2 + (A_z - (B_{z0} + z_s))^2\right]^{1/2} \text{and } \Delta z_t = z_u - z_0 \tag{3.9}$$

where l_{s0} is the initial strut length, B_{y0} and B_{z0} are the initial coordinates of the upper strut mount B, and z_0 is the vertical road input, as shown in Fig. 3.2.

The dissipative energy contributing to the generalized forces in the system is derived as:

$$D = \frac{1}{2} C_s (\Delta \dot{l})^2 + \frac{1}{2} C_t (\Delta \dot{z}_t)^2 \tag{3.10}$$

where C_s and C_t are the viscous damping coefficients of the strut and the tire, respectively. $\Delta \dot{z}_t$ and $\Delta \dot{l}$ are the time derivatives of the tire and strut deflections, respectively, given by:

$$\Delta \dot{l} = \left[\dot{A}_y (A_y - B_{y0}) + (\dot{A}_z - \dot{B}_z)(A_z - (B_{z0} + z_s))\right]\left[(A_y - B_{y0})^2 + (A_z - (B_{z0} + z_s))^2\right]^{-1/2} \tag{3.11}$$

The equations of motion are derived from the energy equations (3.8) and (3.10) together with the kinematic relations defined in Eqs (3.3) to (3.7). Upon neglecting the contributions due to products of derivative terms, the equations of motion of the kineto-dynamic model are derived as:

$$\begin{aligned}
&m_s \ddot{z}_s + m_u \ddot{y}_u \left(\frac{\partial \dot{y}_u}{\partial \dot{z}_s}\right) + I_{ux} \ddot{\phi} \left(\frac{\partial \dot{\phi}}{\partial \dot{z}_s}\right) + K_s \Delta l \frac{\partial (\Delta l)}{\partial z_s} + K_{tl}(y_u - \phi R) \frac{\partial (y_u - \phi R)}{\partial z_s} + c_s \Delta \dot{l} \frac{\partial \left(\Delta \dot{l}\right)}{\partial \dot{z}_s} = 0 \\
&m_u \ddot{z}_u + m_u \ddot{y}_u \frac{\partial \dot{y}_u}{\partial \dot{z}_u} + I_{ux} \ddot{\phi} \frac{\partial \dot{\phi}}{\partial \dot{z}_u} + K_s \Delta l \frac{\partial (\Delta l)}{\partial z_u} \\
&+ K_{tl}(y_u - \phi R) \frac{\partial (y_u - \phi R)}{\partial z_u} + c_s \delta \dot{l} \frac{\partial \left(\Delta \dot{l}\right)}{\partial \dot{z}_u} + K_t \Delta z_t + c_t \Delta \dot{z}_t = 0
\end{aligned} \tag{3.12}$$

In the above equations, $y_u, \phi, \dot{y}_u, \dot{\phi}, \ddot{y}_u, \ddot{\phi}, \Delta l$ and Δi are defined by the kinematic relations in Eqs (3.3), (3.5), (3.6) and (3.7). Moreover, each term in Eq (3.12) is a function of $\dot{z}_s, \dot{z}_u$ z_s, and z_u, with the exception of $m_s\ddot{z}_s$ and $m_u\ddot{z}_u$.

3.3 Equivalent Spring and Damping Rates

The equations of motion of a conventional quarter-car model, shown in Fig. 3.1, can be written as:

$$m_s\ddot{z}_s + C_{eq}(\dot{z}_s - \dot{z}_u) + K_{eq}(z_s - z_u) = 0$$
$$m_u\ddot{z}_u - C_{eq}(\dot{z}_s - \dot{z}_u) - K_{eq}(z_s - z_u) + C_t(\dot{z}_u - \dot{z}_0) + K_t(z_u - z_0) = 0 \quad (3.13)$$

where K_{eq} and C_{eq} are equivalent vertical stiffness and damping rates of the suspension, respectively. The effectiveness of this simple model could be considerably enhanced by employing equivalent spring and damping rates that can account for the kinematic effects. In this study, the kinematic relations, formulated in Section 3.2.1 are used to identify; (i) equivalent suspension rate, defined as the vertical suspension force acting at the wheel center per unit vertical displacement of the wheel center; and (ii) equivalent damping rate, defined as vertical suspension force at the wheel center per unit vertical velocity of the wheel center [1,16].

3.3.1 Formulations of Equivalent Spring- and Damping Rates

The equivalent spring and damping rates are derived considering the chassis fixed, while a vertical displacement input is imparted at the wheel centre. The effective strut force acting at the wheel center is subsequently derived by considering the suspension kinematics, particularly the wheel camber and the lateral displacement responses during the vertical wheel motion, as illustrated in Fig.3.3. For a given wheel center

displacement, the restoring force developed by the strut ($K_s\Delta l$), along its axis can be related to the equivalent force at joint P of the lower control arm and the wheel spindle, as:

$$F_{PN} = K_s \Delta l \cos\theta_s \frac{l_{OA}}{l_{OP}} \tag{3.14}$$

where θ_s is the strut inclination angle with a normal to the control arm, as shown Fig. 3.3. The equivalent suspension force F_w acting at the wheel center can be related to F_{PN} by considering the instantaneous center of rotation P' of the double wishbone suspension (Fig. 3.3).

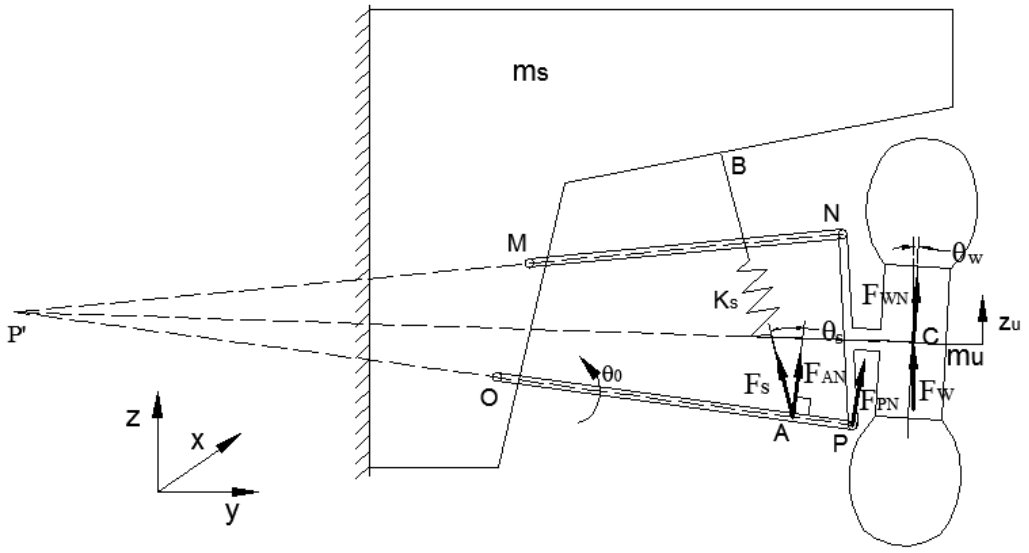

Figure 3.3: Effective force at the wheel center

Since P and C lie on the same rigid body (wheel spindle), the normal component of the equivalent force at the wheel center F_{WN} is related to F_{PN}, as:

$$F_{WN} = \frac{l_{P'P}}{l_{P'C}} F_{PN} \tag{3.15}$$

where F_{WN} acts at the wheel center along the normal to a line joining instantaneous center P' and the wheel center C. In the above equation, $l_{P'P}$ and $l_{P'C}$ are the distances of points P

and C from the instantaneous center, which are related to the angular rotation θ_0 of the lower control arm in the following manner:

$$\frac{l_{P'P}}{l_{P'C}} = \frac{l_{OP}\theta_O}{z_u \cos\theta_w} \tag{3.16}$$

where θ_w is the angle between the force F_{WN} and the fixed vertical axis. The lower control arm rotation θ_O, can be further related to θ_s such that $l_{OA}\theta_O = \Delta l \cos\theta_s$.

The equivalent vertical force at the wheel center, F_W is then derived from the normal force as,

$$F_W = \frac{F_{WN}}{\cos\theta_w} \tag{3.17}$$

Equations (3.14) to (3.17) yield the following expression for the equivalent vertical force,

$$F_W = \frac{K_s}{z_u}\left(\frac{\Delta l \cos\theta_s}{\cos\theta_w}\right)^2 \tag{3.18}$$

In the above expression, the spring deflection Δl is only a function of wheel vertical deflection z_u, when z_s=0. The angles θ_s and θ_w are also functions of z_u considering that these angles can be written in terms of the joint coordinates, N_y, N_z, P_y, P_z, C_y, C_z, A_y and A_z. The small angles θ_s and θ_w are related to the joint coordinates, as:

$$\theta_s = \frac{A_y - B_{y0}}{A_z - B_{z0}} - \frac{P_z - O_{z0}}{P_y - O_{y0}} + \frac{P_{z0} - O_{z0}}{P_{y0} - O_{y0}}; \text{ and } \theta_w = \frac{C_z - P'_z}{C_y - P'_y} \tag{3.19}$$

where P'_y and P'_z are the coordinates of the instantaneous point P' which can be obtained by solving the equations of lines MN and OP as:

$$\begin{aligned} P'_y &= \frac{(N_z - M_{z0})(M_{z0}N_y - M_{y0}N_z) - (P_z - O_{z0})(O_{z0}P_y - O_{y0}P_z)}{(N_y - M_{y0})(P_z - O_{z0}) - (N_z - M_{z0})(P_y - O_{y0})} \\ P'_z &= \frac{(N_y - M_{y0})(M_{z0}N_y - M_{y0}N_z) - (P_y - O_{y0})(O_{z0}P_y - O_{y0}P_z)}{(N_y - M_{y0})(P_z - O_{z0}) - (N_z - M_{z0})(P_y - O_{y0})} \end{aligned} \tag{3.20}$$

Although the angles θ_s and θ_w are functions of z_u, the variations in these angles with respect to z_u are very small. Assuming small variations in these angles, the suspension rate K_{eq} is obtained by differentiating the wheel force in Eq (3.18) with respect to z_u. The resulting suspension rate can be related to the suspension stiffness, as:

$$K_{eq} = \frac{\partial F_W}{\partial z_u} = K_s \Psi \tag{3.21}$$

where $\Psi = \frac{\Delta l}{z_u}\left(2\frac{\partial(\Delta l)}{\partial z_u} - \frac{\Delta l}{z_u}\right)\left(\frac{\cos\theta_s}{\cos\theta_w}\right)^2$ is the geometry factor that yields the equivalent suspension rate incorporating the suspension kinematics, while the rate of change of strut length with respect to z_u can be obtained from:

$$\frac{\partial \Delta l}{\partial z_u} = \left[(A_y - B_{y0})^2 + (A_z - B_{z0})^2\right]^{-1/2}\left[(A_y - B_{y0})\frac{\partial A_y}{\partial z_u} + (A_z - B_{z0})\frac{\partial A_z}{\partial z_u}\right] \tag{3.22}$$

The equivalent damping force $F_{Wd,}$ at the wheel center is derived in a similar manner as:

$$F_{Wd} = \frac{C_s}{\dot{z}_u}\left(\frac{\Delta \dot{l}\cos\theta_s}{\cos\theta_w}\right)^2 \tag{3.23}$$

This leads to an expression for the equivalent damping rate as:

$$C_{eq} = \frac{\partial F_{Wd}}{\partial \dot{z}_u} = C_s\left(\frac{2\delta \dot{l}}{\dot{z}_u}\frac{\partial(\Delta \dot{l})}{\partial \dot{z}_u} - \left(\frac{\Delta \dot{l}}{\dot{z}_u}\right)^2\right)\left(\frac{\cos\theta_s}{\cos\theta_w}\right)^2 \tag{3.24}$$

The above equation can be further simplified in terms of another geometry factor Ψ_d, in a similar manner to that of the equivalent spring rate. The equivalent damping thus is directly related to the strut damping coefficient, as:

$$C_{eq} = C_s \Psi_d \; ; \quad \text{where } \Psi_d = \frac{\Delta \dot{l}}{\dot{z}_u}\left(2\frac{\partial(\Delta \dot{l})}{\partial \dot{z}_u} - \frac{\Delta \dot{l}}{\dot{z}_u}\right)\left(\frac{\cos\theta_s}{\cos\theta_w}\right)^2 \tag{3.25}$$

Equations (3.21) and (3.25) derive the equivalent spring and damping rates of a double wishbone suspension as a function of the wheel spindle vertical displacement and velocity relative to the chassis.

The geometry factor Ψ is a function of z_u for a given joint coordinates and may be considered as analogous to the square of the 'installation ratio' [1]. A further examination of the geometry factor Ψ in conjunction with Eqs (3.9) and (3.22) suggests that it is dependent on the ratio of the distance of the strut mounting point lower control arm (A) from the pivot (O) to the control arm length (l_{OA}/l_{OP}), and on the coordinates of the strut mounts (A and B). The coordinates of the strut mounts are related to those of joints O and P, as it is evident from Eq (3.9). The geometry factor thus accounts for the total suspension kinematic effects. This further suggests that variations in the joint coordinates, which are generally carried out during suspension tuning, can alter the equivalent suspension rates, and thus, influence the dynamic responses of the suspension.

3.3.2 Variations in Equivalent Spring and Damping Rates

The effective spring and damping rates of the suspension, however, tend to vary during vertical motions of the chassis and the wheel, which may alter the vehicle ride and handling properties. The variations in the effective spring and damping rates are analyzed considering the coordinates of various suspension joints (Fig. 3.2) as given in Section 2.4.4, such that: M=(0.430, 0.818); N=(0.644, 0.852); O=(0.365, 0.360); P=(0.743, 0.347); C=(0.787, 0.452); A=(0.660, 0.350) and B=(0.615, 0.920), while these coordinates are taken in meters. The variations in the effective spring and damping rates, evaluated from Eqs (3.21) and (3.25), respectively, by considering the chassis fixed (z_s = 0), while the wheel center is subjected to a very low frequency (0.1 Hz) harmonic

displacement of 0.12 m amplitude, while, the variations in the rates are illustrated in Fig. 3.4 (a) and (b), respectively. The figures show the variations in the suspension spring rate with the wheel vertical travel, and the damping rates as a function of wheel vertical velocity. The results in the figures suggest that the effective spring and damping rates decrease under upward wheel motion (jounce) and increase during rebound, while the variations are asymmetric in jounce and rebound. The results also show nearly symmetric variations in the wheel rate under small wheel displacements, and relatively lower changes in the suspension rate and damping rate in rebound compared to jounce.

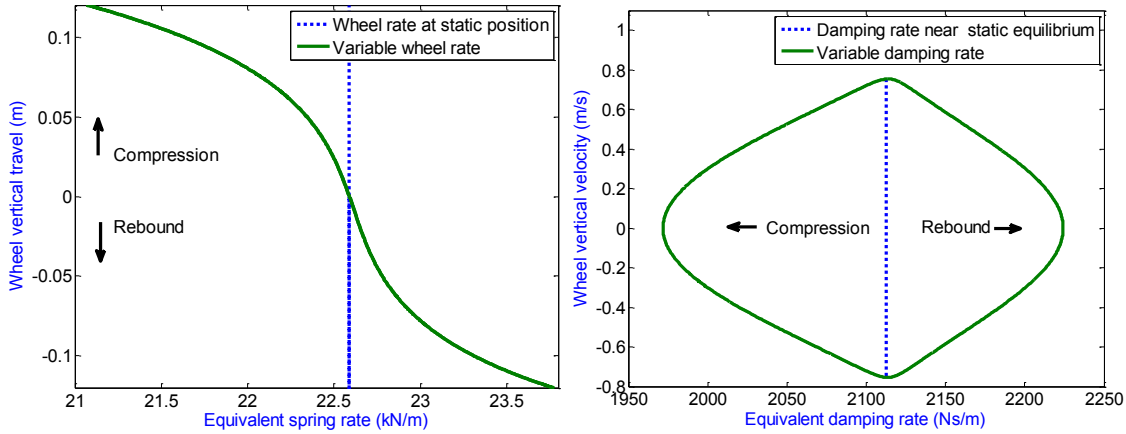

(a) (b)

Figure 3.4: Variations in (a) wheel rate; and (b) damping rate of the suspension under $z_u = 0.12 \sin(2\pi t)$ m and $z_s = 0$

3.4 Dynamic Response Analyses

The kineto-dynamic formulations presented in sections 3.2 and 3.3 are solved to determine the kinematic and dynamic responses to harmonic and transient excitations. The model parameters used in simulation are summarized in Table 3.1 [97, 147]. The results attained are discussed in the following sections.

Table 3. 1: Vehicle and suspension data [97, 147]

Parameter	Value
Sprung mass (m_s)	439.38 kg
Unsprung mass (m_u)	42.27 kg
Unsprung mass moment of inertia about x axis (I_{ux})	1.86 kg-m^2
Suspension spring stiffness (K_s)	38404 N/m
Suspension damping rate (C_s)	3593.4 Ns/m
Tire vertical stiffness (K_t)	200 kN/m
Tire damping rate (C_t)	352.27 Ns/m
Tire lateral stiffness (K_{tl})	100 kN/m
Tire effective radius (R)	0.35 m

3.4.1 Responses to Harmonic Inputs

Apart from variations in the spring and damping rates, the tire lateral compliance can also influence the vertical dynamics of the system, particularly when the wheel track and the camber angle add up to increase the lateral displacement of the tire-ground contact point. Furthermore, the sprung and unsprung masses are constrained by the suspension linkages, which can also alter the dynamic properties. The combined effects of variations in the suspension and damping rates, tire lateral forces and the constraints imposed by the suspension linkages are illustrated by comparing the dynamic responses of the kineto-dynamic model with those of a conventional quarter-car model under harmonic and idealized bump excitations. The conventional model employs equivalent suspension and damping rates in the vicinity of the static equilibrium operating point (Figs. 3.4 (a) and (b)).

The dynamic responses of the kineto-dynamic and the linear quarter-car model are evaluated under sinusoidal displacement at the tire ground interface with z_{0max} as the displacement amplitude. The responses are evaluated in terms of sprung-mass displacement ratio, $z_s/z_{0\max}$, and the rattle space ratio, $(z_s\text{-}z_u)/z_{0\max}$. Figures 3.5 (a) and (b)

illustrate the steady-state sprung mass displacement ratio responses of the two models under two different displacement amplitudes (z_{0max}= 0.05 and 0.08 m) at a frequency of 1 Hz. It can be observed that the conventional model shows symmetric variations in the responses about the static equilibrium, irrespective of the excitation amplitude with peak displacement ratio near 2.1. Moreover, the displacement ratio response is independent of the excitation amplitude due to the assumed linearity. The proposed kineto-dynamic model, however, exhibits a small asymmetry in the responses in jounce and rebound. The peak responses of the kineto-dynamic model are lower compared to those of the conventional model. The peak ratio under z_{0max}= 0.05 m is observed to be near 1.96 during the upward motion of the sprung mass and nearly 1.95 during the downward displacement. The peak displacement ratio increases slightly when the input amplitude is increased to 0.08 m. The asymmetry in the response can be attributed to kinematics of the suspension giving rise to asymmetric variation in the camber angle, suspension rate and damping rate, as shown in Figs. 3.4 and 3.5, respectively. During the jounce (sprung mass upward displacement), total lateral displacement of tire-ground contact point is larger compared to that of rebound owing to variations in the camber angle and the wheel track.

Figures 3.6 (a) and (b) compare the rattle space ratio responses of the kineto-dynamic and the conventional model under the two displacement excitation amplitudes. The results show considerable deviations between the responses of the two models for both excitation amplitudes. The kineto-dynamic model yields considerably lower peak rattle space compared to the linear model, particularly under the lower excitation. This is partly attributed to slight difference in the sprung mass natural frequency of the kineto-dynamic model from that of the linear model. It can also be observed that the rattle space response

of the kineto-dynamic model lags that of the conventional model slightly during upward displacement, and it leads the conventional model peak response during the downward motion, which can be attributed to non-linearity due to kinematic constraints imposed by the suspension linkages in the kineto-dynamic model.

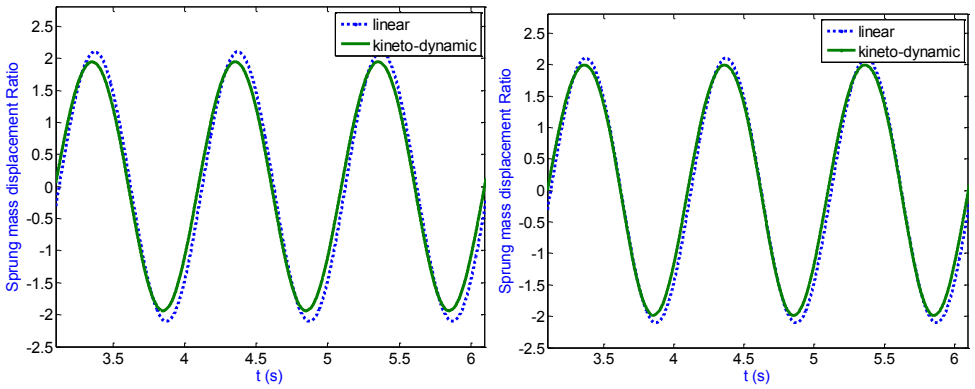

Figure 3.5: Sprung mass displacement ratio response to harmonic excitations at 1 Hz: (a) z_{0max}=0.05 m; and (b) z_{0max}=0.08 m.

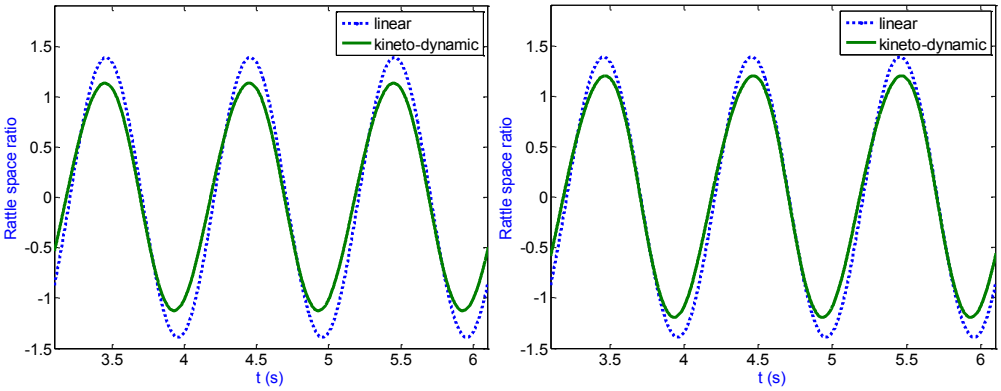

Figure 3.6: Rattle space ratio response to harmonic excitations at 1Hz: (a) z_{0max}=0.05 m; and (b) z_{0max}=0.08 m.

3.4.2 Responses to Idealized Bump Excitations

The transient responses of the kineto-dynamic and linear quarter-vehicle models are evaluated under an idealized bump excitation with positive and negative vertical displacements to study the effects of suspension kinematics causing variations in the

suspension and damping rates, camber angle and wheel track. The bump excitation is idealized by a rounded pulse displacement, given by [148]:

$$z_0(t) = z_{0\max} \frac{(2.71828)^2}{4} (\gamma\omega_0 t)^2 (2.71828)^{-\gamma\omega_0 t} \tag{3.26}$$

where z_{0max} is the maximum amplitude, ω_0=2π and γ is the pulse severity parameter, which directly relates to rate of change of the displacement. The above formulation is also applied to synthesize a negative displacement, idealizing a pothole input, by letting z_{0max}<0, in order to study the asymmetry in the transient responses. Figure 3.7 illustrates the positive and negative normalized rounded pulse displacement excitations to the model for different severity parameters (γ =1, 3 and 5).

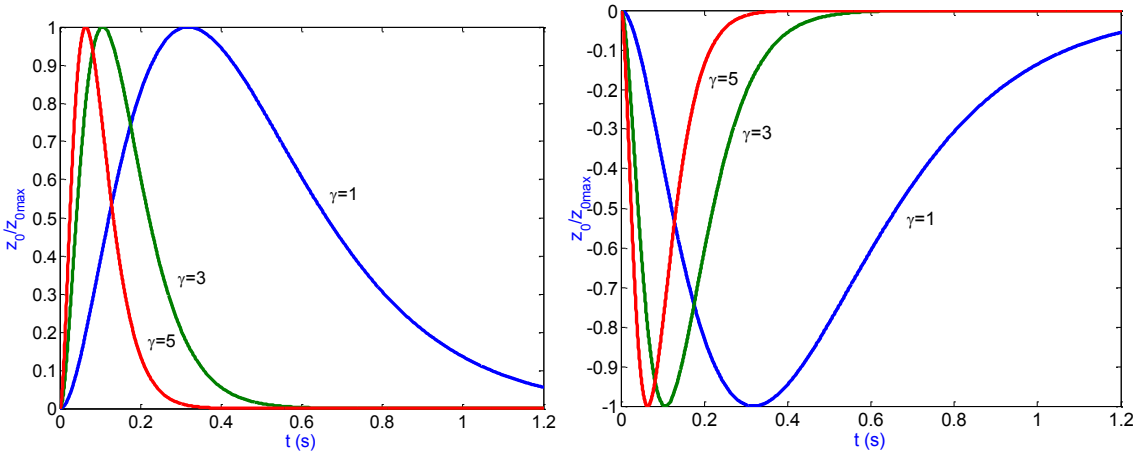

Figure 3.7: The rounded pulse displacement input corresponding to different severity factors: (a) idealized bump excitation; and (b) idealized pothole excitation.

The dynamic responses are evaluated for two different amplitudes of excitations, namely z_{0max}=±0.05m and ±0.1m, in terms of sprung mass acceleration ratio ($\ddot{z}_s / \omega_0^2 z_{0\max}$), the rattle space ratio ($(z_s - z_u)/z_{0\max}$) and the dynamic tire force ratio (dynamic tire force/static tire force), considered to provide measures of passenger comfort, vertical packaging space availability and the road holding ability of the suspension, respectively.

The dynamic and kinematic responses are further evaluated by the peak responses, defined by: sprung-mass shock acceleration ratio, $SSAR = |\ddot{z}_s|_{\max} / \omega_0^2 z_{0\max}$ and peak relative displacement ratio, $SRDR = |z_s - z_u|_{\max} / z_{0\max}$; and peak tire dynamic force ratio, *TDFR*.

Figure 3.8 illustrates the sprung mass acceleration ratio responses of the conventional and the kineto-dynamic models subject to positive and negative rounded pulse excitations with a severity factor, γ=1. The conventionl model, as expected, responds symetrically to the positive and negative pulse inputs, while the peak response is near 0.8 under both excitation amplitudes. The results also suggest that the free oscillation response occurs at 1.04 Hz. The kineto-dynamic model, however, shows asymmetric responses to bump and pothole inputs. Moreover, the peak acceleration ratio is slightly larger than that of the conventional model under positive pulse excitation. A larger deviation in the peak response, however, can be observed under the negative excitation. The peak acceleration ratios under 0.05 and 0.1 m excitations are 0.95 and 1.05. These asymmetric variations in the response are attributable to suspension kinematics leading to asymmetric suspension and damping rates, and tire lateral force, which tend to show greatest influences during suspension compression. The results in Fig. 3.8 also demonstrate that the free oscillation of the kineto-dynamic model occurs at 1.12 Hz, while rate of decay of oscillation is higher than that of the conventional model.

The rattle space ratio responses of both the models under the two rounded pulse inputs with γ=1, are presented in Fig. 3.9. Although the peak reponses of both the models under the positive displacement occur at about the same instant, the kineto-dynamic model response tends to lead that of the linear model under the negative excitation, which

is attributed to the higher sprung mass frequency of the kineto-dynamic model and variations in the damping rate.

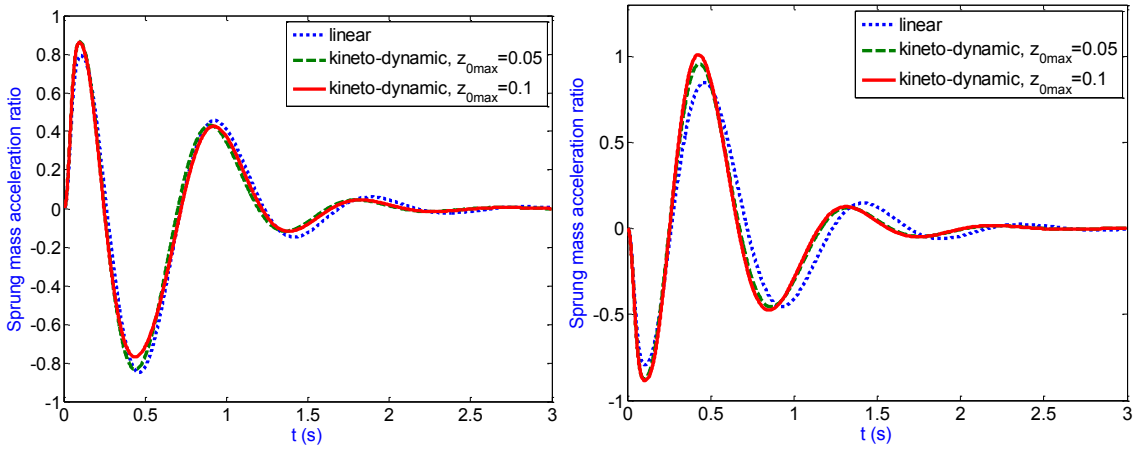

Figure 3.8: Sprung mass acceleration ratio ($\ddot{z}_s / \omega_0^2 z_{0\max}$) response to: (a) idealized bump excitation (z_{0max}=0.05 and 0.1 m); and (b) idealized pothole excitation (z_{0max}=0.05 and 0.1 m)

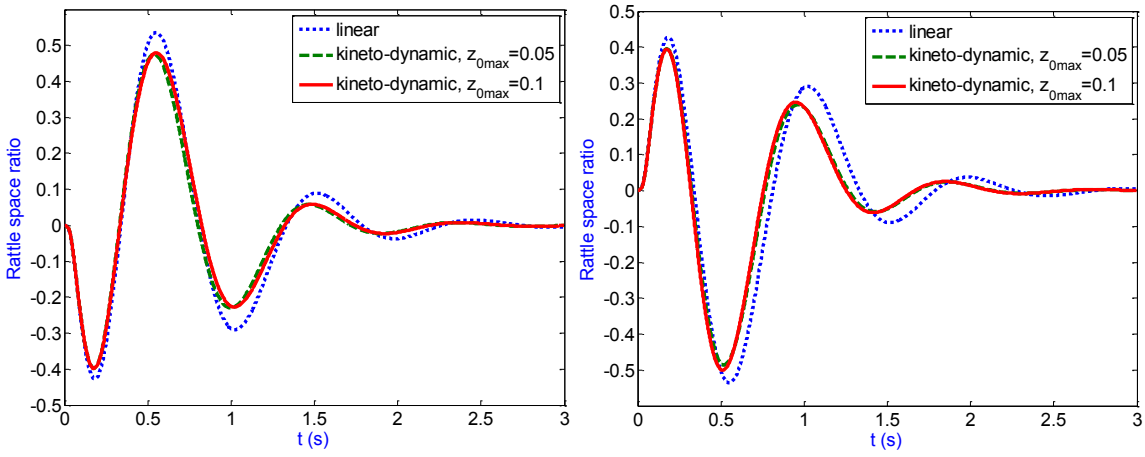

Figure 3.9: Rattle space ratio ($(z_s - z_u)/z_{0\max}$) response to: (a) idealized bump excitation (z_{0max}=0.05 and 0.1 m); and (b) idealized pothole excitation (z_{0max}=0.05 and 0.1 m)

Figure 3.10 presents the tire dynamic force ratio responses of both the models to rounded pulse inputs. The conventional model responds symmetrically to positive and negative inputs, as expected, with peak dynamic force ratio being 0.31 under 0.1m excitation. The tire dynamic force ratio response of the kineto-dynamic model, however, deviates considerably from that of the conventional model. The peak force ratio is

significantly higher for the bump input, particularly near the peak input displacement. The kineto-dynamic model, however, exhibits lower peak response under the negative input compared to the linear model. The asymmetric tire force response is attributed to suspension kinematics leading to large camber variations, particulary under large displacement inputs.

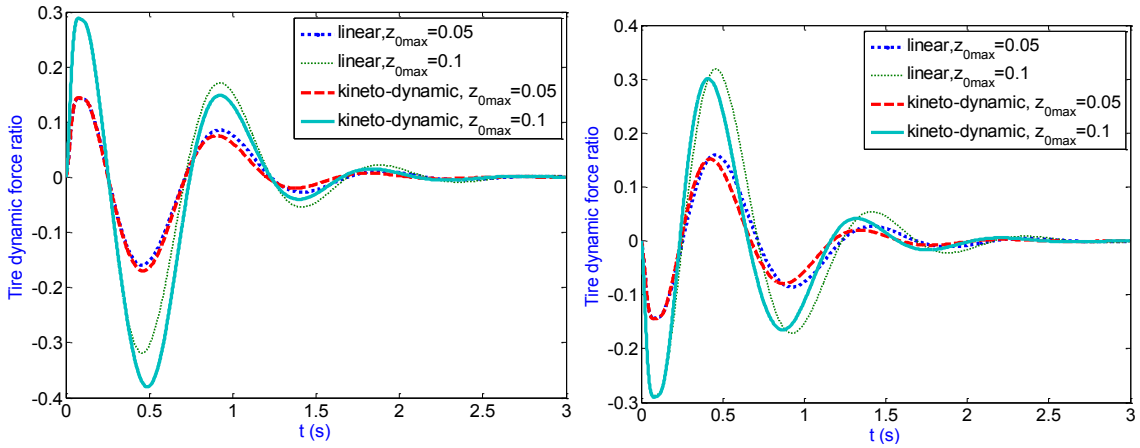

Figure 3.10: Tire dynamic force ratio response to: (a) idealized bump excitation (z_{0max}=0.05 and 0.1 m); and (b) idealized pothole excitation (z_{0max}=0.05 and 0.1 m)

The peak responses of both the models to rounded pulse displacement excitations are further summarized in Table 3.2 in terms of *SSAR*, *SRDR* and *TDFR*. The results are presented for ±0.05m and ±0.1m inputs with severity factors of γ=1 and 5. The peak sprung mass acceleration and relative displacement responses of the linear model, as expected, are identical under negative and positive inputs, irrespective of the peak displacement, while the *TDFR* under 0.1 m excitation is twice that under 0.05 m input. The kineto-dynamic model, however, shows different peak responses under positive and negative excitations, while the differences are more significant for γ=1 compared to γ=5. The peak responses of the kineto-dynamic model to more severe pulse input (γ=5) are quite comparable to those of the linear model except for *SSAR*, which is higher for the

kineto-dynamic model. These suggest that the non-linearity and asymmetry in the responses due to suspension kinematics are more pronounced under the lower frequency excitation. Under the higher frequency excitation, the responses are predominantly influenced by the unsprung mass properties.

Table 3.2: Comparisons of dynamic responses of the kineto-dynamic and linear models to positive (bump) and negative (pothole) rounded pulse displacement inputs of different peak magnitude (z_{0max}=0.05 and 0.1m) and severity factors (γ=1 and 5).

Performance Measure	Pulse severity factor, γ	Linear Model Bump/pothole		Kineto-dynamic Model			
				Bump	Pothole	Bump	Pothole
		z_{0max} = 0.05m	z_{0max} = 0.1m	z_{0max} = 0.05m		z_{0max} = 0.1m	
SSAR	1	0.85	0.85	0.87	0.97	0.86	1.01
	5	3.51	3.51	4.03	4.02	4.00	4.02
SRDR	1	0.54	0.54	0.47	0.49	0.48	0.51
	5	0.91	0.91	0.88	0.88	0.89	0.88
TDFR	1	0.16	0.32	0.14	0.15	0.38	0.30
	5	0.85	1.70	0.85	0.85	1.70	1.70

3.5 Suspension Synthesis With Constrained Lateral Space

With an increasing demand for larger subframe space, particularly for hybrid vehicles for placing the batteries [3], a suspension synthesis that can provide greater lateral subframe space without compromising the dynamic performances would be desirable, although it may involve difficult design compromises. The suspension lateral space availability is directly related to the links geometry, which may be characterized by the coordinates of joints *M, N, O* and *P*. The proposed kineto-dynamic model could be effectively applied to identify optimal or near optimal joint coordinates with consideration of both the dynamic and kinematic suspension properties. This feature of the model is illustrated through a parametric sensitivity analysis.

3.5.1 Sensitivity Analysis

The influence of variation in the lateral space on the selected kinematic and dynamic measures are evaluated under variations in the coordinates of joints *M, N, O* and *P*. The variations in the *y*- coordinates are limited to ±5 cm about the nominal values, while the variation in the coordinates of *P* is limited only to -5 cm due to limited clearance between the wheel and joint *P*. The effects of variations in the joint coordinates are evaluated under 0.05 m positive and negative rounded pulse excitation (γ=1). The influences of the joint coordinates on dynamic and kinematic responses are evaluated considering the lateral space as the constraint. In addition to the *SSAR*, *SRDR* and *TDFR,* the responses are also evaluated to determine the camber displacement ratio, ($CDR = |\phi|_{\max} / z_{0\max}$) and the wheel-center lateral displacement ratio, ($WLDR = |y_u|_{\max} / z_{0\max}$), known to influence the directional behavior of a vehicle and the tire wear characteristics.

Tables 3.3 and 3.4 show the sensitivity of the selected performance measures to the variation in the lateral coordinates of the joints under positive and negative pulse displacement inputs, respectively. The tables present the responses normalized by those of the nominal geometry suspension. The tables also include the sensitivity of the geometry factor Ψ to the variations in the joint coordinates normalized to that of the nominal geometry (Ψ=0.59). It can be observed that most of the responses are strongly influenced by the considered variations in the joint coordinates. Moreover, the effects are highly coupled. The results show conflicting effects of variations in the measures under the bump and pothole excitations, while the *TDFR* response appears to be least sensitive to such variations since it is mostly affected by the unsprung mass responses. For example, a positive change in the *y*- coordinate of point *M* yields slightly lower peak

sprung mass acceleration ratio under a pothole input, and slightly higher under the bump excitation. A similar conflicting effect of a positive change in the coordinate of *N* can be observed in *WLDR*, and that in the coordinate of *O* on the *CDR* and *WLDR*. A negative change in joint *M* can decrease the camber angle variation significantly without compromising other dynamic responses. The negative change in the joint *M* coordinate, however, increases the lateral space requirement of the suspension, while a positive change in the *y*- coordinate of joint *O* can reduce the suspension lateral space requirement. The geometry factor Ψ is predominantly influenced by the coordinates of lower control arm joints, particulary the joint *P*. Moreover, an increase in *SSAR* response is not always associated with an increase in the suspension rate. For example, a negative change in the *y*- coordinate of joint *N* results in a 1% decrease in the effective rates, while the *SSAR* increases by 6%. The corresponding *CDR* and *WLDR* increases substantially, by 18% and 14%, respectively. These suggest that tire lateral compliance also contributes to higher vertical acceleration response.

The results in Tables 3.3 and 3.4 suggest that a positive change in the *y*- coordinate of joint *O* yields beneficial effects in *SSAR* under both inputs, and *CDR* and *WLDR* under the negative input. Similarly, a positive change in the coordinate of *N* also yields beneficial effects in *SSAR* and *CDR* under both inputs and *WLDR* under the negative input. The combined effect of positive changes in the coordinates of both the *N* and *O* joints are thus further evaluated in order to reduce the suspension lateral space requirements. The results obtained under pulse excitations along positive and negative directions, are also summarized in Tables 3.3 and 3.4.

Table 3.3: Influence of variations of the suspension joint coordinates on the normalized dynamic and kinematic responses of the kineto-dynamic model subject to positive rounded pulse displacement input ($\gamma = 1$; and $z_{0max} = 0.05$ m).

Coordinate Variation	*Ψ*	*SSAR*	*TDFR*	*SRDR*	*CDR*	*WLDR*
Nominal	1.00	1.00	1.00	1.00	1.00	1.00
M_y (-5 cm)	1.00	0.98	1.00	1.02	0.88	1.21
M_y (+5 cm)	0.99	1.01	1.00	0.98	1.24	1.21
N_y (-5 cm)	0.99	1.06	0.94	0.94	1.18	1.14
N_y (+5 cm)	1.00	0.95	1.06	1.04	0.91	1.29
O_y (-5 cm)	1.07	1.05	1.00	0.96	0.96	0.86
O_y (+5 cm)	0.92	0.93	1.00	1.06	1.08	1.43
P_y (-5 cm)	1.28	1.16	1.12	0.83	0.88	0.79
N_y (+5 cm), O_y (+5 cm)	0.92	0.89	1.06	1.02	1.00	1.71
N_y (+5 cm), O_y (+10 cm)	0.81	0.80	1.12	1.11	1.20	2.43

Table 3.4: Influence of variations of the suspension joint coordinates on the normalized dynamic and kinematic responses of the kineto-dynamic model subject to negative rounded pulse displacement input ($\gamma = 1$; and $z_{0max} = -0.05$ m).

Coordinate Variation	*Ψ*	*SSAR*	*TDFR*	*SRDR*	*CDR*	*WLDR*
Nominal	1.00	1.00	1.00	1.00	1.00	1.00
M_y (-5 cm)	1.00	1.00	1.00	1.00	0.84	0.89
M_y (+5 cm)	0.99	0.99	1.00	0.96	1.24	1.26
N_y (-5 cm)	0.99	1.01	1.00	0.92	1.17	1.16
N_y (+5 cm)	1.00	0.98	1.07	1.02	0.88	0.89
O_y (-5 cm)	1.07	1.01	1.07	0.94	0.95	0.95
O_y (+5 cm)	0.92	0.98	0.93	1.04	1.07	1.11
P_y (-5 cm)	1.28	1.10	1.13	0.82	0.81	0.68
N_y (+5 cm), O_y (+5 cm)	0.92	0.96	1.00	1.10	0.94	1.05
N_y (+5 cm), O_y (+10 cm)	0.81	0.94	0.93	1.12	1.04	1.32

The results suggest that positive variations in lateral coordinates of both the joints yield considerable reduction in *SSAR* under both inputs and *CDR* under the negative inputs, with only slight increase in the *SRDR* and *WLDR*. Owing to the benificial effects of these changes, the *y*- coordinate of joint *O* was increased by 10 cm in an attempt to further reduce the suspension lateral space requirement. The results show further

reduction in *SSAR* but significantly higher *CDR* and *WLDR* responses. The results thus suggest that a +5 cm change in the coordinate of *N* and *O* would offer a reasonably good design compromise leading to total decrease of 12% in the lateral packaging.

Figure 3.11 shows the variations in the camber angle and half wheel-track responses of the modified suspension geometry (5 cm change in the *y*-coordinates of joints *O* and *N*) together with those of the nominal suspension geometry to 0.05 m bump input. Although, the modified geometry yields only minimal changes in the camber angle variation, the peak wheel-track variation of the modified suspension is significantly higher than the nominal suspension.

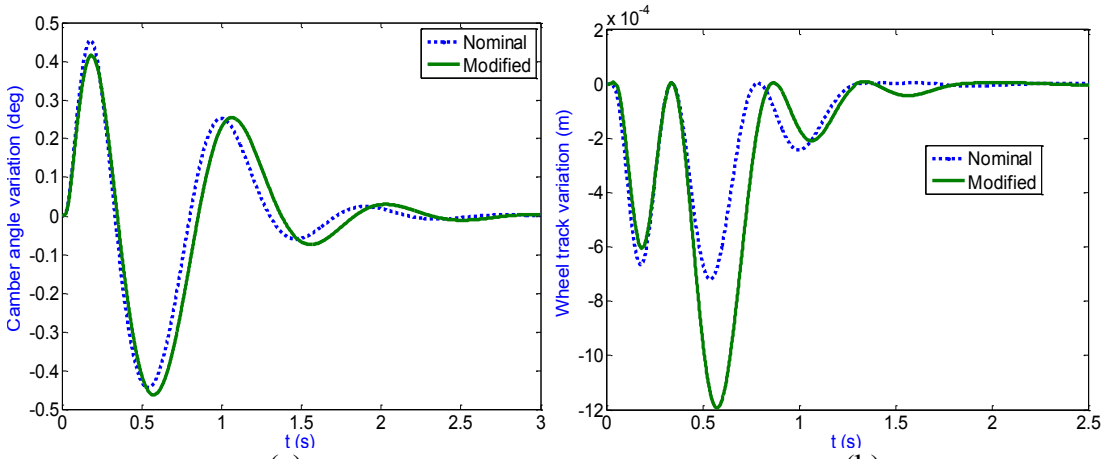

(a) (b)

Figure 3.11: Comparison of (a) camber angle; and (b) half wheel-track variations of the nominal and modified suspension geometry (joints *O* and *N* displaced by +5 cm) under +0.05 m pulse excitation.

The sensitivity analysis results suggest that variations in the joint coordinates would lead to compromises in both the kinematic and dynamic performance measures. Consequently, a suspension synthesis objective may be formulated to achieve minimal *SSAR*, *SRDR*, *CDR* and *WLDR* responses with a practical limit constraint on the lateral packaging space with joints coordinates being the design variables. The limit constraint on the lateral packaging space can be specified as $(C_{y0} - O_{y1}) < \sigma_1 (C_{y0} - O_{y0})$ and $(C_{y0} -$

M_{y1})< $\sigma_2(C_{y0}$-$M_{y0})$, where the subscripts '*0*' and '*1*' refer to the nominal and the identified design variables or the coordinates, and σ_1 and σ_2 would serve as constants defining the target reduction factor. The nominal wheel track, however, must be maintained in identification of most desirable joint coordinates.

3.6 Influences of Joint Bushing Compliance

The suspension joint bushings, which are generally made flexible, can influence the kinematic and dynamic responses of the vehicle in a significant manner. Conventional studies related to the synthesis of vehicle suspension, in general, ignore influences of the joint bushing compliance on the dynamic responses. Swayze *et al*. [149] studied the influence of joint bushings vertical compliance on the vertical dynamic responses of a vehicle employing a 5-DOF quarter car model. Studies related to the torsional stiffness of the flexible bushings in conjunction with vehicle models have been reported in a limited number of studies [52-54], while the majority of them employed multibody dynamic full vehicle models for the studies. Such vehicle models, however, require a large number of data related to vehicle which are generally available only at the final stages of vehicle design. This part of the study investigates the influences of nonlinearity due to joint bushing compliance on the kineto-dynamic responses of the quarter-car model comprising double wishbone type of suspension with compliant bushing joints between upper- and lower control arms and the chassis.

The kineto-dynamic quarter-car model shown in Fig. 3.2 is modified to include flexible bushings at the joints between the upper- and lower control arms and the chassis (points *M* and *O*, repsectively) as illustrated in Fig. 3.12. The flexible bushings at the chassis joints are modeled as linear torsional springs which cause restoring forces due to

any rotation of the upper- or lower control arms about the joints M or O, respectively. Unlike the model considered in Fig. 3.2, this modified model also considers the nonlinearity due to wheel hop.

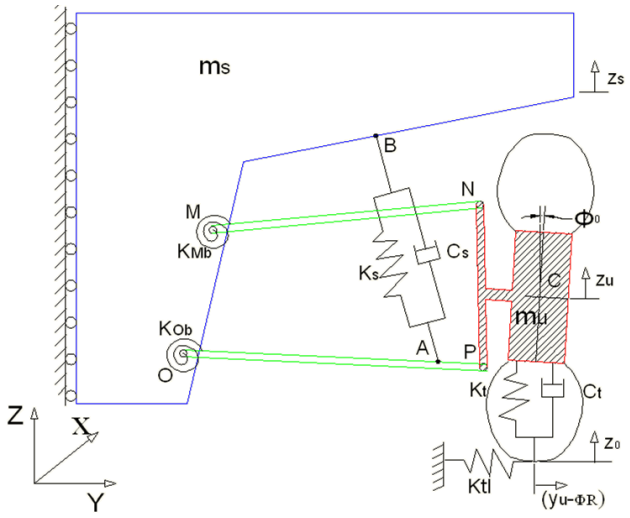

Figure 3.12: Kineto-dynamic model comprising flexible bushings at the linkage-chassis joints

3.6.1 Dynamic Formulations with Flexible Bushing

In addition to the kinetic and dissipative energies considered in section 3.3 through Eqs (3.8) and (3.10), the total potential energy of the system are formulated considering the contributions due to the linear torsional springs representing the joint bushings as:

$$U = \frac{1}{2}K_s(\Delta l)^2 + \frac{1}{2}K_s(\Delta z_t)^2 + \frac{1}{2}K_{tl}(y_u - \phi R)^2 + \frac{1}{2}K_M(\theta_M)^2 + \frac{1}{2}K_O(\theta_O)^2 \tag{3.27}$$

where K_M and K_O are the torsional spring rates (linear) of compliant bushings at joints M and O, respectively, while θ_M and θ_O denote upper- and lower control arm rotations, which upon small angle approximations can be obtained as:

$$\theta_M = \frac{N_z - M_z}{N_y - M_{y0}} - \frac{N_{z0} - M_{z0}}{N_{y0} - M_{y0}}; \text{ and } \theta_O = \frac{P_z - O_z}{P_y - O_{y0}} - \frac{P_{z0} - O_{z0}}{P_{y0} - O_{y0}}; \tag{3.28}$$

The equations of motion derived from the potential energy equation given in Eq (3.27) in conjunction with the kinetic (T) and dissipative (D) energy equations given in Eqs (3.8) and (3.10) are written as:

$$m_s\ddot{z}_s + m_u\ddot{y}_u\left(\frac{\partial\dot{y}_u}{\partial\dot{z}_s}\right) + I_{ux}\ddot{\phi}\left(\frac{\partial\dot{\phi}}{\partial\dot{z}_s}\right) + f_{ss} + f_{tls} + f_{ds} = -9.81m_s$$

$$m_u\ddot{z}_u + m_u\ddot{y}_u\frac{\partial\dot{y}_u}{\partial\dot{z}_u} + I_{ux}\ddot{\phi}\frac{\partial\dot{\phi}}{\partial\dot{z}_u} + f_{su} + f_{tlu} + f_{du} + f_{tsu} + f_{tdu} = -9.81m_u \qquad (3.29)$$

where f_{ss}, f_{su}, f_{ds} and f_{du} represent the suspension spring and damper forces acting on the sprung and the unsprung masses, respectively, such that:

$$f_{ss} = K_s\Delta l\frac{\partial(\Delta l)}{\partial z_s};\ f_{su} = K_s\Delta l\frac{\partial(\Delta l)}{\partial z_u};\ f_{ds} = C\Delta\dot{l}\frac{\partial(\Delta\dot{l})}{\partial\dot{z}_s};\text{and } f_{du} = C\Delta\dot{l}\frac{\partial(\Delta\dot{l})}{\partial\dot{z}_u} \qquad (3.30)$$

In Eq (3.29) f_{tls} and f_{tlu} represent the wheel forces on sprung and unsprung masses due to the tire lateral compliance, while the f_{tsu} and f_{tdu} represent the wheel forces due to vertical stiffness and damping properties of the tire, acting on the unsprung mass. Considering the wheel hops (potential tire loss of contact with the ground), the forces f_{tlj} ($j = s, u$), f_{tsu} and f_{tdu} are obtained as:

$$\left.\begin{aligned} f_{tlj} &= K_{tl}(y_u - \phi R)\frac{\partial(y_u - \phi R)}{\partial z_j} \\ f_{tsu} &= K_t\Delta z_t\ ;\ f_{tdu} = C_t\Delta\dot{z}_t \end{aligned}\right\} \quad \Delta z_t < \delta_{st},$$

$$\left.\begin{aligned} f_{tlj} &= 0; f_{tsu} = 0; f_{tdu} = 0 \end{aligned}\right\} \quad \Delta z_t \geq \delta_{st}, \qquad j = s,u \qquad (3.31)$$

where δz_t is the tire deflection obtained as z_t-z_0 and δ_{st} is the static tire deflection corresponding to static equilibrium, can be expressed as:

$$\delta_{st} = \frac{9.81(m_s + m_u)}{K_t} \qquad (3.32)$$

In the above equation (3.31), $\Delta\dot{z}_t$ is the time derivative of the vertical tire deflection Δz_t.

3.6.2 Influences of Joint Bushings under Harmonic Inputs

The combined effects of spring and damping rate variations, tire lateral compliance, suspension linkage constraints and the joints compliance are studied by comparing the dynamic responses of the kineto-dynamic quarter-car model with those of a conventional quarter-car model under harmonic and idealized bump excitations. In order to illustrate the influence of bushing compliance, the responses of the model are also compared with the responses of the same model assuming the joints are free (non-flexible) with no resistance to relative motion between the connecting links. The influences of the joints bushing flexibility on the kinematic responses are investigated by comparing the responses of the kineto-dynamic model with free and flexible joints. In addition to the model parameters considered in section 3.4, the torsional stiffness of bushings at both upper- and lower control arm joints (K_M and K_O) were taken as 80 Nm/rad [150] for the simulation.

The dynamic responses of the kineto-dynamic model with free joints and flexible joints, and the conventional quarter-car model are evaluated under sinusoidal displacement at the tire ground interface. The dynamic responses are evaluated in terms of sprung-mass acceleration ratio, ($\ddot{z}_s/\omega_0^2 z_{0\max}$) and the rattle space ratio, (z_s-z_u)/z_{0max} under 1.1 Hz harmonic excitation of 0.06 m peak amplitude ($z_{0\max}$=0.06 m).

Figure 3.13 (a) and (b) illustrate the steady-state sprung mass acceleration ratio and rattle space ratio responses of the three models (conventional, kineto-dynamic with free and flexible joints) under the harmonic excitation. It can be observed from the figures that the conventional model shows symmetric variations in the acceleration and rattle space responses about the static equilibrium, as was discussed in section 2.4.1. The

kineto-dynamic model, however, exhibits asymmetric variations in the responses in jounce and rebound irrespective of type of joint considered, while, the magnitude of the asymmetry seems to be slightly larger when bushing flexibility is considered. It can be seen from the Fig. 3.13(a) that the peak acceleration ratio responses attained from kineto-dynamic model in the upward direction are near 2.06 and 2.18 with free joint and flexible joint models, respectively. The result suggests that the bushing torsional compliance could increase the sprung mass acceleration by approximately 5%, attributed to the bushing spring torque being transmitted to the sprung mass together with the suspension spring force. The Fig. 3.13(a) also shows that kineto-dynamic model attains considerably smaller peak downward acceleration as compared to that in upward direction. The asymmetry in the sprung mass acceleration response is attributed to suspension kinematics.

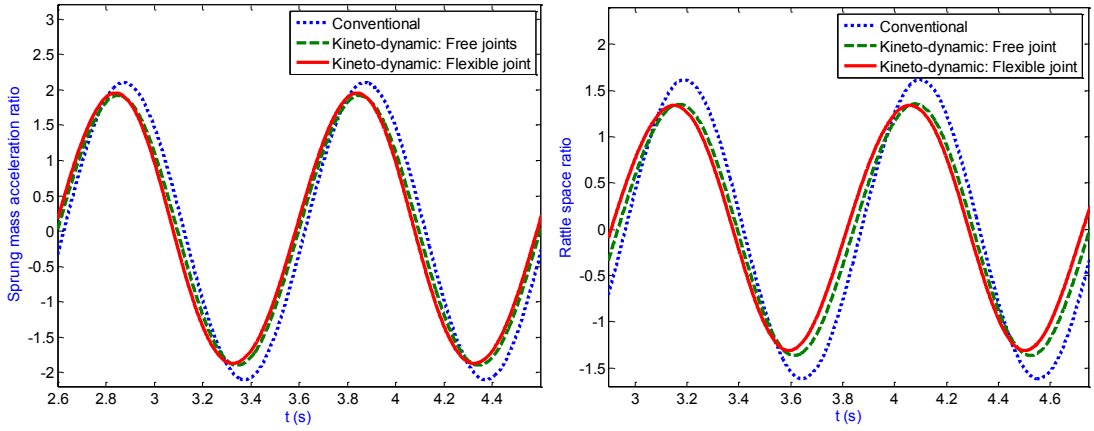

(a) (b)

Figure 3.13: Comparisons of (a) sprung mass acceleration ratio ($\ddot{z}_s / \omega_0^2 z_{0\max}$); and (b) rattle space ratio response of the kineto-dynamic model with free and flexible joints, and conventional model to harmonic excitations at 1.1 Hz and $z_{0\max}$=0.06 m.

The rattle space ratio responses of the kineto-dynamic and the conventional model as illustrated in Fig. 3.13(b) show considerable deviation between the responses of the kineto-dynamic model and those of the conventional model, while flexibility of the joints

causes less significant influence on the rattle space ratio responses. The kineto-dynamic model with free and flexible joints yields considerably lower peak rattle space response as compared to that of the conventional model.

The rotation angles of the suspension control arms are evaluated under the harmonic input since the bushing torque generated at the linkage joints is proportional to the magnitude of control arm rotations (Eq (3.27)). Figures 3.14 (a) and (b) show the rotations of upper control arm (UCA) and lower control arm (LCA) of the kineto-dynamic model with free and flexible joints in steady state condition under harmonic excitations. It can be seen that the upper control arm, in general, rotates more than the lower control arm, attributable to smaller length of the UCA compared to that of LCA. The figure further demonstrates that the kineto-dynamic model with flexible joints yield 5% lower rotation of the UCA and LCA as compared to that of the model with free joints. The reduction in the control arm rotation response of the kineto-dynamic model with flexible joints bushing can be attributed to the torsional stiffness of joint bushings that offer resistance to the control arm rotation.

The kinematic responses of the kineto-dynamic model with free and flexible joints are further evaluated in terms of variations in the camber angle and wheel track under the harmonic inputs, as illustrated Fig. 3.15. The results show asymmetric variations in both the responses during jounce and rebound. The peak responses of the model with free joints are 5% more than that of the model with flexible joints. For example, peak camber angle when free joints are considered is -2.42°, while the peak camber angle response with flexible joints is -2.29°. The results thus suggest that suspension joints with torsional compliance would decrease the variations in the camber angle and the wheel track. The

results in the Figs. 3.15 further suggest that peak magnitudes of camber angle and wheel track response occur at different time.

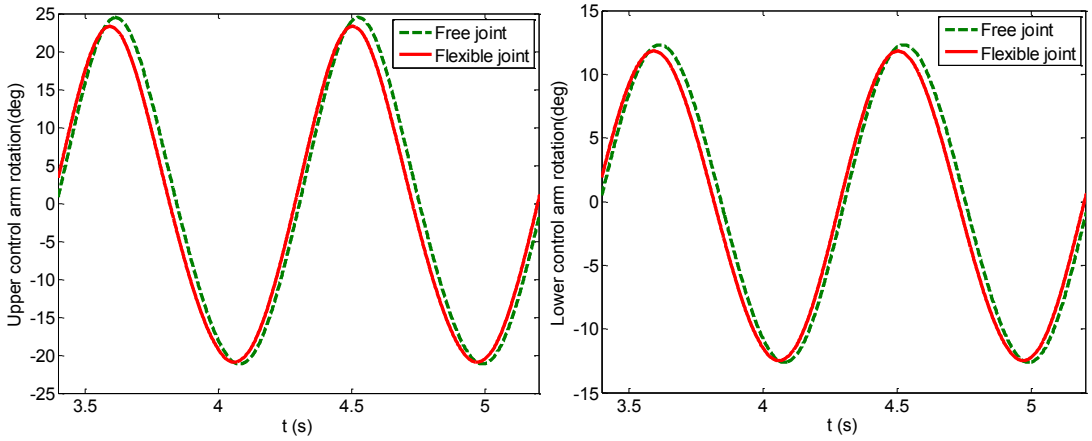

(a) (b)

Figure 3.14: Comparisons of (a) upper and (b) lower control arm rotations of the kineto-dynamic model with free and flexible joints under harmonic excitations at 1.1 Hz and z_{0max}=0.06m

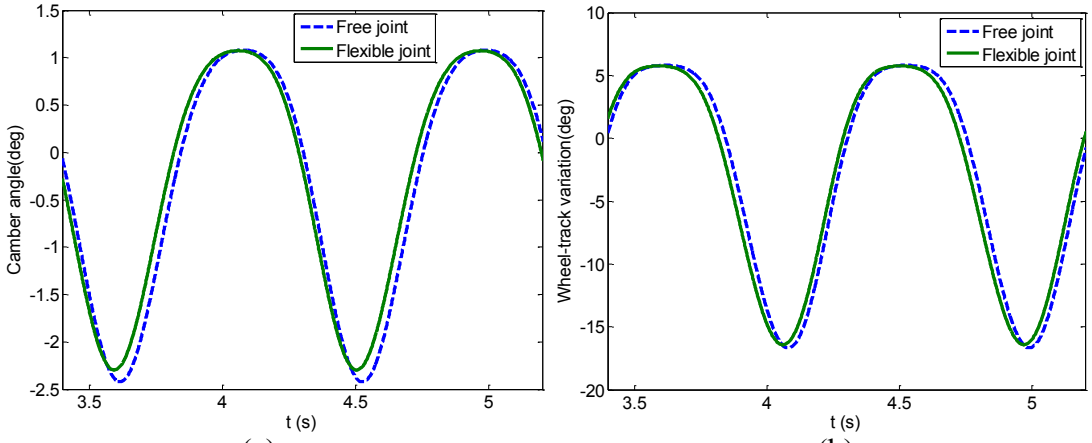

(a) (b)

Figure 3.15: Comparisons of (a) camber angle and (b) half- wheel track variation responses of the kineto-dynamic model with free and flexible joints under harmonic excitations at 1.1Hz and z_{0max}=0.06m

3.6.3 Influences of Bushing Compliance under Idealized Bump Excitations

The transient responses of the conventional and kineto-dynamic quarter-vehicle model with free and flexible bushings are evaluated under idealized bump excitations as given in Eq (3.26) with positive and negative vertical displacements to study the coupled effects of suspension kinematics and flexible bushing joints. The pulse severity parameter γ in

Eq (3.26) is written in terms of vehicle forward velocity V considering the peak of the displacement input occurs at a distance of 0.4 m from the beginning of the bump or pothole, such that:

$$\gamma = \frac{2V}{0.4\omega_0} = \frac{5V}{\omega_0} \tag{3.33}$$

Figure 3.16 illustrates the positive and negative normalized rounded pulse displacement excitations for different forward velocities (1.5, 4 and 8 m/s). The dynamic responses are evaluated for two different forward velocities (1.5 and 8 m/s) with amplitude of excitations z_{0max}=±0.1 m. The responses are evaluated in terms of sprung mass acceleration ratio, ($\ddot{z}_s / \omega_0^2 z_{0max}$) and tire force ratio (tire force/static force) responses.

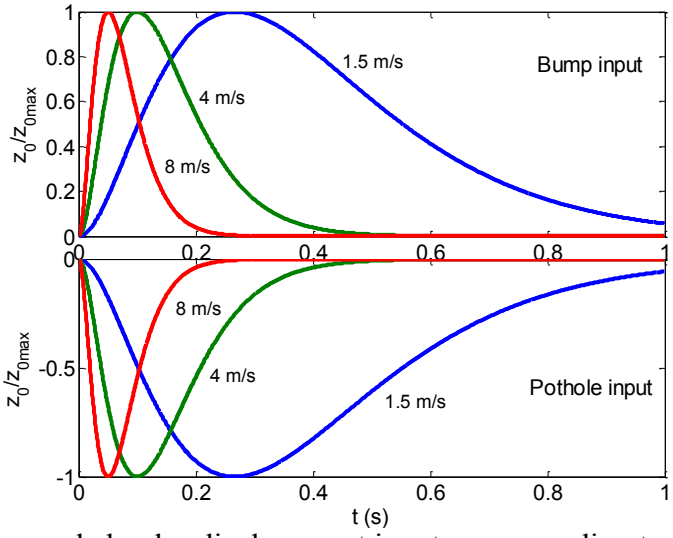

Figure 3.16: The rounded pulse displacement input corresponding to different forward velocities: (a) idealized bump excitation; and (b) idealized pothole excitation

The sprung mass acceleration ratio responses of the kineto-dynamic model with free and flexible joints are compared with that of the conventional model with equivalent spring rates under positive and negative rounded pulse excitations at forward velocity of 1.5 m/s are shown in Figs. 3.17 (a) and (b). As discussed in section 3.4.2, the conventionl model responds symetrically to positive and negative pulse inputs with peak acceleration

ratio response at 0.95, and the free oscillation response occurs at 1.05 Hz. The peak acceleration ratio responses of the kineto-dynamic model are slightly larger than that of the conventional model under positive displacement pulse excitation (Fig. 3.17 (a)), irrespective of the joint conditions considered in this study. Under the pothole input, the second peak acceleration responses of the kineto-dynamic model exhibit a larger deviation from that of the conventional quarter car model with equivalent rates. The peak response of the kineto-dynamic model with flexible joints under the positive and negative displacement inputs are 1.1 and 1.18, respectively, while the model with free joints exhibits peak acceleration ratio responses as 1.05 and 1.1, respectively. The results thus suggest that the flexible joints increase the acceleration responses of the sprung mass by nearly 5%. The results in the Figs. 3.17 (a) and (b) also show that the free oscillation of the proposed kineto-dynamic model occurs at 1.11 and 1.18 Hz, respectively, when free and flexible joint conditions are considered in the model.

Figures 3.18 (a) and (b) presents the tire force ratio response of the conventional and the kineto-dynamic model with free and flexible joints under rounded pulse positive and negative inputs at forward velocity of 1.5 m/s. The conventional model responds symmetrically to bump and pothole inputs with minimum force ratio at -0.36 and -0.35 under bump and pothole excitations, respectively. The tire force ratio response of the kineto-dynamic model, however, deviates from that of the conventional model, which under the bump input are at -0.38 and -0.43 with free and flexible joints, respectively. The results suggest that the suspension joint bushing compliance could increase the tire force variations under input. Under the pothole input, the first negative peak tire force is

insensitive to the type of joints, while the first positive, and second negative peak responses are different with free or flexible joints.

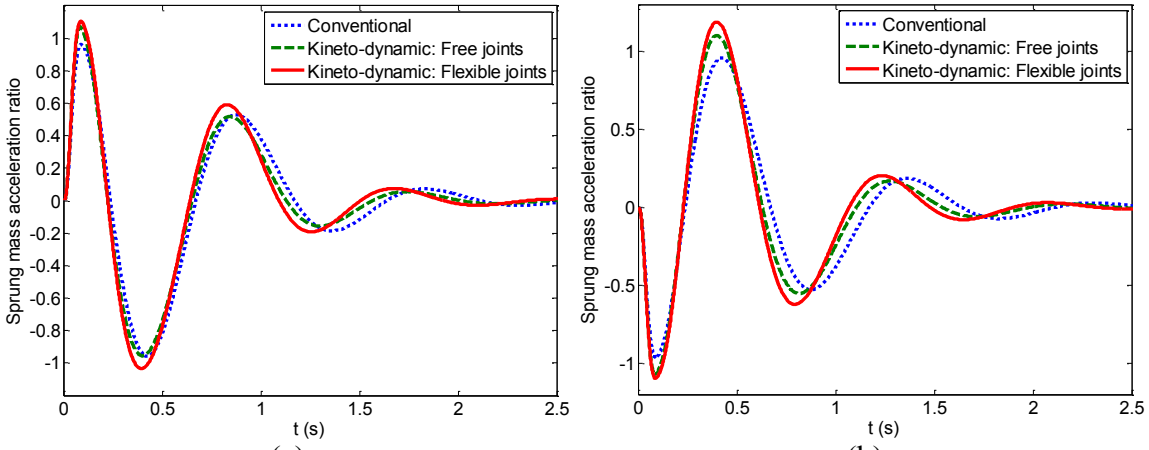

Figure 3.17: Comparisons of sprung mass acceleration ratio ($\ddot{z}_s / \omega_0^2 z_{0\max}$) responses of the kineto-dynamic model with free and flexible joints, and conventional model to idealized: (a) bump; and (b) pothole excitation (forward velocity=1.5m/s and z_{0max}=0.1m)

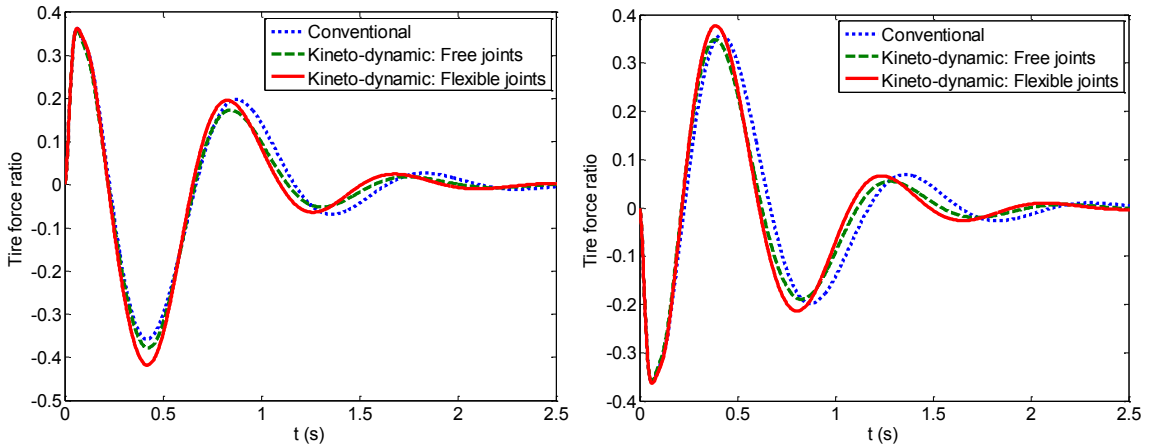

Figure 3.18: Comparisons of tire force ratio responses of the kineto-dynamic model with free and flexible joints, and conventional model to idealized: (a) bump; and (b) pothole excitation (forward velocity=1.5 m/s and z_{0max}=0.1 m)

The tire force responses of the kineto-dynamic model, in general, tend to lead that of conventional model irrespective of the type of joints considered. The responses of the kineto-dynamic model with flexible joints lead that of the model with free joints under both bump and pothole excitations as seen in the Figs. 3.18 (a) and (b), although the

magnitude of the lead is very small. It can also be seen in the figure that the tire does not lose contact (tire force ratio yields magnitude greater than -1) with the ground under this excitation.

The tire force ratio responses of the kineto-dynamic model with free and flexible joints were also evaluated under idealised rounded pulse inputs at higher forward velocity of 8 m/s and $z_{0max} = \pm 0.1$ m (results not shown). It was observed that the tire loses contact with the ground under both positive and negative displacement inputs irrespective of the type of joints considered. At higher forward velocity, however, the responses were less influenced by the suspension kinematics or by the torsinal stiffness of the joint bushings. The tire force response seemed to be predominantly influenced by the unsprung mass properties under such excitations.

3.6.4 Bushing Stiffness Sensitivity Analysis

The results in section 3.6.2 and 3.6.3 suggest that the suspension joints torsional compliance considered in this study exhibit considerable (to the order of 5%) influences on the kinematic and dynamic responses of the kineto-dynamic model. It was thus considered desirable to study the infuence of variation in the bushing stiffness from the nominal value on the dynamic responses. The study would be instrumental either in the synthesis of bushing stiffness or in the analysis of vehicle responses under joint bushings with deteorated conditions. It needs to be emphasized that elastomeric bushings tend to change the stiffness properties with time or when exposed to different working conditions. A sensitivity analysis is carried out by investigating the dynamic responses after varying the bushing stiffness individually by 50% from its nominal value in both

positive and negative senses. The sprung mass acceleration ratio responses are investigated under bump excitation at a forward velocity of 1.5 m/s.

Figures 3.19 (a) and (b) show the sprung mass acceleration ratio response of the kineto-dynamic quarter-car model with 50% variations in the stiffness of the UCA and LCA joint bushings under bump input. It can be seen that increase in the UCA bushing stiffness results in increase in the peak acceleration response. The peaks of the acceleration ratio response are near 1.24 and 1.15 when the UCA bushing stiffness values are varied by 50% in positive and negative sense, respectively, from the nominal value. The results suggest that the peak acceleration responses vary nearly 5% and 2.5%, respectively from that with the model with nominal bushing stiffness. The figure further shows that the variation in the LCA bushing does not influence the acceleration ratio response under this excitation. This negligible influence of bushing stiffness of the LCA joint is attributable to the lower rotation angles of LCA.

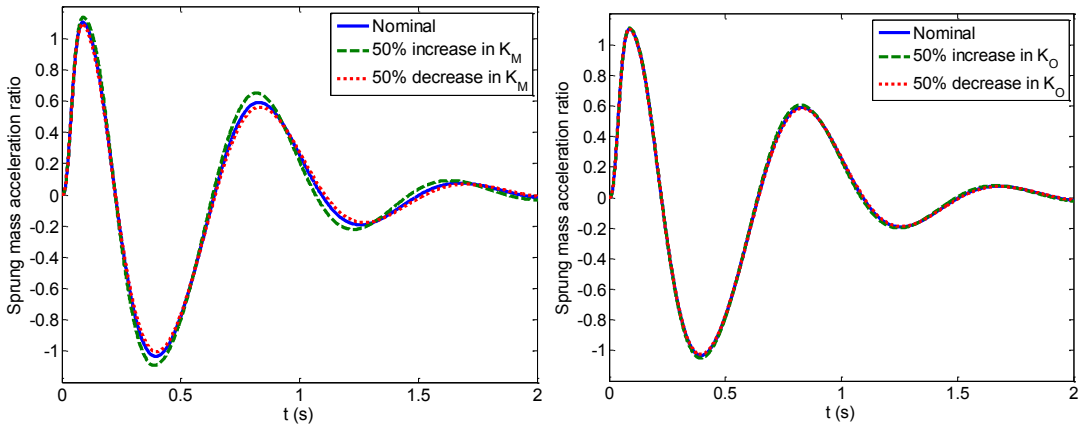

Figure 3.19: Comparison of sprung mass acceleration ratio response of the kineto-dynamic model with variation in bushing stiffness of (a) joint *M*; and (b) joint *O* under idealized bump excitation (forward velocity=1.5 m/s and z_{0max}=0.1 m)

The sensitivity analysis results thus suggest that decreasing the torsional stiffness of the upper control arm has benificial influence on the sprung mass acceleration. The

results also show that increment in the bushing stiffness of UCA joint could increase the sprung mass acceleration repsonses.

3.7 Summary

This chapter presented the study of couplings between the suspension kinematics, tire lateral compliance and joints flexibility with the vertical dynamics of the vehicle. A kineto-dynamic quarter car model is proposed in order to account for contributions due to kinematics of a double wishbone suspension to the dynamic responses, which may also facilitate suspension synthesis. The formulations for the in-plane 2-DOF kineto-dynamic model are used to obtain equivalent suspension and damping rates that may be employed in a conventional quarter car model for analysis of responses in an efficient manner. The consideration of the kineto-dynamics of the suspension revealed coupling between the vertical, lateral and camber responses, which was attributed to lateral compliance of the tire and suspension kinematics, and could not be obtained using the equivalent model. The dynamic responses to harmonic and idealized rounded pulse excitations, evaluated in terms of sprung mass vertical acceleration, suspension rattle-space and dynamic tire force, also showed asymmetric variations, while the degree of asymmetry was dependent on the amplitude and frequency of the inputs, and suspension joint coordinates.

Both the kinematic and dynamic responses are strongly dependent upon the suspension joint coordinates. The variations in the joint coordinates however would involve difficult compromise between the kinematic and dynamic response measures. The proposed model enable suspenson synthesis and analysis of couplings between the selected kinematic and dynamic responses, and lateral packaging space, which may be vital for future vehicle suspensions that must carry large volumes of fuel cells or batteries. This

study has revealed 5% variations in the kinematic and dynamic responses of the suspension system due to the joint bushing flexibility. Torsional stiffness of the joint bushings were observed to be additive to the suspension spring stiffness causing an increased sprung mass acceleration. The sensitivity analysis results have shown that decreasing the torsional stiffness of the upper control arm has beneficial influence on the sprung mass acceleration, while, the influence of variation in the lower control arm joint bushing was negligible.

The asymmetric responses of vehicle model due to suspension kinematics and tire lateral compliance may have to be taken into consideration in design of suspension dampers, which invariably exhibit asymmtric properties in compression and rebound. The coupled effects of damper asymmetry and the asymmetry in suspension kinematics on the dynamic and kinematic responses of the suspension needs to be studied in order to synthesize a good asymmetric suspension damper. Kineto-dynamic model, as proposed in this chapter, is necessary for such studies and for optimal synthesis of automotive dampers.

CHAPTER 4

KINETO-DYNAMIC ANALYSIS WITH AN ASYMMETRIC DAMPER, AND OPTIMAL DAMPER SYNTHESIS

4.1. Introduction

Automotive suspensions invariably employ asymmetric dampers, which exhibit higher damping coefficient in rebound than in compression. It has been however pointed that the reasons for such asymmetry have not been explicitly quantified [117], which is most likely attributed to highly complex dependence of different performance measures on the damping asymmetry. Furthermore, the effects of damping asymmetry greatly depend upon the nature of excitation and suspension responses. The suspension damping properties and their effects on various vehicle performance measures have been extensively investigated [107-111]. The reported studies have invariably ignored the asymmetry in damping, and the results thus do not permit the design guidance for damping asymmetry, which has been limited to a general rule of thumb suggesting that a rebound to compression damping asymmetry ratio in the order of 2 or 3 would reduce the magnitude of the force transmitted to the sprung mass while negotiating a bump [1, 2]. Only a few studies, however, have attempted to quantify the effects of asymmetric damping on the vehicle responses to transient excitations idealizing bumps or potholes [91, 117, 118].

Apart from the asymmetry in suspension damping, the suspension kinematics and tire lateral compliance also contribute to the asymmetry in the responses as shown in Chapter 3. The ride dynamic response of a vehicle would thus be expected to depend upon the coupled effects of damper, suspension and tire compliance asymmetry. On the other hand, the suspension kinematic responses are affected by the joint coordinates in a

complex manner, which are generally selected to achieve a compromise among variations in roll and bump camber, toe angles, and wheel track and wheelbase [4]. The asymmetry in the kinematic responses during upward and downward wheel motions, particularly in wheel camber and track variations can be seen in the Figs. 2.5, 2.6 and 2.11. The damping asymmetry, which affects the dynamic responses of the vehicle in a significant manner, may also affect the kinematics of the suspension.

Synthesis of optimal damper characteristics in compression and rebound has been a challenging task, which is mostly attributed to couplings among the different performance measures together with complex dependence on various parameters of an asymmetric multi-stage damper. Many studies have attempted to identify optimal damper parameters in order to achieve enhanced compromises among the ride, suspension deflection and road holding measures [92, 126, 127]. Although these studies have yielded important guidelines for the suspension damper synthesis, the findings were generally based on considerations of limited performance measures, while the damping asymmetry had been ignored in most of the studies. The synthesis of a suspension damper may involve consideration of the kinematic responses apart from the widely known complexities involving design compromises to satisfy the conflicting ride comfort, rattle space and road-holding measures. Furthermore, the study of influences of the damper asymmetry on the dynamic and kinematic responses as a function of the vehicle forward speed under different road excitations is necessary.

In this chapter of the dissertation, the influences of damper asymmetry coupled with kinematics of a double wishbone suspension on the kinematic and dynamic responses are investigated using a kineto-dynamic quarter-car model of the vehicle. The effects of

damping asymmetry on the dynamic and kinematic responses are evaluated under harmonic and idealized bump and pothole excitations. The conflicting design requirements under bump and pothole type of excitations are initially analyzed. An optimization problem is formulated comprising peak sprung mass acceleration with constraint on the suspension travel space, and solved to seek design guidance on damper asymmetry that would yield an acceptable compromise among the performance measures under the idealized bump and pothole excitations considered in the study. The dynamic and kinematic responses of the model with single- and two-stage asymmetric dampers are further evaluated under random road excitations over a range of forward velocities. Finally, an optimal synthesis of a two-stage asymmetric damper to yield compromise between the conflicting performance measures under random road inputs are presented in this chapter.

4.2 Kineto-dynamic Quarter-car Model with Asymmetric Damper

The equations of motion of the kineto-dynamic quarter-car model, as shown in the Fig. 3.2, in the generalized coordinates, z_s and z_u, are written considering the forces developed by the suspension spring, damping and the tire, as given in Eq (3.29). Among the various force components of Eq (3.29), the spring forces f_{ss} and f_{su}, and the tire forces $f_{tls,}$, $f_{tlu,}$ f_{tsu} and f_{tdu} are obtained as explained in Eqs (3.30) to (3.32) of Section 3.6.1, while the damper forces, f_{dj} (j=s, u) are obtained as explained in the following section.

4.2.1 Asymmetric Damper Models

Suspension damper with asymmetric damping properties in compression and rebound is considered in the kineto-dynamic vehicle model. The force-velocity characteristics of

the damper are characterized by piecewise linear functions in both compression and rebound. Two different types of piecewise linear force-velocity functions are considered for the relative analyses; namely, single-stage (bilinear) and two-stage asymmetric damper as shown in Fig. 4.1. The figure also shows the linear equivalent characteristics of the bilinear damper (Fig. 4.1 (a)).

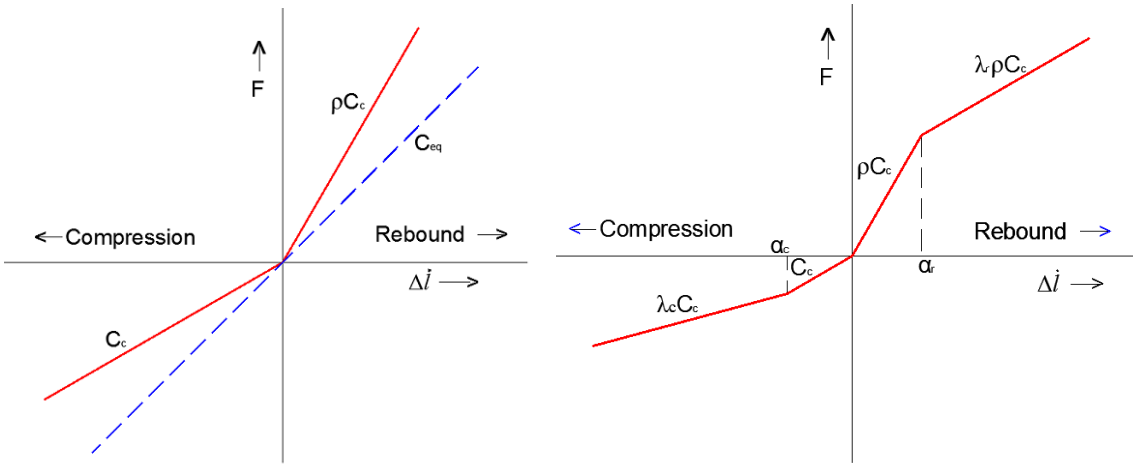

(a) (b)

Figure 4.1: Piecewise linear force-velocity characteristics of: (a) single-stage asymmetric (bilinear) and the linear equivalent damper; and (b) two-stage asymmetric damper

Bilinear Damper

The force-velocity characteristics of the bilinear damper model as shown in Fig. 4.1(a) is expressed in terms of compression damping coefficient, C_c and rebound damping coefficient, C_r, while, the rebound damping coefficient is related to the compression damping coefficient by a damper asymmetry ratio ρ, such that: $C_r=\rho C_c$. The compression damping coefficient, C_c of the bilinear damper can also be expressed in terms of the compression mode damping ratio ζ_c and the critical damping coefficient C_{crit} as $C_c=\zeta_c C_{crit}$. The compression and rebound damping forces acting on the sprung and

unsprung masses due to the bilinear damper, denoted by $f_{dj\text{-}c}$ and $f_{dj\text{-}r}$ (j=s, u), respectively, can be obtained as:

$$f_{dj-c} = C_c \Delta\dot{l} \frac{\partial(\Delta\dot{l})}{\partial \dot{z}_j} \qquad \Delta\dot{l} < 0$$

$$f_{dj-r} = \rho C_c \Delta\dot{l} \frac{\partial(\Delta\dot{l})}{\partial \dot{z}_j} \qquad \Delta\dot{l} \geq 0 \qquad j=s,u \tag{4.1}$$

where $\Delta\dot{l}$ is the time-derivative of the strut deflection as given in Eq (3.11), which is a complex function of the suspension joint coordinates and linkage lengths. The linear equivalent damping coefficient C_{eqv} is realized assuming dissipated energy similarity between the linear and bilinear asymmetric dampers, such that [88, 117]:

$$C_{eqv} = C_c\,(1+\rho)/2 \tag{4.2}$$

The damping force due to the equivalent linear damper on sprung and unsprung masses, f_{dj} are estimated by the relation, $f_{dj} = C_{eqv}\Delta\dot{l}$

Two-Stage Asymmetric Damper:

For the two-stage damper model shown in Fig. 4.1(b), the low-speed rebound damping coefficient C_r is related to the low-speed compression damping coefficient C_c as in the case of the bilinear damper. The high-speed rebound and compression damping coefficients are related to the respective low speed damping coefficients through the reduction factors, λ_r and λ_c, respectively. The transition from low- to high-speed damping in compression and rebound is assumed to occur at velocities, α_c and α_r, respectively, which are also referred to as the damper saturation limits in compression and rebound, beyond which the damping forces are determined by the respective high velocity damping coefficients. Such a piecewise linear damper model incorporating low- and

high-speed behaviors in both the compression and rebound has been proven to yield sufficiently accurate estimation of the dynamic responses of the vehicle under all driving manoeuvres [122]. The compression and rebound forces, $f_{dj\text{-}c}$ and $f_{dj\text{-}r}$, due to the two-stage asymmetric damper can be obtained as:

$$f_{dj-c}=\begin{cases} C_c\Delta\dot{l}\dfrac{\partial(\Delta\dot{l})}{\partial\dot{z}_j} & \alpha_c \le \Delta\dot{l} < 0 \\ \left(\alpha_c+\lambda_c(\Delta\dot{l}-\alpha_c)\right)C_c\dfrac{\partial(\Delta\dot{l})}{\partial\dot{z}_j} & \Delta\dot{l} < \alpha_c \end{cases} \qquad j= s,\ u$$

$$f_{dj-r}=\begin{cases} \rho C_c\Delta\dot{l}\dfrac{\partial(\Delta\dot{l})}{\partial\dot{z}_j} & 0 \le \Delta\dot{l} < \alpha_r \\ \left(\rho\alpha_r+\lambda_r\rho(\Delta\dot{l}-\alpha_r)\right)C_c\dfrac{\partial(\Delta\dot{l})}{\partial\dot{z}_j} & \Delta\dot{l} \ge \alpha_r \end{cases} \qquad j= s,\ u \qquad (4.3)$$

According to Eqs (4.1) and (4.3), the damping force acting on the sprung and unsprung masses is asymmetric about the equilibrium position of the system, when the asymmetry factor ρ is non-unity. Moreover, these equations show that the damping forces acting on the sprung and unsprung masses are complex functions of kinematics of suspension apart from the damper asymmetry and reduction factors. It should also be noted that the low-speed compression and rebound damping coefficients of the two-stage damper are equal to that of bilinear damper, while, consideration of high-speed reduction factors and saturation limits in compression and in rebound reduces the effective damping of the two-stage damper. Figure 4.2 compares the force velocity characteristics of bilinear, linear equivalent and two-stage damper models considered in this study.

4.2.2 Analysis of Damping Force Asymmetry

The nonlinear damping force due to a single-stage asymmetric damper has been expressed as a combination of a symmetric force component, arising from ρ=1, and a

discontinuous force component attributed to deviation of the asymmetry ratio from the unity value, such that [120]:

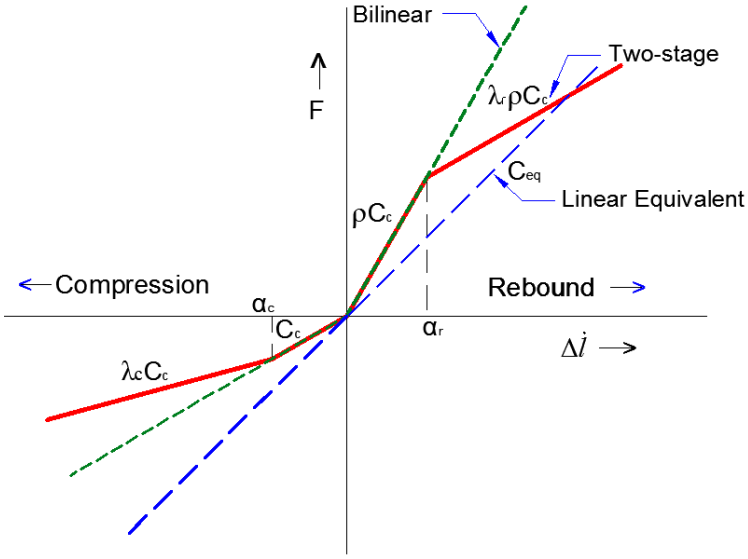

Figure 4.2: Comparisons of force velocity characteristics of the two-stage and bilinear asymmetric and equivalent linear damper

$$f_{ds} = f_{ds-c} + \begin{cases} f_{ds-r} - f_{ds-c} & \Delta\dot{l} \geq 0 \\ 0 & \Delta\dot{l} < 0 \end{cases} = f_{ds-c} + f_{dis} \tag{4.4}$$

where $f_{ds\text{-}c}$ is the compression force, considered as the symmetric component and f_{dis} is the discontinuous force component that is considered to be acting during rebound only. The nonlinear damping force of a two-stage asymmetric damper considered in this study can also be expressed in terms of a symmetric force component arising during strut compression, and a discontinuous force component, which is related to the asymmetry ratio and the saturation limits of the damper. The magnitude of the discontinuous force component f_{dis}, is thus defined for four different operating conditions related to the strut velocity: (*i*) the strut velocity is within the low-speed range in both compression ($\Delta\dot{l} > \alpha_c$) and rebound ($\Delta\dot{l} < \alpha_r$); (*ii*) low-speed in compression ($\Delta\dot{l} > \alpha_c$) with high-speed in rebound ($\Delta\dot{l} > \alpha_r$); (*iii*) high-speed in compression ($\Delta\dot{l} < \alpha_c$) with low-speed in rebound ($\Delta\dot{l} < \alpha_r$); and

(*iv*) high-speed in both compression ($\Delta\dot{l} < \alpha_c$) and rebound ($\Delta\dot{l} > \alpha_r$). The discontinuous force components corresponding to these four strut velocity ranges can be expressed as:

$$f_{dis} = \begin{cases} C_c(\rho - 1)\Delta\dot{l}\dfrac{\partial(\Delta\dot{l})}{\partial\dot{z}_s} & \alpha_c < \Delta\dot{l} < \alpha_r \\ C_c\left(\rho\alpha_r + \lambda_r\rho(\delta\dot{l} - \alpha_r) - \Delta\dot{l}\right)\dfrac{\partial(\Delta\dot{l})}{\partial\dot{z}_s} & \Delta\dot{l} > \alpha_c \;\&\; \Delta\dot{l} > \alpha_r \\ C_c\left(\rho\Delta\dot{l} - \alpha_c - \lambda_c(\Delta\dot{l} - \alpha_c)\right)\dfrac{\partial(\Delta\dot{l})}{\partial\dot{z}_s} & \Delta\dot{l} < \alpha_c \;\&\; \Delta\dot{l} < \alpha_r \\ C_c\left((\rho\alpha_r - \alpha_c) + \lambda_r\rho(\Delta\dot{l} - \alpha_r) - \lambda_c(\Delta\dot{l} - \alpha_c)\right)\dfrac{\partial(\Delta\dot{l})}{\partial\dot{z}_s} & \Delta\dot{l} < \alpha_c \;\&\; \Delta\dot{l} > \alpha_r \end{cases} \tag{4.5}$$

A simplified expression for the discontinuous force due to asymmetric damping can be achieved by considering the compression and rebound reduction factors, λ_c and λ_r as unity (λ_c=λ_r=1), such that:

$$f_{dis} = C_c(\rho - 1)\Delta\dot{l}\frac{\partial(\Delta\dot{l})}{\partial\dot{z}_s} \tag{4.6}$$

Equation (4.6) represents a simple single-stage asymmetric (bilinear) damping property. The magnitude of the discontinuous force due to damper asymmetry may be directly related to the deviations in the steady-state mean position of the sprung mass from its static equilibrium, which has been demonstrated in a few studies [88, 89] in terms of mean shift or dynamic drift. An estimate of this mean shift δ_{mean}, in the sprung mass position under a harmonic excitation may be obtained directly from the discontinuous force magnitude and the suspension spring stiffness as [112]:

$$\delta_{mean} = \frac{f_{dis}}{2K_s} \tag{4.7}$$

From Eqs (4.5) and (4.6), it is observed that the magnitude of f_{dis} is dependent upon the damping asymmetry ratio ρ, the reduction factors λ_r and λ_c, and the saturation limits, α_c and α_r.

4.3 Responses of Kineto-dynamic Model with Asymmetric Damper to Harmonic Inputs

The kineto-dynamic model comprising asymmetric damper is analyzed under harmonic excitations to study the influence of damping asymmetry on the kinematic and dynamic responses. In addition to the kineto-dynamic quarter-car model parameters considered in Table 3.1 of Chapter 3, the nominal damping properties assumed for simulation are C_c=2386 Ns/m and ρ=2 for a bilinear damper, and λ_c= λ_r=0.5, and -α_c=α_r=0.2 m/s for a two-stage asymmetric damper. The nominal coordinates of the suspension linkage joints *M*, *N*, *O*, *P*, *C, A* and *B*, as shown in Fig. 3.2, are taken in meters as: *M*(0.430, 0.818), *N*(0.644, 0.852), *O*(0.365, 0.360), *P*(0.743, 0.347), *C*(0.787, 0.452), *A*(0.660, 0.349) and *B*(0.615, 0.920), respectively. It can be recalled that the kinematic response characteristics of the chosen suspension under wheel vertical excitation with respect to chassis are such that the wheel exhibits a negative camber during jounce travel and a positive wheel camber during the rebound motion (Fig. 2.11).

The kineto-dynamic models with equivalent linear and bilinear dampers are initially analyzed under a 0.05 m amplitude harmonic excitation at a frequency of 1.2 Hz. The responses are evaluated in terms of the sprung mass displacement z_s, the unsprung mass displacement relative to the sprung mass z_u-z_s, and variations in the camber angle and the wheel track. The influence of damping asymmetry on the kinematic and dynamic responses is evaluated by comparing the responses of the kineto-dynamic model with

asymmetric and equivalent linear damping. The simulations are performed for two types of asymmetry: (i) C_r=2C_c (ρ=2); and (ii) C_r=0.5C_c (ρ=0.5). The compression damping coefficients corresponding to the selected asymmetry ratios were chosen to achieve constant value of the equivalent linear damping rate, using Eq (4.2). For the latter case, ρ=0.5, C_c was thus chosen twice that for the first case, ρ=2.

The sprung mass displacement and relative displacement responses of the kineto-dynamic model with linear (Eq 4.2) and bilinear (Eq 4.1) dampers (ρ=2 and 0.5) under the harmonic excitation are demonstrated in Fig. 4.3. The linear damper model yields peak sprung mass displacements of 0.096 and -0.097 m. The slight asymmetry in the response is attributable to the suspension kinematics and coupling between the tire lateral compliance and the vertical dynamics. The positive and negative peak displacements of the sprung mass with the bilinear damper (0.082 and -0.108 m for ρ=2, and 0.11 and -0.084 m for ρ=0.5), however, differ considerably. These cause the mean position of the sprung mass to shift from the equilibrium position by -13 mm for ρ=2, and by +13 mm for ρ=0.5. Thus, a larger rebound to compression ratio in damping causes a negative (downward) shift in the sprung mass mean position, while a larger compression to rebound ratio results in an upward shift in the mean position.

The relative displacement response peaks of the kineto-dynamic model with linear damper approach 0.076 and -0.075 m, in the positive and negative directions, respectively, while those of bilinear dampers are 0.088 and -0.062 m for ρ=2, and 0.064 and -0.089 m for ρ=0.5. The total suspension stroke of the model with linear and bilinear dampers is quite comparable, which suggests negligible effect of damper asymmetry on the steady-state suspension travel response. The bilinear damper, however, yields a shift

in the mean relative position of the unsprung mass with respect to the sprung mass in the order of 13 mm for ρ=2, and -12.5 mm for ρ=0.5, as seen in Fig. 4.3 (b). The magnitudes of shifts are also quite comparable with those observed in the sprung mass displacement response in Fig. 4.3 (a), which suggests relatively small effect of damper asymmetry on the unsprung mass displacement response.

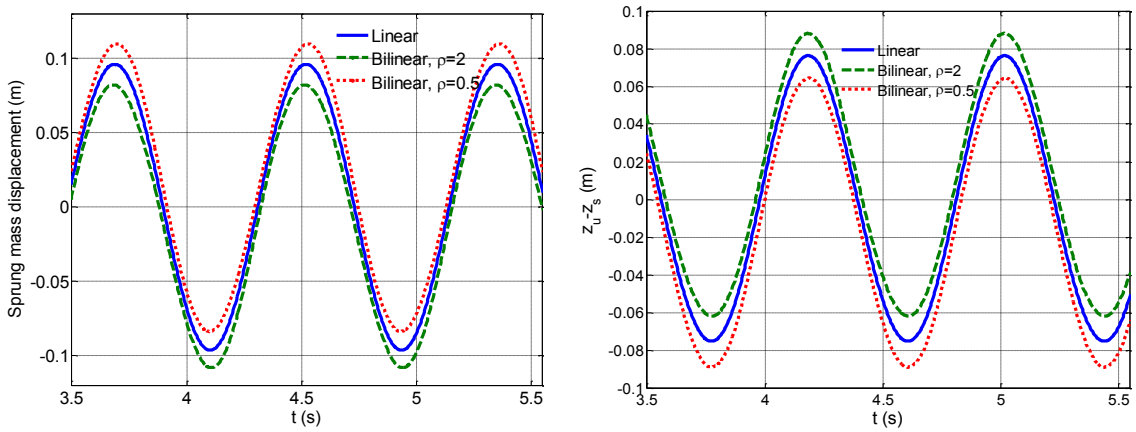

(a) (b)

Figure 4.3: Comparisons of steady state (a) sprung mass displacement and (b) relative displacement responses of the model with equivalent linear and bilinear asymmetric dampers under a harmonic excitation, $z_0(t)$=0.05 *sin* (2.4πt)

The asymmetry in the suspension deflection response (z_u-z_s) of the bilinear damper, shown in Fig. 4.3 (b), also causes greater asymmetric variations in the kinematic responses such as the camber angle and the wheel track that are related to the suspension stroke. Figure 4.4 illustrates the camber angle and wheel track variation responses of the model with linear and bilinear damper models under the given harmonic excitation. Although total suspension strokes of the kineto-dynamic model is not influenced by the damper asymmetry, the peak camber angle response seems to be greatly affected by the damping asymmetry.

The wheel camber of the model with equivalent linear damper varies from -2.2° in compression to 1.04° during rebound, while the bilinear damper with higher rebound to compression ratio (ρ=2) yields camber variations from -2.68° in compression to 0.94° in rebound, as seen in Fig. 5(a). The damper model with ρ=0.5 causes the camber angle to vary from -1.76° in compression to 1.11° in rebound. While the model with linear damping exhibits considerable asymmetry in camber variation attributed to the suspension kinematics, a higher rebound damping (ρ=2) increases the peak wheel camber variation by 0.48° and a lower rebound damping (ρ=0.5) reduces camber by 0.46°. This additional asymmetric variation in the wheel camber is attributed to the mean shift in the unsprung mass relative position with respect to that of the chassis. Studies have shown that a camber angle of 1° could cause a vehicle tire to generate 80 N lateral force [4]. A variation in the camber angle in the order of 0.48° may thus lead to change in the lateral force of each tire in the order of 40 N, which may influence the handling dynamics of the vehicle, in addition to causing accelerated tire wear.

The wheel camber variations together with the wheel lateral displacement also instigate asymmetric variations in the vehicle track, as seen in Fig. 4.4 (b). It can be seen that the peak wheel track variation during rebound approaches -11 mm for the equivalent linear damper, and -14 and -18 mm, respectively, for the bilinear dampers with asymmetry ratios of 2 and 0.5, during rebound. The peak wheel track variation during the compression is nearly 4.5 mm irrespective of the type of damper employed. Although a higher rebound to compression asymmetry ratio yields greater camber angle variation, the wheel track variation is found to decrease due to the inward motion of the wheel centre during wheel vertical travel.

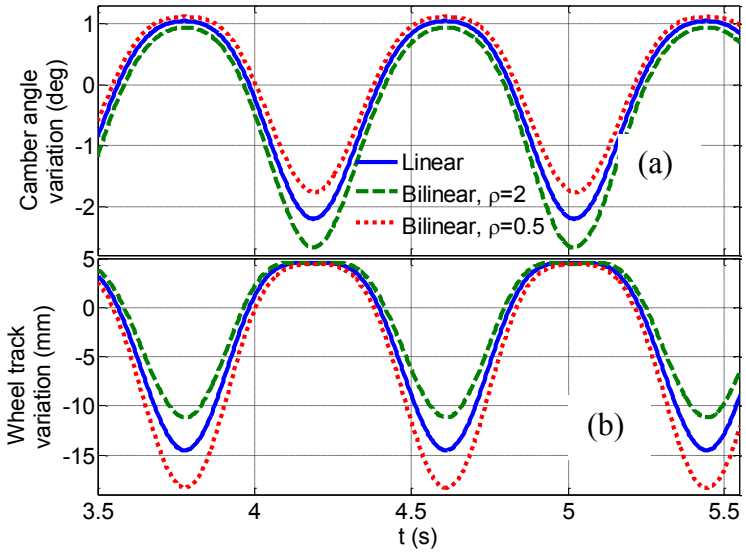

Figure 4.4: Comparisons of variations in steady-state: (a) camber angle; and (b) wheel track responses to a harmonic excitation at 1.2 Hz

The symmetric and discontinuous components of the damping force developed by the bilinear damper model, computed from Eq (4.6), are illustrated in Fig. 4.5 considering ρ=2, together with the equivalent linear damper force. The symmetric force component of the bilinear damper is considerably smaller than the linear damper force, while the peak magnitude of the discontinuous force (938.4 N) is identical to that of the peak symmetric force of the bilinear damper. For the nominal suspension spring rate, this would yield a 0.0125 m shift in the sprung mass mean position.

The results in Figs. 4.3 to 4.5 and the corresponding observations could not be generalized since these have been evaluated under a harmonic excitation in the vicinity of the sprung mass natural frequency. The results, however, provide important insight to the relation between the kinematic responses and the damper asymmetry under steady state conditions. The changes in axle lateral force attributed to the camber angle variations, presented in the Fig. 4.4 (a), may diminish when both wheels of the axle undergo similar camber angle variation. The presence of a bump excitation to only one wheel of the axle,

however, could induce a large bump camber change, leading to considerable variation in the tire lateral force, and slip angles. Furthermore, the damper asymmetry could also influence other suspension kinematic responses including the bump steer and wheel base variation. An investigation of the influences of damping asymmetry on such responses, however, would necessitate formulations and analyses of a three-dimensional model.

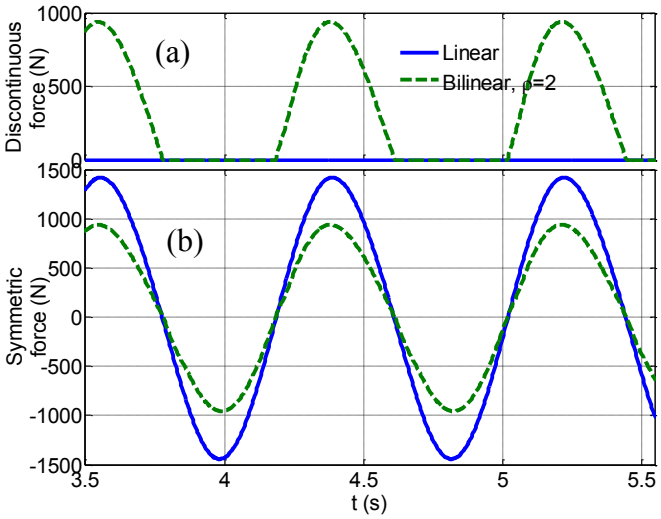

Figure 4.5: (a) Discontinuous force component of the bilinear damper; and (b) comparison of the symmetric force due to bilinear damper with the equivalent linear damping force under a harmonic excitation, $z_0(t)=0.05\ sin\ (2.4\pi t)$.

4.4 Responses of Asymmetric Damper to Idealized Bump and Pothole Inputs

Transient responses of the kineto-dynamic model with asymmetric damper are evaluated under rounded pulse displacement inputs, defined in Eq (3.26) with the pulse severity parameter as given in Eq (3.33). The peak displacement input is assumed to occur at a distance of 0.4 m from the beginning of the bump or pothole input of peak magnitude, z_{0max}=30 mm. This bump and pothole profiles are selected to ensure that the total circumference of the wheel under consideration maintains contact with the ground

during the forward motion, although a loss of tire-road contact may occur at higher speeds. The responses to pothole inputs described by a negative rectangular pulse input considered in a few studies [92, 118] may result in greater loss of tire-road contact due to abrupt changes of the profile.

4.4.1 Influences of Bilinear Damper Asymmetry

The responses of the kineto-dynamic model with bilinear damper are evaluated in terms of the sprung mass acceleration; the ratio of unsprung mass relative displacement to the maximum displacement input (rattle space ratio), $(z_u\text{-}z_s)/z_{0max}$; and the dynamic tire force ratio, the ratio of tire force variation to the static tire force. The influences of the damper asymmetry on the dynamic responses are investigated by comparing the responses of the kineto-dynamic model comprising bilinear dampers (ρ=2 and 0.5) with those of the linear damper model. Figure 4.6 (a) compares the sprung mass acceleration response of the models with equivalent linear and bilinear asymmetric dampers under the idealized bump and pothole inputs. The results suggest that the suspension with greater rebound to compression damping asymmetry ratio (lower compression damping) yields a significant reduction in the first response peak under a bump excitation. This result is in agreement with that reported in [119], although the corresponding negative acceleration peak can also be observed, which was not reported in the same study.

Under the idealized pothole input, the results show an increase in the first peak response and a decrease in the subsequent peaks in the acceleration response. Lower rebound to compression asymmetry ratio (ρ=0.5), on the other hand, yields lower acceleration peak to a pothole input and higher peak under the bump input. Considering that the human ride comfort is directly related to the sprung mass vertical acceleration,

the results show that the choice of ρ=2 would not be appropriate under a pothole excitation. This contradicts the earlier studies which suggest the use of dampers with rebound to compression ratio in the order of 2 [1] or 3 [2].

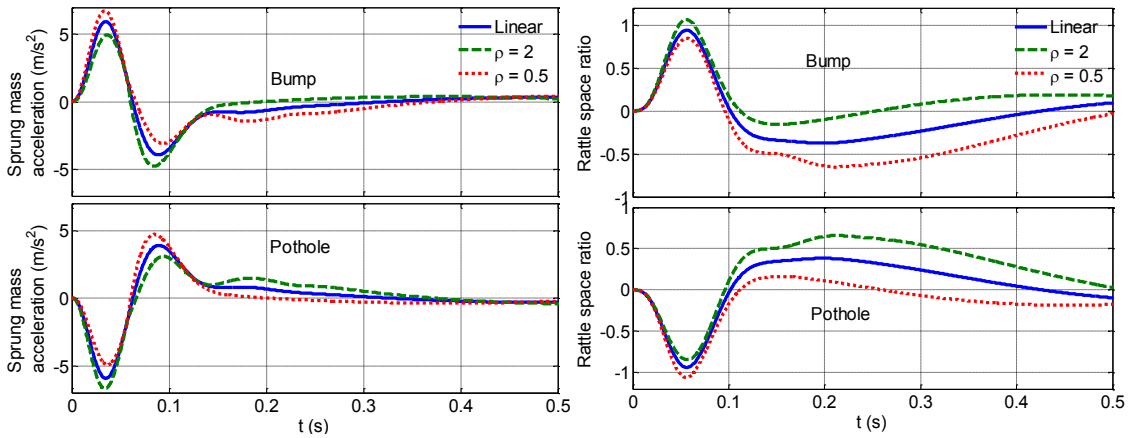

Figure 4.6: Comparisons of: (a) sprung mass acceleration; and (b) relative displacement ratio responses of the model with linear and bilinear dampers under idealized bump and pothole inputs

The figures also show that the magnitudes of the peak acceleration responses of the model with equivalent linear damper to bump and pothole excitations are slightly different due to contributions of the suspension kinematics and coupling of the tire lateral compliance with the vertical dynamics. Furthermore, the peak-to-peak accelerations due to the linear and bilinear damping rates are approximately the same. The damper with higher rebound to compression ratio (ρ=2) exhibits larger peak rattle space ratio response (near 1.1) compared to that of the damper with ρ=0.5 (near 0.8) under the bump excitation, while an opposite effect can be observed under the pothole excitation, as seen in Fig. 4.6 (b). The linear damper, on the other hand, yields a peak response ratio of 0.95. The larger peak suspension travel response of the model with the asymmetric damper also indicates occurrence of a larger bump camber response. Although the increment in

the camber angle under this excitation (not shown) was only 0.1°, a larger bump camber would be expected under a larger displacement input.

The variations in the dynamic tire force ratio responses of the model with linear and bilinear dampers are compared in Fig. 4.7 (a) corresponding to a forward speed of 10 m/s. At this speed, the displacement input approaches its peak value at 0.04 s. The dynamic tire force ratio approaches its peak value prior to the displacement input peak. The peak tire force ratio responses of the model with different dampers, however, are quite comparable. The minimum tire force ratio responses approach -0.45, -0.52 and -0.41 under the bump input, and -0.71, -0.73 and -0.69 under the pothole input, respectively, with linear, bilinear ρ=2 and bilinear ρ=0.5 damper models. The damper with higher rebound to compression ratio thus shows greater variations in the tire force under bump excitation, which could be related to relatively lower road holding property and greater wheel hop tendency. This is quite evident from the responses attained under the 50 mm excitation at a speed of 12 m/s, as seen in Fig. 4.7 (b). The results show that the bilinear damper with ρ=2 results in loss of tire-road contact under the bump input, which is not evident with the linear and bilinear (ρ=0.5) dampers. The pothole excitation, however, yields loss of tire contact, irrespective of the damper model employed. This is attributed to substantial extension of the tire spring prior to peak input displacement.

A further analysis of the tire and suspension deflection responses revealed that both the tire and suspension springs initially undergo compression under the bump input, and the tire spring goes into extension prior to the suspension spring. The peak compression of the suspension spring and peak extension of the tire spring occur simultaneously which is also evident from the rattle space and tire force responses shown in Figs. 4.6 (b) and

4.7 (a). The bilinear damper with larger rebound to compression asymmetry ratio yields greater peak suspension compression and larger tire spring extension. Higher rebound to compression ratio in damping causes larger extension of the tire spring as compared to that with the linear damper, thus causing reduction in the tire force. Similarly, higher compression to rebound ratio in damping causes increment in the minimum tire force ratio response under the bump input.

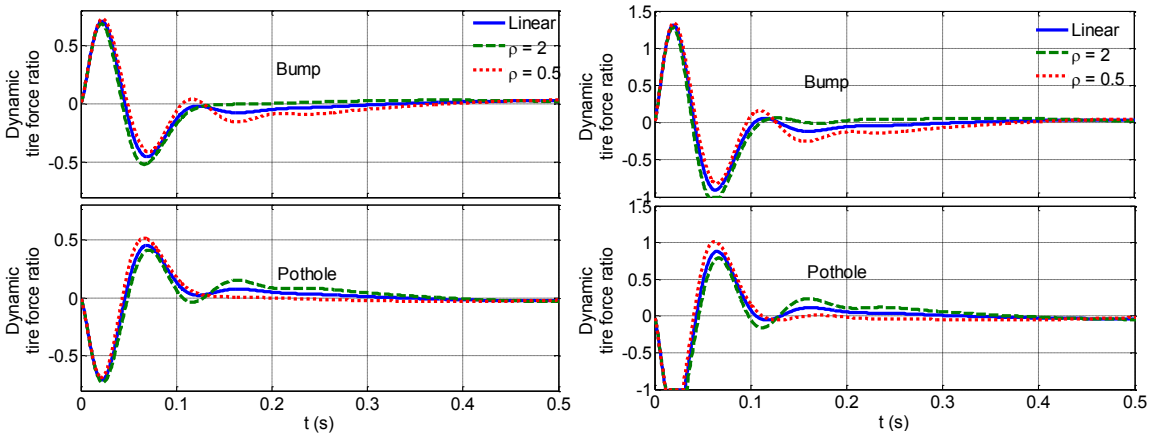

Figure 4.7: Comparisons of the dynamic tire force ratio responses of the model with linear and bilinear dampers under idealized bump and pothole inputs: (a) z_{0max}=30 mm, V=10 m/s; and (b) z_{0max}=50 mm, V=12 m/s

The wheel hop tendency of the kineto-dynamic model with the bilinear and equivalent linear models are further investigated under 50 mm peak displacement excitations and various forward speeds in the 4 to 16 m/s range. The response is evaluated in terms of the normalized wheel lift-off, defined as the ratio of the wheel lift-off duration to a reference time taken as 5 times the time corresponding to the peak input displacement. The results, presented in Fig. 4.8, clearly show that a higher rebound to compression damping asymmetry ratio yields higher normalized tire lift-off duration compared to the linear or the bilinear damper (ρ=0.5), particularly under the bump input. Under the bump input, the kineto-dynamic model with bilinear damper (ρ=2) exhibits loss of tire-road contact at

speeds above 10 m/s, while the linear damper exhibits loss of tire-road contact at speeds above 12 m/s. The lower rebound to compression damping asymmetry ratio (ρ=0.5), however, retains the tire contact with the road in the entire selected speed range.

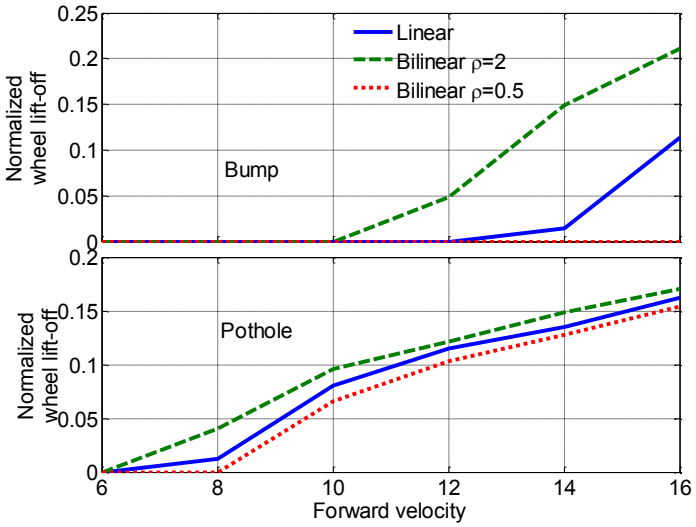

Figure 4.8: Comparison of normalized wheel lift-off responses of the model with linear and bilinear dampers under idealized bump and pothole input at different vehicle forward velocities

The wheel lift-off under a pothole input occurs at a significantly lower velocity, irrespective of the damper used. This is attributed to nearly in-phase suspension spring and tire extension. The bilinear damper with ρ=2 and linear damper exhibits wheel lift-off at speeds as low as 6 m/s. Under both the bump and pothole excitations, in general, the wheel lift-off duration is larger with a bilinear damper with higher rebound to compression asymmetry ratio than that with a linear damper or with a bilinear damper with ρ=0.5. The results in the Figs. 4.7 and 4.8 suggest that the suspension with an equivalent linear damping would yield better road holding performance under both the bump and pothole excitations as compared to the bilinear asymmetric dampers.

4.4.2 Influences of Two-stage Asymmetric Damper

The results presented in Figs. 4.6 to 4.8 are attained for single-stage asymmetric dampers, where the compression and rebound damping coefficients remain constant, irrespective of the damper velocity (λ_r and λ_c=1). A sensitivity analysis is conducted to further investigate the influences of the two-stage asymmetric damper parameters, namely, the asymmetry ratio, ρ, reduction factors, λ_r and λ_c, and damper saturation limits, α_r and α_c on the dynamic responses. The responses to idealized bump and pothole excitations with z_{0max}=30 mm (such that the tires do not lose contact with the ground) are evaluated in terms of: *i*) first and second peaks in the sprung mass acceleration, denoted as $(\ddot{z}_s)_{\text{p-1}}$ and $(\ddot{z}_s)_{\text{p-2}}$; *ii*) root mean square (rms) sprung mass acceleration, denoted as $\ddot{z}_{\text{sRMS}}$; *iii*) the first peak in suspension travel ratio (the ratio of the unsprung mass relative displecement with respect to the sprung mass and the peak displacement input), denoted as RDR_{p}; *iv*) the peak-to-peak suspension travel ratio, denoted as RDR_{pp}; and *v*) the tire dynamic force ratio defined as ratio of rms tire dynamic load to the static tire load, and denoted as *TFR*. The rms values of the acceleration and tire force fluctuation are evaluated over a time duration of five times the time corresponding to the peak input displacement. This time duration is considered to be sufficient for the transients to settle down or to reduce to a very small magnitude.

Sensitivity analysis is performed by considering variations in the asymmetric damper parameters, namely: 50, 150 and 200% of the nominal asymmetry ratio of 2 (ρ=1, 3 and 4), and 50 and 200% of the nominal reduction factors of 0.5 (λ_r, λ_c=0.25 and 1) and the nominal saturation limits of 0.2 m/s (α_r=0.1 and 0.4; α_c=-0.1 and -0.4 m/s). The sensitivity studies are conducted considering variations in only one of the parameters,

while all the other parameters are held at their respective nominal values. Tables 1 and 2 illustrate the results of the sensitivity analysis attained under the bump and pothole inputs, respectively. The tables also present the responses of the model with nominal damper parameters (ρ=2; λ_r =λ_c =0.5; α_r=0.2 m/s; and α_c=-0.2 m/s). It should be noted that the low speed damping coefficient was selected as identical to that considered for the bilinear damper (C_c=2386 Ns/m).

A comparison of the nominal parameter model results with those attained with the bilinear damper in Fig. 4.6 (a) suggests that reduction or saturation in the damping force yields relatively lower first and second peaks in sprung mass acceleration responses under both the bump and pothole excitations. The magnitudes of the first and second peaks in the sprung mass acceleration response of the model with bilinear damper (ρ=2 and λ_r=λ_c=1) under a bump input were obtained as 4.95 and -4.79 m/s^2, respectively, which reduced to 3.99 and -3.88 m/s^2 with the two- stage nominal damper. The saturation limits in the damping force (λ_r=λ_c=0.5) resulted in even greater reductions in the peak acceleration under the pothole excitation (from -6.69 and 3.08 m/s^2 with the bilinear damper to -5.51 and 2.32 m/s^2 with the two- stage asymmetric damper), as seen in Fig. 4.3 (a) and Tables 4.1 and 4.2. The results suggest that lower high-speed damping or damping force saturation would be preferable for enhancement of ride comfort while negotiating a bump or a pothole. Fukushima *et al.* [119] suggested lighter damping on the basis of results attained with a bilinear asymmetric damper, although the damping force saturation could not be considered in their study. A lower value of the high-strut velocity damping (λ_c=0.25), however, yields slightly higher first peak rattle space ratio response (RDR_p from 1.1 to 1.17) under the bump input, while its effect on the *TFR* was negligible.

The results in Table 4.1 suggest that an increment in ρ or in λ_r yields higher negative peak acceleration responses under both the positive (bump) and negative (pothole) displacement inputs. This is attributable to higher rebound damping force compared to the compression damping. The effect on RDR_{p} during compression under the bump input is thus very small, while the RDR_{p} during rebound decreases considerably resulting in lower RDR_{pp} value (Table 4.1). Higher rebound damping also yields lower RDR_{p} (during extension) under the pothole excitation, while the effects on RDR_{pp} are very small (Table 4.2). Increments in both ρ and λ_r also cause larger *TFR* under both the inputs due to greater tire deflection as it was observed from Fig. 4.7.

Relaxing the damping force saturation in the compression mode (λ_c=1) reduces the first peak in suspension travel (RDR_{p}) considerably under the bump excitation, while the effect on the RDR_{p} under the negative input is not observed. This is attributable to higher compression mode damping at higher strut velocity, which results in relatively lower negative peak in sprung mass peak acceleration, $(\ddot{z}_s)_{\mathrm{p\text{-}2}}$, and the *TFR* under the bump input, while an opposite trend in $(\ddot{z}_s)_{\mathrm{p\text{-}2}}$ is observed under the negative displacement input. The higher high- speed compression damping, however, yields considerable increase in the magnitude of the $(\ddot{z}_s)_{\mathrm{p\text{-}1}}$ under the bump input, while the effect is negligible under the pothole input. The rms acceleration also tends to be higher under both inputs, which confirms that a lower high- speed compression damping is desirable in view of ride comfort performance. A lower high- speed rebound damping (λ_r=0.25) is also beneficial in view of the rms acceleration responses to both inputs. The lower high-speed damping coefficients (λ_r=λ_c=0.25), however, would yield reduced road holding performance, as observed from the resulting increments in the *TFR*.

Table 4.1: Comparisons of the kineto-dynamic quarter car model responses to idealized bump excitation with variations in the asymmetric damper parameters.

Parameter	$(\ddot{z}_s)_{\text{p-1}}$ (m/s^2)	$(\ddot{z}_s)_{\text{p-2}}$ (m/s^2)	$\ddot{z}_{\text{sRMS}}$ (m/s^2)	RDR_p	RDR_{pp}	TFR
Nominal	***3.99***	***-3.88***	***2.15***	***1.17***	***1.32***	***0.301***
ρ=1	3.99	-2.34	1.83	1.18	1.60	0.313
ρ=3	3.99	-5.06	2.59	1.18	1.21	0.315
ρ=4	3.99	-5.96	3.03	1.18	1.19	0.339
λ_r=1	3.99	-5.10	2.53	1.18	1.24	0.311
λ_r=0.25	3.99	-3.01	1.97	1.18	1.45	0.305
λ_c=1	4.96	-3.72	2.39	1.06	1.32	0.290
λ_c=0.25	3.47	-4.01	2.03	1.25	1.34	0.312
α_r=0.4	3.99	-4.44	2.35	1.18	1.24	0.305
α_r=0.1	3.99	-3.59	2.06	1.18	1.38	0.300
α_c=-0.4	4.32	-3.81	2.26	1.13	1.23	0.296
α_c=-0.1	3.82	-3.91	2.10	1.20	1.30	0.303

Table 4.2: Comparisons of the kineto-dynamic quarter car model responses to idealized pothole excitation with variations in the asymmetric damper parameters

Parameter	$(\ddot{z}_s)_{\text{p-1}}$ (m/s^2)	$(\ddot{z}_s)_{\text{p-2}}$ (m/s^2)	$\ddot{z}_{\text{sRMS}}$ (m/s^2)	RDR_p	RDR_{pp}	TFR
Nominal	***-5.51***	***2.32***	***2.40***	***-0.97***	***1.63***	***0.295***
ρ=1	-4.01	2.33	1.84	-1.17	1.61	0.312
ρ=3	-6.67	2.44	2.87	-0.82	1.64	0.304
ρ=4	-7.55	2.61	3.26	-0.70	1.66	0.322
λ_r=1	-6.69	2.41	2.77	-0.84	1.62	0.298
λ_r=0.25	-4.67	2.33	2.14	-1.07	1.64	0.303
λ_c=1	-5.51	3.07	2.49	-0.97	1.50	0.289
λ_c=0.25	-5.51	1.98	2.38	-0.97	1.71	0.303
α_r=0.4	-6.06	2.36	2.63	-0.89	1.63	0.296
α_r=0.1	-5.23	2.31	2.26	-1.01	1.62	0.295
α_c=-0.4	-5.51	2.66	2.44	-0.97	1.56	0.292
α_c=-0.1	-5.51	2.15	2.38	-0.97	1.64	0.297

Lower saturation limits (α_r, α_c) also yield lower rms acceleration of the sprung mass under both the inputs. A lower value of α_c tends to limit low- speed compression damping to a lower value, which yields lower magnitudes of $(\ddot{z}_s)_{\text{p-1}}$ under the bump input and $(\ddot{z}_s)_{\text{p-2}}$ under the pothole inputs, respectively, with only a slight increase in RDR_{p} under

the bump input. A lower value of α_r, on the other hand, yields lower magnitude of the $(\ddot{z}_s)_{\text{p-2}}$ under the bump input and $(\ddot{z}_s)_{\text{p-1}}$ under the pothole input, respectively. The reductions in α_r and α_c, however, yield only negligible effect on *TFR*, which is mostly attributable to relatively higher compression mode damping, while it must be noted that the compression mode damping is considered constant in this study. The results, in general, show minimal effects of variation in any one of the asymmetric damping properties on the *TFR*, except for high damping asymmetry (ρ=4), which causes considerably higher *TFR*.

4.5 Optimal Synthesis of Asymmetric Damper under Bump and Pothole Inputs

The results in Tables 4.1 and 4.2 clearly show that the kineto-dynamic model responses to bump and pothole excitations vary considerably with changes in the asymmetric damper parameters, while the responses to bump and pothole excitations are generally contradictory. The variations in these responses may also depend upon the vehicle forward speed, and may involve different performance compromises at different speeds. It is thus desirable to seek optimal damper parameters that could yield improved vehicle performances or an improved design compromise under both the excitations at different forward speeds.

4.5.1 Formulation of Performance Index and Optimization Methodology

An optimization problem is formulated to seek damper design parameters for enhanced ride and road holding performance under the bump and pothole types of excitations. The vibration ride comfort performance of a vehicle has been directly related to sprung mass acceleration [1,117], while the ride and road holding dynamic

performance, and camber variation can be related to suspension deflection and tire force responses [2, 92,117]. The optimization problem may thus be formulated to minimize the peak absolute acceleration of the sprung mass under both the bump and pothole inputs, while imposing a limit constraint on the peak suspension deflection, such that:

$$\begin{aligned} &Minimize \quad F(v) = \sum_{V_1}^{V_2} \left|\ddot{z}_s\right|_{peak} \quad ; \\ &Subject\ to \ \frac{\left|z_s - z_u\right|_{peak}}{z_{0\max}} < RDR_{\max} \end{aligned} \tag{4.8}$$

where $v = \{\rho, \lambda_r, \lambda_c, \alpha_r, \alpha_c\}$ is the vector of design parameters, V_1 and V_2 are the lower and upper bounds of the vehicle speed, and RDR_{max} is the maximum allowable rattle space ratio. In this study, V_1 and V_2 are chosen as 2.5 and 10 m/s, while RDR_{max} is taken as 1.3 (maximum *RDR* attained with the asymmetric damper of compression mode damping ratio 0.1).

The above optimization problem was solved using a gradient-based, sequential quadratic programming (SQP) algorithm available in the Matlab optimization toolbox [151], while considering different vehicle speeds in the range considered with an incremental step of 2.5 m/s. The solutions of the optimization problem were sought for two different values of low- speed compression-damping coefficients, which were chosen to achieve low-speed compression damping ratio ζ_c of an equivalent linear system of 0.1 and 0.2. Limit constraints were defined so as to achieve the solutions in the feasible ranges, namely: $1 \le \rho \le 6$; $0.25 \le \lambda_c \le 1$; $0.25 \le \lambda_r \le 1$; $0.1 \le \alpha_r \le 0.4$; and $-0.4 \le \alpha_r \le -0.1$. The solutions of the minimization problem were attained by considering the positive, negative, and both the positive and negative displacement inputs (z_{0max}=50 mm).

4.5.2 Optimization Results and Discussion

The optimization problem generally converged to multiple solutions for different initial design vectors, which were mostly attributed to strong coupling among the various design variables. For instance, identical magnitudes of peak acceleration could be achieved with different combinations of low speed compression damping, damper asymmetry ratio, saturation velocities and high speed damping coefficients. An optimal solution was subsequently chosen so as to achieve minimal *TFR* response under the given excitation, apart from the minimal sprung mass acceleration. Table 4.3 presents the optimal parameters corresponding to the idealized bump and pothole excitations and chosen compression damping ratios, ζ_c=0.1 and 0.2. The solutions are denoted as *Opt-1*$_b$, *Opt-2*$_b$, *Opt-1*$_p$ and *Opt-2*$_p$, where '*1*' and '*2*' represent the compression damping ratio of 0.1 and 0.2, respectively, and subscripts '*b*' and '*p*' represent bump and pothole types of inputs, respectively. Tables 4.4 and 4.5 present the responses of the kineto-dynamic model under bump and pothole inputs, respectively, at forward velocities of 2.5, 5, 7.5 and 10 m/s, together with those the model with nominal damper parameters. The responses are illustrated in terms of $(\ddot{z}_s)_{\text{p-1}}$, $(\ddot{z}_s)_{\text{p-2}}$, $\ddot{z}_{\text{sRMS}}$, RDR_{p}, RDR_{pp}, *TFR* and normalized wheel lift-off, denoted as *NWL*.

Table 4.3: Optimal solutions corresponding to the bump and pothole types of excitations.

Excitation Type	*Solution set*	*Design Parameters*				
		ρ	λ_r	λ_c	α_r (m/s)	α_c (m/s)
Bump	*Opt-1*$_b$ (ζ_c=0.1)	3.00	0.50	0.80	0.20	-0.10
	Opt-2$_b$ (ζ_c=0.2)	1.94	0.31	0.25	0.12	-0.10
Pothole	*Opt-1*$_p$ (ζ_c=0.1)	1.00	0.73	1.00	0.10	-0.40
	Opt-2$_p$ (ζ_c=0.2)	1.00	0.26	0.78	0.10	-0.40

Table 4.4: Comparisons of responses of the kineto-dynamic model with nominal and optimal damper parameters (*Opt-1*$_b$ and *Opt-2*$_b$) under the bump input.

Response	Design	Velocity (m/s)			
		2.5	5	7.5	10
$(\ddot{z}_s)_{\text{p-1}}$ (m/s^2)	*Nom*	*2.86*	*4.80*	*5.92*	*6.52*
	Opt-1$_b$	2.31	4.00	4.94	5.40
	Opt-2$_b$	2.51	4.11	4.97	5.39
$(\ddot{z}_s)_{\text{p-2}}$ (m/s^2)	*Nom*	*-2.40*	*-2.43*	*-4.05*	*-6.17*
	Opt-1$_b$	-2.29	-1.91	-2.79	-4.67
	Opt-2$_b$	-2.47	-2.02	-2.80	-4.61
$\ddot{z}_{\text{sRMS}}$ (m/s^2)	*Nom*	*1.48*	*1.93*	*2.64*	*3.44*
	Opt-1$_b$	1.52	1.64	2.08	2.75
	Opt-2$_b$	1.49	1.69	2.13	2.77
RDR_{p}	*Nom*	*0.65*	*0.99*	*1.15*	*1.20*
	Opt-1$_b$	0.69	1.06	1.23	1.29
	Opt-2$_b$	0.67	1.05	1.23	1.29
RDR_{pp}	*Nom*	*1.11*	*1.31*	*1.37*	*1.37*
	Opt-1$_b$	1.31	1.48	1.52	1.54
	Opt-2$_b$	1.25	1.46	1.52	1.55
TFR	*Nom*	*0.126*	*0.194*	*0.337*	*0.502*
	Opt-1$_b$	0.131	0.190	0.352	0.547
	Opt-2$_b$	0.130	0.194	0.357	0.550
NWL	*Nom*	*0*	*0*	*0*	*0*
	Opt-1$_b$	0	0	0	0.071
	Opt-2$_b$	0	0	0	0.071

The results attained under the bump input (*Opt-1*$_b$ and *Opt-2*$_b$) clearly show strong coupling between ρ, λ_c and ζ_c. The solutions converge toward a higher value of ρ and λ_c (ρ*=3;* λ_c*=0.8*), and a lower value of α_c, when a lower value of ζ_c is chosen (0.1). The optimal values of both ρ and λ_c decrease considerably to their lower limits when ζ_c is relaxed to 0.2 (Table 4.3). In this case, the saturation limit and reduction factor in rebound mode also decrease significantly, since a higher rebound damping yields higher second peak in sprung mass acceleration, particularly at higher forward speeds. The results in Table 4.4 suggest that lower compression damping (ζ_c=0.1; *Opt-1*$_b$) yields

Table 4.5: Comparisons of responses of the kineto-dynamic model with nominal and optimal dampers (*Opt-1*$_p$ and *Opt-2*$_p$) under pothole input.

Response	Design	Velocity(*m/s*)			
		2.5	5	7.5	10
$(\ddot{z}_s)_{\text{p-1}}$ (m/s^2)	*Nom*	-3.85	-6.41	-7.98	-8.67
	Opt-1$_p$	-2.58	-4.05	-4.99	-5.41
	Opt-2$_p$	-2.54	-4.16	-5.03	-5.40
$(\ddot{z}_s)_{\text{p-2}}$ (m/s^2)	*Nom*	3.04	2.99	2.96	3.61
	Opt-1$_p$	2.89	2.29	2.02	3.10
	Opt-2$_p$	2.49	1.90	3.08	5.13
$\ddot{z}_{\text{sRMS}}$ (m/s^2)	*Nom*	1.88	2.71	3.32	3.78
	Opt-1$_p$	1.87	1.93	2.06	2.48
	Opt-2$_p$	1.63	1.70	2.12	2.80
RDR_{p}	*Nom*	-0.59	-0.85	-0.97	-0.99
	Opt-1$_p$	-0.86	-1.06	-1.24	-1.29
	Opt-2$_p$	-0.67	-1.06	-1.24	-1.29
RDR_{pp}	*Nom*	1.47	1.69	1.67	1.63
	Opt-1$_p$	1.80	1.78	1.78	1.78
	Opt-2$_p$	1.38	1.53	.531	1.52
TFR	*Nom*	0.155	0.238	0.352	0.476
	Opt-1$_p$	0.154	0.212	0.381	0.588
	Opt-2$_p$	0.135	0.191	0.350	0.536
NWL	*Nom*	0	0	0	0.071
	Opt-1$_p$	0	0	0	0.051
	Opt-2$_p$	0	0	0	0.051

lowest first and second peaks in acceleration response in most of the speed range, except at 10 m/s, where the peak magnitudes for both values of ζ_c are similar. Both the solutions, *Opt-1*$_b$ and *Opt-2*$_b$, however, yield considerably lower values of RMS, and first and second peak acceleration magnitudes in the entire velocity range considered in the study, when compared to those attained with the nominal damper. Furthermore, both the solutions yield lower magnitudes of negative peaks in the sprung mass acceleration, $(\ddot{z}_s)_{\text{p-2}}$ at 5 m/s velocity compared to those at 2.5 m/s, unlike in the case of nominal damper. This may be attributable to the fact that the excitation frequency corresponding to 2.5 m/s velocity is closer to the first natural frequency of the system.

The responses of the optimal damper to bump excitation further reveal that both the solutions, *Opt-1*$_b$ and *Opt-2*$_b$, yield comparable magnitudes of RDR_{p} and RDR_{pp}, which are only slightly higher than those of the model with the nominal damper. Interestingly, the tire dynamic force ratio (*TFR*) responses of the model with optimal dampers, *Opt-1*$_b$ and *Opt-2*$_b$, tend to be quite comparable in the entire velocity range, but slightly higher than those of the nominal damper. Furthermore, the nominal damper does not cause any wheel lift-off under the bump excitation even at the vehicle velocity 10 m/s, while the optimal dampers cause wheel lift-off (*NWL*=0.071) at this speed as seen in the Table 4.4. These results suggest that the tire road holding, under the bump input, depends upon the effective rebound damping coefficient.

From the results presented in Tables 4.3 and 4.4, it may be deduced that the peak and rms sprung mass acceleration response to a bump input is minimized through lower compression damping, while rebound damping asymmetry should be determined on the basis of suspension travel and road holding requirements. The damper asymmetry ratio is thus strongly dependent upon the compression damping coefficient. A damper asymmetry ratio in the order of 3 or 2 (depending upon ζ_{c}) would be beneficial in achieving improved road holding. These values of damper asymmetry ratio are in good agreement with those suggested by Milliken [1] and Gillespie [2]. Lower rebound damping, however, would be desirable for a damper design with higher compression damping in order to reduce the second peak in sprung mass acceleration.

Unlike the bump input, the solutions attained under the pothole input, *Opt-1*$_p$ and *Opt-2*$_p$, converge to unity value of the asymmetry factor, irrespective of the compression damping ratio ζ_{c} (Table 4.5). This is attributable to the fact that a lower rebound damping

helps reduce the magnitude of the first peak in sprung mass acceleration, as it was observed in Table 4.2. Under the pothole input, the solutions also converged to higher values of high-speed compression damping compared to that in rebound ($\lambda_c > \lambda_r$). The λ_c is significantly larger than λ_r for the higher value of ζ_c, which is opposite to the solutions attained under the bump input. Furthermore, unlike the solutions attained under the bump input, the optimal values of saturation limits in compression under the pothole input tend to be considerably higher than those in rebound ($|\alpha_c| > \alpha_r$). The α_c in both *Opt-1*$_p$ and *Opt-2*$_p$ is at its upper limit of 0.4 m/s, while α_r is at its lower limit of 0.1 m/s. The solution corresponding to a pothole type of input suggest that a symmetric low-speed damping in compression and rebound with considerably lower high- speed damping in rebound would be beneficial in reducing the peak acceleration response. The compression mode damping, however, is determined by the maximum allowable suspension travel, second peak in acceleration and the tire dynamic force ratio. These are further evident from the responses presented in table 4.5.

The solutions *Opt-1*$_p$ and *Opt-2*$_p$ yield considerably lower RMS and peak accelerations, $(\ddot{z}_s)_{\text{p-1}}$ and $(\ddot{z}_s)_{p-2}$, compared to those of the nominal damper in majority of the velocity range considered. The *Opt-2*$_p$ solution, however, yields relatively higher magnitudes of $(\ddot{z}_s)_{p-2}$ at 7.5 and 10 m/s velocity than the *Opt-1*$_p$ solution. This is attributable to higher compression mode damping associated with *Opt-2*$_p$, which was essential for limiting the peak suspension travel, which are considerably higher than those of the nominal damper, as seen in Table 4.5. Considering the first and second peak acceleration responses alone, the *Opt-1*$_p$ solution seems to offer beneficial effects under a pothole type of input. The *Opt-2*$_p$ solution however yields lowest RDR_{pp} and *TFR* values

in most of the velocity range. The *TFR* responses of the optimal solutions at the extreme velocity of 10 m/s, however, tend to be considerably higher than that of the nominal damper, which is most likely caused by the wheel lift-off. The results in general suggest that the *Opt-2*$_p$ solution offers a better design compromise in limiting the RDR_{p} and *TFR* responses.

The solutions attained under the bump and pothole types of excitation appear to be conflicting as seen in Table 4.3. An optimal damper design for realizing lower peak sprung mass acceleration to both the bump and pothole excitations would thus involve a complex design compromise. The solutions of the minimization problem were subsequently attempted by considering the responses to both the bump and pothole inputs ($|z_{0max}|$=50 mm) in order to seek a design compromise. From the previous results, it is evident that such optimization would yield a linear damping in compression and rebound as a design compromise, which would cause higher *TFR* response. Considering the strong coupling between ζ_{c} and ρ, the optimal solutions were attempted by considering two different constant values of ζ_{c} (0.1 and 0.2) together with ρ of either 3 or 2, as determined from the *Opt-1*$_b$ and *Opt-2*$_b$ solutions, respectively. The design parameters were thus reduced to 4 (λ_r, λ_c, α_r and α_c). The resulting optimal parameters denoted as *Opt-1*$_{bp}$ (ζ_{c}=0.1; ρ =3) and *Opt-2*$_{bp}$ (ζ_{c}=0.2; ρ=2) were obtained as: λ_r=0.25; λ_c=0.74; α_r=0.1; α_c=-0.39, and λ_r=0.25; λ_c=0.5; α_r=0.1; α_c=-0.2, respectively. Table 4.6 compares the responses attained with solutions *Opt-1*$_{bp}$ and *Opt-2*$_{bp}$ under bump and pothole inputs in the 2.5 to 10 m/s range.

The results in Table 4.6 suggest that the *Opt-1*$_{bp}$ solution yields lower $(\ddot{z}_s)_{\text{p-1}}$ responses to both bump and pothole inputs compared to those of the model with the nominal

damper (Tables 4.4 and 4.5). The solution *Opt-2*$_{bp}$, on the other hand, yields $(\ddot{z}_s)_{\text{p-1}}$ responses comparable to those of the nominal damper under the bump input, but considerably lower responses under the pothole input. The *Opt-2*$_{bp}$ solution also yields lower value of $\ddot{z}_{\text{sRMS}}$ and $(\ddot{z}_s)_{p-2}$ at lower speeds, while an opposite trend is observed at higher speeds. The *Opt-2*$_{bp}$ solution, however, yields considerably lower values of RDR_{p}, RDR_{pp} and *TFR* responses compared to the *Opt-1*$_{bp}$ solution under both types of excitations.

Table 4. 6: Comparisons of responses of the kineto-dynamic model with *Opt-1*$_{bp}$ and *Opt-2*$_{bp}$ dampers under bump and pothole inputs.

Response	Design	Bump input				Pothole input			
		Velocity(*m*/*s*)							
		2.5	5	7.5	10	2.5	5	7.5	10
$(\ddot{z}_s)_{\text{p-1}}$ (m/s^2)	*Opt-1*$_{bp}$	2.39	4.05	4.95	5.39	-2.68	-4.38	-5.31	-5.72
	Opt-2$_{bp}$	2.86	4.80	5.91	6.52	-3.10	-5.04	-6.15	-6.67
$(\ddot{z}_s)_{\text{p-2}}$ (m/s^2)	*Opt-1*$_{bp}$	-2.72	-2.35	-2.20	-2.95	2.98	2.47	2.25	2.71
	Opt-2$_{bp}$	-2.65	-2.31	-2.42	-3.89	2.81	2.40	2.48	3.70
$\ddot{z}_{\text{sRMS}}$ (m/s^2)	*Opt-1*$_{bp}$	1.68	1.85	2.08	2.50	1.87	2.06	2.23	2.59
	Opt-2$_{bp}$	1.59	2.02	2.47	3.02	1.73	2.16	2.59	3.06
RDR_{p}	*Opt-1*$_{bp}$	0.73	1.06	1.23	1.29	-0.67	-1.03	-1.21	-1.26
	Opt-2$_{bp}$	0.65	0.99	1.14	1.20	-0.63	-0.97	-1.12	-1.17
RDR_{pp}	*Opt-1*$_{bp}$	1.52	1.67	1.72	1.78	1.64	1.81	1.83	1.83
	Opt-2$_{bp}$	1.31	1.53	1.58	1.59	1.44	1.65	1.65	1.64
TFR	*Opt-1*$_{bp}$	0.148	0.213	0.386	0.598	0.153	0.217	0.384	0.585
	Opt-2$_{bp}$	0.138	0.206	0.350	0.528	0.143	0.210	0.351	0.514
NWL	*Opt-1*$_{bp}$	0	0	0	0.071	0	0	0	0.051
	Opt-2$_{bp}$	0	0	0	0	0	0	0	0.061

The influence of optimal damper designs on the wheel camber variations are further investigated and compared with those of the model with the nominal damper, as illustrated in Figs. 4.9 (a) and (b), respectively, under the bump and pothole types of excitations. The figures present the magnitudes of first and second peaks in camber angle

variation of the model with nominal, *Opt-1*$_{bp}$ and *Opt-2*$_{bp}$ dampers. It can be seen that the *Opt-1*$_{bp}$ solution yields larger positive and negative peak camber angle variations compared to those of the nominal and *Opt-2*$_{bp}$ dampers under the bump input in the entire velocity range considered in this study. The negative camber variation response of *Opt-2*$_{bp}$ design, however, is comparable to that of the *Opt-1*$_{bp}$ design. Under the pothole input, both the optimal designs, however, yield lower peak positive and negative camber variations compared to the nominal responses in most of the velocity range, while *Opt-1*$_{bp}$ tends to show large positive but lower negative camber variations than *Opt-2*$_{bp}$. The camber response to the pothole input at the low velocity of 2.5 m/s forms an exception to the above, where the negative peak of the model with *Opt-1*$_{bp}$ tends to be greater, which is attributable to higher second peak in relative displacement response of the unsrpung mass.

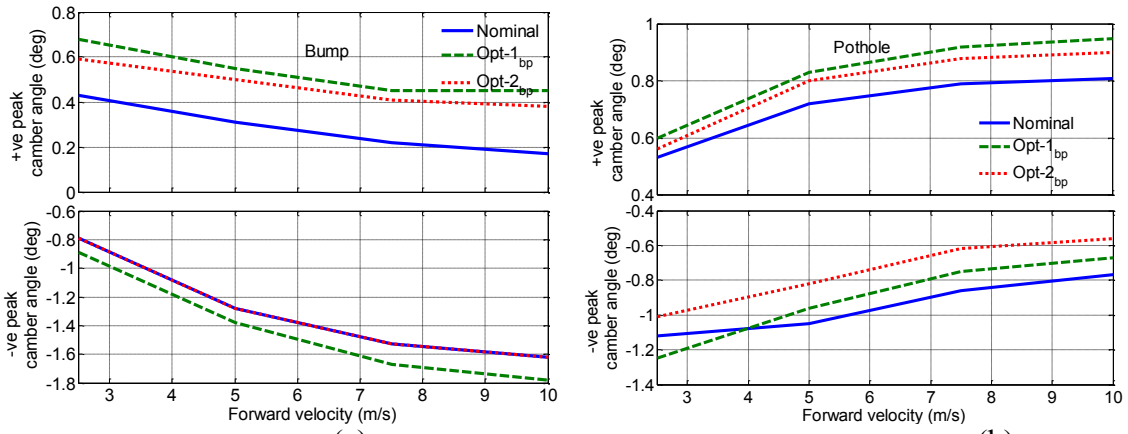

(a) (b)

Figure 4.9: Comparisons of the peak camber angle variation responses of the model with nominal and optimal dampers under idealized: (a) bump; and (b) pothole excitations.

The results in Table 4.6 and Fig. 4.9 suggest that *Opt-2*$_{bp}$ solution forms a better design compromise considering ride comfort, rattle space, road holding and peak camber angle performances under both the bump and pothole inputs. A low-speed compression damping ratio in the order of 0.2, damper asymmetry ratio of 2 coupled with very low

rebound saturation limit and reduction factor, and compression saturation limit in the order of -0.2 m/s with reduction factor around 0.5 can yield an optimal design compromise between the bump and pothole responses.

4.6 Responses of Kineto-dynamic Model with Asymmetric Damper to Random Road Inputs

The results presented in sections 4.4 to 4.5 suggested that synthesis of asymmetric damper is complex due to the various conflicting design requirements under deterministic bump and pothole type of excitations. It has been however suggested in the literature that suspension synthesis is more realistic only if it considers the random road excitations [2, 92]. Different studies have reported optimal damper synthesis under random road excitations [92, 127] employing vehicle models of varying complexities. Optimal damping characteristics suggested by these studies were thus expressed as complex functions of the forward velocity of the vehicle with significant differences in the identified optimal damping coefficients corresponding to lower and higher vehicle velocities. This can be attributed to limited understanding of influences of damper asymmetric properties in relation to the vehicle forward velocity, particularly under random road excitation. The optimal synthesis of suspension damper with asymmetric properties in rebound and compression thus necessiates study of influences of the damper asymmetry on the dynamic and kinematic responses as a function of the vehicle forward speed under random road excitations. The kineto-dynamic responses of the model under varying forward speed are investigated in this section.

4.6.1 Random Road Characteristics

Many studies have reported roughness properties of highways, secondary roads and dirt roads as real valued, zero mean, stationary and Gaussian random fields [66, 92]. In this study, the urban roads roughness, characterized on the basis of measured road elevations reported in a previous study [152], are used for evaluating the dynamic responses of the kineto-dynamic model and the performance measures. Figure 4.10 (a) illustrates the filtered roughness profile of the road over a span of 500 m, while, Fig. 4.10 (b) shows the spatial power spectral density (PSD) of the road. The displacement PSD of the road is also compared with those of different roads classified as 'poor', 'average' and 'good', denoted by roads D, C and B, respectively, in an ISO document [66, 86]. The comparison suggests that the measured road profile corresponds to a poor quality road at low frequencies, and lies between the average and a good road at higher frequencies.

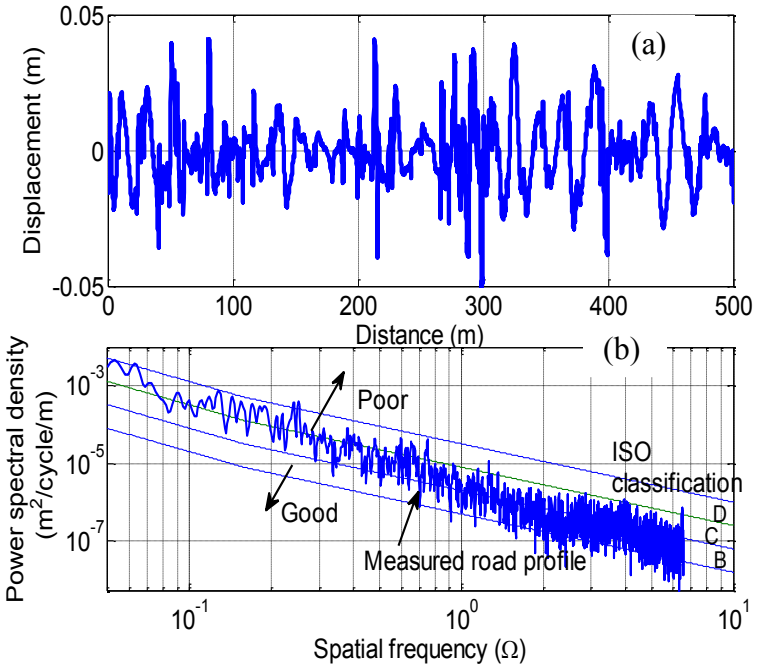

Figure 4.10: Roughness profile of an urban road: (a) elevation vs. distance; (b) spatial PSD of the elevation.

4.6.2 Influences of Bilinear Asymmetric Damper under Random Excitations

Kinematic and dynamic responses of the kineto-dynamic model with bilinear damper are evaluated under the urban road excitation described in Fig. 4.10. The responses are evaluated with three different damper models, including two bilinear dampers with compression mode damping ratios ζ_c=0.2, ρ=2 and ζ_c=0.1, ρ=5, and an equivalent linear damper (ζ=0.3; C_{eqv}=3037.5Ns/m). The dynamic responses of the kineto-dynamic model are evaluated in terms of: rms of sprung mass vertical acceleration and suspension deflection, denoted as $\ddot{z}_{s\,\mathrm{RMS}}$ and $(RD)_{\mathrm{RMS}}$, respectively; ratio of rms tire load fluctuation to the static tire load, denoted as dynamic load coefficient (*DLC*); and percentage time duration of the wheel losing contact with the ground (over the entire road span) or % wheel lift-off. The kinematic responses of the suspension are evaluated in terms of rms of the camber angle variations, denoted as $(\phi)_{\mathrm{RMS}}$. The responses are evaluated under random road excitation at different constant forward speeds in the 30 to 120 km/h range. Figures 4.11 to 4.14 illustrate the dynamic and kinematic responses of the kineto-dynamic model with the two bilinear dampers (ζ_c=0.2, ρ=2; and ζ_c=0.1, ρ=5) and the linear damper (ζ=0.3) in the speed range considered.

Figures 4.11 (a) and (b) compare the sprung mass rms acceleration and *DLC* responses of the model with the three different dampers subjected to rough road input in the 30 to 120 km/h speed range. Although all the dampers yield equal effective damping coefficients, the acceleration and *DLC* responses are influenced by the damper asymmetry and the vehicle forward speed. At speeds below 90 km/h, the kineto-dynamic model with bilinear dampers yields lower rms acceleration compared to the model with linear damper (ζ=0.3). At speeds below 60 km/h, both the bilinear dampers (ζ_c=0.1 and

0.2) yield comparable rms acceleration response, while the model with ζ_c=0.2 yields lower sprung mass acceleration above 60 km/h. The higher compression damping also yields lower *DLC* due to the tire force in the entire speed range, when compared to the bilinear damper with ζ_c=0.1, which is attributable to its higher rebound damping (ρ=5). At speeds above 90 km/h, the model with linear damper yields lower acceleration and *DLC* response compared to the bilinear damper with ζ_c=0.1, but the responses are quite comparable with that of the bilinear damper with ζ_c=0.2. These results suggest that dampers with different asymmetry but identical equivalent damping can yield very different rms acceleration and *DLC* responses, which further depend upon the vehicle velocity.

The percent wheel lift-off and rms relative displacement responses of the model with the three dampers under random road inputs over the velocity range 30 to 120 km/h are presented in Fig. 4.12. The asymmetric bilinear dampers yield considerably higher wheel lift-off and relative displacements compared to the equivalent damper, which contribute to higher *DLC* as seen in Fig. 4.11 (b). This bilinear damper with lower compression damping (ζ_c=0.1) yields significantly higher wheel lift-off duration and relative displacement responses, particularly at speeds above 50 km/h, which is attributable to greater compression mode deflection. Higher compression damping (ζ_c=0.2) tends to reduce both the responses but yields higher wheel lift-off at speeds above 70 km/h compared to the equivalent linear damper.

The results in Fig. 4.12 also show that the $(RD)_{\text{RMS}}$ responses reach their peak values near 100 km/h velocity (near 120 km/h for ζ_c=0.1), and the $(RD)_{\text{RMS}}$ magnitudes decrease at higher speeds. The results suggest that linear damping would be desirable considering

the road holding performance, particularly at higher velocities. Although a point contact tire model tends to emphasize the loss of tire-road contact and thus the variations in the tire forces [96], the results in Figs. 4.11 and 4.12 show relative dynamic responses of bilinear asymmetric and linear equivalent dampers considered in the study.

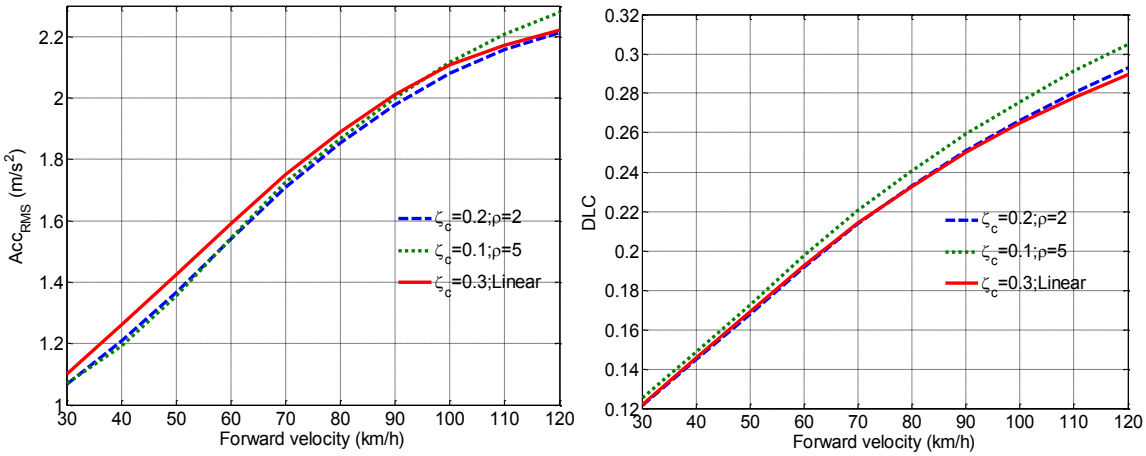

(a) (b)

Figure 4.11: Comparisons of (a) rms acceleration and (b) *DLC* responses of the kineto-dynamic model with bilinear dampers (ζ_c=0.2, ρ=2; ζ_c=0.1, ρ=5) and an equivalent linear damper (ζ=0.3) to random road excitations as a function of forward speed.

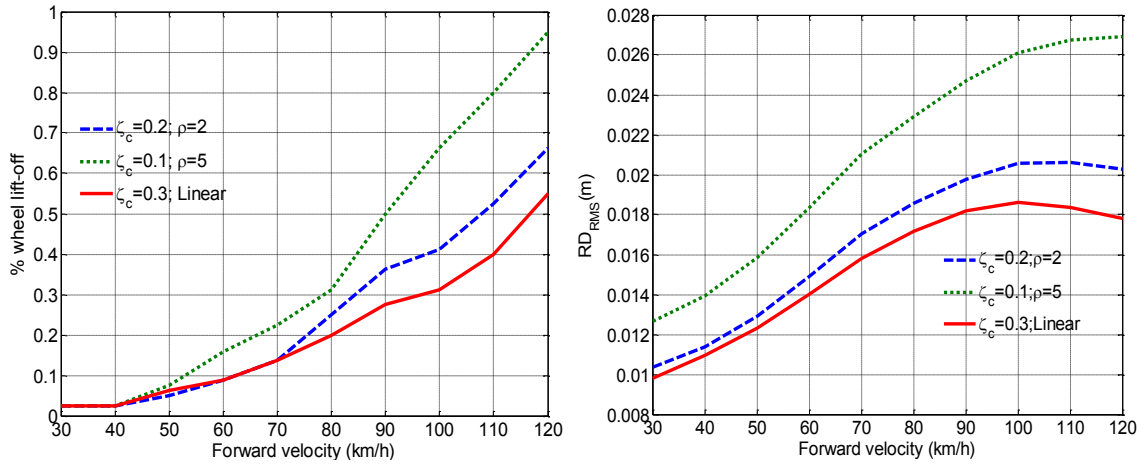

(a) (b)

Figure 4.12: Comparisons of (a) %wheel lift-off and (b) rms relative displacement responses of the kineto-dynamic model with bilinear dampers (ζ_c=0.2, ρ=2; ζ_c=0.1, ρ=5) and an equivalent linear damper (ζ=0.3) to random road excitations as a function of forward speed.

The suspension damping properties also affect the kinematic response of the vehicle. Figure 4.13 (a) compares the rms camber angle variation responses of the model with different dampers. The lowest camber variation, $(\phi)_{\mathrm{RMS}}$ is achieved with the linear equivalent damper in the entire speed range considered, while the bilinear damper with ζ_c=0.1 yields largest camber variation. The $(\phi)_{\mathrm{RMS}}$ responses of the kineto-dynamic model approach peak values in the 100-120 km/h range, for all the dampers considered, as observed in the $(RD)_{\mathrm{RMS}}$ responses. The results in Figs. 4.12 (b) and 4.13 (a) show similar trends in $(RD)_{\mathrm{RMS}}$ responses and camber variations, as it would be expected. The relative differences in the two measures depend upon the type of damping considered and the forward speed. This difference is evaluated by considering ratio of $(\phi)_{\mathrm{RMS}}$ to $(RD)_{\mathrm{RMS}}$ at a forward speed, normalized with the ratio at 30 km/h, termed as the *camber increment ratio* (*CIR*), such that:

$$Camber\ increment\ ratio\left(CIR\right)=\frac{\left((\phi)_{RMS}\right)_V/\left((\phi)_{RMS}\right)_{30}}{\left((RD)_{RMS}\right)_V/\left((RD)_{RMS}\right)_{30}} \tag{4.9}$$

where the subscript '*V*' refers to the velocity considered, and $((\phi)_{\mathrm{RMS}})_{30}$ and $((RD)_{\mathrm{RMS}})_{30}$ are the normalizing values at 30 km/h. Figure 4.13 (b) compares the *CIR* response of the model with different dampers in the velocity range 30 to 120 km/h. At lower velocities (<50 km/h), the *CIR* varies only about 1% for all the dampers considered, suggesting that the camber variation is directly related to the suspension deflection. The *CIR* response, however, is greatly influenced by the damping at speeds above 50 km/h. While the linear damper yields lowest *CIR*, the bilinear damper with ζ_c=0.1 yields largest camber increment ratio. The results suggest that the camber angle variation is disproportional to the suspension deflection, particularly for asymmetric damper with ζ_c=0.1.

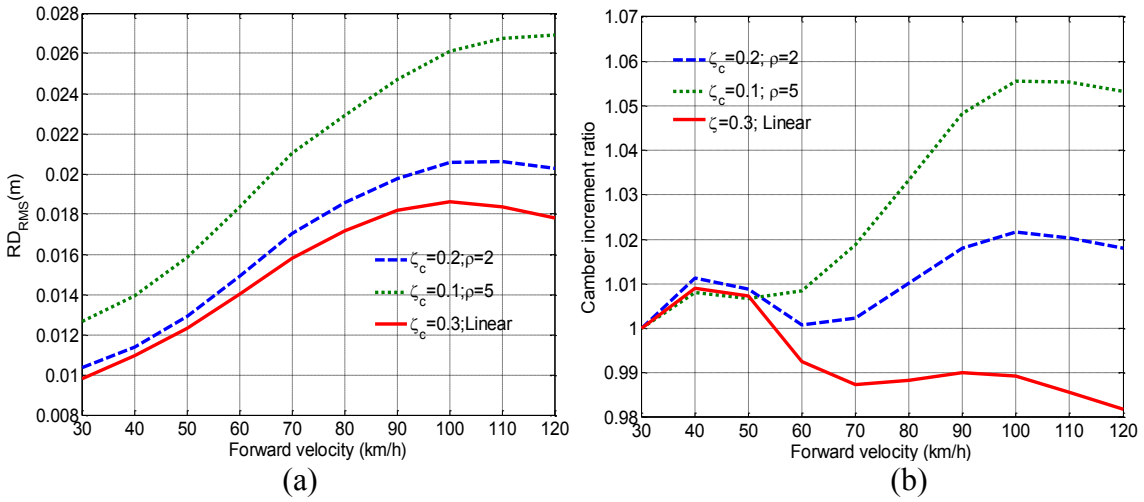

Figure 4.13: Comparisons of (a) rms camber angle variation and (b) camber increment ratio responses of the kineto-dynamic model with bilinear dampers (ζ_c=0.2, ρ=2; ζ_c=0.1, ρ=5) and an equivalent linear damper (ζ=0.3) to random road excitations as a function of forward speed.

Figure 4.14 (a) compares the time-histories of camber variations of the model with linear and bilinear damping (ζ_c=0.1) under the random road excitation at 100 km/h. The bilinear damper yields significantly larger negative peaks, while the linear damper consistently exhibits higher positive camber angle. The magnitudes of positive camber variations of the asymmetric damper, however, are considerably smaller than those in the negative camber. This is attributable to the suspension geometry, which is generally synthesized to achieve a compromise between variations in the roll and bump camber angles [4]. The asymmetric camber variation during upward and downward wheel motions has been shown in Fig. 2.11, and also been widely reported in different kinematic responses [4, 5]. This is also evident in the cumulative probability distribution of the absolute camber angle responses of the model with the three selected dampers in Fig. 4.14 (b). The comparisons show that the linear, and bilinear (ζ_c=0.2 and 0.1) dampers exhibit camber angles of 0.77°, 1.01° and 1.39°, respectively, corresponding to the 95% probability.

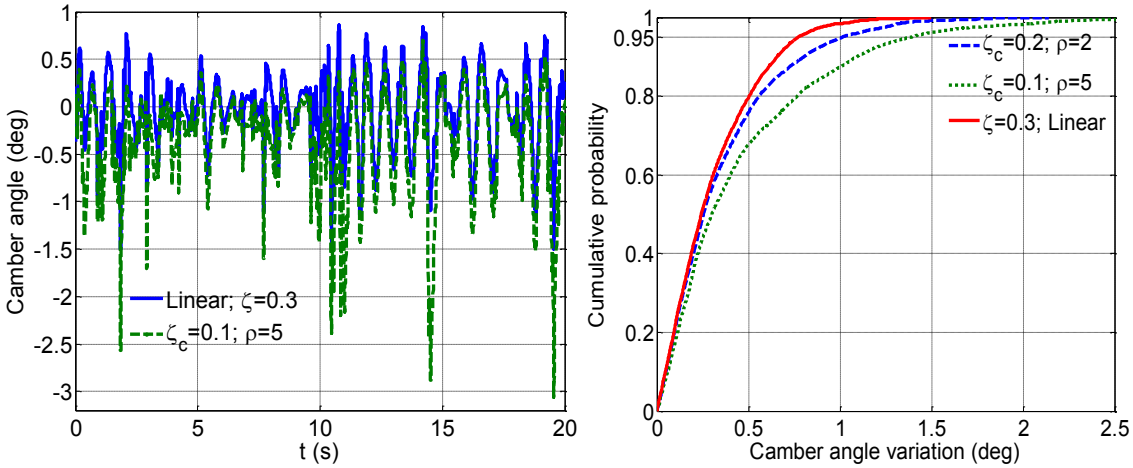

Figure 4.14: Comparison of: (a) time histories of camber variations; and (b) cumulative probability disribution of absolute camber angle of the model with linear and asymmetric bilinear dampers under random road input (speed =100 km/h).

The results clearly show that the damper with ζ_c= 0.1 and greater asymmetry (ρ=5) would yield significantly higher camber angle response, which would also vary with vehicle speed. Although conventional ride dynamic studies ignore possible contributions due to camber variations, it has been suggested that a camber variation in the order of 1^0 would yield a lateral force variation of 80 N for an automobile tire [1, 4]. The suspension damper synthesis thus needs to consider the kinematic responses of the suspension.

The results in Figs. 4.11 to 4.13 suggest that the measures of ride comfort, road holding and suspension deflection performances of a vehicle are complex functions of the vehicle speed. The variations in ride comfort, rattle space and camber measures ($(\ddot{z}_s)_{RMS}$, $(RD)_{\mathrm{RMS}}$ and $(\phi)_{\mathrm{RMS}}$) with speed could be classified in three different zones. All the three measures increase nearly linearly with the vehicle speed up to 50-60 km/h, irrespective of the type of damping considered (Figs. 4 to 6). Further increase in vehicle speed causes nonlinear increases in the responses, which tend to either saturate or decrease at speeds

above 90-100 km/h. These trends, however, could not be generalized to the road holding measures (*DLC* and wheel lift-off).

4.6.3 Influences of Two-stage Asymmetric Damper under Random Excitations

The kinematic and dynamic responses of the kineto-dynamic model are also dependent upon the high speed damping reduction factors and the saturation velocities, apart from the damping asymmetry. The influences of these parameters are evaluated by considering a two-stage asymmetric damper (ζ_c=0.2, ρ=2, λ_r=0.25, λ_c=0.5, α_r= 0.1 m/s and α_c= -0.2 m/s) that has shown to yield a good compromise among the ride, road holding and suspension deflection performance measures under bump and pothole inputs in section 4.5. The low-speed damping coefficients of the selected two-stage damper (ζ_c=0.2 and ρ=2) are identical to those of one of the bilinear damper considered in the section 4.5.2, while the selected damper would yield lower effective damping due to the lower high speed damping (λ_r, λ_c<1). The kinematic and dynamic responses of the model evaluated under the random road excitation in the 30 to 120 km/h forward speed range are summarized in Table 4.7.

The two-stage damper yields considerably lower magnitudes of $(\ddot{z}_s)_{RMS}$ compared to the single-stage bilinear damper in the entire speed range, which is attributable to its lower high speed damping and damping force saturation. The $(\ddot{z}_s)_{RMS}$ value approaches a peak of 1.94 m/s^2 at 100 km/h and decreases with further increase in the vehicle speed. This trend was not observed in case of the linear or bilinear damper, although the rate of increase diminished above 100 km/h. (Fig. 4.11). The reduced high-speed damping, however, causes relatively higher magnitudes of *DLC*, wheel lift-off (*WLO*), $(RD)_{\mathrm{RMS}}$ and

$(\phi)_{RMS}$ responses. Both the *DLC* and *WLO* measures increase with the speed, while the rate increases in *WLO* is higher at higher speeds, as observed for the bilinear damper (Fig. 4.12). The $(RD)_{RMS}$ and $(\phi)_{RMS}$ responses of the model with two-stage asymmetric damper reach their respective peak values near 100 km/h similar to that observed in the case of acceleration. The variations in *DLC* and $(RD)_{RMS}$ show similar tendency at lower speeds, but differ at higher speeds. The camber increment ratio of the two-stage damper was estimated to be 1.02 at 100 km/h, which is nearly same as that of the bilinear damper (Fig. 4.13). This result further suggests nonlinear relation between the camber variation and the suspension deflection. Moreover, the absolute camber angle corresponding to 0.95 cumulative probability at 100 km/h was computed as 1.14^0, which is considerably greater than that of the bilinear damper with ζ_c=0.2 (Fig. 4.14).

Table 4. 7: Kinematic and dynamic responses of the kineto-dynamic model with two-stage asymmetric damping.

Velocity (km/h)	$\ddot{z}_{sRMS}$ (m/s^2)	*DLC*	*WLO*	$(RD)_{RMS}$ (m)	$(\phi)_{RMS}$ (Deg)
30	0.97	0.138	0.03	0.012	0.26
40	1.09	0.168	0.04	0.013	0.30
50	1.23	0.194	0.14	0.015	0.34
60	1.42	0.226	0.28	0.018	0.40
70	1.62	0.253	0.33	0.021	0.47
80	1.72	0.268	0.44	0.023	0.51
90	1.83	0.287	0.65	0.025	0.54
100	1.94	0.309	0.85	0.026	0.57
110	1.88	0.323	1.08	0.024	0.53
120	1.80	0.333	1.30	0.022	0.48

4.7 Optimal Synthesis of Two-stage Asymmetric Damper under Random Inputs

The ride dynamic responses of the vehicle model are strongly influenced by various suspension kinematic and dynamic properties, and damper asymmetry, apart from the road roughness and the speed, in a complex manner. Synthesis of an optimal damper is thus a formidable task, particularly when multi-stage asymmetric damping properties are considered. The few studies that have attempted to identify optimal damping parameters have generally concluded that the optimal parameters would depend upon the forward velocity, design criteria or the target performance chosen and the type and magnitude of excitation such as the road roughness and profiles of the bump/pothole inputs [91, 92, 94, 126]. Although various studies have included combinations of sprung mass acceleration, suspension deflection or working space and tire force response measures in identification of optimal parameters, the kinematic responses have invariably been ignored. This is partly attributable to the use of ride dynamic models that do not permit the analyses of kinematic response, and in-part due to the assumption that suspension kinematics play only limited role in ride dynamics. The results presented in Figs. 4.11 to 4.13, and Table 4.7, however, suggest strong coupling between the kinematic and dynamic responses, and important contributions of the suspension kinematics.

4.7.1 Formulation of Performance Index and Optimization Methodology

Optimal asymmetric damper parameters are sought to achieve acceptable compromise in ride, road holding and camber variation characteristics through minimization of an objective function, $F(v)$, of sprung mass acceleration and tire force as:

$$F(\upsilon) = w\sum_{V_1}^{V_2}\frac{F_1(\upsilon)}{F_{1-nom}} + (1-w)\sum_{V_1}^{V_2}\frac{F_2(\upsilon)}{F_{2-nom}} \tag{4.10}$$

where $F_1(\upsilon)$ and $F_2(\upsilon)$ are rms acceleration and tire force or road holding measure, respectively, given by:

$$F_1(\upsilon) = \sqrt{\frac{1}{T}\int_0^T \ddot{z}_s^2 dt}\,; \text{ and } F_2(\upsilon) = \frac{1}{F_{t-s}}\sqrt{\frac{1}{T}\int_0^T F_{t-d}^2 dt} \tag{4.11}$$

where $F_{t\text{-}s}$ and $F_{t\text{-}d}$ are the static and dynamic tire forces and υ is the design vector, $\upsilon=\{\zeta_c, \rho, \lambda_r, \lambda_c, \alpha_r, \alpha_c\}$. In Eq (4.10), w is the weighting factor, and F_{1-nom} and $F_{2\text{-}nom}$ are the magnitudes of $F_1(\upsilon)$ and $F_2(\upsilon)$ evaluated with nominal damper parameters corresponding to each speed. Owing to the strong dependence of optimal damper parameters on the vehicle forward velocity, as concluded in the reported studies, the weighted optimization function in Eq (4.10) is formulated considering the performance measures at different speeds, where V_1 and V_2 define the lower and upper bounds. In the optimization problem, the camber variation is limited by imposing a limit constraint such that: $\phi<\beta$, where β is the maximum allowable absolute camber angle corresponding to cumulative probability of 0.95, which is computed during each iteration in the solution of the minimization problem at the higher speed of 100 km/h only. Furthermore, the limiting value β was varied in the 1 to 1.2° of camber range (1.14° attained with the nominal damper at 100km/h) so as to study the influence of β on the attained solutions.

The above optimization problem was solved using a gradient-based sequential quadratic programming (SQP) algorithm available in the Matlab optimization toolbox [151], while velocity bounds V_1 and V_2 were taken as 50 and 100 km/h, respectively, with an increment of 25 km/h. These velocity bounds are selected considering that they

represent the three zones of the sprung mass acceleration and camber angle relations with vehicle velocity (Figs. 4.11 to 4.13) identified in the section 4.6. Limit constraints were defined so as to achieve the solutions in the feasible ranges, namely: $0.05 \leq \zeta_c \leq 0.35$; $1 \leq \rho \leq 6$; $0.25 \leq \lambda_r \leq 1$; $0.25 \leq \lambda_c \leq 1$; $0.1 \leq \alpha_r \leq 0.4$; and $0.1 \leq |\alpha_c| \leq 0.4$.

4.7.2 Results and Discussion

Considering the strong coupling among the design variables of the asymmetric damper, the optimal solutions were initially examined to identify an acceptable value of low-speed compression mode damping ratio ζ_c in view of the ride comfort alone. For this purpose, the initial solutions were obtained by letting w=1, and relaxing the upper limit on the camber variation (β) to a very high value of 5° in order to emphasize the sprung mass acceleration alone. Multiple solutions, as would be expected, were obtained with different initial design vectors, particularly for different values of ρ. The solutions, however, generally converged near ζ_c=0.20 for the rough road and range of speed considered, while the high- speed reduction factors in both compression and rebound approached the respective lower bounds. The other design parameters (ρ, α_r and α_c) converged closer to their nominal values. The optimal parameters resulted in rms sprung mass acceleration magnitudes of 1.18, 1.62 and 1.85 m/s^2 corresponding to 50, 75 and 100 km/h forward speeds, which are lower than those attained with the nominal damper (Table 4.7). The identified value of low-speed compression damping ratio was thus considered acceptable for seeking optimal solutions to achieve design compromise among the measures considered. An equality constraint, ζ_c=0.2, was thus subsequently imposed that resulted in slightly reduced design vector, v={ρ, λ_r, λ_c, α_r, α_c}. Moreover, the

more significant design variables (ρ, λ_r, λ_c), being directly related to the non-dimensional ζ_c, would enhance the applicability of the optimal solutions for a wider range of vehicles.

The minimization problem in Eq (4.11) was subsequently solved using three different weighting values (w=0.5, 0.6 and 0.7) and three different limiting values of camber variation (β=1°, 1.1° and 1.2°). The solutions were obtained with nominal values as the initial design vector, although several solutions were sought with different initial design vectors so as to attain the solutions corresponding to minima of the objective function. Moreover, the limit constraints on the design variables were defined as explained previously. The solutions of the minimization problem attained are presented in Table 4.8, while the corresponding responses of the model including $\ddot{z}_{s\text{RMS}}$, DLC, $(\phi)_{\text{RMS}}$ and $(RD)_{\text{RMS}}$ are presented in Figs. 4.15 to 4.18 as a function of the camber limit β. The responses presented in these figures were attained under the random road excitation at different forward speeds (30, 50, 80 and 100 km/h).

The results in Table 4.8 suggest that the solutions are highly influenced by the chosen values of the weighting factor and camber variation limit, β. For w=0.5, relaxing the camber limit β yields lower values of the asymmetry ratio ρ, and the high-speed reduction factor λ_c and saturation limit α_c in compression but higher high-speed rebound reduction ratio λ_r and saturation limit α_r. Limiting the absolute camber variation to 1°, converges to higher damping forces in both compression and rebound modes. Relaxing β to 1.2°, however, converges to lower compression mode damping. This suggests that damper synthesis for minimal camber variation involves compromise in the sprung mass vertical acceleration.

The solutions attained with slightly higher emphasis given to the ride comfort measure (w=0.6 and 0.7) revealed somewhat, opposing trend in ρ with increasing values of β. An increase in β resulted in convergence towards lower λ_r and λ_c, while a definite trend could

Table 4.8: Solutions of the minimization problem with different weighting factors (w) and camber variation limits (β).

w	β	ρ	λ_r	λ_c	α_r (m/s)	α_c (m/s)
0.5	1	2.22	0.35	0.78	0.20	-0.40
	1.1	1.83	0.43	0.68	0.34	-0.35
	1.2	1.70	0.51	0.63	0.35	-0.25
0.6	1	1.68	0.49	0.92	0.30	-0.10
	1.1	1.97	0.30	0.50	0.28	-0.20
	1.2	1.93	0.25	0.45	0.31	-0.24
0.7	1	1.46	0.32	0.67	0.33	-0.37
	1.1	2.00	0.25	0.36	0.21	-0.24
	1.2	1.95	0.25	0.39	0.27	-0.22

not be observed in α_r although the changes are quite small. A lower value of α_c was obtained with relatively higher value of λ_c for w=0.6. The higher weighting on ride comfort (w=0.7) resulted in lower λ_c but higher α_c, most likely leading to comparable effective damping in compression. Reducing the camber variation limit (β=1°) converged towards higher compression mode effective damping, while relaxing the limit β allows the compression mode damping to be lower, which also places a greater demand on the high-speed compression damping. The results thus suggest that a relatively smaller emphasis on the ride comfort would converge to lower low-speed rebound damping as the camber variation is relaxed. A slightly larger emphasis on the ride comfort, however, would generally require higher low-speed rebound damping with increasing β value.

The results in Table 4.8 do not show definite relationships among the various parameters particularly when different weightings and camber limits are considered. This is mostly attributable to strong coupling among various factors in view of the effective

damping. For instance, an effective rebound to compression damping asymmetry could be achieved with different combinations of the low- and high- speed damping characteristics. In this study, the solutions to the minimization problem were also attempted for $\beta<1°$ in order to investigate the possibility of attaining further reduction in the camber angle variations. The solutions, however, failed to converge due to the constraints posed on the compression mode damping (ζ_c=0.2 and $0.25\leq\lambda_c\leq1$). The camber variations could be further reduced by increasing the compression damping (Fig. 4.13 (b)), which would also yield higher rebound damping considering the relations shown in Fig. 4.11 (b).

The sprung mass acceleration response ($\ddot{z}_{sRMS}$), in general, tends to decrease with increase in the weighting factor w at each speed, as seen in Fig. 4.15. Increase in β from 1 to 1.1° causes decrease in the sprung mass acceleration response, irrespective of the weighting factor and the forward speeds, while a further increase in β to 1.2° causes the sprung mass acceleration to decrease only when w=0.5. A higher weighting on the ride comfort (w=0.6 or 0.7) results in increase in the sprung mass acceleration response, particularly at lower speeds of 30 and 50 km/h. The results suggest that increasing w can yield lower sprung mass acceleration response, while relaxing the camber limit beyond a certain value deteriorates the ride comfort measure. The results further suggest that for each value of w there might exist a minimal value of sprung mass acceleration that can be achieved with different β values. The value of β corresponding to this minimal acceleration tends to become smaller as w increases. Such minimal values of acceleration with different constraints on suspension deflection had also been identified by Dahlberg

[94], while synthesizing optimal linear damper under random excitation at a single forward velocity.

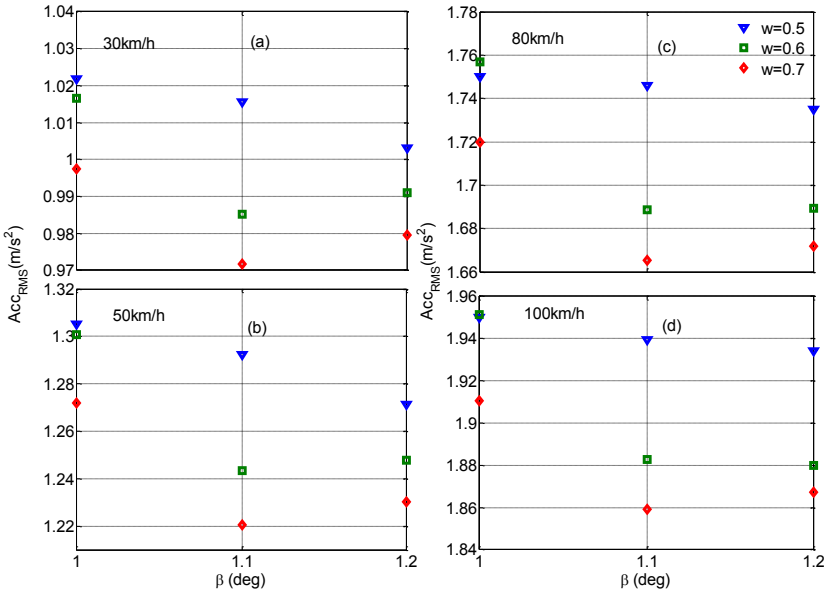

Figure 4.15: Sprung mass rms acceleration responses of the model with optimal damper parameters attained for different weighting factors (w) and camber variation limits (β) under random road input at: (a) 30 km/h; (b) 50 km/h; (c) 80 km/h and (d) 100 km/h.

Unlike the sprung mass acceleration, the *DLC* due to tire force increases with an increase in the weighting factor w and the camber limit β in the forward speed range considered (Fig. 4.16). Lowering the value of w reduces the *DLC* response of the model, as it would be expected, which suggests that solutions corresponding to w=0.5 would yield better road holding properties. It can also be observed from the figure that the 0.5 weighting yields nearly identical *DLC* responses for camber limits of 1 and 1.1°, irrespective of the speed. Furthermore, the weighting of 0.5 and 0.6 yield nearly identical *DLC* values with β=1°, at each of the speeds considered. The results further suggest that the *DLC* is relatively less sensitive to β when a lesser emphasis is placed on the ride comfort measure (w=0.5). The limit imposed on the camber variation, however, plays a significant role with greater emphasis on the ride comfort (w=0.6 and 0.7). Opposite to

the sprung mass acceleration (Fig. 4.15), the *DLC* response tends to approach its maximum at β=1.1° with w=0.7.

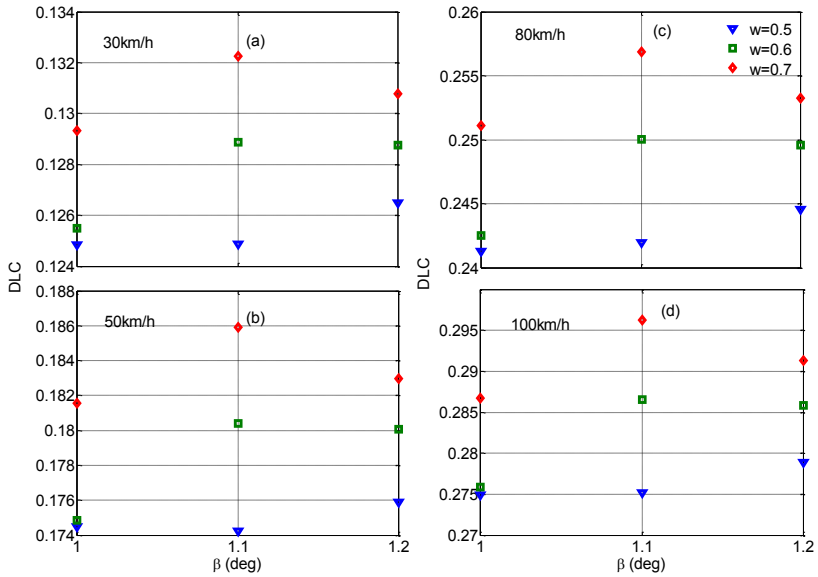

Figure 4.16: The *DLC* responses of the model with optimal damper parameters attained for different weighting factors (w) and camber variation limits (β) under random inputs at: (a) 30 km/h; (b) 50 km/h; (c) 80 km/h and (d) 100 km/h.

The relative displacement $(RD)_{RMS}$ responses of the kineto-dynamic model with optimal damper parameters (Fig. 4.17) increase with an increase in the weighting factor w and the camber limit β with a trend somewhat comparable to that observed in the *DLC* responses (Fig. 4.16). The results show that the $(RD)_{RMS}$ responses approach maximum values with β in the order of 1.1, for a higher weighting on the ride comfort (w=0.6 and 0.7). The optimal solutions with higher weighting yield lower $(RD)_{RMS}$ with further relaxation of the camber limit in the speed range considered. It can further be seen from the figure that unlike the *DLC* responses, the $(RD)_{RMS}$ is sensitive to the camber limit β. The trends in the $(RD)_{RMS}$ corresponding to β=1.1 and 1.2°, however, differ notably from those in the $(\phi)_{RMS}$ shown in Fig. 4.18 for w=0.6 and 0.7 irrespective of the vehicle speed. The solutions attained with lower limiting values of β yield lower rms camber angle

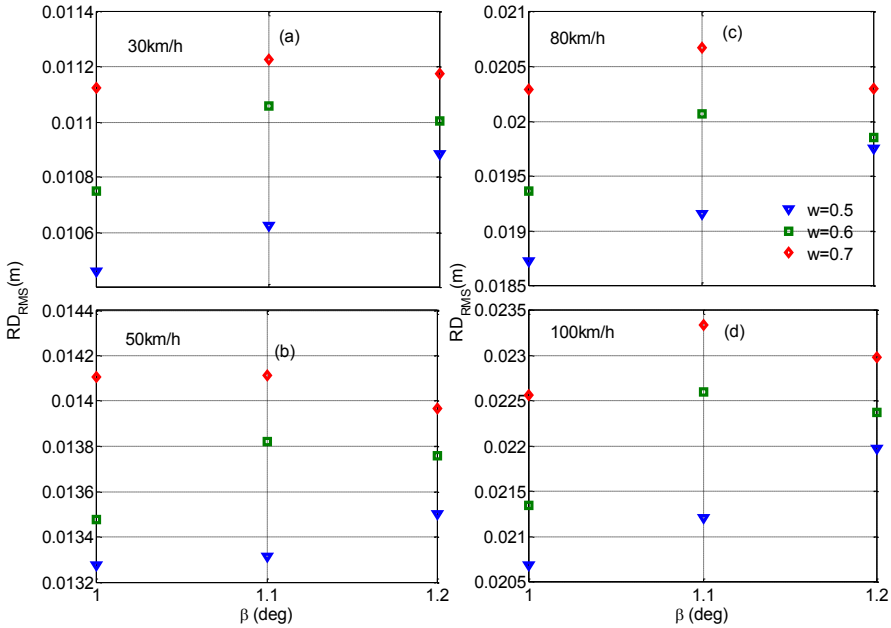

Figure 4.17: The RD_{RMS} responses of the model with optimal damper parameters attained for different weighting factors (w) and camber variation limits (β) under random inputs at: (a) 30 km/h; (b) 50 km/h; (c) 80 km/h and (d) 100 km/h.

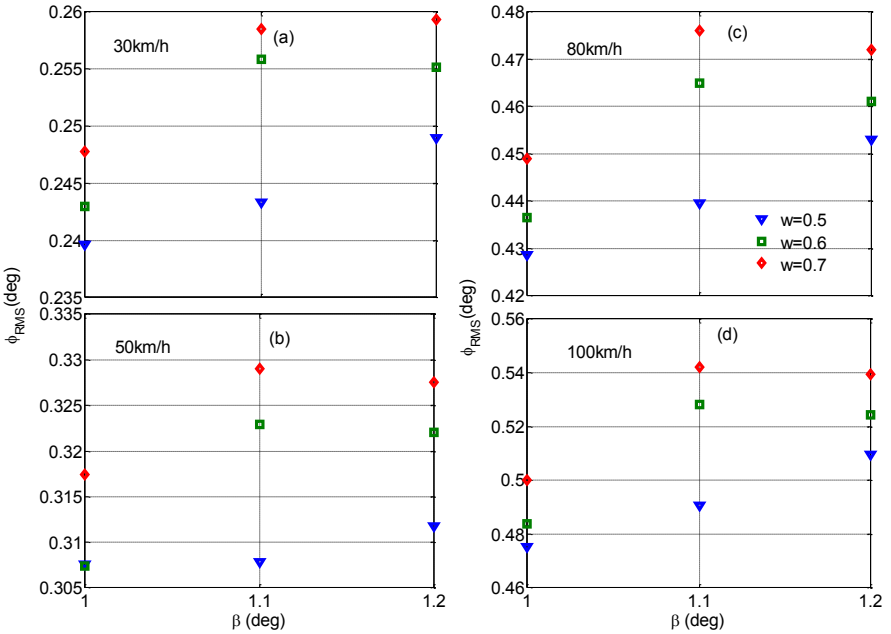

Figure 4.18: The rms camber angle responses of the model with optimal damper parameters attained for different weighting factors (w) and camber variation limits (β) under random inputs at: (a) 30 km/h; (b) 50 km/h; (c) 80 km/h and (d) 100 km/h.

variations, as expected, particularly for w=0.5. The $(\phi)_{RMS}$ responses of the model with β=1° are considerably smaller than those attained with β=1.1°, while the differences in

the $(\phi)_{RMS}$ responses corresponding to β=1.1° and 1.2° are mostly negligible for w=0.6 and 0.7. At vehicle speed exceeding 50 km/h, the rms camber response increases as β increases from 1° to 1.1°, irrespective of the weighting factor.

4.8 Summary

This chapter presented coupled effects of damper asymmetry and the suspension kinematics on the dynamic and kinematic responses of a kineto-dynamic quarter car model comprising a double wishbone suspension coupled with single- and two-stage asymmetric dampers. It has been shown that both the suspension linkages and compression/rebound damping asymmetry contribute to asymmetry in kinematic as well as dynamic responses of the road vehicle. Higher rebound to compression damping asymmetry in general causes a downward shift in the sprung mass mean position, while higher compression to rebound asymmetry ratio causes an upward shift. The mean shift in the unsprung mass displacement relative to the sprung mass causes additional camber angle variation during the wheel vertical motions.

The damping asymmetry of a bilinear damper yields conflicting effects on the sprung mass acceleration response to bump and pothole excitations. A higher rebound to compression damping asymmetry ratio in a bilinear damper helps reduce the magnitude of the first peak in sprung mass acceleration response to bump excitation, but yields higher acceleration under a pothole excitation. In case of two-stage damper with different low and high-speed damping coefficients, lower values of the high-velocity damping coefficients results in considerable reductions in the sprung mass acceleration response under both the inputs. The results suggest that the damping asymmetry ratio is strongly

dependent upon the low-speed compression damping. Under a bump input, asymmetry ratio of 2 and 3 would result in a good compromise between the ride and road holding performance for low- speed compression mode damping ratios of 0.2 and 0.1, respectively. Under a pothole input, however, a linear (asymmetry ratio=1) or higher compression to rebound ratio provide a better design compromise. The results attained through minimization of the sprung mass acceleration with constrained rattle space provided design guidance for the asymmetric dampers under both the bump and pothole excitations.

The simulation results under random road excitation showed that the kinematic and dynamic responses are strongly influenced by the compression/rebound damping asymmetry and the forward speed of the vehicle. This study identified notable consistent trends in the kinematic and dynamic responses of the model with asymmetric damper in three speed ranges: the responses increasing nearly linearly with forward speed in the 30-60 km/h range; increasing nonlinearly in the medium speed range (60-90 km/h); and nonlinearly decreasing or saturating in the higher speed range (100-120 km/h). It is shown that a synthesis of an optimal asymmetric damper is highly complex due to strong coupling among the various damper parameters, namely, the rebound to compression damping asymmetry, high speed damping reduction factors and saturation velocities. The results attained through minimization of a weighted dynamic tire force and ride comfort measure suggest that a compromise solution would strongly depend upon the limit imposed on the camber variation. For minimal camber angle variations, a lower rebound to compression asymmetry in damping would be desirable, while the camber variations

correlate well with the tire force variations, when a greater emphasis is placed on the tire force variations.

The results presented in this chapter are attained considering the vertical dynamic responses of a quarter-car model, while, the consideration of dynamic responses of the vehicle motions in other modes including roll and pitch can further increase the complexity of the design compromises. The camber angle variation response of a suspension during chassis roll is known to be significantly different than that during wheel vertical motion excitations. Similarly, the asymmetry in the dynamic responses could be different, particularly in roll motion mode of the chassis when asymmetric dampers are considered on both sides of the suspension, where one of the strut experiences compression when the other strut undergoes extension. A kineto-dynamic roll-plane vehicle model is therefore necessary for the coupled analyses of kinematic and dynamic responses of the suspension, and for the synthesis of suspension components.

CHAPTER 5

ROLL-PLANE KINETO-DYNAMIC ANALYSES OF DOUBLE WISHBONE SUSPENSION

5.1 Introduction

The ride and roll dynamic performance measures of a vehicle are known to impose conflicting design requirements on the suspension components [2,105]. Soft suspensions are most desirable for enhancing ride comfort, but yield reduced effective roll stiffness, and greater load transfer and roll response of the chassis. Apart from the conflicting dynamic measures, the suspension kinematic measures also impose conflicting demands on suspension geometry synthesis under chassis roll and wheel vertical motions [4]. In particular, minimal variations in the wheel camber under wheel vertical displacement motion (bump camber) and under chassis roll (roll camber) involve conflicting suspension synthesis. The variations in camber and toe angles, and wheel track width responses have been widely investigated under wheel displacement, with fixed chassis or under chassis roll motion in the absence of wheel vertical motion [5, 24]. The effects of both inputs, applied simultaneously, have not been adequately addressed. An optimal suspension synthesis that can yield acceptable compromise among various kinematic performance measures has been recognized to be a challenging task [4, 24]. Furthermore, the larger space requirements of hybrid vehicles necessitate considerations of the suspension synthesis with limited lateral space, which would most likely involve additional compromises among the kinematic and dynamic responses.

From the results attained from the two-DOF kineto-dynamic model in Chapter 4, it was shown that kinematic and dynamic properties of the suspension are also coupled with

the suspension damping asymmetry in a complex manner. The complex dependency of damper asymmetry on the dynamic and kinematic responses would be expected to increase many folds, when coupled vertical and roll motions of chassis are considered. In this chapter, a roll-plane kineto-dynamic vehicle model is formulated to study coupled vertical and roll dynamic responses together with the kinematic properties. The displacement matrix method is employed to derive kinematic formulations, while the Lagrange's method is used to formulate the dynamic model. The conflicting kinematic responses including bump/roll camber and wheel track variations under chassis roll and wheel vertical motions are identified, and the roles of joint coordinates are evaluated. An optimal joints coordinate synthesis considering these conflicting responses together with the constraint on the lateral space is derived. The dynamic responses of the proposed kineto-dynamic model are compared with those of a conventional roll-plane model under idealized bump and pothole inputs. The dynamic and kinematic responses of the model with nominal joint coordinates are further compared with those of model with optimal joint coordinates to illustrate the effectiveness of the optimal synthesis. The influences of damper asymmetry are further evaluated under both bump and pothole excitations.

5.2 Development of Roll-plane Kineto-dynamic Vehicle Model

The two-DOF kineto-dynamic model of double wishbone suspension formulated in Chapter 3 could be extended to the roll-plane vehicle model, as shown in Fig. 5.1. The four-DOF half-car kineto-dynamic model comprises planar representation of the double wishbone type of suspension, as discussed in Chapter 3. The control arms are modeled as mass less elements, and each unsprung mass is assumed to be lumped at the center of gravity (*cg*) of the wheel assembly. For the kineto-dynamic analysis, the tire is modeled

as a combination of a vertical linear spring and a viscous damper, while the lateral compliance of the tire is represented by a lateral linear stiffness, as in the case of the two-DOF model. The chassis and suspension kinematics are formulated considering the chassis, suspension linkages and the wheel spindle as rigid bodies, while the rigid body assumption was also applied to tire when kinematic analyses alone were concerned. The model is formulated assuming vertical (z_s) and roll (ϕ_s) displacements of the sprung mass, and left and right wheels vertical displacements (z_{uL} and z_{uR}) as the generalized coordinates. The rotation of the chassis is assumed to occur about the roll center, *Rc* [153, 154], as shown in the Fig.5.1.

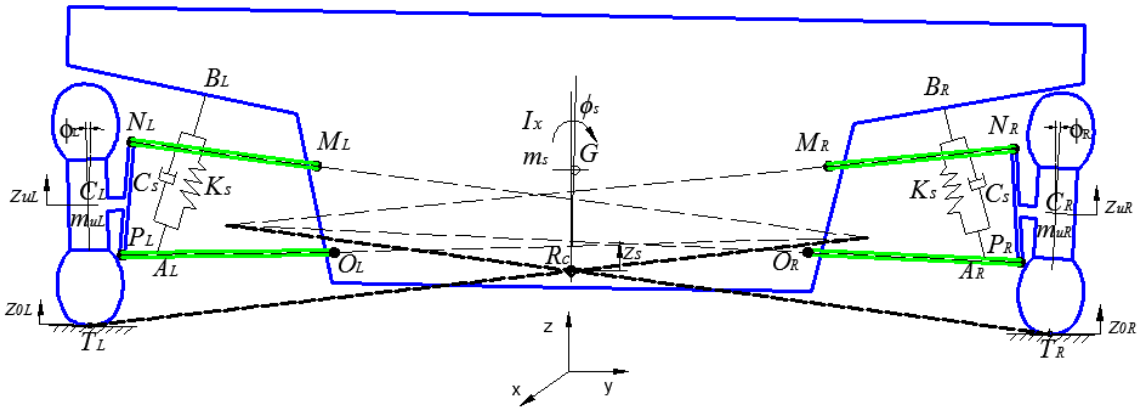

Figure 5.1: Roll-plane kineto-dynamic model of a vehicle with double wishbone type of suspension

5.2.1 Kinematics of the Chassis

A chassis kinematic model is formulated in order to evaluate instantaneous positions of suspension joints on the chassis under chassis rotation and/or vertical motions. The suspension kinematic responses are subsequently determined from coordinates of the linkage joints. A fixed coordinate system is considered with its origin located in the ground, while the sprung mass vertical and rotational displacements are considered about the roll center, *Rc*, of the vehicle body. The initial (Rc_{y0}, Rc_{z0}) and instantaneous (Rc_y,

Rc_z) coordinates of the roll center are related through the displacement matrix, $D_{chassis}$, under a finite displacement of the chassis, given by [138]:

$$D_{chassis}=\begin{bmatrix} a_{22} & a_{23} & Rc_y-(a_{23}Rc_{y0}+a_{23}Rc_{z0}) \\ a_{32} & a_{33} & Rc_z-(a_{32}Rc_{y0}+a_{33}Rc_{z0}) \\ 0 & 0 & 1 \end{bmatrix} \tag{5.1}$$

where a_{22}=a_{33}=cosϕ_s and a_{23}=-a_{32}=sinϕ_s, with ϕ_s being the vehicle body rotation about the roll center. The y- and z- coordinates of chassis-suspension joints, M_R, O_R, M_L and O_L, shown in the Fig. 5.1, can be determined using the displacement matrix $D_{chassis}$, such that:

$$\begin{bmatrix} M_{Ry} & O_{Ry} & M_{Ly} & O_{Ly} \\ M_{Rz} & O_{Rz} & M_{Lz} & O_{Lz} \\ 1 & 1 & 1 & 1 \end{bmatrix} = D_{chassis} \begin{bmatrix} M_{Ry0} & O_{Ry0} & M_{Ly0} & O_{Ly0} \\ M_{Rz0} & O_{Rz0} & M_{Lz0} & O_{Lz0} \\ 1 & 1 & 1 & 1 \end{bmatrix} \tag{5.2}$$

The leading subscripts 'R' and 'L' in Eq (5.2) refer to the right and left suspension joints, respectively, while the second subscripts 'y' and 'z' represent the lateral and vertical axes, respectively. The final subscript '0' refers to the initial coordinate of the joint.

The expansion of the Eq (5.2) yields expressions for the instantaneous coordinates of the suspension joints at the chassis, such that:

$$\begin{aligned} M_{ky} &= a_{22}(M_{ky0}-Rc_{y0})+a_{23}(M_{kz0}-Rc_{z0})+Rc_y \\ M_{kz} &= a_{32}(M_{ky0}-Rc_{y0})+a_{33}(M_{kz0}-Rc_{z0})+Rc_z \\ O_{ky} &= a_{22}(O_{ky0}-Rc_{y0})+a_{23}(O_{kz0}-Rc_{z0})+Rc_y \\ O_{kz} &= a_{32}(O_{ky0}-Rc_{y0})+a_{33}(O_{kz0}-Rc_{z0})+Rc_z \qquad k=R,L \\ G_y &= G_{y0};\ \text{and}\ G_z = G_{z0}+z_s \end{aligned} \tag{5.3}$$

The above equation can be solved to obtain instantaneous coordinates of the chassis-linkage joints for a given chassis rotation ϕ_s about the roll center and/or a vertical displacement of the chassis, z_s.

The velocities of various chassis joints are obtained from the time derivatives of the displacement equations, such that:

$$\begin{aligned}
\dot{M}_{ky} &= \dot{a}_{22}(M_{ky0} - Rc_{y0}) + \dot{a}_{23}(M_{kz0} - Rc_{z0}) \\
\dot{M}_{kz} &= \dot{a}_{32}(M_{ky0} - Rc_{y0}) + \dot{a}_{33}(M_{kz0} - Rc_{z0}) + \dot{R}c_z \\
\dot{O}_{ky} &= \dot{a}_{22}(O_{ky0} - Rc_{y0}) + \dot{a}_{23}(O_{kz0} - Rc_{z0}) \\
\dot{O}_{kz} &= \dot{a}_{32}(O_{ky0} - Rc_{y0}) + \dot{a}_{33}(O_{kz0} - Rc_{z0}) + \dot{R}c_z \qquad k = R, L
\end{aligned} \tag{5.4}$$

where $\dot{R}c_z = \dot{z}_s$, $\dot{a}_{22} = \dot{a}_{33} = -\dot{\phi}_s \sin\phi_s$, and $\dot{a}_{23} = -\dot{a}_{32} = \dot{\phi}_s \cos\phi_s$. Differentiating the velocity expressions with respect to time yields following acceleration expression in joint coordinates:

$$\begin{aligned}
\ddot{M}_{ky} &= -\left(\ddot{\phi}_s \sin\phi_s + \dot{\phi}_s^2 \cos\phi_s\right)(M_{ky0} - Rc_{y0}) + \left(\ddot{\phi}_s \cos\phi_s - \dot{\phi}_s^2 \sin\phi_s\right)(M_{kz0} - Rc_{z0}) \\
\ddot{M}_{kz} &= -\left(\ddot{\phi}_s \cos\phi_s - \dot{\phi}_s^2 \sin\phi_s\right)(M_{ky0} - Rc_{y0}) - \left(\ddot{\phi}_s \sin\phi_s + \dot{\phi}_s^2 \cos\phi_s\right)(M_{kz0} - Rc_{z0}) + \ddot{z}_s \\
\ddot{O}_{ky} &= -\left(\ddot{\phi}_s \sin\phi_s + \dot{\phi}_s^2 \cos\phi_s\right)(O_{ky0} - Rc_{y0}) + \left(\ddot{\phi}_s \cos\phi_s - \dot{\phi}_s^2 \sin\phi_s\right)(O_{kz0} - Rc_{z0}) \\
\ddot{O}_{kz} &= -\left(\ddot{\phi}_s \cos\phi_s - \dot{\phi}_s^2 \sin\phi_s\right)(O_{ky0} - Rc_{y0}) - \left(\ddot{\phi}_s \sin\phi_s + \dot{\phi}_s^2 \cos\phi_s\right)(O_{kz0} - Rc_{z0}) + \ddot{z}_s
\end{aligned} \tag{5.5}$$

5.2.2 Kinematics of the Suspension Linkages

The kinematic analysis of the suspension links is performed to determine variations in the camber angles and wheel track width in terms of the generalized coordinates. For finite displacements of the right and left wheel spindles in the given plane, the displacement matrices, $D_{spindleR}$ and $D_{spindleL}$, of the right and left suspension units, respectively, are formulated as:

$$D_{spindlek} = \begin{bmatrix} a_{22k} & a_{23k} & C_{ky} - (a_{22k}C_{ky0} + a_{23k}C_{kz0}) \\ a_{32k} & a_{33k} & C_{kz} - (a_{32k}C_{ky0} + a_{33k}C_{kz0}) \\ 0 & 0 & 1 \end{bmatrix} \qquad k = R, L \tag{5.6}$$

where a_{22k}=a_{33k}=cosϕ_k and a_{23k}=-a_{32k}=sinϕ_k, k= R, L. In the above equation, ϕ_R and ϕ_L are the right and left spindle rotations, respectively, about the x-axis. C_{ky} and C_{kz} refer to the

lateral and vertical coordinates, respectively, of the k^{th} (k=R, L) wheel center. The instantaneous coordinates of the suspension-spindle joints (N_R, P_R, N_L and P_L) following the displacement can be expressed using the right and left wheel spindle displacement matrices, $D_{spindleR}$ and $D_{spindleL}$, as:

$$\begin{bmatrix} N_{ky} & P_{ky} \\ N_{kz} & P_{kz} \\ 1 & 1 \end{bmatrix} = D_{spindlek} \begin{bmatrix} N_{ky0} & P_{ky0} \\ N_{kz0} & P_{kz0} \\ 1 & 1 \end{bmatrix}; \qquad k = R, L \tag{5.7}$$

The expansion of Eq (5.7) yields eight joints coordinates of the left and right wheel spindles. The above formulation, however, comprises a total of 12 unknown parameters corresponding to the wheel center displacements z_{uR} and z_{uL}, namely: the y and z coordinates of joints N_R, P_R, N_L and P_L; the y coordinates of the wheel centers C_R and C_L; and the camber angles ϕ_R and ϕ_L. Equation (5.7) is thus solved in conjunction with the constraint equations, which for a planar double wishbone suspension may be formulated considering the constant control arm lengths. The expanded form of Eq (5.7) together with the constraint equations thus yields a system of 12 non-linear equations, given by:

$$\begin{aligned}
N_{ky} &= a_{22k}(N_{ky0} - C_{ky0}) + a_{23k}(N_{kz0} - C_{kz0}) + C_{ky} \\
N_{kz} &= a_{32k}(N_{ky0} - C_{ky0}) + a_{33k}(N_{kz0} - C_{kz0}) + C_{kz0} + z_{uk} \\
P_{ky} &= a_{22k}(P_{ky0} - C_{ky0}) + a_{23k}(P_{kz0} - C_{kz0}) + C_{ky} \\
P_{kz} &= a_{32k}(P_{ky0} - C_{ky0}) + a_{33k}(P_{kz0} - C_{kz0}) + C_{kz0} + z_{uk} \\
(N_{ky} - M_{ky})^2 + (N_{kz} - M_{kz})^2 &= l_{MNk}^2 \\
(P_{ky} - O_{ky})^2 + (P_{ky} - O_{ky})^2 &= l_{OPk}^2 \ldots . k = R, L
\end{aligned} \tag{5.8}$$

where l_{MNk} and l_{OPk} (k=R, L) are the lengths of upper and lower control arms, respectively. Equations (5.3) and (5.8) can be simultaneously solved to obtain kinematic

responses of the suspension for given vertical displacements of the left and/or right wheels, and/or vertical and roll displacements of the chassis.

The camber angle variation responses of the left and right wheels (ϕ_L and ϕ_R) for given sprung mass and unsprung mass displacements either individually or simulataneously can be obtained from the solutions of Eqs (5.3) and (5.8). The variations in the wheel track with wheel vertical motion can be evaluated from the lateral displacement of the tire-ground contact points, T_R and T_L, as shown in Fig. 5.1. The rigid body assumption of the tire leads to the expressions for the y- coordinate of the tire-road contact points, T_R and T_L, as:

$$T_{ky} = a_{22k}(T_{ky0} - C_{ky0}) + a_{23k}(T_{kz0} - C_{kz0}) + C_{ky} \tag{5.9}$$

The y- coordinates of the tire-ground contact points, determined by Eq (5.9), determine the wheel track width variations, while the roll center of the vehicle in the roll plane is estimated using the instantaneous centers of rotations of the wheel spindles [5,6], as illustrated in Fig. 5.1.

The velocities of the joint centers between the upper- and lower control arms and the wheel spindle are obtained from time differentiation of Eq (5.8):

$$\begin{aligned}
&\dot{N}_{ky} = \dot{a}_{22k}(N_{ky0} - C_{ky0}) + \dot{a}_{23k}(N_{kz0} - C_{kz0}) + \dot{C}_{ky} \\
&\dot{N}_{kz} = \dot{a}_{32k}(N_{ky0} - C_{ky0}) + \dot{a}_{33k}(N_{kz0} - C_{kz0}) + \dot{z}_{uk} \\
&\dot{P}_{ky} = \dot{a}_{22k}(P_{ky0} - C_{ky0}) + \dot{a}_{23k}(P_{kz0} - C_{kz0}) + \dot{C}_{ky} \\
&\dot{P}_{kz} = \dot{a}_{32k}(P_{ky0} - C_{ky0}) + \dot{a}_{33k}(P_{kz0} - C_{kz0}) + \dot{z}_{uk} \\
&(N_{ky} - M_{ky})(\dot{N}_{ky} - \dot{M}_{ky}) + (N_{kz} - M_{jz})(\dot{N}_{kz} - \dot{M}_{kz}) = 0 \\
&(P_{ky} - O_{ky})(\dot{P}_{ky} - \dot{O}_{ky}) + (P_{kz} - O_{kz})(\dot{P}_{kz} - \dot{O}_{kz}) = 0 \qquad k = R, L
\end{aligned} \tag{5.10}$$

where $\dot{a}_{22k} = \dot{a}_{33k} = -\dot{\phi}_k \sin\phi_k$; and $\dot{a}_{23k} = -\dot{a}_{32k} = \dot{\phi}_k \cos\phi_k$.

5.2.3 Linearization of Kinematic Equations

The nonlinear kinematic equations can be solved to yield the kinematic responses of the model under known inputs at the wheel center and the chassis. The closed form solutions of the unknowns in terms of generalized coordinates would be desirable, in order to correlate the kinematic relations to the dynamic responses, which may be quite complex. A linear system of kinematic relations for the chassis joints could be achieved using small angles assumptions, such that $a_{22}=a_{33}$ 1; and $a_{23}=-a_{33}$ ϕ_s

$$
\begin{aligned}
&M_{ky} = M_{ky0} + \phi_s (M_{kz0} - Rc_{z0}); \;\; M_{kz} = -\phi_s (M_{ky0} - Rc_{y0}) + M_{kz0} + z_s; \\
&O_{ky} = O_{ky0} + \phi_s (O_{kz0} - Rc_{z0}); \; O_{kz} = -\phi_s (O_{ky0} - Rc_{y0}) + O_{kz0} + z_s
\end{aligned} \tag{5.11}
$$

Similarly, the small angle assumptions in the kinematic equations of the suspension linkages yield $a_{22k}=a_{33k}$ 1; and $a_{23k}=-a_{32k}$ ϕ_k. The small angle assumptions in conjunction with the first-order Taylor series approximation of the constraint equations yield the kinematic relations in the linear form as:

$$
\begin{aligned}
&N_{ky} - \phi_k (N_{kz0} - C_{kz0}) - C_{ky} = (N_{ky0} - C_{ky0}) \\
&N_{kz} + \phi_k (N_{ky0} - C_{ky0}) = N_{kz0} + z_{uk} \\
&P_{ky} - \phi_k (P_{kz0} - C_{kz0}) - C_{ky} = (P_{kz0} - C_{ky0}) \\
&P_{kz} + \phi_k (P_{ky0} - C_{ky0}) = P_{kz0} + z_{uk} \\
&(N_{ky0} + M_{ky0} - 2M_{ky}) N_{ky} + (N_{kz0} + M_{kz0} - 2M_{kz}) N_{kz} \\
&\qquad = N_{ky0}^2 + M_{ky0}^2 + N_{kz0}^2 + M_{kz0}^2 - (N_{ky0} + M_{ky0}) M_{ky} - (N_{kz0} + M_{kz0}) M_{kz} \\
&(P_{ky0} + O_{ky0} - 2O_{ky}) P_{ky} + (P_{kz0} + O_{kz0} - 2O_{kz}) P_{kz} \\
&\qquad = P_{ky0}^2 + O_{ky0}^2 + P_{kz0}^2 + O_{kz0}^2 - (P_{ky0} + O_{ky0}) O_{ky} - (N_{kz0} + M_{kz0}) O_{kz}
\end{aligned} \tag{5.12}
$$

It needs to be emphasized that the vertical displacement z_s considered while deriving the above equations is the vertical motion of the sprung mass at the roll center. The motions of the mass center of the sprung mass, z_s' and y_s', and their time derivatives, $\dot{z}_s'$ and $\dot{y}_s'$, can be obtained as:

$$G_y = G_{y0} + \phi_s (G_{z0} - Rc_{z0})\,;\; G_z = -\phi_s (G_{y0} - Rc_{y0}) + G_{z0} + z_s = G_{z0} + z_s\,;$$
$$z'_s = z_s \text{ and } y'_s = (G_z - Rc_z)\phi_s\,;\; \dot{z}'_s = \dot{z}_s \text{ and } \dot{y}'_s = (G_z - Rc_z)\dot{\phi}_s \tag{5.13}$$

Since lateral motion of the sprung mass is ignored in this study, y'_s=0. Eq (5.12) is solved to obtain expressions for the kinematic responses of the left- and right (k=L and R) suspensions, which include the instantaneous coordinates of the joints and the wheel camber angles, in terms of the generalized coordinates, such that:

$$\phi_k = \frac{1}{D_k}\begin{bmatrix} (e_k - 2M_{jy})\left[x_{2k} - (g_k O_{ky} + h_k O_{kz}) - (h_k - 2O_{kz})(P_{kz0} + z_{uk})\right] \\ +(a_k - c_k)(g_k - 2O_{ky})(e_k - 2M_{ky}) \\ -(g_k - 2O_{ky})\left[x_{1k} - (e_k M_{ky} + f_k M_{kz}) - (f_k - 2M_{kz})(N_{kz0} + z_{uk})\right] \end{bmatrix}$$

$$C_{ky} = \frac{1}{D_k}\begin{bmatrix} \left[b_k(e_k - 2M_{ky}) - a_k(f_k - 2M_{kz})\right]\left[(h_k - 2O_{kz})(P_{kz0} + z_{uk}) + (g_k O_{ky} + h_k O_{kz}) - x_{2k}\right] \\ +\left[c_k(h_k - 2O_{kz}) - d_k(g_j - 2O_{ky})\right]\left[(fk - 2M_{kz})(N_{kz0} + z_{uk}) + (e_k M_{ky} + f_k M_{kz}) - x_{1k}\right] \\ +(b_k c_k - a_k d_k)\left[(g_k - 2O_{ky})(e_k - 2M_{ky})\right] \\ +a_k c_k\left[(e_k - 2M_{ky})(h_k - 2O_{kz}) - (g_k - 2O_{ky})(f_k - 2M_{kz})\right] \end{bmatrix}$$

$$N_{ky} = \frac{1}{D_k}\begin{bmatrix} \left[(b_k - d_k)(g_k - 2O_{ky}) + c_k(h_k - 2O_{kz})\right]\begin{bmatrix}(f_k - 2M_{kz})(N_{kz0} + z_{uk}) \\ +e_k M_{ky} + f_k M_{kz} - x_{1k}\end{bmatrix} \\ +a_k(f_k - 2M_{kz})\begin{bmatrix}(a_k - c_k)(g_k - 2O_{ky}) + x_{2k} - (g_k O_{ky} + h_k O_{kz}) \\ -(h_k - 2O_{kz})(P_{kz0} + z_{uk})\end{bmatrix} \end{bmatrix}$$

$$N_{kz} = \frac{1}{D_k}\begin{bmatrix} \left[(d_k - b_k)(g_k - 2O_{ky}) - c_k(h_k - 2O_{kz})\right](e_k - 2M_{ky})(N_{kz0} + z_{uk}) \\ +a_k\left[(h_k - 2O_{kz})(P_{kz0} + z_{uk}) + (g_k O_{ky} + h_k O_{kz}) - x_{2k}\right](e_k - 2M_{ky}) \\ -a_k\left[e_k M_{ky} + f_k M_{kz} + (a_k - c_k)(e_k - 2M_{ky}) - x_{1k}\right](g_k - 2O_{ky}) \end{bmatrix}$$

$$P_{ky} = \frac{1}{D_k}\begin{bmatrix} \left[(b_k - d_k)(e_k - 2M_{ky}) + a_k(f_k - 2M_{kz})\right]\begin{bmatrix}(h_k - 2O_{kz})(P_{kz0} + z_{uk}) \\ +g_k O_{ky} + h_k O_{kz} - x_{2k}\end{bmatrix} \\ -c_k(h_k - 2O_{kz})\begin{bmatrix}(c_k - a_k)(e_k - 2M_{ky}) - e_k M_{ky} - f_k M_{kz} \\ +x_{1k} - (f_k - 2M_{kz})(N_{kz0} + z_{uk})\end{bmatrix} \end{bmatrix}$$

$$P_{kz} = \frac{1}{D_k}\begin{bmatrix} \left[(d_k - b_k)(e_k - 2M_{ky}) + a_k(f_k - 2M_{kz})\right](g_k - 2O_{ky})(P_{kz0} + z_{uk}) \\ -c_k\left[(f_k - 2M_{kz})(N_{kz0} + z_{uk}) + e_k M_{ky} + f_k M_{kz} - x_{1k}\right](g_k - 2O_{ky}) \\ -c_k\left[x_{2k} - g_k O_{ky} - h_k O_{kz} - (c_k - a_k)(g_k - 2O_{ky})\right](e_k - 2M_{ky}) \end{bmatrix} \tag{5.14}$$

where a_k=N_{ky0}-C_{ky0}; b_k=N_{kz0}-C_{kz0}; c_k=P_{ky0}-C_{ky0}; d_k=P_{kz0}-C_{kz0}; e_k=N_{ky0}+M_{ky0}; f_k=N_{kz0}+M_{kz0}; g_k=P_{ky0}+O_{ky0}; h_k=P_{kz0}+O_{kz0}; x_{1k}= $N_{ky0}^2 + M_{ky0}^2 + N_{kz0}^2 + M_{kz0}^2$; $x_{2k} = P_{ky0}^2 + O_{ky0}^2 + P_{kz0}^2 + O_{kz0}^2$; and

$$D_k = [a_k(f_k - 2M_{kz}) - b_k(e_k - 2M_{ky})](g_k - 2O_{ky}) + [d_k(g_k - 2O_{ky}) - c_k(h_k - 2O_{kz})](e_k - 2M_{ky})$$

The lateral displacements of the right and left wheel centers can be obtained from:

$$y_{uk} = C_{ky} - C_{ky0} \tag{5.15}$$

5.2.4 Strut Deflection and Deflection Rate

The restoring force developed by each strut is related to the change in the strut length, given by:

$$\Delta l_k = l_{s0} - \left[(A_{ky} - B_{ky})^2 + (A_{kz} - B_{kz})^2\right]^{1/2} \tag{5.16}$$

where l_{s0} is the initial strut length, assumed to be identical for the left and right struts. In the above expression, (A_{ky}, A_{kz}) and (B_{ky}, B_{kz}) are the instantaneous coordinates of the lower and upper strut mounts, which can obtained from the kinematics of the chassis and suspension as:

$$\begin{aligned} A_{ky} &= O_{ky} + \frac{l_{OA}}{l_{OP}}(P_{ky} - O_{ky}); \qquad A_{kz} = O_{kz} + \frac{l_{OA}}{l_{OP}}(P_{kz} - O_{kz}) \\ B_{ky} &= B_{ky0} + \phi_s(B_{kz0} - Rc_{z0}) \; ; \quad B_{kz} = -\phi_s(B_{ky0} - Rc_{y0}) + B_{kz0} + z_s \end{aligned} \tag{5.17}$$

where l_{OA} and l_{OP} are the distances of the joints A_R and P_R from point O_R (or A_L and P_L from point O_L). The deflection rates of left- and right suspension struts are subsequently estimated from the time derivatives of the displacement expression in Eq (5.16).

5.2.5 Kinematics of Torsion Bar

Torsion bars or the antiroll bars are invariably employed in vehicle suspensions in order to enhance roll stiffness and to reduce dynamic load transfers. An antiroll bar couples vertical motions of the right and left wheels, and develops a resisting roll moment under chassis roll or differential wheel motions. The kinematic motion of a torsion bar thus involves spatial kinematic analysis, as illustrated in the Fig. 5.2.

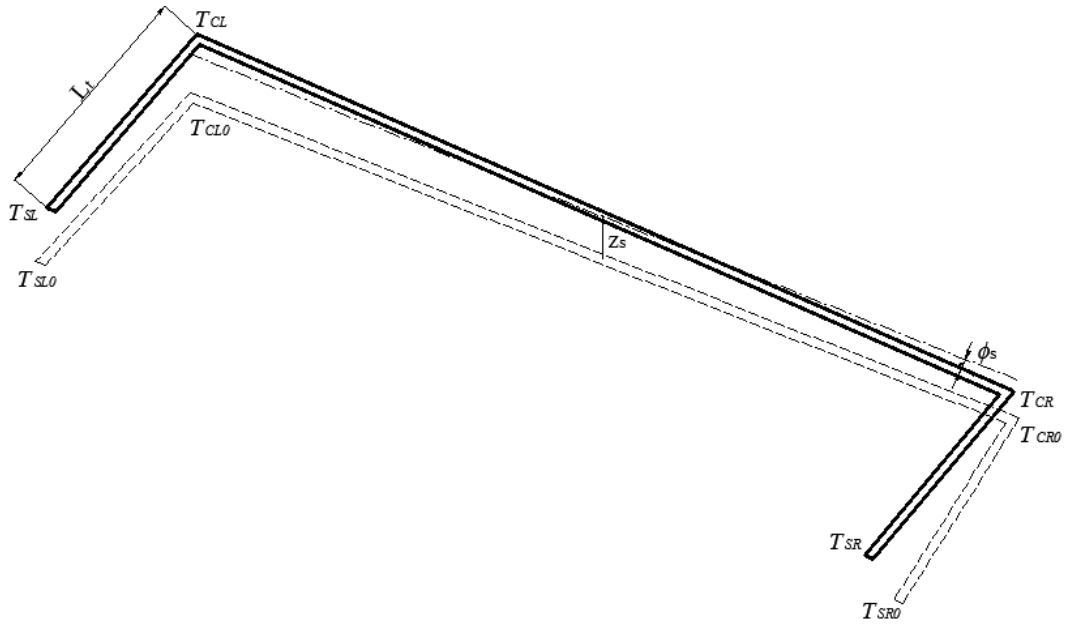

Figure 5.2: Kinematics of the torsion bar

The torsion bar is assumed to be coupled to the chassis at points Tc_L and Tc_R, and to the lower control arms at the points Ts_L and Ts_R, respectively. The instantaneous z-coordinates of the chassis mounting points Tc_k (k=L, R) are estimated from the kinematics of the chassis as:

$$Tc_{kz} = -\phi_s(Tc_{ky0} - Rc_{y0}) + Tc_{kz0} + z_s \tag{5.18}$$

The small angular deformation of the torsion bar θ_T is determined from the changes in the coordinates of the mounting points, as:

$$\theta_T = \frac{1}{L_T}\left[\left(Tc_{Lz} - Ts_{Lz}\right) - \left(Tc_{Lz0} - Ts_{Lz0}\right) + \left(Tc_{Rz} - Ts_{Rz}\right) - \left(Tc_{Rz0} - Ts_{Rz0}\right)\right] \tag{5.19}$$

where L_T is the effective length of the torsion bar between attachment points Ts_R and Tc_R. The subscripts '*z*' and '*0*' are used to represent the *z*- coordinates and the initial coordinates, respectively.

Equation (5.19) can be further simplified to yield:

$$\theta_T = \frac{1}{L_T}\left[\left(Tc_{Lz} - Ts_{Lz}\right) + \left(Tc_{Rz} - Ts_{Rz}\right)\right] - 2\theta_{T0} \tag{5.20}$$

where θ_{T0} is the initial deformation angle of the torsion bar arm with respect to the horizontal axis of the reference coordinate system. The *z*- coordinates of the torsion bar mounting points at the lower control arms Ts_{Rz} and Ts_{Lz}, are obtained from the linkage kinematics, as:

$$Ts_{kz} = O_{kz} + \frac{l_{OTs}}{l_{OP}}(P_{kz} - O_{kz}) \qquad k=R, L \tag{5.21}$$

where l_{OTs} is the length of the lower control arm between the torsion bar mounting point, Ts_R and the chassis joint O_R.

5.3 Kineto-Dynamic Half-car Model

The equations of dynamic motion of the kineto-dynamic half-vehicle system, as shown in Fig. 5.3 are derived using Lagrange's method in a manner similar to that described in Chapter 3 for the quarter-car kineto-dynamic model. The kinetic energy (*T*) of the system is formulated as:

$$T = \frac{1}{2}m_s(\dot{z}_s'^2 + \dot{y}_s'^2) + \frac{1}{2}(I_x + (G_{z0} - Rc_{z0})^2 m_s)\dot{\phi}_s^2 + \frac{1}{2}\sum_{k=R,L} m_{uk}\left(\dot{y}_{uk}^2 + \dot{z}_{uk}^2\right) + \frac{1}{2}\sum_{k=R,L} I_{ukx}\dot{\phi}_k^2 \tag{5.22}$$

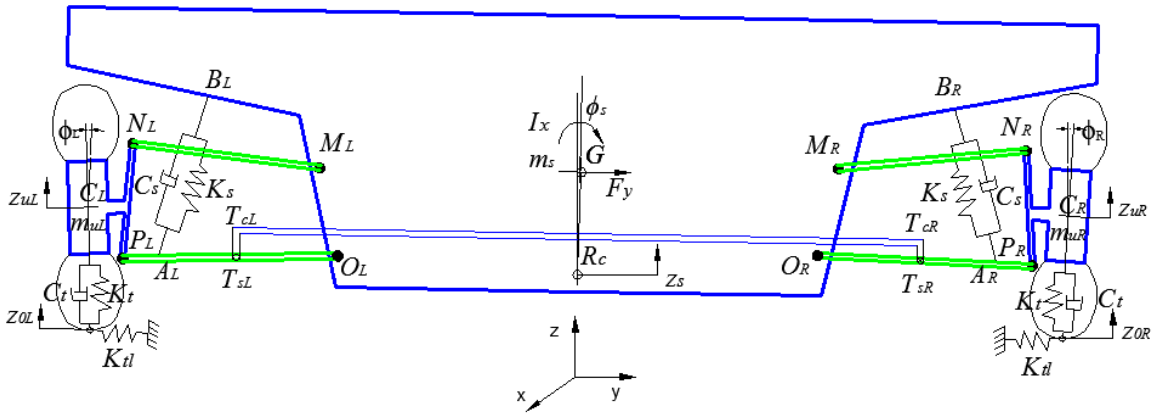

Figure 5.3: Kineto-dynamic half-car model with antiroll bar

where m_s, m_{uR} and m_{uL} are sprung mass, and right- and left unsprung masses, respectively. In the above expression, I_x and I_{ukx} (k=R, L) are the mass moment of inertia of the chassis and the right- and left wheel spindles about x- axis.

The potential energy of the system is expressed as:

$$U = \frac{1}{2}\sum_{k=R,L}\left(K_s(\Delta l_k)^2 + K_t(\Delta z_{tk})^2 + K_{tl}(y_{uk} - \phi_k R_k)^2\right) + \frac{1}{2}K_{tb}\theta_T^2 \tag{5.23}$$

where K_s is the suspension spring rate, K_t is the equivalent tire vertical rate, K_{tb} is the linear stiffness of torsion bar, K_{tl} is the tire lateral stiffness and R_k are the effective radii of the wheels. Moreover, Δl_k are the right- and left suspension spring deflections, as described in Eq (5.16), and Δz_{tk} are the right- and left tire deflections. The total energy dissipated by the system, attributed to the linear strut and tire damping, can be derived as:

$$D = \frac{1}{2}\sum_{k=R,L} C_s(\Delta \dot{l}_k)^2 + \frac{1}{2}\sum_{k=R,L} C_t(\Delta \dot{z}_{tk})^2 \tag{5.24}$$

where C_s and C_t are the viscous damping coefficients of the strut and the tire, respectively, and $\Delta \dot{l}_k$ denote the time derivatives of the right- and left strut deflections, and $\Delta \dot{z}_{tk}$ are the rates of right- and left tires deflection.

5.3.1 Equations of Motion:

The equations of motion for the kineto-dynamic model are formulated from the kinetic (T), potential (U) and dissipative (D) energy functions described in Eqs (5.22) to (5.24). Assuming negligible contributions due to higher order derivative terms, the equations of motion are obtained as:

$$
\begin{aligned}
&m_s\ddot{z}_s + \sum_{k=R,L} m_{uk}\left(\ddot{y}_{uk}\frac{\partial \dot{y}_{uk}}{\partial \dot{z}_s}\right) + \sum_{k=R,L} I_{uxk}\left(\ddot{\phi}_k\frac{\partial \dot{\phi}_k}{\partial \dot{z}_s}\right) + \sum_{k=R,L}\left(f_{ssk}+f_{dsk}+f_{tlsk}\right) + f_{tbs} = -9.81 m_s \\
&(I_x + (G_{z0}-Rc_{z0})^2 m_s)\ddot{\phi}_s + \sum_{k=R,L} m_{uk}\left(\ddot{y}_{uk}\frac{\partial \dot{y}_{uk}}{\partial \dot{\phi}_s}\right) + \sum_{k=R,L} I_{uxk}\left(\ddot{\phi}_k\frac{\partial \dot{\phi}_k}{\partial \dot{\phi}_s}\right) \\
&\qquad + \sum_{k=R,L}(T_{ssk}+T_{dsk}+T_{tlsk}) + T_{tbs} = (G_z - Rc_z)(F_y + 9.81 m_s\phi_s) \\
&m_{uR}\ddot{z}_{uR} + m_{uR}\left(\ddot{y}_{uR}\frac{\partial \dot{y}_{uR}}{\partial \dot{z}_{uR}}\right) + I_{uxR}\left(\ddot{\phi}_R\frac{\partial \dot{\phi}_R}{\partial \dot{z}_{uR}}\right) + f_{suR} + f_{tluR} + f_{duR} + f_{tR} + f_{tbuR} = -9.81 m_{uR} \\
&m_{uL}\ddot{z}_{uL} + m_{uL}\left(\ddot{y}_{uL}\frac{\partial \dot{y}_{uL}}{\partial \dot{z}_{uL}}\right) + I_{uxL}\left(\ddot{\phi}_L\frac{\partial \dot{\phi}_{uL}}{\partial \dot{z}_{uL}}\right) + f_{suL} + f_{tluL} + f_{duL} + f_{tL} + f_{tbuL} = -9.81 m_{uL}
\end{aligned}
\tag{5.25}
$$

where f_{ssk} and f_{suk} (k=R, L) are the right- and left- suspension spring forces acting on the sprung and unsprung masses, respectively, f_{dsk} and f_{duk} are the right- and left- damping forces acting on the sprung and unsprung masses, respectively, and T_{ssk} and T_{dsk} are the moments due to right- and left- suspension spring and damping forces, respectively. In Eq (5.25), f_{tlsk} and f_{tluk} are the vertical tire forces acting on the sprung and unsprung masses, respectively, and T_{tlsk} are the moments imposed on the sprung mass due to the right- and left- tire lateral compliance, respectively. Moreover, f_{tk} are the tire forces, and f_{tbs} and f_{tbuk} are the forces transmitted to the sprung and unsprung masses, and T_{tbs} is the torque transmitted to the sprung mass due to the torsion bar. Assuming linear spring rates, the suspension spring forces f_{ssk} and f_{suk} are related to Δl_k, as:

$$
f_{ssk} = K_s \Delta l_k \frac{\partial(\Delta l_k)}{\partial z_s};\ \text{and}\ \ f_{suk} = K_s \Delta l_k \frac{\partial(\Delta l_k)}{\partial z_{uk}} \qquad k=R,\ L \tag{5.26}
$$

The torque imposed on the sprung mass due to the right- and left- suspension springs, T_{ssk} is related to Δl_k and chassis roll, as:

$$T_{ssk} = K_s \Delta l_k \frac{\partial(\Delta l_k)}{\partial \phi_s} \qquad k=R, L \tag{5.27}$$

Similarly, f_{dsk} and f_{duk} the left- and right suspension damping forces acting on the sprung and unsprung masses, respectively, and T_{dsk}, the torque due to the damper forces acting on the sprung mass, are obtained from:

$$f_{dsk} = C_s \Delta \dot{l}_k \frac{\partial(\Delta \dot{l}_k)}{\partial \dot{z}_s}; f_{duk} = C_s \Delta \dot{l}_k \frac{\partial(\delta \dot{l}_k)}{\partial \dot{z}_{uk}}; \text{ and } T_{dsk} = C_s \Delta \dot{l}_k \frac{\partial(\Delta \dot{l}_k)}{\partial \dot{\phi}_s} \quad k=R,L \tag{5.28}$$

The vertical forces due to the torsion bar exerted on the sprung mass, and left- and right unsprung masses, f_{tbs} and f_{tbuk}, and the torque on the sprung mass, T_{tbs}, are obtained from:

$$f_{tbs} = K_{tb}\theta_T \frac{\partial \theta_T}{\partial z_s}; f_{tbuk} = K_{tb}\theta_T \frac{\partial \theta_T}{\partial z_{uk}}; \text{ and } T_{tbs} = K_{tb}\theta_T \frac{\partial \theta_T}{\partial \phi_s} \qquad k=R, L \tag{5.29}$$

5.3.2 Wheel Hop Conditions

The nonlinearity associated with potential loss of contact between the ground and the tire (wheel hop) can also be incorporated in the kineto-dynamic model. The forces due to the tire viscous dampers, and the lateral and vertical compliance are formulated considering four different possible conditions; namely: (i) both the tires are in contact with the ground (z_{uL}-z_{0L}<δ_u and z_{uR}-z_{0R}<δ_u), where δ_u is the static tire deflection; (ii) left wheel in contact with the ground, while the right wheel loses the ground contact (z_{uL}-z_{0L}<δ_u and z_{uR}-z_{0R}≥δ_u); (iii) right wheel is in contact with the ground, while the left wheel loses the ground contact (z_{uL}-z_{0L}≥δ_u and z_{uR}-z_{0R}<δ_u); and (iv) both wheels lose contact with the ground (z_{uL}-z_{0L}≥δ_u and z_{uR}-z_{0L}≥δ_u):

$$f_{tlsk} = K_{tl}(y_{uk} - \phi_k R_k)\frac{\partial(y_{uk} - \phi_k R_k)}{\partial z_s};\ f_{tluk} = K_{tl}(y_{uk} - \phi_k R_k)\frac{\partial(y_{uk} - \phi_k R_k)}{\partial z_{uk}};$$

$$T_{tlsk} = K_{tl}(y_{uk} - \phi_k R_k)\frac{\partial(y_{uk} - \phi_k R_k)}{\partial \phi_s};\ \text{and}\ f_{tk} = K_t \Delta z_{tk} + C_t \Delta \dot{z}_{tk} \quad ; k=R, L$$

for z_{uL}-z_{0L}<δ_u and z_{uR}-z_{0R}<δ_u

$$f_{tlsR} = 0;\ \ f_{tlsL} = K_{tl}(y_{uL} - \phi_L R_L)\frac{\partial(y_{uL} - \phi_L R_L)}{\partial z_s}$$

$$T_{tlsR} = 0;\ \ T_{tlsL} = K_{tl}(y_{uL} - \phi_L R_L)\frac{\partial(y_{uL} - \phi_L R_L)}{\partial \phi_s}$$

$$f_{tluR} = 0;\ \ f_{tluL} = K_{tl}(y_{uL} - \phi_L R_L)\frac{\partial(y_{uL} - \phi_L R_L)}{\partial z_{uL}}$$

$f_{tR} = 0;\ f_{tL} = K_t \Delta z_{tL} + C_t \Delta \dot{z}_{tL}$ $k=R, L$ for z_{uL}-z_{0L}<δ_u and z_{uR}-z_{0R}≥δ_u

$$f_{tlsR} = K_{tl}(y_{uR} - \phi_R R_R)\frac{\partial(y_{uR} - \phi_R R_R)}{\partial z_s};\ \ f_{tlsL} = 0$$

$$T_{tlsR} = K_{tl}(y_{uR} - \phi_R R_R)\frac{\partial(y_{uR} - \phi_R R_R)}{\partial \phi_s};\ \ T_{tlsL} = 0$$

$$f_{tluR} = K_{tl}(y_{uR} - \phi_R R_R)\frac{\partial(y_{uR} - \phi_R R_R)}{\partial z_{uR}};\ \ f_{tluL} = 0$$

$f_{tsR} = K_t \Delta z_{tR} + C_t \Delta \dot{z}_{tR};\ \ f_{tL} = 0$ $k=R, L$ for z_{uL}-z_{0L}≥δ_u and z_{uR}-z_{0R}<δ_u

$$f_{tlsk} = 0;\ \ T_{tlsk} = 0;\ \ f_{tluk} = 0;\ f_{tk} = 0 \quad k=R, L \ \text{for}\ z_{uL}\text{-}z_{0L} \geq \delta_u \ \text{and}\ z_{uR}\text{-}z_{0R} \geq \delta_u \qquad (5.30)$$

5.3.3 Kineto-Dynamic Suspension Model with Asymmetric Damping

Influences of suspension damping asymmetry on the kinematic and dynamic responses of the proposed half-car model is evaluated by considering asymmetric viscous damping forces acting on the sprung and unsprung masses (f_{dsk}, f_{duk}). The damping forces are described through bilinear and piece-wise linear force-velocity models as in the case of quarter car model. The damping forces developed by two-stage asymmetric dampers in compression and rebound, $f_{djk\text{-}c}$ and $f_{djk\text{-}r}$, and the corresponding moments imposed on the forces on the sprung mass, $T_{dsk\text{-}c}$ and $T_{dsk\text{-}r}$ (k=R, L) are formulated as:

$$
f_{djk-c} = \begin{cases} C_c \Delta\dot{l}_k \dfrac{\partial(\Delta\dot{l}_k)}{\partial \dot{z}_{jk}} & \alpha_c \le \Delta\dot{l}_k \le 0 \\ \left(\alpha_c + \lambda_c(\Delta\dot{l}_k - \alpha_c)\right) C_c \dfrac{\partial(\Delta\dot{l}_k)}{\partial \dot{z}_{jk}} & \Delta\dot{l}_k < \alpha_c; \end{cases} \quad j = s,u;\ k = R,L
$$

$$
f_{djk-r} = \begin{cases} \rho C_c \Delta\dot{l}_k \dfrac{\partial(\Delta\dot{l}_k)}{\partial \dot{z}_{jk}} & 0 \le \Delta\dot{l}_k \le \alpha_r \\ \left(\alpha_r + \lambda_r(\Delta\dot{l}_k - \alpha_r)\right) \rho C_c \dfrac{\partial(\Delta\dot{l}_k)}{\partial \dot{z}_{jk}} & \alpha_r < \Delta\dot{l}_k; \end{cases} \quad j = s,u;\ k = R,L
$$

$$
T_{dsk-c} = \begin{cases} C_c \Delta\dot{l}_k \dfrac{\partial(\Delta\dot{l}_k)}{\partial \dot{\phi}_s} & \alpha_c \le \Delta\dot{l}_k \le 0 \\ \left(\alpha_c + \lambda_c(\Delta\dot{l}_k - \alpha_c)\right) C_c \dfrac{\partial(\Delta\dot{l}_k)}{\partial \dot{\phi}_s} & \Delta\dot{l}_k < \alpha_c; \end{cases} \quad k = R,L
$$

$$
T_{dsk-r} = \begin{cases} \rho C_c \Delta\dot{l}_k \dfrac{\partial(\Delta\dot{l}_k)}{\partial \dot{\phi}_s} & 0 \le \Delta\dot{l}_k \le \alpha_r \\ \left(\alpha_r + \lambda_r(\Delta\dot{l}_k - \alpha_r)\right) \rho C_c \dfrac{\partial(\Delta\dot{l}_k)}{\partial \dot{\phi}_s} & \alpha_r < \Delta\dot{l}_k; \end{cases} \quad k = R,L \tag{5.31}
$$

where C_c is compression damping coefficient, ρ is damping asymmetry ratio, α_c and α_r are the transition velocities in compression and rebound, respectively, and λ_c and λ_r are the respective damping reduction factors. The above equation, together with the equation of motion, Eq (5.25), describe the kineto-dynamics of the half-car model with double wishbone type of suspension and two-stage asymmetric damper.

5.4 Roll-plane Dynamic Model of a Vehicle

The dynamic motions of the vehicle in the roll-plane are generally described by a 4-DOF model as shown in Fig. 5.4 [102, 135]. The responses of the proposed kineto-dynamic half-car model can be conveniently compared with this conventional roll-plane model to evaluate the influences of linkage kinematics. The equations of motion describing the coupled vertical and roll motion are formulated as:

$$
\begin{aligned}
&m_s\ddot{z}_s + f_{sL} + f_{sR} = -9.81m_s \\
&(I_x + (h_{cg} - h_{rc})^2 m_s)\ddot{\phi}_s + Wf_{sL} - Wf_{sR} = 9.81m_s(h_{cg} - h_{rc})\phi_s \\
&m_{uL}\ddot{z}_{uL} - f_{sL} + f_{tL} = -9.81m_{uL} \\
&m_{uR}\ddot{z}_{uR} - f_{sR} + f_{tR} = -9.81m_{uR}
\end{aligned} \tag{5.32}
$$

where W is the half suspension track width, which is generally considered to be identical to half tire track width, h_{cg} and h_{rc} are the mass center and roll center heights of the sprung mass, respectively. The roll motion of the chassis is thus assumed to occur about the roll center. In the above equation, f_{sL} and f_{sR} represent the left- and right- strut forces, and f_{tL} and f_{tR} are the left and right tire forces, respectively. Assuming linear suspension properties, f_{sL} and f_{sR}, can be obtained as:

$$
\begin{aligned}
f_{sL} &= C_{eq}(\dot{z}_s + W\dot{\phi}_s - \dot{z}_{uL}) + K_{eq}(z_s + W\phi_s - z_{uL}) \\
f_{sR} &= C_{eq}(\dot{z}_s - W\dot{\phi}_s - \dot{z}_{uR}) + K_{eq}(z_s - W\phi_s - z_{uR})
\end{aligned} \tag{5.33}
$$

where K_{eq} and C_{eq} are the equivalent spring and damping rates, respectively, which are obtained from the kinematic and force analysis of the double wishbone suspension as illustrated in Chapter 3. The equivalent spring and damping rates are considered in order to account for the kinematic effects of suspension struts mountings coordinates with respect to the unsprung mass center (Fig. 5.2).

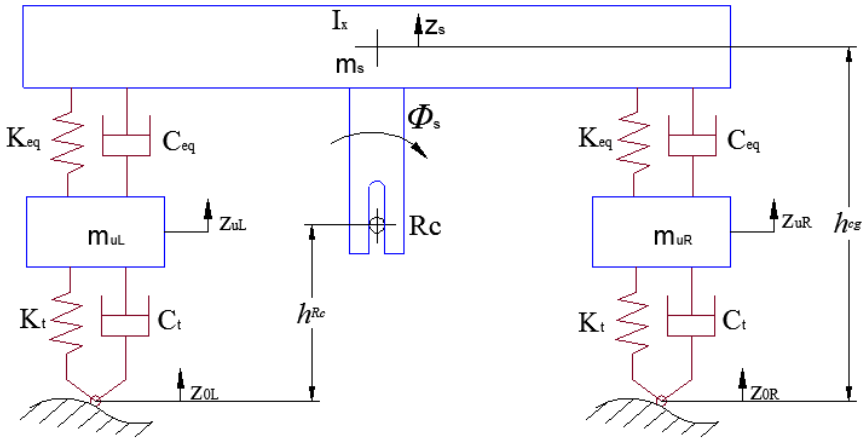

Figure 5.4: Conventional roll-plane half-car model

Considering the wheel hop conditions, described in section 5.3, the left- and right tire forces f_{tL} and f_{tR} are formulated as:

$$\begin{aligned}
&f_{tL} = C_t(\dot{z}_{uL} - \dot{z}_{0L}) + K_t(z_{uL} - z_{0L}); \\
&f_{tR} = C_t(\dot{z}_{uR} - \dot{z}_{0R}) + K_t(z_{uR} - z_{0R}); && \text{for } z_{uL}\text{-}z_{0L}<\delta_u \text{ and } z_{uR}\text{-}z_{0R}<\delta_u \\
&f_{tL} = C_t(\dot{z}_{uL} - \dot{z}_{0L}) + K_t(z_{uL} - z_{0L});\ f_{tR} = 0; && \text{for } z_{uL}\text{-}z_{0L}<\delta_u \text{ and } z_{uR}\text{-}z_{0R}\geq\delta_u \\
&f_{tL} = 0;\ f_{tR} = C_t(\dot{z}_{uR} - \dot{z}_{0R}) + K_t(z_{uR} - z_{0R}); && \text{for } z_{uL}\text{-}z_{0L}\geq\delta_u \text{ and } z_{uR}\text{-}z_{0R}<\delta_u \\
&f_{tL} = 0;\ f_{tR} = 0; && \text{for } z_{uL}\text{-}z_{0L}\geq\delta_u \text{ and } z_{uR}\text{-}z_{0L}\geq\delta_u)
\end{aligned} \tag{5.34}$$

where K_t and C_t are the linear tire spring and damping rates, respectively. In the dynamic model, the lateral motion of chassis is assumed to be caused by the chassis roll, ϕ_s.

5.5 Kinematic Response Analyses and Suspension Geometry Synthesis

The nonlinear kinematic formulations, presented in section 5.2.2, are solved using Newton-Raphson method to obtain kinematic responses of the half-car model, particularly the variations in the bump and roll camber angles and the wheel track under either vertical motions of the wheels or roll motion of the chassis or a combination of sprung and unsprung masses motions. The simulations are performed for joint coordinates of a typical double wishbone suspension, presented in chapter 2 [146]. Considering the symmetry between left and right suspensions, the coordinates of linkage suspension joints alone are defined: M_R(0.430, 0.818), N_R(0.644, 0.852), O_R(0.365, 0.360), P_R(0.743, 0.347), C_R(0.787, 0.452), A_R(0.660, 0.349) and B_R(0.615, 0.920). The left suspension is considered to be symmetric to the right suspension about a vertical line through the mass center of the vehicle body. Initial camber angles of the wheels are

assumed to be zero, since the analyses are concerned with variations in the responses alone.

5.5.1 Kinematic Response Analyses

The kinematic responses are evaluated in terms of: (i) the bump camber angles under vertical displacement inputs at the wheel centers with fixed chassis; (ii) roll camber response to chassis roll input; and (iii) variations in the bump/roll camber angles under simultaneously applied wheel centers displacements and chassis roll inputs. The wheel centers with fixed chassis was subjected to 100 mm peak harmonic jounce and rebound motion at a frequency of 1 Hz, such that z_{uR}=z_{uL}=100sin(2πt) mm and z_s= 0. The analyses were performed considering two different types of simultaneous harmonic inputs, namely: (i) relatively large chassis roll coupled with smaller wheel bump motions (ϕ_s=5sin(2πt)°; z_{uR}= z_{uL}=50sin(2πt) mm; and z_s=0); and (ii) relatively large wheel bump motions coupled with smaller chassis roll motion (ϕ_s=3sin(2πt)°; z_{uR}= z_{uL}=100sin(2πt) mm; and z_s= 0). The responses of the right- and left- wheels to simultaneous harmonic inputs, thus defined, can be related to the outer and inner wheels of a vehicle negotiating a corner. In the first half of the simultaneous harmonic inputs, both the wheels undergo jounce, while the chassis undergoes a positive (clockwise) roll motion. This could be related to the outer (right) and inner (left) wheels undergoing jounce while negotiating a corner (left turn of the vehicle). In a similar manner, both the suspensions undergo rebound motion during the second half of the harmonic inputs, while the chassis undergoes a negative (counterclockwise) roll, which corresponds to the outer (left) and inner (right) wheels undergoing rebound while negotiating the corner.

Figure 5.5 compares the bump camber responses of the right and left wheels under wheel vertical excitations alone (z_{uR}=z_{uL}=100sin(2πt) mm), and combined wheel displacement and chassis roll (ϕ_s=3sin(2πt)°). Under vertical wheel displacements alone, both the wheels exhibit negative camber angle during jounce travel, which approach approximately -3.4° at 100 mm jounce. During rebound, the wheels exhibit positive camber with a maximum of 1.1°, suggesting asymmetric variations in jounce and rebound. Under the simultaneous wheel vertical and chassis roll inputs, the camber angle response of the right wheel in jounce reduces considerably, which is attributable to the compensating effect of the positive roll camber due to chassis roll. The right wheel under jounce displacement coupled with simultaneously applied positive chassis roll can be considered as the outer wheel of a vehicle negotiating a corner and undergoing a jounce motion. The camber angle of the right wheel in rebound in a similar manner would represent the inner wheel of the vehicle. It can be further seen that the net camber angle response of the right wheel in rebound tends to be negative with a peak value near -2°.

The left wheel in jounce under the combined wheel vertical and chassis roll input, would represent the inner wheel of a vehicle negotiating a corner and undergoing jounce. It can be observed from the figure that the net camber angle of the left wheel in jounce goes further negative with a peak value near -4.5°. The left wheel under rebound travel with simultaneously applied negative chassis roll input represents the outer wheel of a vehicle negotiating a corner and undergoing rebound. The figure shows that the net camber angle of the left wheel in rebound under simultaneous inputs increases considerably as compared to the bump camber, and exhibits a peak response near 4°. It is widely suggested to minimize the net wheel camber of the outer wheel of a vehicle

negotiating a corner due to the greater load transfer to these wheels to achieve reduction in the camber thrust [5]. The lateral load transfer to the outer wheels would yield greater lateral force developed at the tires due to camber angle (camber thrust). A suspension synthesis thus needs to consider the net camber angle responses of the right- and left-wheels undergoing jounce and rebound, respectively, under simultaneous inputs due to wheel motion and chassis roll. The results in Fig. 5.5 suggest that the net camber angle response of the left-wheel in jounce and rebound is considerably large.

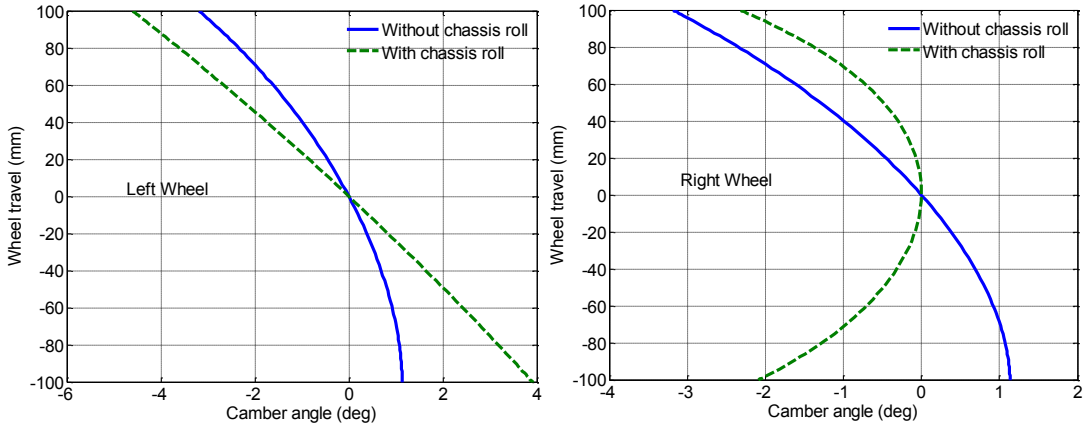

(a) (b)

Figure 5.5: Variations in camber angles of: (a) the left; and (b) the right wheels under wheel vertical displacement inputs alone (z_{uR}, z_{uL}=100sin(2πt)) with fixed chassis, and coupled with 3° chassis roll input (ϕ_s=3°sin(2πt), z_s= 0)

Figure 5.6 demonstrates the roll camber responses of the right and left wheels under chassis roll input alone, and under simultaneously applied wheel vertical displacement inputs (z_{uR}, z_{uL} =50sin(2πt) with z_s= 0 and ϕ_s= 5°sin(2πt)). Under a positive chassis roll, the right wheel exhibits positive camber with peak value of nearly 3°, while the left wheel exhibits a negative camber angle with peak value approaching nearly -4°. The camber angle responses to chassis roll are thus asymmetric with respect to the chassis roll, with peak roll camber under positive chassis roll (3°) being less than that under the negative

chassis roll (-4°). The responses to simultaneous inputs, presented in Fig. 5.6, illustrate similar significance of the chassis roll as that observed in Fig. 5.5. The right wheel exhibits decrement in the net camber angle, while the left wheel exhibits increment in the net camber angle under simultaneous inputs as compared to those under the chassis roll alone.

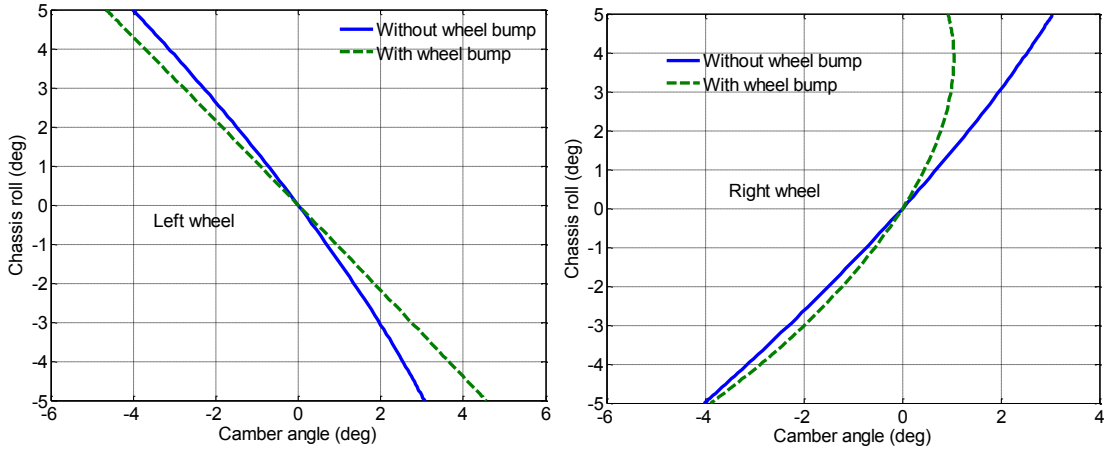

(a) (b)

Figure 5.6: Variations in camber angles of: (a) the left; and (b) the right wheels under a chassis roll input alone (ϕ_s =5°sin(2πt)) and chassis roll input coupled with wheels vertical displacements, z_{uR}, z_{uL} =50 sin(2πt).

5.5.2 Sensitivity Analysis

A reduction in lateral packaging space of the suspension could be realized through variations in y- coordinates of joints O_R and M_R in a positive direction, while a similar change would be necessary for joints O_L and M_L to maintain a symmetry. A sensitivity analysis is thus initially performed out to study the influences of changes in the suspension joint coordinates on the kinematic responses, including the roll center height, bump and roll camber angles, and the track width variations. The analyses are performed by considering ±40 mm variations in y- and z- coordinates of various joints, and responses are evaluated in terms of: (i) variation in the roll center height with respect that

of the nominal suspension geometry, Δ(RCH); (*ii*) peak bump camber angles under 100 mm of jounce and rebound, $\Delta(\phi_R)_{jou}$ and $\Delta(\phi_R)_{reb}$; (*iii*) peak variations in wheel track width under 100 mm of wheel jounce and rebound, $\Delta(TW)_{jou}$, and $\Delta(TW)_{reb}$; and (*iv*) peak roll cambers of right- wheel under positive, and negative chassis roll of 5°. The peak net camber angles of the right wheel in jounce, $\Delta(\phi_R)_{jou}$, and the left wheel in rebound, $\Delta(\phi_R)_{reb}$, are further evaluated under simultaneous 100 mm wheel displacements and 3° chassis roll. The responses were evaluated with change in a single coordinate at a time, while all other joint coordinates were held as nominal. The variation in the *y*-coordinate of joint P_R, however, was limited to a negative change only, due to limited lateral space between the lower control arm joint (P_R) and the wheel center (C_R). The variation in a given coordinate, however, is considered symmetric for both the right- and left-side suspension links.

The results of the sensitivity analysis are summarized in Table 5.1. The variation in a joint coordinate along the *y*- or *z*- axis is indicated by the subscript of the joint, while the superscript '+' or '-' refer to the increase or decrease in the coordinate. For instance, notation O_y^+ in Table 5.1 denotes a 40 mm increase in *y*- coordinates of joints O_R and O_L with respect to the nominal values. It can be seen that a positive change in *y*- coordinates of joints *O* causes reductions in the peak jounce camber and track width under wheel vertical displacements, peak roll camber under negative chassis roll, and peak jounce camber angle under simultaneous inputs, with marginal increases in the peak rebound camber angle and track width responses under wheel vertical displacements. A positive change in *y*- coordinate of joint *M* causes a marginal reduction in the peak rebound camber angle and track width under wheel vertical displacements alone, and the peak roll

Table 5.1: Sensitivity of the kinematic responses of the half-car model to changes in the *y* and *z* coordinates of the linkage joints under vertical wheels displacement, chassis roll, and simultaneous wheels displacement and chassis roll inputs.

Excitation	Static	Wheel vertical displacement				Chassis roll		Simultaneous	
Parameter	Δ(RCH) (mm)	$\Delta(\phi_{ur})_{jou}$ (deg)	$\Delta(\phi_{ur})_{reb}$ (deg)	Δ(TW)$_{jou}$ (mm)	Δ(TW)$_{reb}$ (mm)	$\Delta(\phi_{ur})_{roll}$ (deg)	$\Delta(-\phi_{ur})_{roll}$ (deg)	$\Delta(\phi_{ur})_{jou}$ (deg)	$\Delta(\phi_{ul})_{reb}$ (deg)
Nominal	0	-3.19	1.14	5.9	-22.2	3.08	-4.05	-2.32	3.91
O_y^+	4.7	-3.07	1.38	4.9	-25.5	3.13	-3.94	-2.10	3.99
O_y^-	-3.9	-3.27	0.95	7.2	-19.6	3.04	-4.15	-2.55	3.82
O_z^+	123.2	-4.16	2.44	2.1	-39.2	2.36	-3.22	-3.62	4.63
O_z^-	-125.4	-2.16	0.19	-4.2	-5.3	0.21	-2.16	-0.97	3.19
P_y^-	4.1	-3.13	1.35	5.2	-24.9	3.11	-3.96	-2.21	3.98
P_z^+	-116.7	-2.32	0.21	-3.1	-5.1	3.72	-4.88	-3.24	4.51
P_z^-	98.5	-3.92	2.25	17.0	-36.8	2.53	-3.35	-1.23	3.21
M_y^+	13.9	-4.19	1.03	10.7	-21.3	2.55	-4.04	-4.32	3.95
M_y^-	-9.7	-2.52	1.26	3.8	-22.8	3.44	-4.06	-1.06	3.88
M_z^+	-75.9	-1.19	-0.40	-0.5	-10.4	4.44	-5.56	-4.69	4.88
M_z^-	68.6	-5.09	3.15	15.1	-31.4	1.81	-2.74	0.41	2.56
N_y^+	-9	-2.62	1.24	4.0	-22.7	3.4	-4.07	-1.28	3.88
N_y^-	12.6	-3.96	1.05	9.6	-21.5	2.65	-4.03	-3.78	3.96
N_z^+	58.7	-4.79	2.92	13.6	-30.4	2.01	-2.9	-4.69	4.88
N_z^-	-102.7	-1.28	-0.44	-0.3	-9.7	4.40	-5.65	0.42	2.56

camber of the right wheel under positive chassis roll, while all other responses tend to be generally higher. The results suggest that suspension synthesis to achieve reduction in the lateral space thus, necessitates compromises among the performance measures.

The results in Table 5.1 further show that changes in *y* coordinates of all the joints yield relatively smaller influence on the Δ(RCH) response, while variations in the *z*-coordinates yield substantial changes in Δ(RCH), irrespective of the direction of change, as it would be expected. Positive changes in *z*- coordinates of lower control arm-chassis joint *O* and upper control arm-spindle joint *N*, and negative changes in *z*-coordinates of lower control arm-spindle joint *P* and upper control arm-chassis joint *M* yield substantially higher roll center. Opposite changes in these coordinates yield an opposing effect on the roll center height. The wheel track variation response to wheel vertical displacements seems to be most sensitive to positive variations in *z*-coordinates of joints *O* and *N*, and negative variations in *z*-coordinates of joints *M* and *P*. Negative changes in *z*- coordinates of joints *O* and *N*, or a positive changes in *z*- coordinates of joints *P* and *M* tend to reduce the wheel track variations in both jounce and rebound, while these changes yield substantially lower roll center height. These results suggest the need for a design compromise between the roll center height and wheel track variations.

The positive and negative changes in a coordinate, in general, yield an opposing influence on the selected performance measures except for the peak wheel track variations. For example, a positive change in *z*- coordinates of joints *O* yield higher peak bump camber angles in both jounce and rebound, while a negative change causes reduction in both the responses.

It can be observed that the changes (positive or negative) in the *y* or *z*- coordinates that cause reduction in peak bump camber angle also results in an increase in peak roll camber response, except for the negative changes in the *z*- coordinates of the lower control arm-chassis joints *O*. For example, a positive change in *y*- coordinates of joints *O* yields lower peak jounce camber but higher rebound camber, while an opposing effect on the roll camber is evident from Table 5.1. These results further suggest that the bump and roll camber angle responses are conflicting with respect to a change in the coordinates of the joints. A negative change in *z*- coordinates of joints *O*, however, could yield only small variations in both the bump and roll camber angle responses, while the corresponding roll center height decreases substantially.

The results further show an interesting coupling between the net camber angle, and roll and bump camber responses. Notable reductions in the peak net camber angle during rebound occur for negative changes in vertical coordinates of joints *O*, *P*, *M* and *N*. Similar degrees of reductions also occur in peak roll camber under negative chassis roll, and in peak rebound camber under wheel vertical displacements. While the results from the sensitivity analysis could be interpreted to derive design guidelines in view of the performance measures and the inputs considered, the need for deriving a design compromise is also evident, particularly for realizing minimal variations in bump/roll camber and wheel track responses over the entire range of the inputs.

5.5.3 Selection of Optimal Joint Coordinates

The results of the sensitivity analysis suggest that the joint coordinates influence the kinematic performance measures significantly in a highly complex manner, while the influences on different measures are generally conflicting. Synthesis of a suspension for

achieving reduction in the lateral packaging space would thus involve compromises among the bump/roll camber, roll center height and track width variations. It is thus desirable to seek optimal joint geometry that could yield an acceptable design compromise among the conflicting kinematic performance measures while achieving reduction in the lateral packaging space.

A suspension synthesis objective is thus formulated to identify joint coordinates that would yield minimal variations in the bump/roll camber angle and the track width under wheel vertical displacement and chassis roll motions with constrained lateral space. A weighted performance index is thus formulated as:

$$F(v) = w_1 F_1(v) + w_2 F_2(v) + w_3 F_3(v) \tag{5.36}$$

where $F_1(v)$ and $F_2(v)$ are the sum of squares of variations in the bump camber, and wheel track over the entire range of wheel vertical travel, respectively, and $F_3(v)$ is the sum of the squares of the roll camber response over the entire range of chassis roll, such that:

$$F_1(v) = \int_{z_{u\min}}^{z_{u\max}} (\Delta\phi_R)^2 dz_u \; ; F_2(v) = \int_{z_{u\min}}^{z_{u\max}} (\Delta TW)^2 dz_u \; ; \text{ and } F_3(v) = \int_{\phi_{s\min}}^{\phi_{s\max}} (\Delta\phi_R)^2 d\phi_s \tag{5.37}$$

where the integration limits (z_{umin}, z_{umax}) and (ϕ_{smin}, ϕ_{smax}) refer to minimum and maximum wheel displacements and chassis roll inputs, respectively. In the performance index in Eq (5.36), w_1, w_2 and w_3 are the weighting factors of individual measures, and v is the vector of design variables comprising the y- and z- coordinates of the joints M, N, O and P. The weighted performance index was minimized using the gradient based sequential quadratic programming algorithm available in Matlab Optimization Toolbox

[151] to seek optimal joint coordinates, while a reduction in the lateral packaging space was sought by introducing inequality constraints. The lateral packaging space is expressed in terms of lateral distance between the *y*- coordinates of the joints *O* and *M*, and that of the wheel center *C*, while the reduction required in the lateral space of the optimal synthesis is expressed by fractional factors σ_1 and σ_2 of the nominal suspension geometry, such that:

$$\begin{aligned}(C_{y0} - M'_{y0}) &\le \sigma_1 (C_{y0} - M_{y0}) \\ (C_{y0} - O'_{y0}) &\le \sigma_2 (C_{y0} - O_{y0})\end{aligned} \tag{5.38}$$

where M'_{y0} and O'_{y0} are the *y*- coordinates of the joints *M* and *O*, respectively, identified from solutions of the minimization problem. The difference between the roll center heights of the optimal and nominal suspensions with respect to the corresponding static positions was also limited through a limit constraint with β_l and β_u, being the lower and upper limits, respectively, such that: $\beta_l \le \Delta(RCH) \le \beta_u$

The nominal coordinates were taken as the initial design vector, and *y*- and *z*-coordinates were bounded within ±80 mm and ±30 mm of the nominal values with the exception of *y*-coordinate of joint *P*, which was bounded within -80 and +20 mm. The solutions of the minimization problem were observed to be strongly dependent upon the weighting factors used in the performance index. The weighting factors were initially chosen to obtain nearly equal contributions of each measure to the weighted performance index. The subsequent solutions, however, were attained for different combinations of the weighting factors. Considering the comparable magnitudes of the camber angle and track width variations of the nominal geometry, identical weighting factors for each component (w_1=w_2) provided acceptable solutions for joint coordinates: *M′*(0.480, 0.838), *N′*(0.714,

0.862), O'(0.415, 0.392) and P'(0.750, 0.377). These coordinates resulted in approximately 10% and 12% reductions in the lateral space for the lower and upper control arms, respectively. The robustness of the optimal design, however, could be achieved by considering variations in the weighting factors.

The kinematic responses of the identified suspension synthesis are compared with those of the nominal geometry suspension to illustrate relative benefits of the synthesis. Figure 5.7 compares wheel track variation responses of the optimal and nominal suspension geometries under wheel vertical displacement inputs alone and simultaneous chassis roll and wheels displacements. The results suggest that the optimal synthesis yields lower wheel track variation during wheel jounce under wheels displacement input with only slight increase during wheel rebound beyond 75 mm. Under the simultaneous inputs, the optimal synthesis also yields lower track variations in jounce but higher in rebound above 50 mm compared to that of the nominal geometry suspension. Figure 5.8 compares the camber angle variation response of the suspensions under wheel vertical motion with and without the chassis roll. The results show that the optimal synthesis yields considerably lower bump and net camber angle variation compared to those of the nominal suspension over the entire jounce travel of the wheel under both types of excitations. The bump and net camber responses of the optimal synthesis in the rebound region are comparable with those of the nominal suspension.

The roll center height of the optimal synthesis in the static position was obtained as 106.5 mm, which represents only 1 mm deviation from that of the nominal geometry suspension. Although, the optimization method proposed here resulted in a slight increment in the roll camber responses, with beneficial effects in terms of reductions in

the bump camber and wheel track variation in jounce coupled with 10% reduction in the suspension lateral packaging space, the identified coordinates may be considered as an acceptable design compromise. Further, the total roll response of vehicle under handling maneuvers can be controlled by using anti-roll bars.

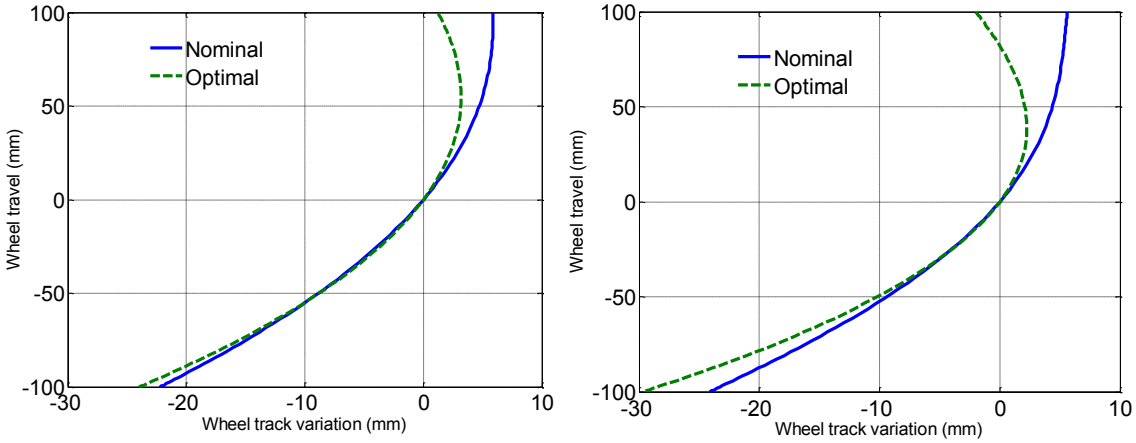

(a) (b)

Figure 5.7: Comparisons of variations in wheel track responses of the optimal and nominal geometry suspensions under wheel vertical travel inputs: (a) without chassis roll; and (b) with chassis roll

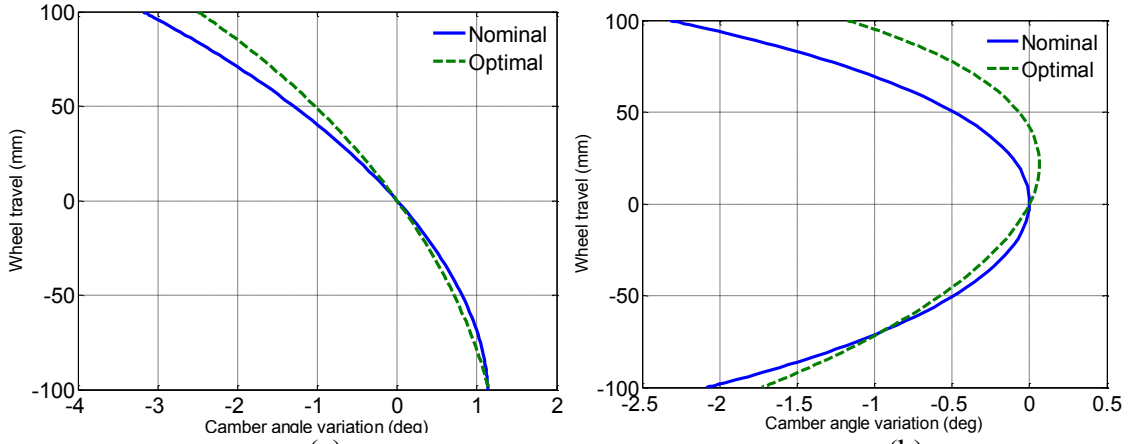

(a) (b)

Figure 5.8: Comparisons of variations in camber angle of the right wheel of optimal and nominal geometry suspensions under wheel vertical travel inputs: (a) without chassis roll; and (b) with chassis roll input

Although 10 and 12% reductions in the lateral space was achieved in terms of change in the *y*- coordinates of lower and upper control arms, reduction in the length was limited to that of lower control arm. The length of lower control arm is seen to be decreased by

12%, while that of the upper control arm is increased by 12%. This suggests that minimizing the bump/roll camber angle may not be feasible with reduction in the control arm lengths, and a compromise in the vertical space may be necessary.

5.6 Kineto-dynamic Responses of the Roll-Plane Vehicle Model

The kineto-dynamic formulations presented in Sections 5.3 are solved to determine the kinematic and dynamic responses of the vehicle model to transient excitations representing idealized 'bump' and 'pothole' excitations, as described in Section 3.6.3. The model parameters used in simulation are summarized in Table 5.2. The results attained are discussed in the following sections.

5.6.1 Influences of Suspension Linkage Kinematics

Dynamic responses of the proposed kineto-dynamic roll-plane vehicle model are compared with those of the conventional model so as to illustrate the influences of suspension kinematics on the dynamic responses. The transient responses of both the models to idealized bump and pothole inputs of 50 mm amplitude at the right wheel (obtained by numerical solutions of kineto-dynamic formulations) are evaluated at a forward velocity of 3 m/s, in terms of: sprung mass acceleration at the mass center (cg); sprung mass roll angle; and left- and right tire force ratios. The results presented in Figs. 5.9 and 5.10 suggest considerable contributions of the kinematics to the dynamic responses.

The peak sprung mass acceleration responses of the conventional model (section 5.4) with equivalent spring and damping rates are lower than those of the kineto-dynamic model under both bump and pothole type excitations, as seen in Fig. 5.9 (a).

Table 5.2: Vehicle and suspension data

Parameter	Value
Sprung mass (m_s)	878.76 kg
Sprung mass moment of inertia about x- axis (I_x)	247.00 kg-m^2
Unsprung mass (m_{uR} and m_{uL})	42.27 kg
Unsprung mass moment of inertia about x- axis (I_{ux})	1.86 kg-m^2
Suspension spring stiffness (K_s)	38404 N/m
Suspension damping rate (C_s)	3593.4 Ns/m
Tire vertical stiffness (K_t)	200 kN/m
Tire damping rate (C_t)	352.27 Ns/m
Tire lateral stiffness (K_{tl})	100 kN/m
Tire effective radius (R)	0.35 m
Torsion bar stiffness (K_{tb})	560 Nm-rad

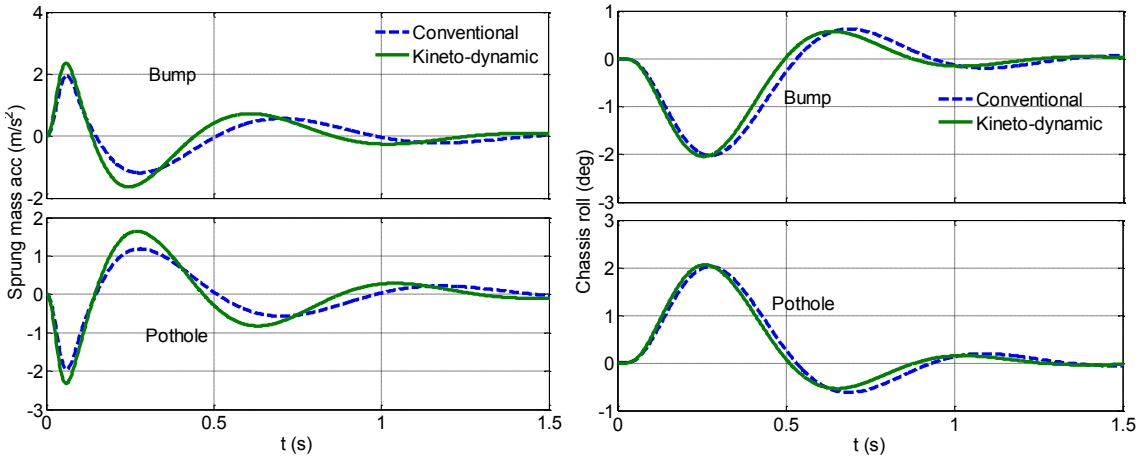

Figure 5.9: Comparisons of sprung mass responses of kineto-dynamic and conventional roll-plane models under idealized bump and pothole type excitations (z_{0max}=±50 mm): (a) vertical acceleration; and (b) chassis roll angle.

The acceleration responses of the kineto-dynamic model to bump and pothole excitations are asymmetric, as it was observed in the quarter-car model responses (Fig. 3.8). Furthermore, the oscillations in the kineto-dynamic model responses occur at a slightly higher frequency than that of the conventional model responses. The peak chassis roll angle response of the kineto-dynamic model is also slightly higher than that of the conventional model, while the conventional model exhibits higher second peak in the roll angle response, as seen in Fig. 5.9 (b). The results also suggest a slightly higher roll

frequency and roll damping of the kineto-dynamic model in comparison to the conventional roll dynamic model. Slight increase in the vertical frequency (attributed to an increase in the effective spring rate) was also observed in the kineto-dynamic quarter-car model.

The tire force ratio responses of left- and right wheels of the conventional and the kineto-dynamic model to bump and pothole inputs of ±50 mm amplitude are compared in Figs. 5.10 (a) and (b), respectively. The results suggest that inclusion of suspension linkages in the dynamic model affects the left tire force ratio response significantly under both bump and pothole inputs. The kineto-dynamic model response during the excitation period appears to be more nonlinear than that of the conventional model, which can be attributed to suspension linkages kinematics and tire lateral compliances. The peak left tire force of the kineto-dynamic model under bump and pothole inputs are slightly greater than that of the conventional model. The right-tire force response of the kineto-dynamic model is comparable to that of the conventional model, while the oscillations in the kineto-dynamic model response occur at a slightly higher frequency.

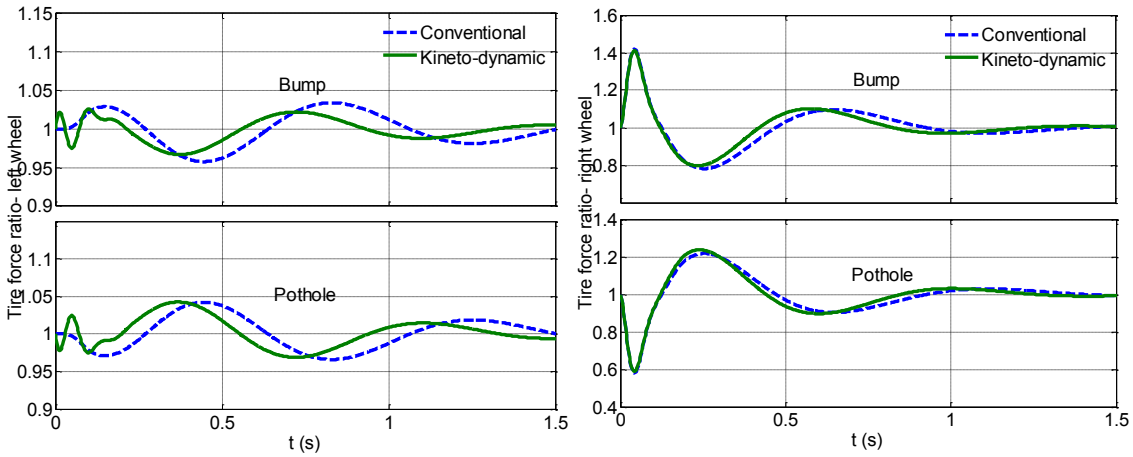

Figure 5.10: Comparisons of tire force ratio responses of kineto-dynamic and conventional roll-plane models under idealized bump and pothole type excitations (z_{0max}=±50 mm) of: (a) the left; and (b) the right tires.

5.6.2 Effects of Optimal Suspension Geometry

The above results suggest notable contributions of the suspension kinematics on the dynamic responses. Variations in suspension joint coordinates are thus expected to influence the dynamic responses of the vehicle, as it was observed for the quarter vehicle model. The optimal suspension synthesized in section 5.5.3 on the basis of kinematic responses to wheel vertical displacement or chassis roll is employed in the kineto-dynamic model to study the effects on the dynamic responses. The kinematic and dynamic responses of the kineto-dynamic half car model with the optimal joint coordinates are compared with those of the model with nominal joint coordinates in terms of: sprung mass acceleration; chassis roll angle; normalized load transfer (load transfer normalized by the total wheel load); and variations in the camber angle and wheel track under idealized bump and pothole inputs (z_{0max}=±50 m; forward velocity=3 m/s) applied at the right wheel. The results presented in the Figs. 5.11 to 5.13 are also discussed in view of the optimization method used in the study.

The results in Fig. 5.11 (a) show that the kineto-dynamic model with the optimal joint coordinates yields lower peak acceleration responses compared to the model with nominal coordinates under bump and pothole excitation. The peak acceleration response of the model with optimal coordinates is approximately 2.00 m/s^2, which is 11% lower than that of the model with nominal coordinates. The peak roll angle responses of the kineto-dynamic model with optimal joint coordinates under idealized bump and pothole excitations are also slightly lower than that those of the model with nominal suspension geometry. The magnitudes of second peak in roll angle, however, tend to be slightly higher for the optimal suspension geometry. The lower first peak is attributed to lower

effective roll stiffness, while the higher second peak is due to lower roll damping of the model with optimal coordinates. The results in Fig. 5.11 (a) and (b) suggest that the optimal coordinates selected on the basis of kinematic response alone cause significant change in the effective spring and damping rates, which could influence the ride and handling dynamics of the vehicle considerably.

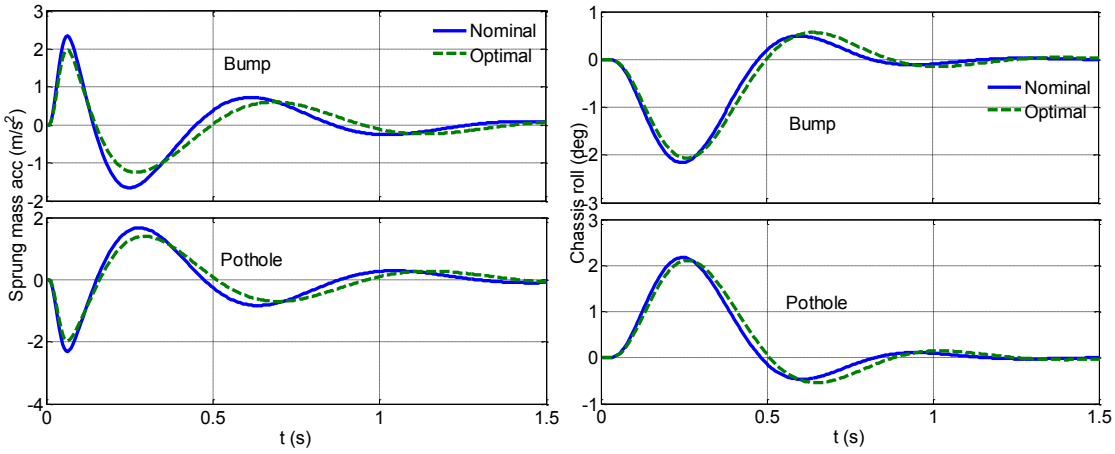

(a) (b)

Figure 5.11: Comparisons of sprung responses of kineto-dynamic model with nominal and optimal joint coordinates under idealized bump and pothole type of excitations (z_{0max}=±50 mm): (a) vertical acceleration; and (b) chassis roll angle.

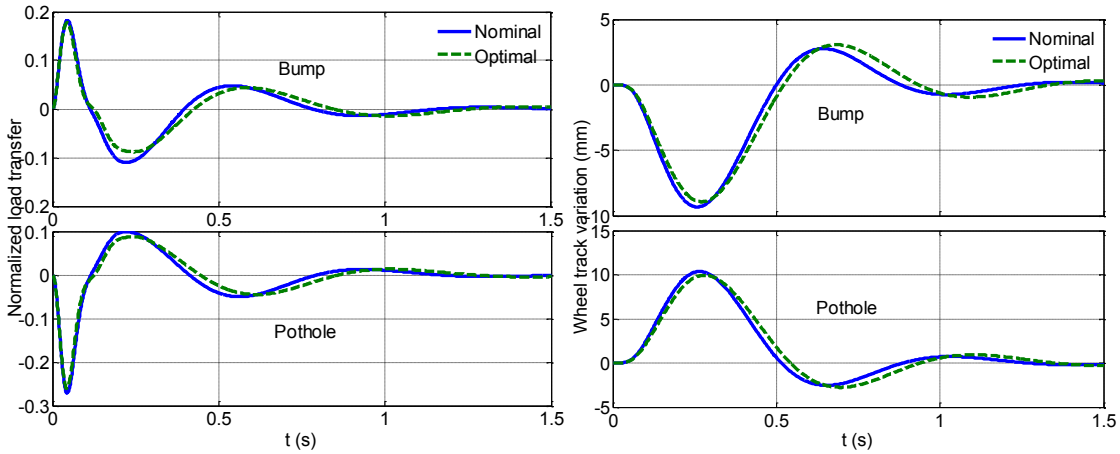

(a) (b)

Figure 5.12: Comparisons of responses of kineto-dynamic model with nominal and optimal joint coordinates under idealized bump and pothole type excitations (z_{0max}=±50mm): (a) normalized load transfer; and (b) wheel track variation

Figure 5.12 (a) shows the lateral load transfer response of the kineto-dynamic model with nominal and optimal joint coordinates. The peak load transfer responses of both the models are generally lower under a bump input than under the pothole input (the peak magnitudes of 0.18 and 0.28 under bump and pothole inputs). This is mainly attributed to the larger total tire force (sum of left- and right tire forces) under bump input than that under the pothole input. Under the bump input, the tire spring undergoes compression initially, while under the pothole input it experiences expansion. Both nominal and optimal joint coordinates yield comparable responses during the period of input, while the model with nominal coordinates yields slightly higher peak responses during the free oscillations. Variations in wheel track responses of the model with nominal and optimal joint coordinates follow the similar trend observed in the sprung mass roll angle, as seen in Fig. 5.12 (b).

The peak camber angle variation responses of both the wheels with optimal joint coordinates are considerably lower compared to those of the model with nominal coordinates, particularly the first peaks, under both bump and pothole type inputs as shown in Figs. 5.13. The second peak in camber variation response of the model with optimal joint coordinates, however, is higher compared to that with the nominal coordinates. Considering that the magnitudes of the second peaks in camber variation responses are significantly lower, it may be deduced that the optimization method adopted in this study also yields beneficial effects under transient excitations. The results in Figs. 5.13 (a) and (b) suggest that the left wheel exhibits higher camber angle response than the right wheel. It needs to be noted here that the right wheel undergoes a vertical displacement relative to the chassis, while the vertical motion of the left wheel (due to

tire spring compression) is very small. The net camber angle variation of the right wheel is thus considerably lower.

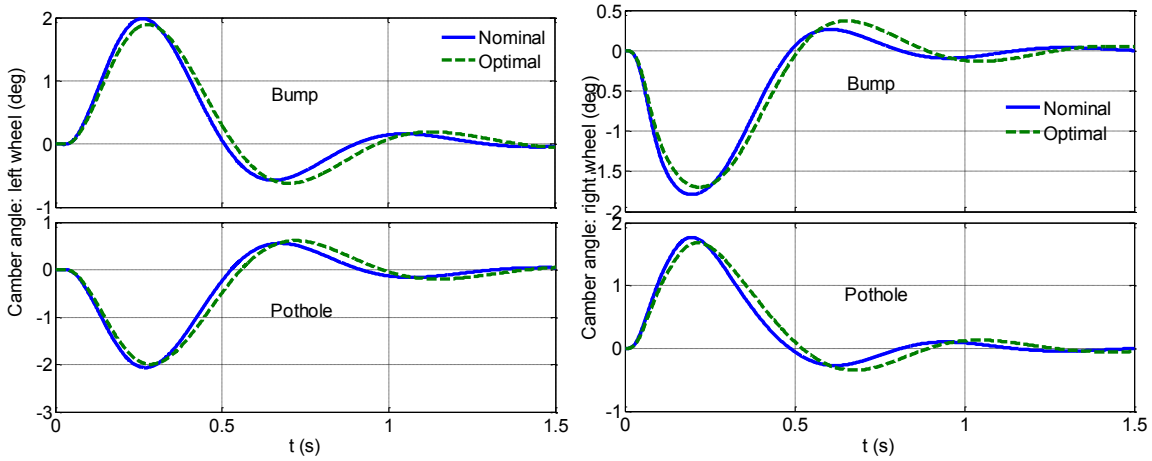

Figure 5.13: Comparisons of camber angle variations of kineto-dynamic model with nominal and optimal joint coordinates under idealized bump and pothole type excitations (z_{0max}=±50 mm): (a) the left; and (b) the right wheel.

The results in the Figs. 5.11 and 5.12 (a) suggest that the suspension kinematics contributes considerably to the dynamic responses of the proposed half-car model, particularly due to variations in the effective spring and damping rates. The suspension geometry factor ψ that relates the effective spring rate to the actual spring rate of the suspension with the optimal joint coordinates was estimated as 0.54 (Section 3.3), which is lower than that of the nominal geometry (0.59). Apart from the linkage/joints geometry, the variation in the wheel rate would also depend upon the strut mounting locations. The influences of variations in the strut mounting locations are thus investigated by varying the y- coordinates of the upper- (B_y) and lower- (A_y) strut mounts in the positive and negative senses by 50 mm. The changes in the coordinates of the optimal geometry suspension were realized individually, while maintaining the other coordinates at their nominal positions (optimal joint coordinates selected in section 5.4).

Furthermore, the optimal upper and lower control arms joints coordinates selected in the previous section were considered for the study. Figures 5.14 and 5.15 illustrate effects of variations in the lower and upper strut mounts location on the sprung mass acceleration and roll angle responses of the kineto-dynamic model under an idealized bump input of 50 mm amplitude at the right wheel.

A negative change in y- coordinate of the lower strut mount (A_y-) results in significant increase (in the order of 30%) in the sprung mass vertical acceleration and roll angle responses of the kineto-dynamic model as seen in Figs. 5.14 (a) and (b). The vertical and the roll oscillation frequencies increase considerably, which suggests that reducing the distance of the lower mount from the chassis joint increases the effective wheel rate. On the other hand, a positive change in the strut lower mount location causes reduction in these responses and the oscillation frequency. Variations in the y- coordinate of the strut upper mount, however, cause relatively less significant influences on the sprung mass acceleration response, as seen in Fig. 5.15 (a). The sprung roll angle response is almost insensitive to variations in the upper strut mount location. The results thus suggest that the dynamic response of the roll-plane vehicle model are highly sensitive to the lower strut mount coordinates, which demands considerable attention during suspension synthesis.

The influences of variations in the strut mounting locations on the camber and wheel track variation responses were also evaluated, although the results are not presented. It is evident from the results in Figs. 5.11 to 5.15 that the kinematic and dynamic responses are strongly influenced by the suspension joint coordinates and strut mounts. The selection of optimal coordinates thus involves study of both kinematic and dynamic

responses rather than the kinematic responses alone, and the proposed kineto-dynamic model would be instrumental in deriving such optimal joint coordinates. Defining an objective function involving kinematic and dynamic responses such as camber angle and wheel track variations, sprung mass acceleration and roll angle response and tire force variations under transient or random excitations, with joint coordinates as the design vector could yield optimal suspension joint coordinates of the double wishbone suspension.

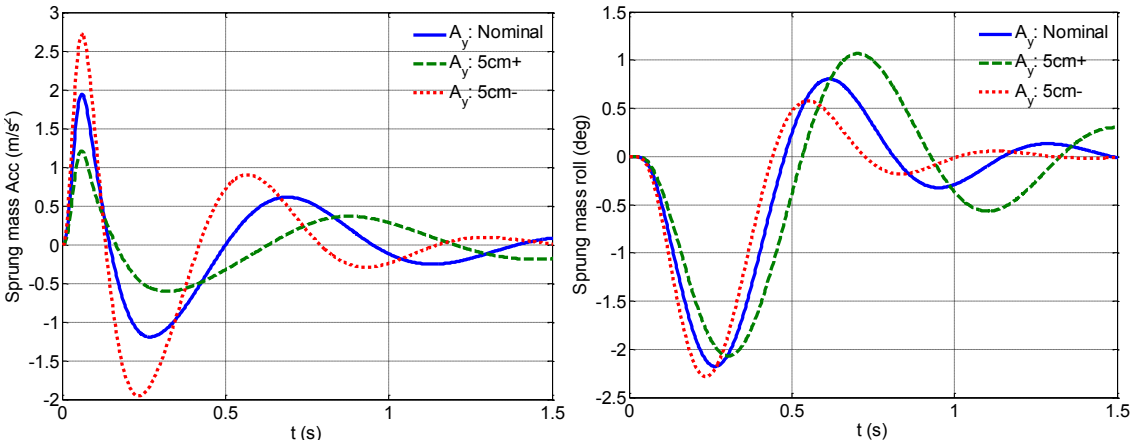

(a) (b)

Figure 5.14: Effects of variations in the lower strut mount coordinates on the responses of the sprung mass to an idealized bump excitation: (a) vertical acceleration; and (b) roll angle.

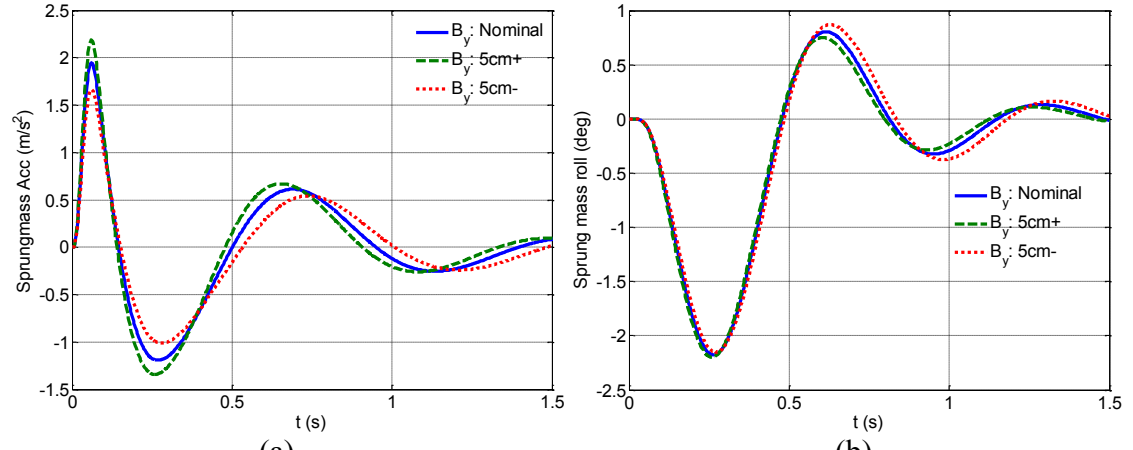

(a) (b)

Figure 5.15: Effects of variations in the upper strut mount coordinates on the responses of the sprung mass to an idealized bump excitation: (a) vertical acceleration; and (b) roll angle.

5.6.3 Influences of Anti-roll Bar on the Kinematic Response Measures

Auxiliary roll stiffness such as antiroll bars help to reduce the sprung mass roll angle and lateral load transfers under lateral excitation due to steering inputs, while the antiroll bars are also known to increase the roll angle response of the sprung mass under differential vertical road inputs [101]. The influences of antiroll bar on the suspension kinematic responses, however, could not be found in the literature. The sprung mass roll angle, wheel track variation, and the left- and right wheels camber angle variation responses of the kineto-dynamic model with and without an antiroll bar are thus evaluated under the bump and pothole inputs at the right wheel. The results presented in Figs. 5.16 and 5.17 consider effects of the antiroll bar on both the kinematic and dynamic responses.

The roll angle response of the model with antiroll bar is higher compared to that of the model without the antiroll bar, under both the bump and pothole excitation, as seen in Fig. 5.16 (a). The addition of an antiroll bar increases the effective roll stiffness and thus the roll frequency, which is evident from the roll angle response. The peak roll-angle responses of the model with and without antiroll bar are at 1.95° and 2.3°, respectively, under the bump and pothole inputs. The oscillations in the responses with and without antiroll bar occur near 1.35 and 1.7 Hz frequency, respectively. The higher roll angle response with the antiroll bar is most likely attributed to variations in suspension kinematic responses, which are strongly affected by the relative motions between the sprung and unsprung masses. The effect on the wheel track variation responses, however, is negligible as seen in Fig. 5.16 (b), which is attributable to negligible lateral

motion of the left wheel-ground contact point under bump excitation at one wheel, particularly when the lateral DOF of the sprung mass is neglected.

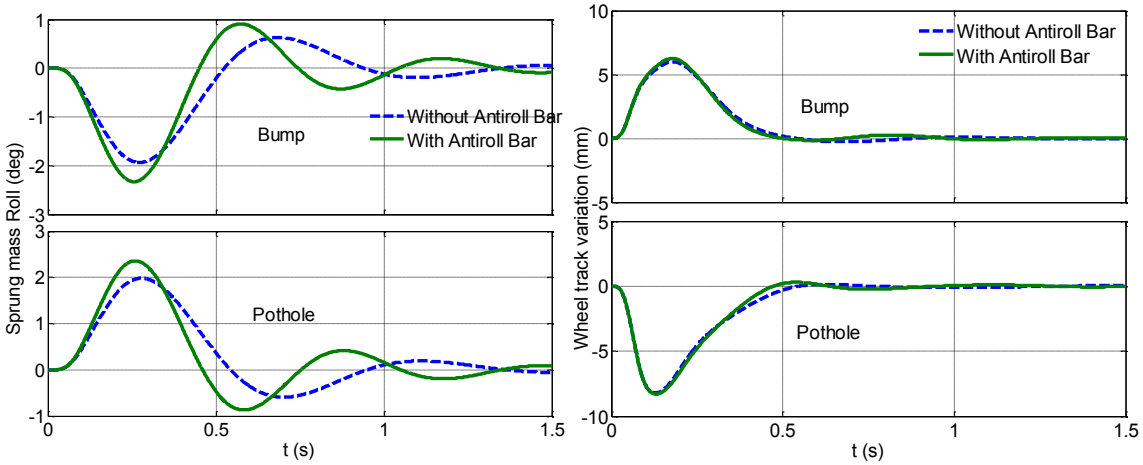

(a) (b)

Figure 5.16: Effects of antiroll bar on the sprung mass roll angle and wheel track variation responses of the kineto-dynamic model under idealized bump and pothole type excitations (z_{0max}=±50 mm): (a) sprung mass roll angle; and (b) wheel track variation.

The presence of an antiroll bar also causes significant changes in the camber angle responses of both the left- and right wheels, as shown in the Figs. 5.17 (a) and (b), respectively. The results show that peak left wheel camber is greater than that of the right wheel, irrespective of the antiroll bar and the type of input. This is attributed to the opposing bump and roll camber of the right wheel that undergoes a vertical motion during the bump. The net camber angle variation, however, is predominantly determined by the magnitude of the sprung mass roll angle. This can be observed from the oscillations in the camber variation responses, which follow a trend similar to that observed in the roll angle response (Fig. 5.16 (a)). The results in Figs. 5.16 and 5.17 clearly suggest that addition of an antiroll bar in the suspension could change the camber angle response under differential road inputs at two wheels of an axle, which would further depend upon the antiroll bar stiffness. Synthesis of antiroll bar, thus poses an

additional design challenge in terms of kinematic responses, apart from the commonly known design compromises between ride and roll angle under lateral inputs. Previous studies have failed to identify this additional design compromise due to simpler vehicle and suspension models considered in these studies.

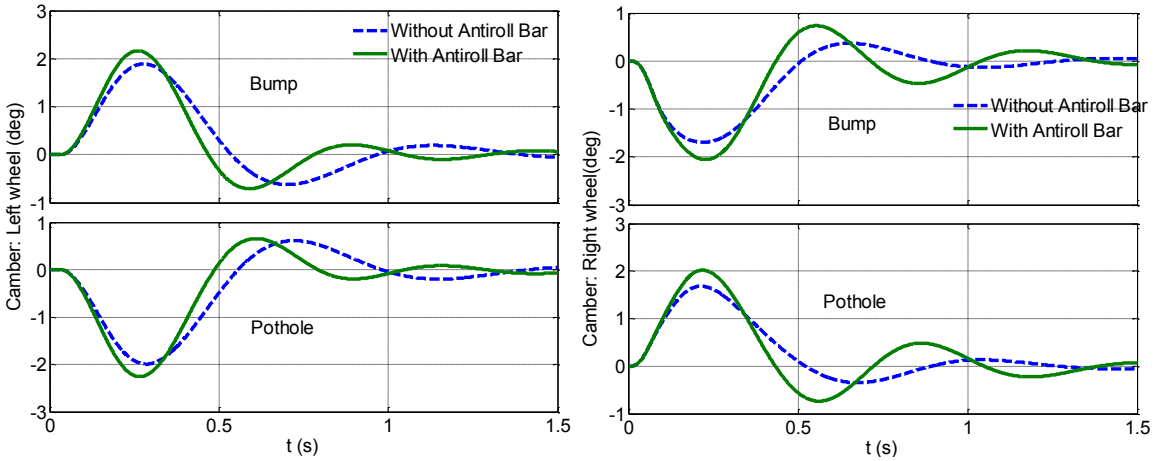

Figure 5.17: Comparisons of camber angle variation responses of the kineto-dynamic model with and without antiroll bar under idealized bump and pothole type excitations (z_{0max}=±50 mm): (a) the left wheel; and (b) the right wheel.

5.6.4 Influences of Suspension Damping Asymmetry

The influence of damper asymmetry on the kinematic and dynamic responses of the kineto-dynamic roll-plane model of the vehicle is evaluated under bump and pothole type of excitations at the right wheel. Two types of asymmetric dampers were selected for the relative analyses similar to those described in section 4.6.2 for the quarter car model: (a) ζ_c=0.1 and ρ=5; and (b) ζ_c=0.2 and ρ=2. Sprung mass vertical acceleration and roll angle, and left- and right wheel camber angle variation responses of the kineto-dynamic roll-plane model with asymmetric damper are compared with those of the model with the linear equivalent damper in Figs. 5.18 to 5.19, under 50 mm bump and pothole inputs at a forward velocity of 3 m/s.

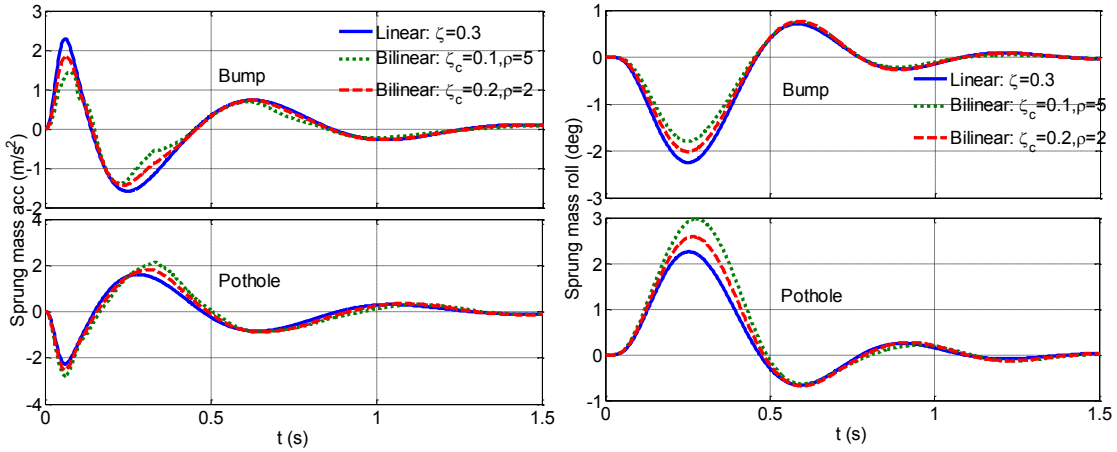

(a) (b)

Figure 5.18: Comparisons of sprung mass responses of the kineto-dynamic model with bilinear (ζ_c=0.1; ρ=5 and ζ_c=0.2; ρ=2) and linear equivalent dampers under idealized bump and pothole type excitations (z_{0max}=±50 mm): (a) vertical acceleration; and (b) roll angle.

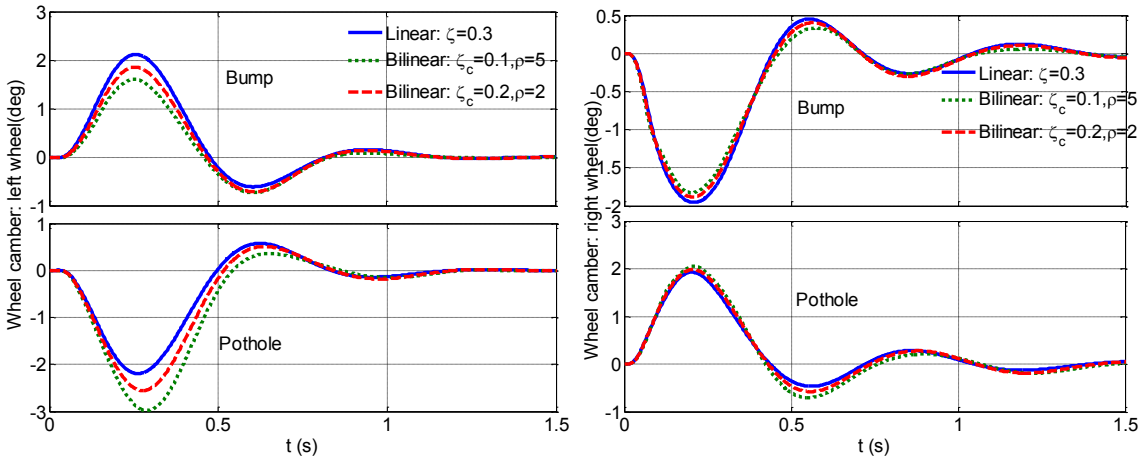

(a) (b)

Figure 5.19: Comparisons of camber angle variations of the kineto-dynamic model with bilinear (ζ_c=0.1; ρ=5 and ζ_c=0.2; ρ=2) and linear equivalent dampers under idealized bump and pothole type excitations (z_{0max}=±50 mm): of (a) the left wheel; and (b) the right wheel.

The kineto-dynamic model with light compression damping (ζ_c=0.1, ρ=5) yields lower peak sprung mass acceleration and roll angle response of the model with other dampers. Both the peak acceleration and roll responses of the same damper, however, are relatively higher under the pothole input, as seen in Fig. 5.18 (a) and (b). The peak sprung mass response of the model with linear and bilinear damper with compression mode damping ratios 0.2 and 0.1, respectively, are 2.2, 1.8 and 1.5 m/s^2, under the bump input, and

-2.25, -2.5 and -2.7 m/s^2 under the pothole input. The results show trends similar to those obtained from the quarter car kineto-dynamic model (section 3.4.2). The responses were also obtained under pure vertical motions at both the wheels, which were identical to those obtained for the quarter-car model. The peak roll responses of the model with linear and bilinear dampers with compression mode damping ratio 0.2 and 0.1, respectively, are -2.2, -2 and -1.8° under the bump input, and 2.2, 2.55, and 3° under the pothole input. The results in the figure thus suggest that the roll angle responses of the model with bilinear dampers are opposite under the bump and pothole inputs. The model with lower compression mode damping (ζ_c=0.1) yields significantly larger roll angle response compared to those of the model with linear and bilinear damper (ζ_c=0.2) under the pothole type input. It is thus evident that the damper synthesis demands an additional design compromise in terms of conflicting roll angle response under bump and pothole excitations.

Damping asymmetry also yields important influence on the camber angle variation responses of the suspension, particularly that of the left wheel (when excitation is given to the right wheel), as shown in the Fig. 5.19 (a) and (b). The peak camber variations of the unexcited wheel (left wheel) are 2.1, 1.9 and 1.5°, respectively, under the bump excitation with the linear and bilinear damper with compression damping ratios of 0.2 and 0.1. Under the pothole input, the kineto-dynamic model with linear damper exhibits considerably smaller left wheel camber variation response compared to those of the model with bilinear damper. The influence of damper asymmetry on the camber variation response of the right wheel (excited wheel), on the other hand, is less significant, as seen in the Fig. 5.19 (b). It should be noted that the camber responses shown in the figures are

the net results of bump and roll cambers, and the excited wheel experiences both the bump and roll, while the unexcited wheel experiences only the roll camber. This clearly suggests that the asymmetric damping could influence roll camber response of a suspension apart from the bump camber, as observed in Chapter 4. Such a coupling between the roll camber and the damper asymmetry has not been identified in the reported studies.

The results in Figs. 5.18 and 5.19 show significant influences of asymmetric damping on the kinematic and dynamic responses of the roll-plane vehicle model, while the results are limited to a very low vehicle speed (3 m/s). The influences of damper asymmetry on the responses are thus further investigated over a wide range of forward speeds (3 to 15 m/s). Figures 5.20 to 5.21 illustrate the peak magnitudes of kinematic and dynamic responses of the model with three different dampers as a function of vehicle forward velocity.

The peak sprung mass acceleration and roll angle responses of the model with linear and bilinear dampers are compared in Figs. 5.20 (a) and (b), respectively, as a function of the speed. Under the bump input, the bilinear damper with lower compression mode damping (ζ_c=0.1; ρ=5) yields lowest peak acceleration response at speeds below 7 m/s and lowest roll angle at speeds below 12 m/s. The increase in peak acceleration at higher velocities is attributable to increase in the second peak rather than the first peak response, which is in agreement with the results observed in Chapter 4. A similar trend was also observed in the second peak in roll angle response of the model with ζ_c=0.1 under bump input at speeds above 12 m/s. The model with equivalent linear damper yields highest acceleration at speeds below 10 m/s and highest roll angle in the entire speed range. The

bilinear damper with ζ_c=0.2 yields lowest peak sprung mass acceleration and roll angle response to bump inputs at speeds above 7 m/s. Under the pothole input, linear damper yields lowest peak acceleration and roll angle responses in the entire speed range. The results suggest conflicting design demands on the damper synthesis and that a bilinear damper with ζ_c=0.2 could yield good compromises in responses to bump and pothole excitations.

The camber angle variation responses of the left- and right wheels of the kineto-dynamic roll-plane model with linear and bilinear dampers under bump and pothole inputs are presented in Figs. 5.21 (a) and (b), respectively. The peak left wheel camber angle response, which is mainly due to contribution of the roll camber angle, exhibits trend similar to the peak roll angle response, as shown in Fig. 5.20 (b). Under the bump input, higher peak camber angle of the left wheel is observed for the model with linear dampers until the speed of 12.5 m/s, while above this speed, the model with ζ_c=0.1 yields higher peak camber responses. The left wheel camber variation under the pothole input is more uniform, with the linear damper yielding the lowest camber variation in the entire velocity range, as seen in Fig. 5.21 (b). At speeds below 7 m/s, the kineto-dynamic model with linear damper yields higher right wheel camber response, which is attributed to the higher roll angle at lower velocities. The bump camber which is opposite in direction to that of the roll camber reduces the net camber response (compared to the left wheel camber responses). At high velocity bump and pothole inputs, however, the contribution of roll camber is higher compared to that of bump camber in the net camber variation response. The results thus suggest that at lower velocities (below 7 m/s), bilinear dampers

with lower compression damping yield lower camber variation response, while above 7m/s, linear dampers yield lower camber variation.

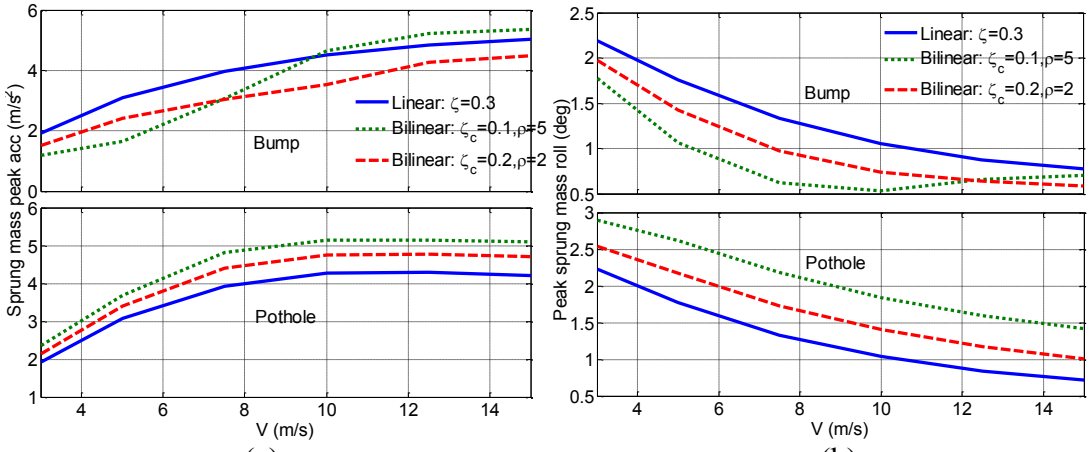

Figure 5.20: Comparisons of sprung mass responses of kineto-dynamic model with bilinear (ζ_c=0.1; ρ=5 and ζ_c=0.2; ρ=2) and linear equivalent dampers under idealized bump and pothole type excitations (z_{0max}=±50 mm) in the forward velocity range 3-15 m/s: (a) vertical acceleration; and (b) roll angle.

Lower compression mode damping yields slight beneficial influences on the normalized load transfer response of the model at low velocity (3-5 m/s) bump inputs, while the load transfer response of the model with the same damper at velocities above 5 m/s is considerably larger compared to those with the other dampers as seen in Fig. 5.22. Furthermore, under bump excitations, the bilinear dampers with ζ_c=0.1 cause wheel lift-off (normalized load transfer=1) at a relatively lower speed of 10 m/s, while the bilinear dampers with ζ_c=0.2 and the linear dampers yield wheel lift-off at higher speed of 12.5 and 15 m/s, respectively. Wheel lift-off of the model under pothole input, in general, occurs at much lower velocities than those observed under the bump inputs, irrespective of the type of damper employed. The bilinear damper with ζ_c=0.1 yields normalized load transfer of 1 at 7.5 m/s, while the linear and higher compression damping bilinear dampers yield wheel lift-off at only slightly higher speeds. Ironically, linear damper

yields better (lower) load transfer response under both bump and pothole inputs in the entire velocity range.

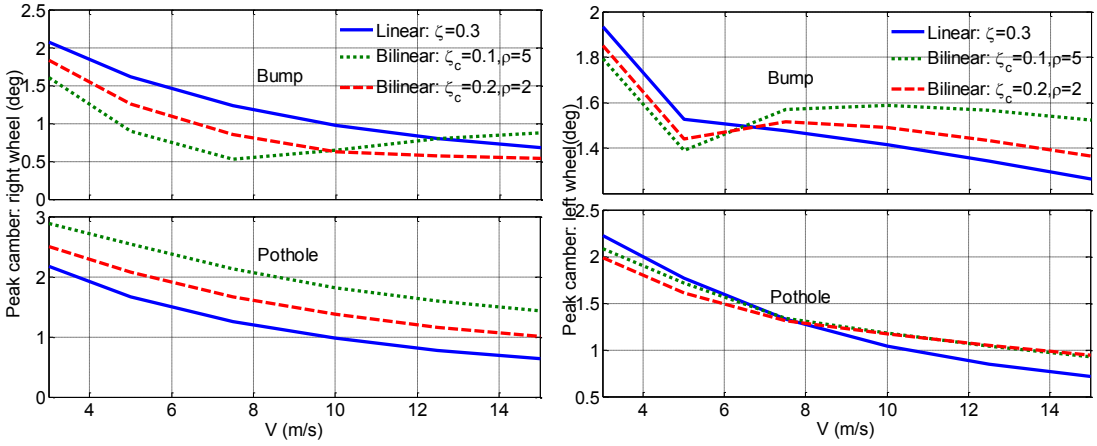

(a) (b)

Figure 5.21: Comparisons of camber angle variation responses of kineto-dynamic model with bilinear (ζ_c=0.1; ρ=5 and ζ_c=0.2; ρ=2) and linear equivalent dampers idealized bump and pothole type excitations (z_{0max}=±50 mm), in forward velocity range 3-15 m/s: (a) the left wheel; and (b) the right wheel.

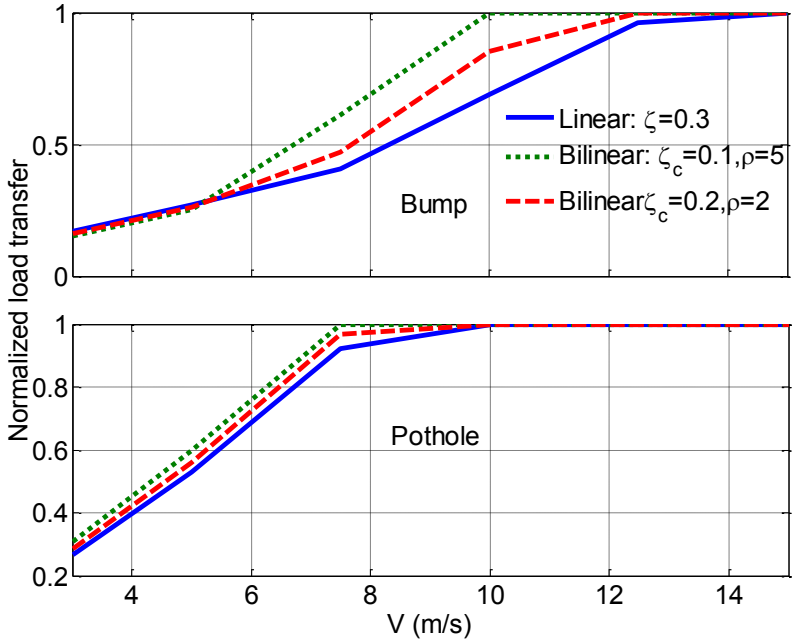

Figure 5.22: Comparisons of normalized load transfer response of kineto-dynamic model with bilinear (ζ_c=0.1; ρ=5 and ζ_c=0.2; ρ=2) and linear equivalent dampers under idealized bump and pothole type excitations (z_{0max}=±50 mm), in the forward velocity range 3-15 m/s.

The results in Figs. 5.18 to 5.22 thus suggest significant influences of asymmetric dampers on the dynamic and kinematic responses, which are also complex functions of the vehicle forward velocity and type of inputs. The responses of the model would further depend upon the saturation limits and high-speed reduction ratios of the asymmetric damper. Synthesis of an asymmetric damper would thus necessitate consideration of the kinematic and dynamic responses of the kineto-dynamic half-car model under different inputs including random road excitations. Further, the results have also suggested a complex coupling between the vertical excitation and the dynamic load transfer which is also a function of the lateral excitation. Consideration of simultaneous vertical wheel and lateral excitation at the sprung mass *cg* could yield considerable information about further couplings between the responses, which are instrumental and vital for the synthesis of the suspension components including an asymmetric damper.

5.7 Summary

A kineto-dynamic roll-plane vehicle model comprising double wishbone suspension is formulated and suspension geometry is synthesized considering the kinematic responses and lateral space constraints. The results attained from a sensitivity analysis suggested that changes in *z*- coordinates of any joint cause relatively more significant influence on the kinematic performances compared to those in the *y*- coordinates, while the y-coordinates of some of the joints are most critical in view of the lateral packaging space. The joint coordinates that reduce the bump camber variation under wheel vertical motion, generally caused higher roll camber under chassis roll. The optimal geometry synthesis obtained through minimization of a composite performance index comprising the kinematic responses and constrained lateral packaging space resulted in 10 and 12%

reductions in the lateral space required for lower and upper control arms, together with reductions in variations in bump camber and track width responses under wheels vertical displacement, although the roll camber increased only slightly. The results thus suggest that achieving minimal lateral packaging space would necessitate compromise in the vertical packaging space.

Comparisons of dynamic responses of the kineto-dynamic model with those of a conventional model showed significant contribution of the kinematic linkages. Higher sprung mass vertical and roll frequencies were observed from the kineto-dynamic responses compared to those of the conventional model. Furthermore, the camber angle variation response is strongly influenced by the antiroll bar, which has not been reported in previous studies. The kineto-dynamic responses also revealed complex dependency upon damper asymmetry ratio, vehicle forward speed and type of input. An asymmetric damper synthesis is thus a complex task involving a large number of design compromises among the vertical and roll dynamic, and kinematic performance measures. Formulation of a performance index comprising dynamic and kinematic responses of the model, and subsequent minimization of the performance index would be instrumental in obtaining an optimal asymmetric damper.

CHAPTER 6

INFLUENCES OF SUSPENSION GEOMETRY, DAMPER AND JOINT BUSHING FAULTS

6.1 Introduction

Dynamic responses of a road vehicle are influenced by properties of suspension components, such as spring, damper and bushings in a significant manner. The responses of the vehicle could vary with change in suspension component properties, which are most likely to occur due to continued usage under varying operating conditions including weather and changing ambient temperature. Faults in the suspension system could arise from wear and tear, aging or as a result of past collisions, which could alter the dynamic responses or might cause breakdown of vehicles. An early warning of such faults in the suspension components, however, could eliminate unexpected vehicle breakdowns. A few studies have proposed suspension fault diagnostics using vehicle models of varying complexities [54, 55, 61, 62], while these have mostly focused on faults in suspension dampers. Suspension fault, attributable to bushing clearances in upper bushing mount has been reported in a single study [62]. The study has concluded notable difference in the dynamic responses of the unsprung mass with bushing faults. Recent studies have reported significant attention to the synthesis of control arm bushings during vehicle design stage [53]. Furthermore, joint bushings are widely known to undergo wear and stiffen with age [38, 42]. The influences of such faults in control arm joint bushings on the dynamic responses, however, have not been reported in the literature.

Analytical quarter-car and half-car kineto-dynamic models presented in previous chapters could be extended to full car model and to include more comprehensive bushing characteristics. Such formulations, however, are very complex and demanding.

Alternatively, commercially available multibody dynamic tool, ADAMS/car provides suitable platform for suspension and vehicle dynamic model development and subsequent analyses. This chapter presents study of influences of faulty suspension components on the dynamic responses of a full vehicle model developed in ADAMS/car. Four different types of suspension faults are considered in this study: (a) deformed suspension linkage; (b) faulty damper; (c) joints bushings clearances; and (d) aged bushings. The responses of the full-vehicle model with suspension faults, subjected to field measured random road excitations are compared with those of the model with normal suspensions. The results are discussed in connection with the development of an early warning based suspension fault diagnostic system.

6.2 Full-vehicle Model Development in ADAMS/car

A 95- DOF full-vehicle model comprising essential components of a vehicle, such as linkage suspension and steering systems, struts, power train, brake system, tires and vehicle bodies, is developed in ADAMS/car platform to evaluate the influences of suspension faults on the dynamic responses of a vehicle. The full-vehicle model, as illustrated in Fig. 6.1 is developed employing vehicle component subsystems available in ADAMS/car database library. The model comprises of double wishbone linkage mechanisms in both front and rear suspension systems and rack and pinion steering mechanism with two wheel steering system. The struts, comprising linear springs and nonlinear dampers are mounted on the lower control arm of the suspensions. Linkages between wheel knuckle and the chassis are joined to the chassis through revolute joints, while each of the joints excepting the ball joints (between control arm and spindle)

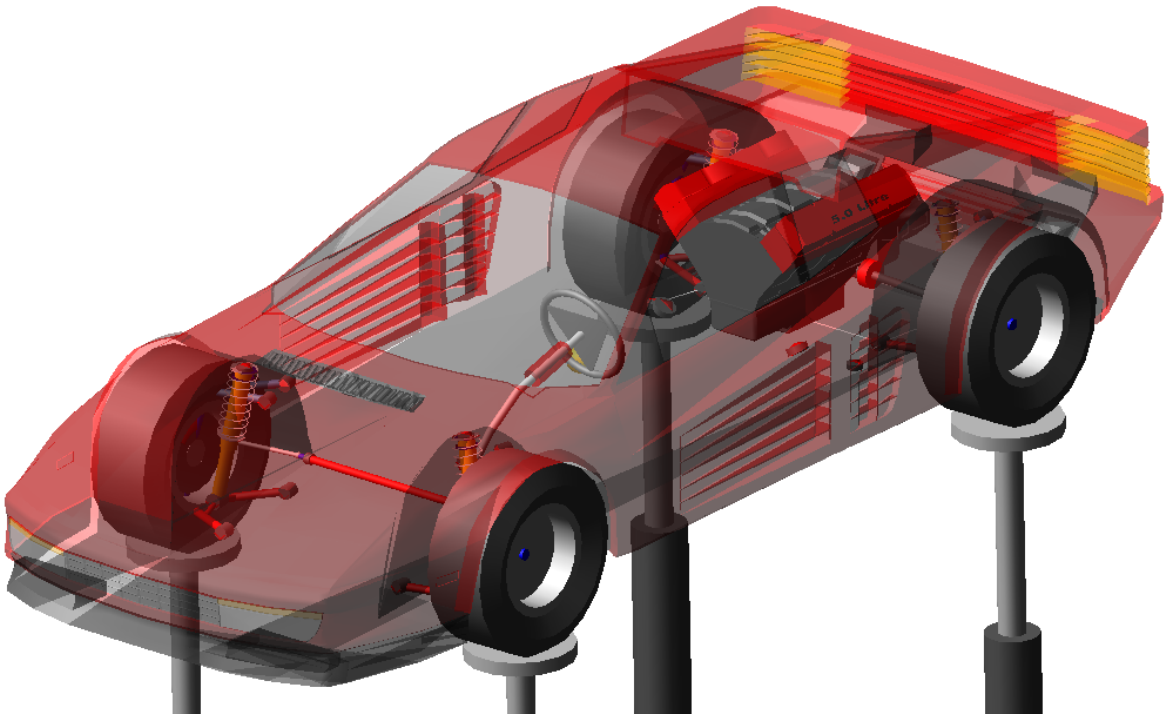

Figure 6.1: Multi-body dynamic full-vehicle model with four post test rig facility in ADAMS/car platform.

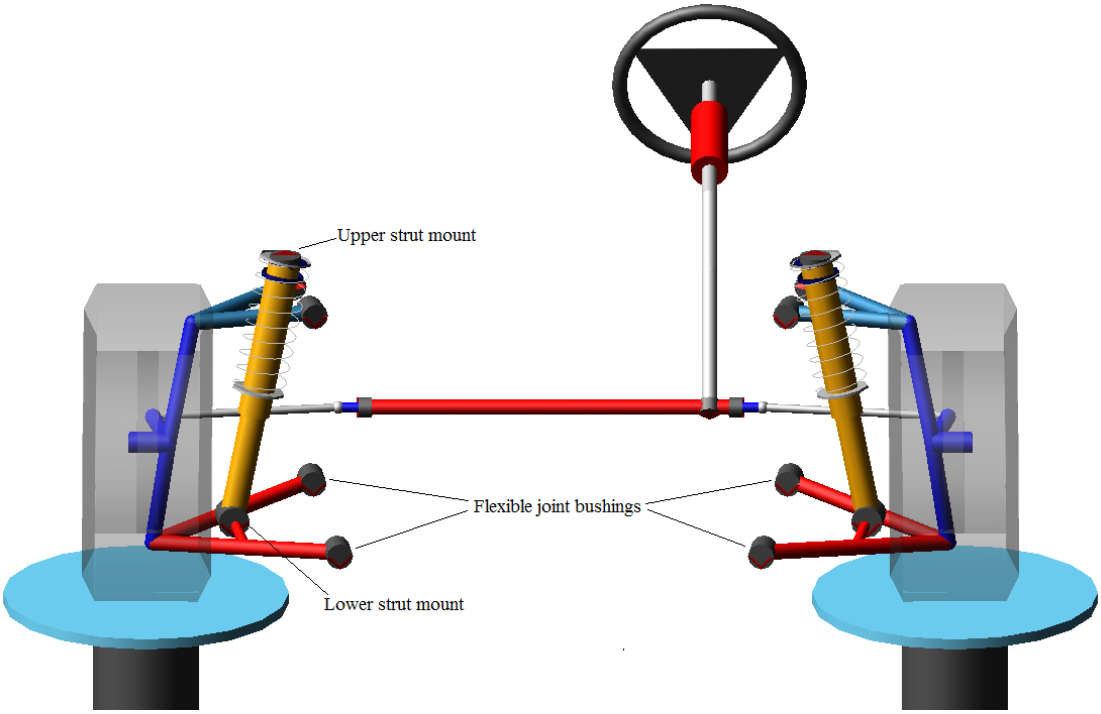

Figure 6.2: Double wishbone front suspension assembly

comprises flexible bushings, as illustrated in the Fig. 6.2. The tires in the vehicle model are considered as vertical spring and viscous dampers for evaluating vertical dynamic responses, while the model also considers Pacjecka tire model for estimating lateral tire forces, if required.

6.2.1 Bushing Model

Suspension bushings comprise flexible elastomeric material in between inner and outer steel casings. The joint bushings properties, in general, are characterized by force-displacement and moment-rotation relations, while ADAMS/car permits definition of bushing properties in and about three axes (*x*- *y*- and *z*) [28]. Figure 6.3 illustrates force-displacement and moment-rotation functions of upper and lower arm joint bushings along and about three axes. Force-displacement relations are mostly nonlinear, while moment-rotation relations are more or less linear, except that of UCA about z- axis. Furthermore, torsional stiffness of UCA (upper control arm) bushings is greater than that of LCA (lower control arm) joints, attributable to the larger influences of UCA bushings on the ride quality, as observed in section 3.6.4.

6.2.2 Bushing Fault Modeling

Two types of bushing faults are considered in this study: (i) bushings with clearance; and (ii) aged bushing. Bushing clearance is modeled as discontinuity in the force-displacement relations, while it is assumed that the maximum discontinuity is limited to 1 mm in all the bushings, excepting that at strut upper mount, which is considered to possess 2 mm clearance. The defective bushings are thus assumed to offer a very small restoring force (in order to eliminate singularity) during initial 0.5 mm of deformation in both compression and extension modes, as illustrated in Fig. 6.4.

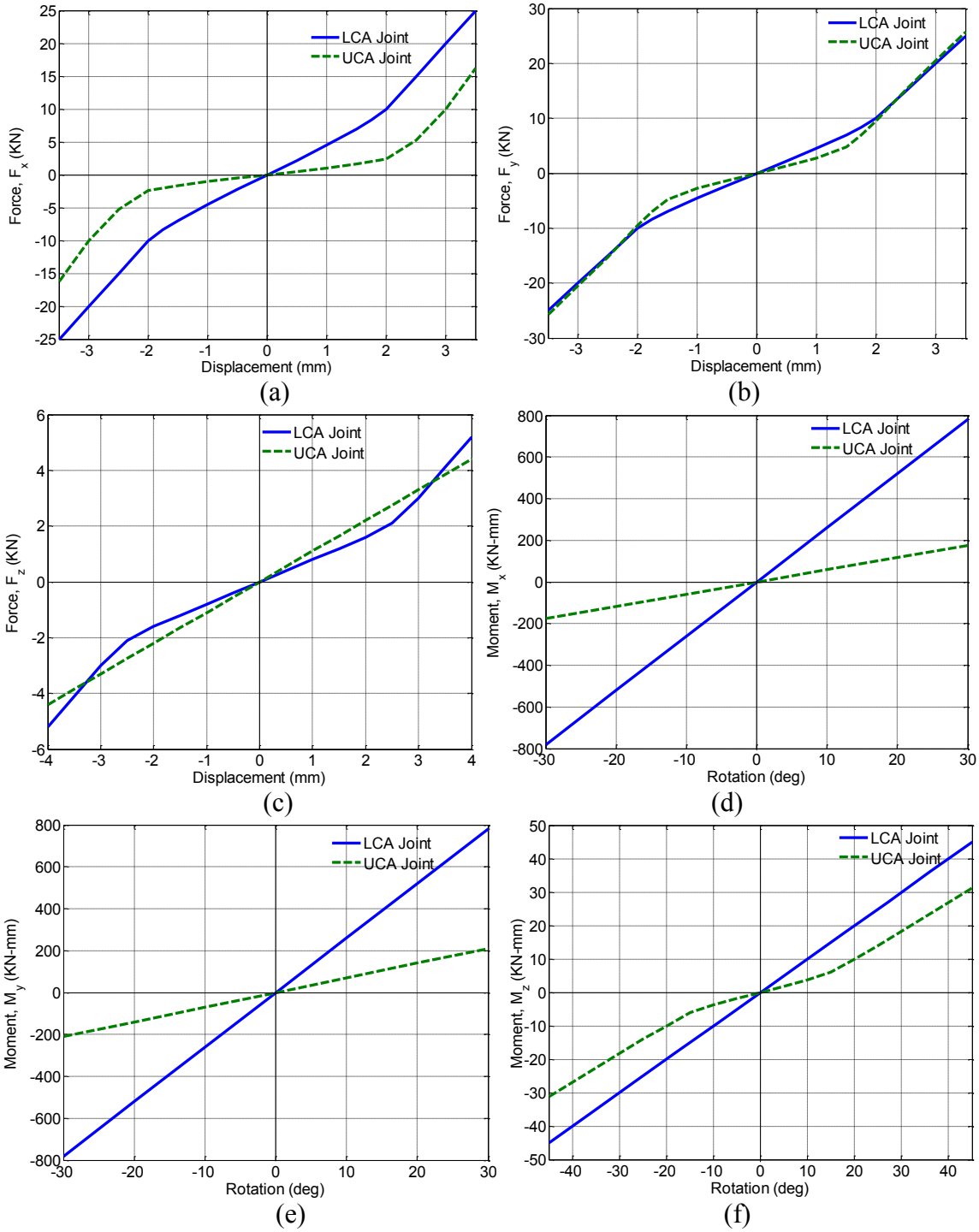

Figure 6.3: Characteristics of upper and lower control arm joint bushings in terms of: (a) force-displacement function along *x*- axis (radial); (b) force-displacement relation along *y*- axis (radial); (c) force-displacement relation along *z*- axis (axial); (d) moment-rotation relation about x- axis (radial); (e) moment-rotation relation about y- axis (radial); and (f) moment-rotation relation about z axis (axial).

The figures compare the characteristics of UCA and LCA bushings with clearance along *x*- and *z*- directions with that of the nominal ones, while the figures also illustrate the characteristics of aged bushings, which are modeled assuming an increase in the bushing stiffness. In this study, an increment of 50% in the stiffness is considered for the aged bushings, as illustrated in Fig. 6.4. It is further assumed that a bushing fault changes the properties in one direction only at any time.

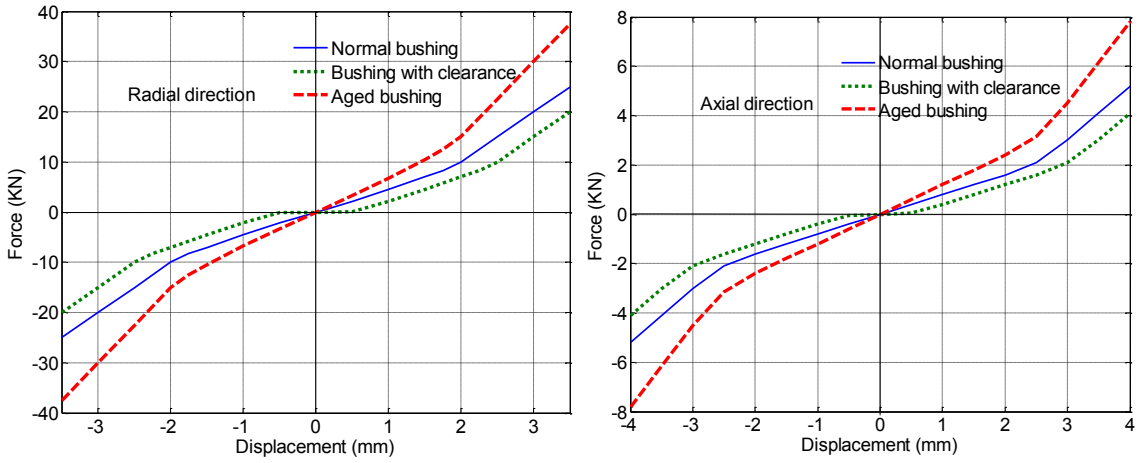

(a) (b)

Figure 6.4: Comparisons of force-displacement relations of LCA joint bushings in clearance and aged conditions with the nominal bushings along: (a) x- and y- axes (radial); and (b) z- axes (axial).

6.2.3 Modeling of Geometry and Damper Faults

A fault in suspension geometry is assumed to be due to an asymmetry in the suspension linkage kinematics in two sides of an axle. Such asymmetry in suspension mechanisms could easily occur following a collision of the vehicle. Suspension linkage length could get altered due to linkage deformation which also would change joint coordinates. In this study, geometry faults in the suspension are modeled by varying the joint coordinates. Fault in an automotive damper is often modeled by its lower damping coefficient as compared to the normal damper [54, 61]. Two levels of damper faults are

analyzed in this study: (i) 25% decay; and (ii) 50% decay in dampers, represented by 25 and 50% reduction in the damping coefficients.

6.3 Four-post Test Rig Full-vehicle Analyses

ADAMS/ride is an extension plug-in provided in the ADAMS/car tool for ride analysis of vehicle models. Assembled full-vehicle model is placed on a four post test rig, as illustrated in Fig. 6.1, which permits analysis with different inputs at the wheel spindle or beneath each of the tires. The input excitation can be defined in the form of displacement, velocity, acceleration or forces, as swept sine wave or road profiles [28]. While ADAMS is enabled with a road profile generator to produce different road profiles, including random roads as per ISO specifications, the road profile set up facility of ADAMS/car also permits user definition of roads in tabular form. The time lag between the front and rear excitations is calculated by the software automatically upon providing the vehicle forward speed. In this study, the urban roads roughness, characterized on the basis of measured road elevations reported in a previous study [152], are used for evaluating the dynamic responses of the full vehicle model and the performance measures. Figure 6.5 illustrates the filtered roughness profile of left and right tracks of the road over a span of 500 m, while the right-track road profile has been used for evaluating asymmetric damper performances in Chapter 4 (Fig. 4.10 (a) and (b)). The differences in the displacement amplitudes of left and right track suggest that the road profile could induce roll disturbances apart from the vertical irregularities.

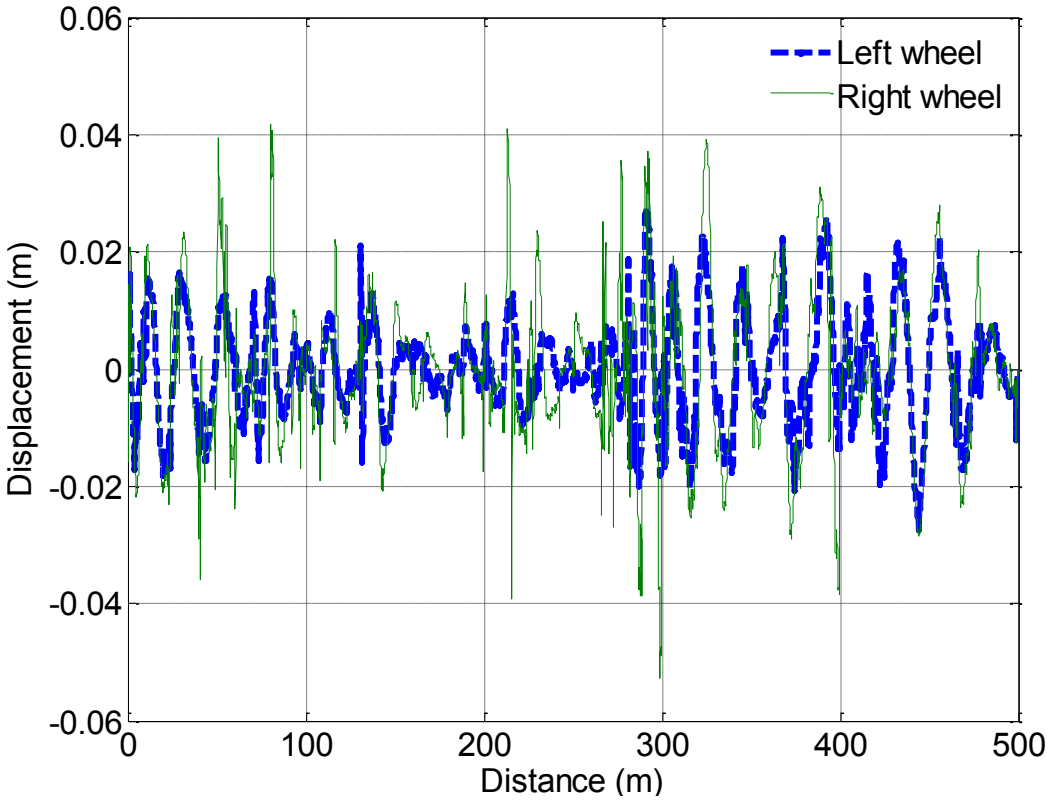

Figure 6.5: Roughness profile of left and right tracks in an urban road in terms of elevation and distance

6.4 Influence of Deformed Suspension Linkage

Influences of suspension linkage asymmetric deformation are evaluated by considering variations in the coordinates of lower control arm outer ball joint (between control arm and spindle) of front-left suspension. The full-vehicle kineto-dynamic model is subjected to random road excitations, as described in section 6.3 at 50 and 100 km/h vehicle forward speed, and the simulations are performed for 20 seconds. The dynamic responses are evaluated in terms of rms acceleration of vehicle chassis, wheel spindle and the lower control arm of front-left suspension. The responses of the model with 10 mm changes in *x*-, *y*- and *z*- coordinates of lower control arm outer joint of front left suspension are compared with those of the model with nominal suspension, and are

illustrated in Table 6.1. It may be noted that the variations to the joint coordinates are realized by negative changes in the respective coordinates.

The results in the table show minimal influence of suspension joint coordinate variations on the chassis vertical acceleration response, and small but notable influences on the spindle and lower control arm responses. Change in *y*- coordinate of LCA outer joint exhibits greater influence on the vertical acceleration responses as compared to that of variations in *x*- and *z* directions at lower speed of 50 km/h. The change in *y*-coordinates causes 0.011, 0.335 and 0.131 m/s^2 (1.5, 3.5, 2.6%) changes in chassis, spindle and LCA vertical acceleration responses, respectively, at 50 km/h as compared to those of the suspension without any faults. At higher speed of 100 km/h, however, variation in *z*- coordinate shows greater influence on the acceleration responses. The results of previous study of this work have clearly suggested that a change in joint coordinate would change the wheel rate of suspension (Section 3.5.1), which is major contributing factor for the changes in the acceleration responses.

Table 6.1: Influences of asymmetric linkages on the responses of full vehicle model under random road excitations.

Response →	Chassis vertical rms acceleration (m/s^2)		Wheel spindle vertical rms acceleration (m/s^2)		LCA vertical rms acceleration (m/s^2)	
Coordinate variation	50 km/h	100 km/h	50 km/h	100 km/h	50 km/h	100 km/h
Nominal	**0.901**	**1.429**	**10.998**	**18.346**	**3.851**	**6.204**
x-	0.900	1.428	10.986	18.324	3.880	6.220
y-	0.912	1.430	10.663	18.003	3.759	6.104
z-	0.905	1.431	11.090	18.378	3.850	6.202

While this study is limited to the vertical acceleration responses alone, roll and pitch angle response could also be influenced by the asymmetric suspension linkage geometry

of an axle. Furthermore, the joint coordinates influence kinematic responses such as camber and toe angle variations in a significant manner, which further influences ride and handling dynamics of the vehicle. Coupling of the lateral compliance of the tire with the vertical dynamics is not included in the ADAMS/ride default analyses, while its inclusion, generally, requires extended tire models. Moreover, simultaneous variations in two joint coordinates or larger variations than that considered in this study (>10 mm) in a coordinate could exhibit more significant influences on the vehicle dynamic responses.

The results in Table 6.1 suggest identifiable variations in the rms acceleration responses of wheel spindle and LCA. A frequency domain analysis is further considered, which would also be necessary for diagnosis of faults in the suspension kinematics. Power spectral density (PSD) of acceleration responses of LCA and wheel spindle of the model under random road excitations at 50 km/h speed are generated using Matlab Signal Processing Tool Box, as illustrated in the Figs. 6.5 (a) and (b). It is seen in the figure that the LCA exhibits two peak responses, while the second peak would likely corresponds to that of wheel spindle natural frequency. Variations in the joint coordinates considered in this study show notable peak responses of the LCA and the spindle. The results in the figure suggest that the changes in the joint coordinates exhibit negligible influences on the wheel spindle peak frequency or the second peak frequency of LCA. A close observation of the first peak responses of the spectrum of LCA vertical acceleration, however, shows that there exist small variations (in the order of 0.06 Hz) in the frequencies corresponding to the peak magnitudes. Similar variations in the frequencies corresponding to the peak magnitudes of chassis acceleration spectrum have also been observed (not shown). The results thus suggest that an asymmetry in suspension joint

coordinates with respect to vehicle center would influence the suspension responses, while this asymmetry could be identified from the frequency response of the lower control arm accelerations. Furthermore, wavelet analysis of the acceleration signal is shown to be effective in the fault identification [54, 55] which, however, is not investigated in the present study. The wavelet analysis yields information that is localized in both time and frequency whereas the standard Fourier analysis is only localized in frequency.

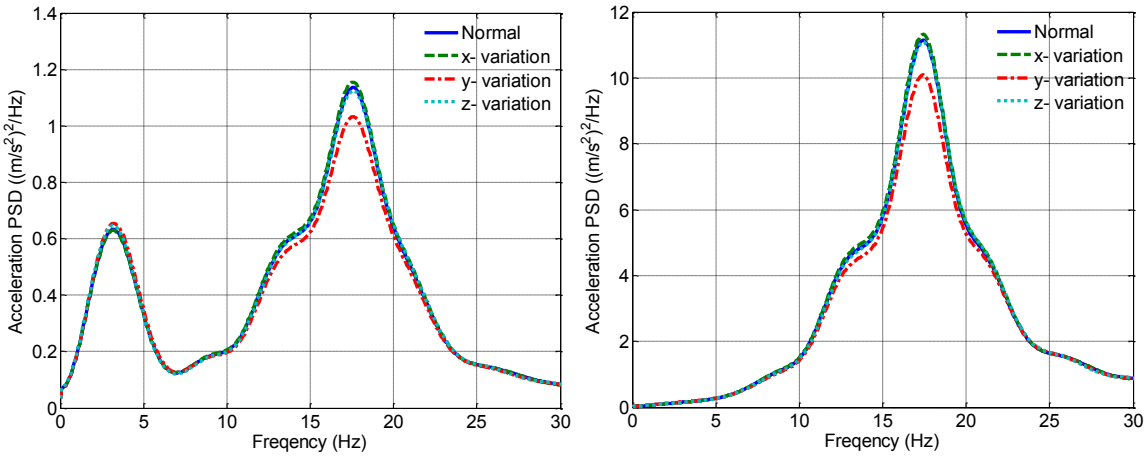

Figure 6.6: Comparisons of Power Spectral Density (PSD) of unsprung mass vertical acceleration responses of full vehicle model with deformed and normal linkages: (a) lower control arm (LCA); and (b) wheel spindle

6.5 Influence of Defective Damper

Defect in a suspension damper, perhaps due to leaking of hydraulic fluid could influence the dynamic performances of a suspension. The influences of damper fault on the dynamic responses are investigated by considering 25 and 50% reduction in the force-velocity characteristics of the front left suspension damper. The responses of the full vehicle model with defective dampers subjected to random road excitations at 50 and 100 km/h vehicle forward speeds are compared with those of the model with normal damper. As in the case of kinematic deformation analysis, the simulations are performed for 20

seconds. The dynamic responses, evaluated in terms of rms acceleration of vehicle chassis, wheel spindle and the front-left suspension lower control arms are illustrated in Table 6.2.

The results in the table suggest that a fault in one of the damper in a full vehicle model could influence the vertical acceleration responses of the chassis, wheel spindle or LCA. It is seen that the influence of the damper fault is dependent upon the vehicle forward speed. At lower speed of 50 km/h, decrease in the damping coefficient of the damper exhibit negligible influence on the sprung mass acceleration (<1%), while at 100 km/h, near 2.5% increase in the sprung mass rms acceleration is observed. Wheel spindle and LCA vertical acceleration responses on the other hand, exhibit increasing tendency with decrease in the damping coefficient of the defective damper, and decreasing trend with increase in the speed. Wheel spindle exhibits 7.2 and 15.8% increases at 50 km/h, and 6.5 and 12.3% increases at 100 km/h, respectively, in the rms acceleration response. LCA vertical accelerations (rms) increase by 6.7 and 14.2% at 50 km/h and 6.1 and 11.7% at 100 km/h, respectively. The results clearly suggest significant influence of the defective damper on the unsprung mass dynamic responses.

Table 6.2: Influences of defective damper in one of the suspensions on the responses of full vehicle model under random road excitations.

Response →	Chassis vertical rms acceleration (m/s^2)		Wheel spindle vertical rms acceleration (m/s^2)		LCA vertical rms acceleration (m/s^2)	
Damper condition	50 km/h	100 km/h	50 km/h	100 km/h	50 km/h	100 km/h
Nominal	**0.901**	**1.429**	**10.998**	**18.346**	**3.851**	**6.204**
25% decay	0.895	1.446	11.794	19.542	4.110	6.582
50% decay	0.902	1.461	12.743	20.609	4.400	6.931

The power spectral density (PSD) of the wheel spindle and the LCA vertical acceleration responses of the model with defective dampers are compared with those of the model with a normal damper in Fig. 6.6. The results suggest significantly large deviations in the peak magnitudes in spectra of LCA (both first and second) and wheel spindle accelerations. The second (dominant) peaks of LCA and the peaks of the wheel spindle are seen to occur at nearly identical frequencies irrespective of the condition of the damper. The LCA spectra, however, reach the first peak magnitudes at different frequencies with damper condition (normal damper-3.18 Hz, 25% defective damper- 3.11 Hz and 50% defective damper- 3.05 Hz). The results in Fig. 6.7 clearly suggest decrease in the LCA vertical vibration frequencies with decrease in the damping coefficient of the suspension damper. As in the case of deformed suspension linkages, frequency response of the measured LCA accelerations could be conveniently employed to detect the damper faults in a vehicle suspension.

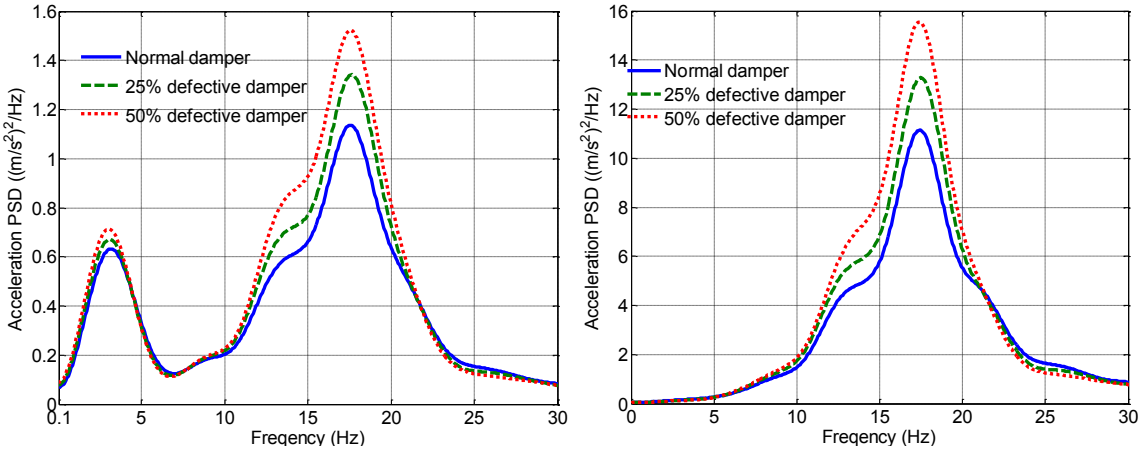

Figure 6.7: Comparisons of Power Spectral Density (PSD) of unsprung mass vertical acceleration responses of full vehicle model with defective and normal dampers: (a) lower control arm (LCA); and (b) wheel spindle

6.6 Influence of Joint Bushings Faults

Influences of joint bushing faults on the dynamic responses of the full vehicle model are evaluated by representing the bushing characteristics as illustrated in Fig. 6.4. Clearances at strut upper and lower mounts, and lower and upper control arm front bushings (Fig. 6.2) are considered in this study for the relative analysis. Effects of an axial clearance of 2 mm in the upper strut mount and a radial clearance of 0.5 mm in the lower strut mount are evaluated under random road excitations at 50 and 100 km/h vehicle speed. Three different types of bushing faults are analyzed in the case of LCA (lower control arm) and UCA (upper control arm) bushings: (i) 1 mm radial clearance; (ii) 3° angular clearance; and (iii) 50% increase in the bushing stiffness due to aging. The bushing defects are considered in front left suspension alone, and each fault is considered independently. Each of the bushing faults is analyzed at both lower and higher speeds (50 and 100 km/h), while the acceleration response of the control arm corresponding to faulty bushing (LCA or UCA) is evaluated, in addition to the wheel spindle response.

The rms acceleration of chassis, wheel spindle and LCA of the model with defective strut bushings are compared with those of the model with nominal bushings, as illustrated in Table 6.3. The results in the table suggest that a clearance in the upper strut bushing could influence the dynamic response of lower control arm and the wheel spindle considerably with a minimal influence (<1%) on the sprung mass acceleration at both 50 and 100 km/h forward velocity. The upper strut mount clearance causes increase of 15 and 7% in the wheel spindle and 12.7 and 6% in the LCA vertical acceleration responses at 50 and 100 km/h speeds, respectively. It is thus seen that the degree of influences of upper strut bushing clearance is strongly dependent upon the vehicle forward speed. This

can be attributable to the fact that at higher acceleration excitations (higher forward velocities), the suspension properties exhibit lesser influences than the tire properties on the dynamic responses. The results in the table further show that a radial clearance in strut lower bushing (in the order of 0.5 mm) exhibits minimal influences on the sprung and unsprung mass responses.

Table 6.3: Influences of strut bushings clearance in one of the suspensions on the responses of full vehicle model under random road excitations.

Response →	Chassis vertical rms acceleration (m/s^2)		Wheel spindle vertical rms acceleration (m/s^2)		LCA vertical rms acceleration (m/s^2)	
Bushings fault	50 km/h	100 km/h	50 km/h	100 km/h	50 km/h	100 km/h
Nominal	**0.901**	**1.429**	**10.998**	**18.346**	**3.851**	**6.204**
Upper strut mount	0.911	1.437	12.645	19.713	4.340	6.593
Lower strut mount	0.901	1.429	11.000	18.333	3.850	6.198

Power spectral density (PSD) of LCA and wheel spindle acceleration responses of the model with faulty upper and lower strut bushings are compared with that of the model with nominal bushings in Fig. 6.8. A clearance in the upper strut mount cause an amplification in the peak magnitudes of the spectrum of both wheel spindle and LCA responses as compared to that of model with the nominal bushings. A slight variation in the frequencies corresponding peak magnitude of LCA and wheel spindle spectrum (nearly 0.02 Hz) is also observed. As expected, clearance in the lower strut mount does not exhibit any influence in the frequency spectrum. Although a clearance in the upper strut mount influences the dynamic response considerably, an identification of the fault from the frequency spectrum seems to be complex. A further study of the response employing wavelet analysis technique might be instrumental.

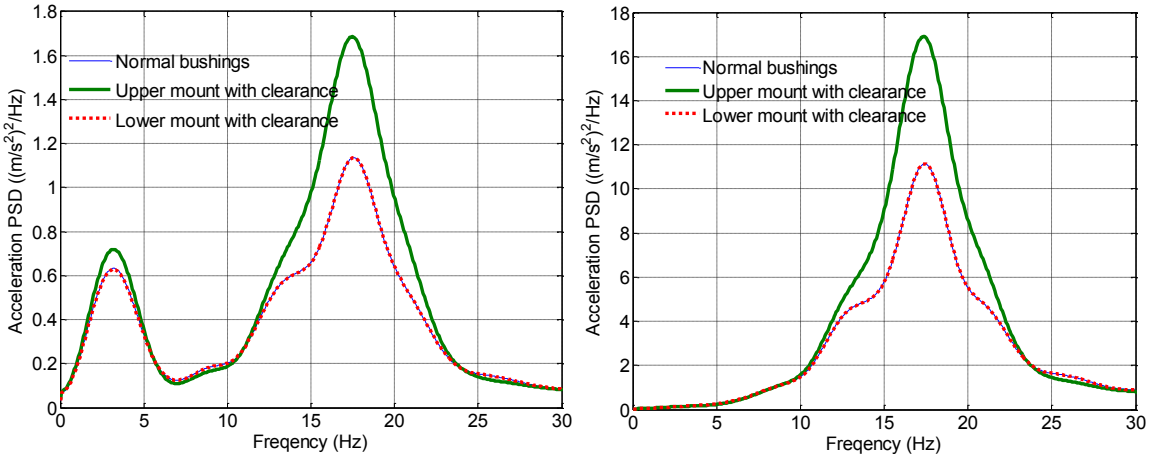

Figure 6.8: Comparisons of Power Spectral Density (PSD) of unsprung mass vertical acceleration responses of full vehicle model with and without clearance in strut bushings: (a) lower control arm (LCA); and (b) wheel spindle

Table 6.4 illustrates the rms acceleration responses of the wheel spindle and LCA with faults in the LCA front bushing, while Table 6.5 shows the rms acceleration responses of the wheel spindle and UCA with faults in the UCA front bushing under random excitation at 50 and 100 km/h. The tables also compare the responses of the model with nominal bushings. The results in both the tables suggest that considered bushing faults exhibit minimal influences on the wheel spindle or control arm vertical acceleration responses, although the degree of influences are slightly dependent on the vehicle speed. It needs to be emphasized here that both lower and upper control arms comprise two bushing joints at the chassis, while this study was limited to bushing faults in one joint alone.

The results in Table 6.3 to 6.5 suggest that the strut upper mount clearance is the most influential bushing defect among all of the faults considered in this study. However, it needs to be noted that the study considered a larger clearance (2 mm) at the upper strut mount bushing compared to that at other bushings. A 1 mm discontinuity in the force-displacement relation of bushing represents only 0.5 mm clearance in a physical joint.

Larger clearance in any bushings could affect the dynamic responses in larger magnitude, which however requires further studies.

Table 6.4: Influences of lower control arm bushing clearance in one of the suspensions on vertical acceleration response of LCA and wheel spindle under random road excitations.

Response →	Wheel spindle vertical rms acceleration (m/s^2)		LCA vertical rms acceleration (m/s^2)	
Bushings fault	50 km/h	100 km/h	50 km/h	100 km/h
Nominal	**10.998**	**18.346**	**3.851**	**6.204**
LCA radial clearance	10.982	18.340	3.848	6.208
LCA torsional clearance	11.072	18.339	3.870	6.201
LCA aged bushings	10.970	18.339	3.851	6.215

Table 6.5: Influences of upper control arm bushing clearance in one of the suspensions on vertical acceleration response of UCA and wheel spindle under random road excitations.

Response →	Wheel spindle vertical rms acceleration (m/s^2)		UCA vertical rms acceleration (m/s^2)	
Bushings fault	50 km/h	100 km/h	50 km/h	100 km/h
Nominal	**10.998**	**18.346**	**3.729**	**6.030**
UCA radial clearance	10.939	18.325	3.706	6.015
UCA torsional clearance	11.057	18.349	3.744	6.030
UCA aged bushings	10.989	18.356	3.726	6.031

6.7 Feasibility of a Fault Diagnostic System

The results in Section 6.4 to 6.6 suggest that asymmetric kinematic linkage, defective damper and clearance in upper strut mount bushings cause variation in the frequencies corresponding to first peak magnitudes of LCA accelerations. A close observation of the results, however, suggests that a defective damper and upper mount clearance cause reduction in the LCA vibration frequency, while the deformed linkage causes increase in the frequency. The results corresponding to a decayed damper or strut mount bushing clearance could be easily generalized, while the faults due to linkage deformation cannot

be generalized, since this study is limited to variations in the joint coordinate in one direction only. It can be noted that a negative change in *y*- coordinate of the LCA outer joint exhibited higher influence among the variations considered, while this change is known to cause increase in wheel rate (Section 3.6.5). Furthermore, damper fault does not influence the peak frequency of the spindle, while strut mount bushing fault exhibits a small influence on the wheel spindle peak frequency. This information could be used to identify an approximate source of fault from the acceleration response of the LCA.

Based upon this preliminary study, a fault diagnostic system could be proposed, which would comprise four accelerometers mounted on the lower control arms of each suspension. The system also necessitates a processing unit that could convert the time response of the accelerometer into frequency domain. The processing unit should be capable of comparing the real time responses with prerecorded data corresponding to the suspension without faults, while correlating with the forward speed of the vehicle. As discussed previously, wavelet analysis of the acceleration response would also be necessary for precise identification of the source of fault, which should also be facilitated in the processing unit.

6.8 Summary

This chapter presented the study of influences of suspension faults such as asymmetrically deformed suspension linkage, defective damper and bushings clearances on the dynamic responses of a vehicle and suspension through analyses of a full vehicle model developed in ADAMS/car platform. Suspension linkage deformation was modeled by considering changes in joint coordinate of lower control arm outer joint of front left suspension. Damper defect due to leaking of hydraulic fluid was assumed to cause

reduction in the damping coefficient, and such defective damper was represented by 25 and 50% reduction in the force-velocity characteristics. Flexible joint bushings in the full vehicle model were represented by force-displacement and moment-rotation relations along and about three axes, respectively. Clearance in a bushing was modeled by discontinuity in the force-displacement characteristics, while the study also considered influences of aged bushing assuming an increase in the force-displacement characteristics.

Vertical acceleration responses of the chassis, control arm and wheel spindle are analyzed to evaluate the influences of suspension faults considered in this study. The spectral analysis revealed that data measured from the lower control arm can be conveniently employed to detect the suspension faults due to linkage asymmetry or defective damper, and can be used to yield an early warning of the faults. Upper strut bushing clearance showed considerable influence on the control arm acceleration response, while other bushing faults exhibited negligible influence. Determination of an exact source and type of faults, however, would necessitate employment of additional tools such as wavelet analysis, apart from the spectral analysis used in this study.

CHAPTER 7

CONCLUSIONS AND RECOMMENDATIONS FOR FURTHER STUDIES

7.1 Dissertation Research Highlights

This dissertation research has presented methodology to systematically investigate the influences of various suspension nonlinearities, particularly the linkage kinematics, tire lateral complaince, damper asymmetry and flexible joint bushings, on the kinematic and dynamic responses of a vehicle. These are illustrated through developments and analyses of kineto-dynamic quarter- and half-car models incorporating the suspension linkages, tire lateral and bushing compliance, and asymmetric dampers. A methodology for synthesis of optimal suspension geometry (joint coordinates) has been presented considering the coupled kinematic and dynamic responses with contraint on the lateral packaging space for potential applications in emerging hybrid vehicle designs. Synthesis of an asymmetric two- stage damper has also been presented considering design compromises between the ride, rattle space, road holding and camber angle performances in an attempt to develop design guidance. A full vehicle model in ADAMS/car is further analyzed to study the influences of faulty bushings, dampers and kinematic linkages on the dynamic responses.

The major highlights and contributions of the dissertation research are briefly summarized below:

- Single-wheel kinematic models of two types of suspensions, quadra-link and double wishbone, are proposed to study the kinematic responses, which could be employed for synthesis of suspension geometry. Laboratory-measured data were applied to demonstrate validity of the 3- dimensional kinematic model of the

quadra-link suspension. A sensitivity analysis method was proposed to investigate the influences of various suspension joint coordinates on the kinematic responses. A planar kinematic model of the double wishbone suspension is also formulated for anaysis of roll-plane kinematic responses, including variations in camber angle, wheel track and wheel center lateral displacement.

- A kineto-dynamic quarter car model comprising linkage kinematics of a double wishbone type of suspension is proposed to study coupled kinematic and dynamic responses of suspension and vehicle model. The significance of coupling between the kinematic and dynamic responses is illustrated by comparing the responses of the proposed model with those of a conventional dynamic model with equivalent spring and damping rates. A methodology for deriving equivalent spring rate and damping rates incorporating the contributions of linkage kinematics, is further presented. The contributions due to compliance of suspension joint bushing to the kinematic and dynamic responses are investigated assuming bushings as torsional springs.
- Owing to the lack of design guidance on suspension damping asymmetry, the kineto-dynamic model is enhanced by incorporating single- and two- stage asymmetric damping in order to seek a design guideline. The effects of damping asymmetry on the coupled dynamic and kinematic responses are thoroughly evaluated under harmonic and idealized bump and pothole excitations, and the conflicting design requirements under different excitations are illustrated. A constrained optimization problem is formulated and solved to seek design guidance for synthesis of a two-stage asymmetric damper that would yield an acceptable

compromise among the performance measures under idealized bump and pothole excitations.

- The coupled dynamic and kinematic responses of the model with single- and two-stage asymmetric dampers are further evaluated under random road excitations over a range of forward velocities. An optimal synthesis of a two-stage asymmetric damper is presented to yield compromise between conflicting performance measures corresponding to ride, rattle space, road holding and camber angle responses under random road inputs.
- The coupled kinematic and dynamic responses in the roll plane are analyzed through development and analysis of a four-DOF, kineto-dynamic roll-plane vehicle model comprising double wishbone type of suspensions. A methodology to derive a suspension synthesis is subsequently proposed. The conflicting kinematic responses including bump/roll camber and wheel track variations under chassis roll and wheel vertical motions are identified, and a set of optimal joints coordinate synthesis is attempted considering the conflicting responses coupled with the lateral space constraint. The influences of asymmetric damping and an antiroll bar on the kinematic and dynamic responses are further presented under selected excitations.
- A full-vehicle model comprising double wishbone type of suspensions at both front and rear axles is developed in ADAMS/car platform to study the influences of faults in suspension bushings and linkage on the kinematic and dynamic responses. The study was limited to two types of bushing faults, namely the clearances in the bushing with reduction in bushing stiffness; and aged bushings with increase in the bushing stiffness.

7.2 Major Conclusions

This dissertation revealed significant coupling among various kinematic and dynamic performance measures of vehicle suspensions. The results of the study yielded important design guidelines pertaining to suspension geometry and damper synthesis. Major conclusions drawn from this study are summarized below:

(a) The kinematic and dynamic performance measures of a vehicle are coupled through the linkage (independent) suspension design. A suspension design synthesis therefore must be based on coupled kineto-dynamic analyses.

(b) The linkage suspensions yield asymmetric variations in camber, caster and toe angles, and wheel base and wheel tracks with respect to the static position under a wheel vertical motion.

(c) Each of the kinematic responses and the articulation of a double wishbone suspension are very sensitive to variations in the upper control arm joints coordinates. The front (camber link) and rear (toe link) lower links of the quadra-link suspension exhibit large influences on the camber and toe angle responses, respectively, apart from the other responses.

(d) A double wishbone suspension with closer upper and lower ball joints would yield lower variations in camber angle and wheel track responses under wheel jounce and rebound motions.

(e) The dynamic responses of a kineto-dynamic quarter car model to harmonic and idealized rounded pulse excitations are generally asymmetric attributed to the suspension kinematics, while the degree of asymmetry is dependent on the amplitude and frequency of the inputs, and suspension joint coordinates. The

asymmetry in suspension damping in compression and rebound further contributes to asymmetry in the dynamic responses.

(f) Both the kinematic and dynamic responses of a kineto-dynamic quarter model under bump/pothole inputs are strongly dependent upon the suspension joint coordinates, while variations in the joint coordinates involve difficult compromises between the kinematic and dynamic response measures.

(g) The flexible joint bushings can lead to nearly 5% variations in the kinematic and dynamic responses of the suspension system. A decrease in torsional stiffness of the upper control arm bushing yields a benificial influence on the sprung mass acceleration, while a variation in the lower control arm joint bushing offers negligible influence.

(h) Higher rebound to compression damping asymmetry in general causes a downward shift in the sprung mass mean position, while higher compression to rebound asymmetry ratio causes an upward shift. The mean shift in the unsprung mass displacement relative to the sprung mass causes additional camber angle variation during the wheel vertical motions.

(i) The damping asymmetry of a bilinear damper yields conflicting effects on the sprung mass acceleration response to bump and pothole excitations. A higher rebound to compression damping asymmetry helps reduce the magnitude of the first peak in sprung mass acceleration to bump excitation, but yields higher acceleration under a pothole excitation. In case of two-stage damper with different low and high-speed damping coefficients, lower values of the high-velocity

damping coefficients resulted in considerable reductions in the sprung mass acceleration response under both the inputs.

(j) The damping asymmetry ratio is strongly dependent upon the low-speed compression damping. Under a bump input, asymmetry ratio of 2 and 3 could result in a good compromise between the ride and road holding performance for low-speed compression mode damping ratios of 0.2 and 0.1, respectively. Under a pothole input, however, a linear or higher compression to rebound damping asymmetry ratio would be a better design compromise.

(k) Kinematic and dynamic responses of a road vehicle with asymmetric damper subjected to random road excitation would be strongly influenced by the compression/rebound damping asymmetry and the forward speed of the vehicle. With an asymmetric damper, notable consistent trends in the kinematic and dynamic responses of the model could be identified in three speed ranges: the responses increasing nearly linearly with forward speed in the 30-60 km/h range; increasing nonlinearly in the medium speed range (60-90 km/h); and nonlinearly decreasing or saturating in the higher speed range (100-120 km/h).

(l) A synthesis of an optimal two-stage asymmetric damper is highly complex due to strong couplings among the various damper parameters, and would strongly depend upon the limit imposed on the camber variation. For minimal camber angle variations, a lower rebound to compression damping asymmetry would be desirable, while the camber variations correlate well with the tire force variations, when a greater emphasis is placed on the tire force variations.

(m) The roll-plane kinematic analysis of a double wishbone suspension revealed that the joint coordinates that reduce the bump camber variation under wheel vertical motion, generally cause higher roll camber under chassis roll. Achieving minimal lateral packaging space may necessitate compromise in the vertical packaging space, because reduction in both control arms lengths and variations in the bump/roll camber together may not be feasible.

(n) Inclusion of antiroll bar in a suspension, apart from causing increase in the sprung mass vertical acceleration and roll angle responses under bump excitation at one wheel of the axle, could also increase the camber angle variation response considerably.

(o) Suspension faults such as deformed linkage, defective damper and clearance bushings could influence the dynamic responses of the lower control arm of a full vehicle model with double wishbone suspension. Power spectral density of the lower control arm vertical acceleration response could be used to identify the suspension faults in an approximate manner.

(p) Clearance in strut upper mount bushing causes increase in the amplitude of the unsprung mass vertical accelerations, while clearances in lower or upper control arm bushings exhibit minimal influence.

7.3 Recommendations for Further Studies

This desertation research has helped identifying important couplings between the suspension kinematics and dynamic responses of a road vehicle, which is related to the suspension geometry and damping asymmetry in a highly complex manner. While this study has enabled yielding a few significant conclusions and design guidance relevant to

suspension geometry and asymmetric damper synthesis, further works in this direction would be highly desirable for improved suspension synthesis, particularly for future electric vehicles with constrained packaging space. Some of the recommended further studies are listed below:

- Define kinematic and dynamic performance requirements based upon kineto-dynamic vehicle model responses.
- Synthesis of a suspension system based upon coupled kinematic and dynamic performance measures employing 3- dimensional suspension and vehicle model.
- Synthesize a suspension system considering lateral packaging space constraints apart from the kineto-dynamic performance measures.
- Employ multi-objective optimization methodologies for the synthesis of multi-stage asymmetric damper.
- Explore active/semi active linkages for enhanced kinematic and dynamic performances.
- Develop early warning based suspension fault diagnostic system.

REFERENCES

1. Milliken W F and Milliken D L, (1995) *Race Car Dynamics*, SAE Inc. Warrendale, PA, USA.
2. Gillespie T D, (1992) *Fundamentals of Vehicle Dynamics*, SAE Inc. Warrendale, PA, USA.
3. Fuhs A, (2009) *Hybrid Vehicles and the Future of Personal Transportation,* CRC Press, Boca Raton.
4. Reimpell J and Stoll H, (1996) *The Automotive Chassis: Engineering Principles*, SAE Inc. Warrendale, PA, USA.
5. Simionescue P A and Beale D, (2002) *Synthesis and Analysis of the Five-link Rear Suspension System Used in Automobiles*, Mechanism and Machine Theory, Vol 37, pp 815-832.
6. Lee D M A, Pasocoe D M and ElMaraghy W H, (1993) *An Analysis of the Multi-link Independent Suspension System*, Int. Journal of Vehicle design, Vol 14/1, pp 44-58.
7. Raghavan M, (1991) *Suspension Kinematic Structure for Passive Control of Vehicle Attitude*, Int. Journal of Vehicle Design*,* Vol 12/5&6, pp 525-547.
8. Shim T and Velusamy P C, (2006) *Influence of Suspension Properties on Vehicle Roll Stability*, SAE Paper, 2006-01-1950.
9. Heuze L, Ray P, Gogu G, Serra L and Andre F, (2003) *Design Studies for a New Suspension Mechanism*, IMechE Part D, Journal of Automobile Engineering, Vol 217, pp 329-335.
10. Blundell M V, (1999) *The Modeling and Simulation of Vehicle Handling Part 1: Analysis Method*, IMechE Part K, Journal of Multibody Systems Dynamics, Vol 213, pp 103-118.
11. Cronin D L, (1981) *MacPherson Strut Kinematics*, Mechanism and Machine Theory, Vol 16/6, pp 631-644.
12. Knapczyk J and Dzierzek S, (1995) *Displacement and Force Analysis of Five-Rod Suspension with Flexible Joints*, Journal of Mechanical Design, Vol 117, pp 532-538.

13. Raghavan M, (1996) *Number and Dimensional Synthesis of Independent Suspension Mechanisms*, Mechanism and Machine Theory, Vol 31/8, pp 1141-1153.
14. Suh C H, (1989) *Synthesis and Analysis of Suspension Mechanisms With Use of Displacement Matrices*, SAE Paper, 89098.
15. Rae W J and Kasprzak E M, (2002) *Kinematics of a Double A-arm Suspension Using Euler Orientation Variables*, SAE Paper, 2002-01-0279.
16. Manes E N and Starkey J M, (2004) *Derivation of the Three-dimensional Installation Ratio for Dual A-arm Suspensions*, SAE Paper, 2004-01-3535.
17. Hiller M and Frick S, (1993) *Five-link Suspension,* Vehicle System Dynamics, Vol 22, pp 254-262.
18. Nalecz A G, (1987) *Investigation into the Effect of the Suspension Design on Stability of Light Vehicles*, SAE Paper, 870497.
19. Suh C H and Radcliff C W, (1978) *Kinematics and Mechanisms Design*, John Wiley & Sons, New York.
20. Kang H Y and Suh C H, (1994) *Synthesis and Analysis of Spherical-Cylindrical (SC) Link in the McPherson Strut Suspension Mechanism*, Journal of Mechanical Design, Vol 116, pp 599-606.
21. Mantaras D A, Luque P and Vera C, (2004) *Development and Validation of a Three-Dimensional Kinematic Model for the McPherson Steering and Suspension Mechanisms*, Mechanism and Machine Theory, Vol 39, pp 603-619.
22. Rocca E and Russo R, (2002) *A Feasibility Study on Elasto-kinematic Parameter Identification for a Multilink Suspension*, IMechE Part D, Journal of Automobile Engineering, Vol 216, pp 153-160.
23. Wach W, and Struski J, (2006) *Rear Wheels Multi-link Suspension Synthesis with the Application of a Virtual Mechanism*, SAE Paper, 2006-01-1376.
24. Habibi H, Shiraz K K and Shishesaz M, (2008) *Roll Steer Minimization of McPherson-Strut Suspension System using Genetic Algorithm Method*, Mechanism and Machine Theory, Vol 43, pp 57-67.
25. Wach W and Struski J, (2006) *Rear Wheels Multi-link Suspension Synthesis with the Application of a Virtual Mechanism*, SAE Paper, 2006-01-1376.

26. Knapczyk, J and Maniowski M, (2006) *Elastokinematic Modeling and Study of Five-Rod Suspension With Subframe*, Mechanism and Machine Theory, Vol 41, pp 1031-1047.
27. Shim T and Velusamy P C, (2007) *Suspension Design and Dynamic Analysis of a Lightweight Vehicle*, Int. Journal of Vehicle Design, Vol 43, No 1-4, pp 258-280.
28. ADMAS/car-User's Manual, MD.ADAMS/2007r2/help
29. Ozdalyan B, Blundell M V and Philips B, (1988) *Comparison of Suspension Rig Measurements With Computer Simulation*, International Conference on SIMULATION, Conference Publication No. 457, IEE 1998, pp 133-139.
30. Bae S, Lee J M , Choi W J, Yun J R and Tak T O, (2003) *Axiomatic Approach to the Kinematic Design of an Automotive Suspension System With the McPherson Strut Type*, Int. Journal of Vehicle Design, Vol 31, pp 58-71.
31. Chatillon M M, Jezequel L, Coutant P, and Baggio P, (2006) *Hierarchical Optimization of the Design Parameters of a Vehicle Suspension System*, Vehicle System Dynamics, Vol 44, pp 817-839.
32. Fijita K, Hirokawa N, Akagi S, and Hirata T, (1998) *Design Optimization of Multi Link Suspension System for Total Vehicle Handling and Stability*, Proceedings of 7th AIAA/USAF/NASA/ISSMO/Symposium on Multidisciplinary Analysis and Optimization-Part 1, St. Louis, MO, pp 620-630.
33. Mitchell S C, Smith S, Damiano A, Durgavich J and MacCracken R, (2004) *Use of Genetic Algorithms with Multiple Metrics Aimed at the Optimization of Automotive Suspension Systems*, SAE Paper, 04MSEC-59
34. Li L, Xia C and Qin W, (2007) *Analysis of Kinetic Characteristic and Structural Parameter Optimization of Multi-link Suspension*, SAE Paper, 2007-01-3558.
35. Deo H V and Suh N P, (2004) *Axiomatic Design of Automobile Suspension and Steering Systems: Proposal for a Novel Six Bar Suspension*, SAE Paper, 2004-01-0811.
36. Sharp R S and Dodu M, (2004) *Kinematic Cross-linking in Automotive Suspension Systems*, Vehicle System Dynamics-Supplement, Vol 41, pp 63-72.
37. Hamedi B, Catala A, Canellas S and Elahimehr A, (2007) *A New Hybrid (Bi-fuel) Vehicle Suspension Development*, SAE Paper, 2007-01-0861.

38. Wineman A, Dyke T V and Shi S, (1998) *A Nonlinear Visco-elastic Model for One Dimensional Response of Elastomeric Bushing*, Int. Journal of Mechanical Science, Vol 40, pp 1295-1305.
39. Yoo W S, Baek W K and Sohn J H, (2004) *A Practical Model for Bushing Components for Vehicle Dynamic Analysis*, Int. Journal of Vehicle design, Vol 36, pp 345-364
40. Piquet B, Mass C A and Capou F, (2007) *Next Generation of Suspension Bushings: Review of Current Technologies and Expansion Upon New 3rd Generation Product Data*, SAE Paper, 2007-01-0850.
41. Kadlowec J, Wineman A and Hulbert H, (2003) *Elastomer Bushing Response: Experiments and Finite Element Modeling*, Acta Mechanica, Vol 163, pp 25-38.
42. Blundell M V, (1998) *The Influence of Rubber Bush Compliance on Vehicle Suspension Movement*, Materials and Design, Vol 19, pp 29-37
43. Lee S B and Wineman A, (1999) *A Model for Non-linear Visco-elastic Axial Response of an Elastomeric Bushing*, Int. Journal of Non linear Mechanics, Vol 34, pp 779-793
44. Pu Y, Sumali H and Gaillard C L, (2001) *Modeling of Non Linear Elastomeric Mounts: Part 1 Dynamic Testing and Parameter Identification*, SAE Paper, 2001-01-0042.
45. Pu Y, Sumali H and Gaillard C L, (2001) *Modeling of Non Linear Elastomeric Mounts: Part 2 Comparing Numerical Model and Test Results*, SAE Paper, 2001-01-0043.
46. Dzierzek S, (2000) *Experiment Based Modeling of Cylindrical Rubber Bushings for the Simulation of Wheel Suspension Dynamic Behavior*, SAE Paper, 2000-01-0095.
47. Messonnier J, Fauroux J C, Gogu G and Montezin C, (2006) *Geometric Identification of an Elasto-kinematic Model in a Car Suspension*, IMechE Part D, Journal of Automobile Engineering, Vol 220/9, pp 1209-1220
48. Messonnier J, Fauroux J C, Gogu G and Montezin C, (2006) *Iterative Identification of Stiffness Parameters in a Car Suspension Elasto-kinematic Model*, IMechE Part D, Journal of Automobile Engineering, Vol 220/11, pp 1477-1489.

49. Knapczyk J and Maniowski M, (2006) *Stiffness Synthesis of a Five-rod Suspension for Given Load-displacement Characteristics*, IMechE Part D, Journal of Automobile Engineering, Vol 220, pp 879-889.
50. Caputo A, Spina M and Guglielmino E, (2003) *Sensitivity of Suspension System Performance to Bushing Stiffness Variation- an Evaluation Methodology*, SAE Paper, 2003-01-0237.
51. Kang J S, Yun J R and Lee J M, (1997) *Elasto-kinematic Analysis and Optimization of Suspension Compliance Characteristics*, SAE Paper, 970104.
52. Yang X and Medepalli S, (2005) *Sensitivities of Suspension Bushings on Vehicle Impact Harshness Performances*, SAE Paper, 2005-01-0827.
53. Kim J H, Sin H C, Kang B J and Kim N W, (2006) *Characteristic Study of Bushing Compliance of Stresses in a Vehicle Suspension System by the Taguchi Method*, IMechE Part D, Journal Automobile engineering, Vol 220/10, pp 1383-1399.
54. Azadi S and Soltani A, (2007) *Application of Wavelet Analysis to the Suspension System Fault Detection of a Vehicle*, SAE Paper, 2007-01-2370.
55. Azadi S and Soltani A, (2009) *Fault Detection of Vehicle Suspension System Using Wavelet Analysis*, Vehicle System Dynamics, Vol 47, pp 403-418.
56. Flores P and Ambrosio J, (2004) *Revolute Joints with Clearance in Multibody Systems*, Computers and Structures, Vol 82, pp 1359-1369.
57. Flores P, Ambrosio J, Claro J C P and Lankarani H M, (2007) *Dynamic Behavior of Planar Rigid Multi-body Systems Including Revolute Joints With Clearance*, IMechE, Part K:, Journal of Multibody Dynamics, Vol 221, pp 161-174.
58. Chunmei J, Yang Q, Ling F and Ling Z, (2002) *The Non-linear Dynamic Behavior of an Elastic Linkage Mechanism with Clearances*, Journal of Sound and Vibration, Vol. 249, pp 213-226.
59. Rhee J and Akay A, (1996) *Dynamic Response of a Revolute Joint with Clearance*, Mechanism and Machine Theory, Vol 31, pp 121-134.
60. Flores P, Ambrosio J, Claro J C P and Lankarani, H M, (2006) *Dynamics of Multibody Systems With Spherical Clearance Joints*, Journal of Computational and Nonlinear Dynamics, Vol 1, pp 240-247.

61. Metallidis P, Verros G, Natsivas S, and Papadimitriou C, (2003) *Fault Detection and Optimal Sensor Location in Vehicle Suspensions*, Journal of Vibration and Control, Vol 9, pp 337-359.
62. Metallidis P, Stavrakis I, Natsivas S, (2008) *Parametric Identification and Health Monitoring of Complex Ground Vehicle Models,* Journal of Vibration and Control, Vol 14, pp 1021-1036.
63. Crolla D A, *Vehicle Dynamics-Theory into Practice*, (1996) IMechE Part D, Journal of Automobile Engineering, Vol 210, pp 83-94.
64. Ellis J R, (1994) *Vehicle Handling Dynamics*, Mechanical Engineering Publication Limited, London.
65. Metz L D, (2004) *What Constitutes Good Handling*, SAE Paper 2004-01-3532.
66. Wong J Y, (2001) *Theory of Ground Vehicles*, John Wiley & Sons, Inc.
67. Nalecz A G and Bindmann A C, (1989) *Handling Properties of Four Wheel Steering Vehicles*, SAE Paper, 890080.
68. Hac A and Bodie M O, (2002) *Improvements in Vehicle Handling Through Integrated Control of Chassis Systems*, Int. Journal of Vehicle Design, Vol 29/1, pp 83-110.
69. Bodie M O and Hac A, (2000) *Closed Loop Yaw Control of Vehicles Using Magneto-rheological Dampers,* SAE Paper, 2000-01-0107.
70. Data S and Frigerio F, (2002), *Objective Evaluation of Handling Quality*, IMechE Part D, Journal of Automobile Engineering, Vol 216, pp 297-305.
71. Pacejka H B, (2002), *Tyre and Vehicle Dynamics*, Oxford: Butterworth-Heinemann.
72. Pacejka H B and Bakker E, (1993) *The Magic Formula Tire Model*, Vehicle System Dynamics-Supplement, Vol 21, pp 1-18.
73. Pacejka H B and Besselink I J M, (1997) *Magic Formula Tire Model With Transient Properties,* Suppl. Vehicle System Dynamics, Vol 27, pp 234-249.
74. Jansen S T H and Oosten J J M V, (1995) *Development and Evaluation of Vehicle Simulation Models for a 4WS Application*, Vehicle System Dynamics, Vol 24, pp 343-363.
75. O'Kane C and Timoney S, (2004) *Investigation of Four Wheel Steering Algorithms for a Formula SAE Car*, SAE Paper, 2004-01-1066.

76. Hegazy S, Rahnejat H and Hussain K, (2000) *Multi-body Dynamics in Full-vehicle Handling Analysis Under Transient Maneuver*, Vehicle System Dynamics, Vol 34, pp 1-24.
77. Blundell M V, (1999) *The Modeling and Simulation of Vehicle Handling Part 2: Vehicle Modeling*, IMechE Part K, Journal of Multibody Systems Dynamics, Vol 213, pp 119-134.
78. Blundell M V, (1999) *The Modeling and Simulation of Vehicle Handling Part 3: TireModeling*, IMechE Part K, Journal of Multibody Systems Dynamics, Vol 214, pp 1-32.
79. Blundell M V, (1999) *The Modeling and Simulation of Vehicle Handling Part 4: Handling Simulation*, IMechE Part K, Journal of Multibody Systems Dynamics, Vol 214, pp 71-94.
80. Sayers M W and Han D, (1996) *A Generic Vehicle Model for Simulating Handling and Braking*, Vehicle System Dynamics-Supplement, Vol 25, pp 599-613.
81. Hegazy S, Rahnejat H and Hussain K, (1999) *Multi-body Dynamics in Full-vehicle Handling Analysis*, IMechE, part K, Journal of Multibody Systems Dynamics, Vol 213, pp 19-31
82. ISO-3888, (1975) Passenger Cars- Test Track for a Severe Lane-change Maneuver.
83. Cao D, (2008) *Theoretical Analyses of Roll- and Pitch-Coupled Hydro-pneumatic Strut Suspensions*, PhD Thesis, Concordia University, Canada.
84. Sharp R S, (1991) *Computer Codes for Road Vehicle Dynamic Models*, Proceedings of Autotech 91, Brimingham, UK.
85. Sharp R S and Crolla D A, (1987) *Road Vehicle Suspension System Design- a Review*, Vehicle System Dynamics, Vol 16, pp 167-192.
86. ISO 2631-1, (1997) *Mechanical Vibration and Shock Evaluation of Human Exposure to Whole Body Vibration-part 1: General requirements*.
87. Sharp R S and Hassan S A, (1986) *An Evaluation of Passive Automotive Suspension Systems with Variable Stiffness and Damping Parameters*, Vehicle System Dynamics, Vol 15, pp 335-350.

88. Rajalingham C and Rakheja S (2003) *Influence of Suspension Damper Asymmetry on Vehicle Vibration Response to Ground Excitation*, Journal of Sound and Vibration, Vol 266, pp 1117-1129.
89. Warner B and Rakheja S (1996) *An Investigation of the Influence of High Performance Dampers on the Suspension Performance of a Quarter Vehicle*, SAE Paper, 962552.
90. Kim C, Ro P I, and Kim H, (1999) *Effect of the Suspension Structure on Equivalent Suspension Parameters,* Proceedings of IMechE, Journal of Automobile Engineering, Vol 213, pp 457-470.
91. Verros G, Natsivas S and Stepan G (2000) *Control and Dynamics of Quarter-Car Models with Dual-rate Damping*, Journal of Vibration and Control, Vol 6, pp 1045-1063.
92. Verros G, Natsiavas S, and Papadimitriou C, (2005) *Design Optimization of Quarter-Car Models with Passive and Semi-active Suspensions Under Random Road Excitation*, Journal of Vibration and Control, Vol 11, pp 581-606.
93. Hac A, (1987) *Adaptive Control of Vehicle Suspension*, Vehicle System Dynamics, Vol 16, pp 57-74.
94. Dahlberg T, (1978) *Ride Comfort and Road Holding of a 2-DOF Vehicle Traveling on a Randomly Profiled Road*, Journal of Sound and Vibration, Vol 58, pp 179-187.
95. ISO/TC108/SC2/WG4 N57, (1982) Reporting Vehicle Road Surface Irregularities.
96. Captain K M, Boghani A B, and Wormley D N, (1979) *Analytical Tire Models for Dynamic Vehicle Simulation*, Vehicle System Dynamics, Vol 8, pp 1-32.
97. Sun T, Zhang Y and Barak P, (2002) *Quarter Vehicle Ride Model*, SAE Paper, 2002-01-1581
98. Kim C and Ro P I, (1998) *A Sliding Mode Controller for Vehicle Active Suspension Systems with Non-linearities,* IMechE part D, Journal of Automobile Engineering, Vol 212, pp. 79-92.
99. Hrovat D, (1997) *Survey of Advanced Suspension Developments and Related Optimal Control Applications*, Automatica, Vol 33, pp 1781-1717.

100. Sun T, Zhang Y and Barak P, (2002) *4 DOF Vehicle Ride Model*, SAE Paper 2002-01-1580.
101. Barak P, Panakanti N and Desai T, (2004) *Effect of Chassis Design Factors (CDF) on the Ride Quality Using a Seven Degree of Freedom Vehicle Model*, SAE Paper 2004-01-1555.
102. Yagiz N, Hacioglu Y and Taskin Y, (2008) *Fuzzy Sliding-Mode Control of Active Suspensions*, IEEE Transactions on Industrial Electronics, Vol 55/11, pp 3883-3890.
103. Rill G, (1986) *Steady State Cornering on Uneven Roadways*, SAE Paper, 860575.
104. Mashadi B, Crolla D A, (2005) *Influence of Ride Motions on the Handling Behavior of Passenger Vehicle*, IMechE Part D: Journal of Automobile Engineering, Vol 219, pp 1047-1058.
105. Stone M R, Demetrou M A, (2000) *Modeling and Simulation of Vehicle Ride and Handling Performance*, Proceedings of the 15th IEEE International Symposium on Intelligent Control (ISIC 2000).
106. Warner B, (1996), *An Analytical and Experimental Investigation of High Performance Suspension Dampers*, PhD Thesis, Concordia University, Canada.
107. Anderson R J, and Fan Y, (1990) *Dynamic Testing and Modeling of a Bus Shock Absorber*, SAE Paper 902282
108. Duym S, Stiens R and Rebrouck K (1997) *Evaluation of Shock Absorber Models*, Vehicle System Dynamics, Vol 27, pp 109-127.
109. Basso R, (1998) *Experimental Characterization of Damping Force in Shock Absorber with Constant Velocity Excitation*, Vehicle System Dynamics, Vol 30, pp 431-442.
110. Duym S W R, (2000) *Simulation Tools, Modeling and Identification, for an Automotive Shock Absorber in the Context of Vehicle Dynamics*, Vehicle System Dynamics, Vol 33, pp 261-285.
111. Gacka S P and Doherty C G, (2006) *Design Analysis and Testing of Dampers for a Formula SAE Race Car*, SAE Paper, 2006-01-3641

112. Sohn H C, Hong K S And Hedrick J K, (2000) *Semi-active Control of the MacPherson Suspension Systems: Hardware-in-the-loop simulations*, Proceedings of IEEE, Int. Conference on Control Application, Anchorage, USA.
113. Misselhorn W E, Theron N J and Els P S, (2006) *Investigation of Hardware-in-the-loop for Use in Suspension Development*, Vehicle System Dynamics, Vol 44, 2006, pp 65-81.
114. Batterbee D C and Sims N D, (2007) *Hardware-in-the-loop Simulation of Magnetorheological Dampers for Vehicle Suspension Systems*, IMechE Part I Journal of Systems and Control Engineering, Vol 221, pp 265-272.
115. Xiaoxi H, (2009) *Modeling and Analysis of a Semi-active Magneto-rheological Damper Suspension Seat and Controller Synthesis*, Master Thesis, Concordia University, Canada.
116. Ma X Q, (2006) *Dynamic Characterization of a Magneto-rheological Fluid Damper and Synthesis of a Semi-active Suspension Seat*, PhD Thesis, Concordia University, Canada.
117. Dixon J C, (2007) *The shock Absorber Handbook*, SAE Inc, Warrendale, PA.
118. Simms A and Crolla D, (2002) *The Influence of Damper Properties on Vehicle Dynamic Behavior*, SAE Paper, 2002-01-0319.
119. Fukushima N, Hidaka K and Iwata K, (1983) *Optimum Characteristics of Automotive Shock Absorbers Under Driving Conditions and Road Surfaces*, Int. Journal of Vehicle Design, Vol 4, pp 463-473.
120. Eslaminasab N, (2007) *Development of a Semi-active Intelligent Suspension System for Heavy Vehicles*, PhD Thesis, University of Waterloo, Canada.
121. Ahmed A K W and Rakheja S, (1991) *An Equivalent Linearization Technique for the Frequency Response Analysis of Asymmetric Dampers*, Journal of Sound and Vibration, Vol 153, pp 537-542.
122. Calvo J A, Lopez-Boada B, San Roman J L and Gauchia A, (2009) *Influence of a Shock Absorber Model on a Vehicle Dynamic Simulation*, Proc of IMechE Part D: Journal of Automobile Engineering, Vol 223, pp 189-202.

123. He Y, and McPhee J, (2007) *A Review of Automated Design Synthesis Approaches for Virtual Development of Ground Vehicle Suspensions*, SAE Paper, 2007-01-0856.

124. Gobbi M and Mastinu G, (2001), *Analytical Description and Optimization of the Dynamic Behaviour of Passively Suspended Road Vehicles*, Journal of Sound and Vibration, Vol 245, pp 457-481.

125. Scheibe F and Smith M C, (2009) *Analytical Solutions for Optimal Ride Comfort and Tire Grip for Passive Vehicle Suspensions*, Vehicle System Dynamics, Vol 47, pp 1229-1252.

126. Georgiou G, Verros G and Natsiavas S, (2007), *Multi-objective Optimization of Quarter-car Models with a Passive or Semi-active Suspension System*, Vehicle System Dynamics, Vol 45, pp 77-92.

127. Georgiou G and Natsiavas S, (2009), *Optimal Selection of Suspension Parameters in Large Scale Vehicle Models*, Vehicle System Dynamics, Vol 47, pp 1147-1166.

128. Hong K S, Jeon D S, Yoo W S, Sunwoo H, Shin S Y, Kim C M and Park B S, (1999) *A New Model and an Optimal Pole-placement Control of the MacPherson Suspension System,* SAE Paper, 1999-01-1331.

129. Anderson E, Sandu C, and Southward S, (2007) *Multibody Dynamic Modeling and System Identification of a Quarter-car Test Rig with McPherson Strut Suspension,* SAE Paper, 2007-01-4184.

130. Jonsson M, (1991) *Simulation of Dynamical Behavior of a Front Wheel Suspension,* Vehicle System Dynamics, Vol 20, pp 269-281.

131. Stenson C Asplund and Karlsson L, (1994) *The Nonlinear Behavior of a MacPherson Strut Wheel Suspension,* Vehicle System Dynamics, Vol 23, pp 85-106.

132. Fallah M S, (2010) New Dynamic Modeling and Practical Control Design for Macpherson Suspension System, Ph D Thesis, Concordia University, Canada.

133. Joo D S, (1999) *Fuzzy Logic Controller of Nonlinear Active Suspension Active Suspension System*, PhD Thesis, University of Detroit, Detroit.

134. Cole D J and Cebon D, *Truck Suspension Design to Minimize Road Damage*, IMechE Part D, Journal of Automobile Engineering, Vol 210, pp 95-107.
135. Stone and Cebon, (2002) *A Preliminary Investigation of an Active Roll Control System for Heavy Vehicles*, 6th International Symposium on Advanced Vehicle Control, AVEC2002 Hiroshima, Japan.
136. Hudha K, Jamaluddin H, Samin P M and Rahman R A, (2003) *Semi Active Roll Control Suspension (SARCS) System on a New Modified Half Car Model*, SAE Paper, 2003-01-2274.
137. Bastow D, (1993) *Car Suspension and Handling*, SAE Inc. Warrendale, USA.
138. Suh C H, (1991), *Suspension Analysis with Instant Screw Axis Theory*, SAE Paper, 910017.
139. http://www.2carpros.com/forum/2004-chrysler-sebring-alignment-vt215020.html (accessed Sept 2010).
140. Edara R and Shih S, (2004) *Effective Use of Multibody Dynamics Simulation in Vehicle Suspension System Development*, SAE Paper, 2004-01-1547.
141. Holdman P and Kohn P, (1998) *Suspension Kinematics and Compliance-Measuring and Simulation*, SAE Paper, 980897.
142. Das S, Ramamurthy P and Mahajan S, (2007) *Correlation Issues and Simulation of Kinematics and Compliance in Automotive Suspensions*, SAE Paper, 2007-26-046.
143. Morse P, (2004) *Using K&C Measurements for Practical Suspension Tuning and Development*, SAE Paper, 2004-01-3547.
144. Nalecz A G, (1989) *Application of Sensitivity Methods to Analysis and Synthesis of Vehicle Dynamics Systems*, Vehicle System Dynamics, Vol 18, pp 1-44.
145. Technical Service Bulletin for Chrysler/Plymouth/Dodge Cars.
146. Raghavan M, (2004) *Suspension Design for Linear Toe-change Curves: A Case Study in Mechanical Synthesis,* Transaction of ASME, Journal of Mechanical Design, Vol 126, pp 278-282.
147. Loeb J S, Guenther D A, Chen H F and Ellis J R, (1990), *Lateral Stiffness, Cornering Stiffness and Relaxation Length of the Pneumatic Tire*, SAE Paper, 900129.

148. Rakheja S and Sankar S (1985) *Vibration and Shock Isolation Performance of a Semi Active "on-off" Damper*, Transactions of ASME, Journal of Vibration, Acoustics, Stress, and Reliability in Design, Vol 107, pp 398-403.
149. Swayze J L, Bacharch B I and Shankar S R, (1999) *Suspension Force Optimization Using Quarter Car Model with Elastomeric Elements*, SAE Paper, 1999-01-0753.
150. Garcia M J T, Kari L, Vinolas J and Gil-Negrete N, (2007), *Torsion Stiffness of a Rubber Bushing: a Simple Engineering Design Formula Including the Amplitude Dependence*, Journal of Strain Analysis, Vol 42, pp 13-21.
151. Matlab Product Help, MathWorks Inc 2007.
152. Rakheja S, Wang Z and Ahmed A K W, (2001), *Urban Bus Optimal Passive Suspension Study*, Final Report, Transport Canada, TP13787E.
153. Dixon J C, (1987) *The Roll Center Concept in Vehicle Handling Dynamics,* IMechE Part D, Journal of Automobile Engineering, Vol 201, pp 69-78.
154. Gerrard M B, (1999) *Roll Centers and Jacking Forces in Independent Suspensions-a First Principles Explanation and a Designer's Toolkit*, SAE Paper, 1999-01-0046.